CRANFIELD UNIVERSITY

MOHAMMAD ASGARYAN

Prediction of the remaining service life of superheater and reheater tubes in coal-biomass fired power plants

School of Applied Sciences
PhD

PhD
Academic Year: 2009 - 2013

Supervisor: Dr. N.J. Simms
Dr. S. Wu
April 2013

CRANFIELD UNIVERSITY

School of Applied Sciences

PhD

Academic Year 2009 - 2013

MOHAMMAD ASGARYAN

Prediction of the remaining service life of superheater and reheater tubes in coal-biomass fired power plants

Supervisor: Dr. N.J. Simms
Dr. S. Wu
April 2013

This thesis is submitted in partial fulfilment of the requirements for the degree of Doctor of Philosophy

ABSTRACT

As a result of concern about the effects of CO_2 emssions on the global warming, there is increasing pressure to reduce such emissions from power generation systems. The use of biomass co-firing with coal in conventional pulverised fuel power plants has provided the most immediate route to introduce a class of fuel that is regarded as both sustainable and carbon neutral as it produces less net CO_2 emissions. In the future it is anticipated that increased levels of biomass will be required to use in such systems to accomplish the desired CO_2 emissions targets. The use of biomass, however, is believed to result in severe fireside corrosion of superheater and reheater tubing and cause unexpected early failures of tubes, which can lead to significant economic penalties. Moreover, future pulverised fuel power systems will need to use much higher steam temeptures and pressures to increase the boiler efficiency. Higher operating temperatures and pressures will also increase the risk of fireside corrosion damage to the boiler tubing and lead to shorter component life.

Predicting the remaining service life of superheater and reheater tubes in coal-biomass fired power plants is therefore an important aspect of managing such power plants. The path to this type of failure of heat exchangers involves five processes: combustion, deposition, fireside corrosion, steam-side oxidation, and creep. Various models or partial models each of these processes are available from existing research, but to fully understand the impact of new fuel mixtures (i.e. biomass and coal) and changing operating conditions on such failures, an integrated model of all of these processes is required.

This work has produced an integrated set of models and so predicted the remaining service life of superheater/reheater tubes based on the three frameworks which have been developed by analysing those models used in depicting the five processes: one was conceptual and the other two were based on mathematical model. In addition, the outputs of the integrated mathematical models were compared with the laboratory generated data from Cranfield University as well as historical data from Central Electricity Research Laboratories.

Furthermore, alternative models for each process were applied in the model and the results were compared with other models results as well as with the experimental data. Based on these comparisons and the availability of models constants the best models were chosen in the integrated model.

Finally, a sensitivity analysis was performed to assess the effect of different model input values on the residual life superheater and reheater tubing. Mid-wall metal temperature of tubes was found to be the most important factor affecting the remaining service life of boiler tubing. Tubing wall thickness and outer diameter were another critical input in the model. Significant differences were observed between the residual life of thin-walled and thick-walled tubes.

Keywords:

Coal-biomass, model integration, hoop stress, mid-wall metal temperature, sensitivity analysis

ACKNOWLEDGEMENTS

I would like to express my great gratitude to my kind and patient supervisors Dr. Nigel Simms and Dr. Shaoimin Wu for their guidance, continuous support, encouragement and assistance throughout my PhD.

I wish to thank my subject advisor Professor John Oakey and Dr Tanvir Hussian for their great guidance and advice.

Acknowledgement and thanks are also extended to the staff of the department, in particular Miss Jessica Greenwood (Secretary) for her help and support of organising meetings.

I also want to thank Ala Khodier who kindly gave me his lab data to validate my model.

I would also like to express my deepest gratitude to my whole family Mum, Dad, brothers and sisters for their encouragement and support throughout every step of my study in the U.K.

I would finally like to extend my sincere thanks to my friends Angela and Gwynne Elder, Saleh Asgaryan, Ali Hadadian, Shohreh Ghazali, Alireza Alghassi, Gavin Walker, Graham Lewis, Roger Fowler, Grivin Chipula and David Kane.

TABLE OF CONTENTS

LIST OF FIGURES

LIST OF TABLES

LIST OF ABBREVIATIONS

A	A constant
A_i	A constant
A_{duct}	Surface area of target, m^2
A_f	Cross-sectional area at the point of the fracture, m^2
A_{free}	Cross section of the gas path, m^2
A_o	Original cross-sectional area, m^2
A_{op}	Actual operating time, h
A_P	Particle surface area, m
a_f	Accumulate frequency, %
B	A constant
B_i	A constant
$B_E(t,\theta)$	Deposition growth rates due to Brownian and Eddy diffusion, kg/s
b	A constant
C	A constant
C_c	Cunningham's factor
C_{ash}	Mass concentration of fly ash particle, kg/m^3
C_i	Condensation flux of the *i-th* condensable vapour, kg/m^3
c_i	A constant
$C_{p,m}$	Concentration of melted particles in the gas stream, kg/m^3
$C_{p,s}$	Concentration of solid particles in the gas stream, kg/m^3
C_w	Particle concentration of at the wall of the cold surfaces, kg/m^3
C_{FS}	Fuchs-Sutugin correction factor
C_{rate}	Corrosion rate, nm/h
c	A constant
D_i	Diffusion coefficient of species *i*, m^2/s
D_B	Brownian diffusivity, m^2/s
D	Diameter of the tube, m
d_p	Particle diameter, μm
d	A constant
E	Modulus of elasticity, Pa
E_{life}	Expected creep life in the absence of fireside corrosion, h
F_T	Thermophoretic forces, N
f_p	Probability of the particles to be centrifuged out of the eddy

f_{stick}	Total sticking coefficient
f_{am}	Ash melt fraction
f(T)	Sticking probability for the ash particles or deposit
f_v	Frequency of vortex shedding, s^{-1}
f	A constant
f_e	Fraction of the entrained ash
H	Thermophoretic coefficient, m/s
H_F	Heat flux, W/m^2
h	Heat transfer coefficient, $W/(m^2K)$
$I_f(t,\theta)$	Deposition rate by large particle impactions, kg/s
$I_w(t,\theta)$	Deposition rate of middle-sized particles, kg/s
$[i]$	Concentration of species *i*, $mole/m^3$
k_{diff}	Specific oxygen diffusion rate coefficient, $(m/s)^{-1}$
k_s	Char oxidation coefficient, $(m/s)^{-1}$
k_0	Pre-exponential factor, s^{-1}
k_c	Rate constant of chemical reactions, s^{-1} or 1/(sPa)
k_{cr}	Creep pre-exponential factor, $(MPa)^{-n}/h$
k_e	Erosion coefficient
k_B	Boltzmann constant, JK^{-1}
k_n	Knudsen number
k_t	thermal conductivity, W/(mK)
K_P	Parabolic rate constant, $(\mu m)^2/h$ or $(gcm^{-2})^2/s$
K_L	Linear rate constant, µm/h
L	A constant
l	Tube length, m
l_i	Deposits thickness, m
M_i	Molecular weight of species *i*, g/mole
$M_{L,co}$	Metal loss due to fireside corrosion, µm
$M_{L,ox}$	Metal loss due to steam-side oxidation, µm
$M_{L,cr}$	Metal loss due to creep deformation, µm
m_j	Mass of the *j-th* volatile products released from coal, kg
m_∞	Mass of volatiles released from coal after very long residence time, kg
m_{char}	Single char mass, kg
$m(t,\theta)$	Deposit weight at *t* and angular position θ, kg
m	A constant
m_i	Mass of deposit per area, kg/m^2
$\dot{m}_{fuel}$	Mass flow rate of the fuel, kg/s
N	Reaction order
n	Exponent

n_w	Unit normal to the wall
P_1	Probability of particles hitting the surface
P_2	Probability of melted particle sticking to the surface
P_3	Probability of solid particle sticking to the surface
P	Internal steam pressure, Pa
p_i	Partial pressures of condensing vapours in the vicinity of tubes, Pa
P_g	Flue gas pressure, Pa
P_{O2}	Partial pressure of oxygen, Pa
P_B	Partial pressure of gaseous reactant, Pa
Pr	Prandtl number
P_{OSD}	Orr-Sheryy-Dorn parameter
P_{LM}	Larson-Miller parameter
P_{MS}	Manson-Succop parameter
p_{si}	Saturation pressure of *i-th* component, Pa
Q	Activation energy, J/mole
$\dot{Q}_f$	Flue gas volume flow rate, m^3/s
R $\dot{R}$	Universal gas constant, J/(moleK)
R_C	Rate of chemical reactions, mole/(m^3s)
Re	collection parameter
R_t	Reynolds number
R_{life}	Total thermal resistance, W/(mK)
r	Residual service life, h
r_i	Radius of particle, m
$S_H(t,\theta)$	Tube radius, m
$S_f(t,\theta)$	Shedding rate by drop detachment, kg/s
Stk	Mass accumulation rate in a control domain caused by melt film, kg/s
Stk_e	Stoke number
Sh	Effective Stokes number
Sc	Sherwood number
Sr	Schmidt number
T	Strouhal number
T_H	Temperature, K or °C
t	Deposition rates by thermophoresis, kg/s
u	Time, s or h
V	Velocity, m/s
W_{th}	Volatile matter in coal
X_i	Wall thickness of the tube, mm
X	Mole fraction of species *i*
X_{life}	Oxide thickness, μm

x_0	expected creep life under combined effects of stress and corrosion, h
Y	Limiting distance from the cylinder surface at $\theta=2\pi$, m
β	Mas transfer coefficient, m/s
ξ_i	Condensation efficiency
θ	Angle of impaction, °
θ_{bf}	Blowing factor
ρ	Density, kg/m^3
η_t	Target efficiency
η_I	Local impaction efficiency
σ	Applied stress, Pa
ε	Strain
$\dot{\varepsilon}_s$	Creep rate, h^{-1}
μ	Dynamic viscosity, Pa.s
Γ	A correlation
ν	Kinematic viscosity, m^2/s
ϕ_i	Deposit porosity
λ	Thermal diffusivity, m^2/s

1 INTRODUCTION

1.1 Motivation

The needs for increasing amounts of electricity and widespread concerns about the effects of emissions of greenhouse gases on enhanced global warming are two key driving forces in the development of the power generation industries around the world. The latest International Energy Authority (IEA) predictions indicate a 40% increase in primary energy demand by 2030 [1].

Concerns about the increasing emissions of CO_2, and other greenhouse gases, into the earth's atmosphere have been growing during the last two decades; consequently, there have been increasing efforts to reduce the amount of CO_2 released into the atmosphere. For example, the Kyoto Protocol committed many countries in the world to reduce greenhouse gases emissions by 5.2% by 2008-2012 compared to 1990 level. The latest UK government target is also for an 80% reduction in CO_2 emissions by 2050 [1]. In the UK large traditionally coal-fired power stations are major sources for CO_2 emissions. The potential routes to reduce CO_2 emissions (all of which have advantage and disadvantages) in power generation systems are being developed including [1]:

- Increasing power plant efficiencies; e.g. by increasing steam temperatures/pressures
- Fuel switching; e.g. by increasing the proportion of biomass mixed with coal
- Carbon capture and storage (CCS)
- Increasing the proportion of other sources of energy such as nuclear or renewable energy; e.g. wind, wave, solar power.

New solid fuel combustion systems can apply higher steam temperatures (e.g. targets of 650, 700 and 760°C set by different organizations), higher levels of biomass (up to ≈30%) mixed with coal and incorporate a post combustion CCS system [1].

Co-firing is the simultaneous combustion of two or more fuels in the same boiler. Co-firing of biomass with coal in existing thermal power plants to generate electricity has been used as a near-term, low cost way to use biomass for reducing CO_2 emissions. Co-firing biomass with coal has been implemented in about 150 power stations, either as pilot scales or commercial scales [2]. Approximately, 100 of these are in Europe, mainly

in Germany, Finland, Denmark and U.K [2]. As a result of different national policies, for example, national regulations committed Danish power plants to burn annually at least 1 million tons of straw by the year 2004 [3]. In addition, in the UK, the levels of biomass co-firing have steadily increased during the past 10 years up to 10% for some biomass-coal mixtures, with the use of still higher levels being actively examined [4]. Biomass is the world's fourth largest energy, and its contribution fraction is about 14% [5]. The motivations for using more energy from biomass are both that as a renewable fuel it reduces net CO_2 emissions and to utilize biomass residues and wastes [6].

Advantages of co-firing of coal with biomass, other than net CO_2 reduction, are:

- Co-firing of coal with biomass reduces SO_x and NO_x emissions due to the lower sulphur and nitrogen content in biomass than in coal [6].
- Combustion of biomass with coal in coal-fired boilers is a practical approach to partial substitution of fossil fuel in conventional power plants [7].
- Addition of biomass can also improve the ignition characteristics of coal [5].

However, during combustion of biomass and/or pulverised coal, ash particles formed from mineral matter transformations may deposit onto heat transfer surfaces, causing costly reductions in heat transfer rates and boiler efficiencies [8]. Furthermore, biomass derived-deposits result in high temperature fireside corrosion of heat exchanger tubes induced by the condensation of high levels of alkali chlorides onto the tube surfaces [9]. This will lead to a reduction in the cross-sectional area of the tube wall.

Boiler tubes are critical components in energy conversion systems in which heat energy is used to convert water into high pressure superheated steam, which is subsequently delivered to steam turbines for electric power generation. The combustion gases produced by burning coal and/or biomass in the furnace evaporate water into steam in the waterwall tubes and then pass through the superheater and reheater tubes [10]. The objective of superheater tubes is to increase the steam temperature, after it comes from the boiler drum, to a value higher than saturation to achieve the following goals [11]:

- To increase the thermodynamic efficiency of the turbine where the steam will be expanded.
- To remove the humidity from the steam.

A typical arrangement of superheater and reheater tubes in a boiler of a thermal power plant is shown in Figure 1.1.

Figure 1.1 Typical arrangement of superheater and reheater tubes in a boiler

One of the major objectives in power station development is to pursue a higher thermal efficiency. This can be achieved by increasing the temperature and pressure of the steam entering the turbine [12; 13]. For example an increase in steam temperature from temperatures below 595 to 760°C results in a thermal efficiency increase from 35% to 47%, while reducing CO_2 emissions by approximately 30% [14]. Although increased thermal efficiency brings benefits associated with the conservation of fossil fuels and reduction of CO_2 emissions, the change in steam temperature will affect creep rupture strength, fireside corrosion resistance and steamside oxidation resistance of the superheater and reheater materials [12; 13].

Boiler tube failures can be classified under six major causes [15]:

1. Stress rupture (Creep or long-term overheating failure)
2. Fire side corrosion (High temperature corrosion)
3. Steamside oxidation
4. Fatigue

5. Erosion (e.g. fly ash and/ or coal particle erosion)
6. Lack of quality control.

Superheater tubes are normally located in the final stages of the boiler. The highest pressure and highest temperature steam is carried inside superheater tubes which are exposed to high temperature combustion gases. Consequently, the superheater tubes are most vulnerable to high temperature creep and corrosion failures while furnace wall and economizer tubes operate at lower temperatures where the creep damage can be neglected [16; 17]. Creep rupture failure of superheater/reheater tubes is a principal cause of forced outages of coal and/ or biomass fired boilers [18]. Virtually 90% of failures caused by high temperature creep or long-term overheating taking place in superhetaer and rehetaer tubes [19]. What follows is an example of this kind of failure in a high temperature superheater. Table 2-3 shows boiler operation conditions and the specification of the high temperature superheater tube [20]:

Table 1-1 Operation conditions and tube specifications

Steam flow rate	595kg/h
Steam temperature	540°C
Steam pressure	13.73MPa
Fuel	Pulverised coal
Tube material	SA-213 T22
Outer diameter	44.45mm
Wall thickness	6.6mm

The visual examination of the tube revealed that [20]:

- The rupture was a 38mm- long longitudinal split, showing virtually no reduction in wall thickness.
- The thickness of outer scale and deposits was 0.13cm while the inner scale thickness measured 0.08cm.

Creep was the cause of failure of the superheater tube. At the time of failure the tube metal temperature on its inner surface was about 650°C whereas the safe design oxidation limit for T22 was 605°C at the time when this boiler was designed in the early 1960s. Thick inner scale increased the overall thermal resistance of the tube so that tube metal temperature increased by 44°C. This resulted in overheating of the tube.

Therefore, having a tube metal temperature above 650°C for T22 alloys for a long period of time led to the failure of this tube [20].

Figure 1.1 shows a typical superheater tube from a utility boiler failed by creep. The rupture has a fish-mouth shape.

Figure 1.2 Superheater tube from a utility boiler failed by creep

Another case history is the long term, high temperature failures of a reheater tube. The boiler operation conditions and the specification of the reheater tube are given in Table 2-3 [20]:

Table 1-2 Operation conditions and tube' specification

Steam flow rate	725000kg/h
Steam temperature	540°C
Steam pressure	13.7MPa
Fuel	Pulverised coal
Tube material	SA-213 T22
Outer diameter	44.45mm
Wall thickness	3.8mm

The visual examination of the tube revealed that [20]:

- The failure was a wide-open burst, with the tube wall drawn to a knife-edge at the failure.
- The thickness of outer scale and ash deposits were 0.028 and 0.11cm respectively.
- The steamside scale measured from 0.038 to 0.066cm in thickness.

The insulating effects of steamside oxide layers caused the tube metal temperature to increase. This resulted in overheating of the tube's metal and its eventual failure by creep [20].

During the boiler operation fireside corrosion as well as steam-side oxidation continuously reduce the wall thickness of the heat exchangers tubes and thereby progressively raise the hoop stresses acting on the component [21]. These degradation processes are responsible for accumulating microstructural damages in the tubes leading to a reduction in the load bearing capacity of the tubes. Failure occurs when this falls below a critical level determined by component geometry and loading [10]. Although the material of superhetaer tubes are more resistant compared to other tubes of the boiler, failures of superheater tubes take place more frequently due to their operating conditions [16].

Such an unscheduled tube failure is a major threat to the availability of the boiler. In the past thermal power plants were forced to choose between premature replacement of heat exchanger tubes and excessive outages due to absence of any accurate methodology for predicting the remaining service life of these tubes [18; 22]. This has attracted great interest in predicting the remaining life of heat exchangers in coal-biomass fired power plants. By assessing the extent of damage and the remaining service life of tubes it should be possible to achieve the following goals:

- To achieve the most economic use of the tubes and to plan in advance for tubes replacement in order to avoid failures and unplanned shutdown since unexpected failures cost a lot of money (e.g. several hundred thousand dollars a day) due to lost sales of electricity as well as loss of industrial production [10; 23] .
- To extend the component service life beyond the original design life and subsequently to renew the license for existing thermal power stations [24].

- To make the right decisions, in time, among the possible choices of taking no action, repair or replacement [24].
- To perform a safe operation of the boiler [25].

1.2 Aims and Objectives

1.2.1 Aim

The aim of this project is to develop improved integrated models for the degradation of superheater/reheater tubes to enable better prediction of the remaining service life of these tubes in power stations when co-firing coal and biomass.

1.2.2 Objectives

- To integrate models of fuel combustion, deposition, fireside corrosion, steam-side oxidation, and creep alongside heat transfer. The integrated models should be able to predict the remaining service life of the component.
- To select optimal models for individual mechanisms based on model performance and validation.
- To investigate the performance of the integrated models through sensitivity analysis and model validation.

1.3 Research methodology

Predicting the remaining service life of superheater and reheater tubes in coal-biomass fired power plants is an important aspect of managing such power plants. The path to the failures of heat exchangers in such power plants is made up of five sub-processes:

1. Combustion
2. Deposition
3. Fireside corrosion
4. Steam-side oxidation
5. Creep

Models for each of these sub-processes are available from existing research. Initially, the five models have been integrated using Excel Spreadsheet. Subsequently, the models' predictions were compared to industrial and lab data. In addition, sensitivity

analysis of the integrated models was done in Excel Spreadsheet. Lab data were collected from Cranfield University lab [26] and from C.E.R.L report [21]. An important and on-going part of the research process was to critically review open and grey publications.

1.4 Thesis structure

This thesis is divided into six chapters and five appendices and is organised in the following:

CHAPTER 2 presents a review of literature for coal-biomass combustion models such as volatiles formation and oxidation and mineral matter transformations, ash deposition which includes various mechanism of ash deposition on the tube surfaces, fireside corrosion (high temperature corrosion), steam-side oxidation, and creep of tube's materials.

CHAPTER 3 details the study of the different fuels (coal and/ or biomass) burnt in a thermal power plant, different combustion systems used in power industry such as a fixed bed on a grate, a fluid bed, and a pulverised or entrained bed.

CHAPTER 4 presents the integration of the five models (combustion, deposition, fireside corrosion, steam-side oxidation, and creep), the integrated models predictions, and comparison of the models predictions with the lab and the industrial data, and finally discussions on the results.

CHAPTER 5 presents a sensitivity analysis of the integrated models for various models inputs (e.g. tube mid-wall temperature).

CHAPTER 6 lists the conclusions and suggestions for further study.

2 LITERATURE REVIEW

2.1 Introduction

The operating environments of coal-biomass fired steam generators are among the most severe of any large engineered structure. Superheater/reheater alloys in these applications are expected to have a useful service life of 10 or more years in such operating conditions. On the fireside, issues of high temperature (creep due to long term over-heating) and corrosion (caused by the products of combustion from a variety of coal and/or biomass) can seriously reduce the tube-wall thickness and lead to premature failure. On the steamside, the oxidation of the boiler tube by high-temperature steam can also reduce the tube wall thickness. Tube service temperatures range from 370 to 650°C and higher. To be reliable, tube materials need to possess good high-temperature strength, creep resistance and resist operating environments [20].

The lifing of heat exchangers can be considered as being the result of five sub-processes: combustion, deposition, fireside corrosion, steam-side oxidation, and creep. Therefore, to fully understand the impact of new fuel mixes (i.e. biomass and coal) on heat exchanger tube failures, the integration of models of all of these processes is necessary. There has been found little research on the integration of the five sub-processes in the open literature.

2.2 Solid fuel combustion

2.2.1 Thermal decomposition of coal and biomass

Pyrolytic studies of coal devolatilisation are of interest for obtaining rates of coal decomposition for practical purposes, as well as for the characterisation of coal materials [27]. Thermal decomposition (devolatilisation) of coal and biomass takes place when they are heated up. Both the organic and the mineral parts of the fuel undergo devolatilisation. As a result, gases stored in pores of coal structure during its formation, are released. The solid body that remains after coal and biomass devoaltilisation is called char or coke and contains organic substances and ash. The devolatilisation equation of coal and biomass particles may have the following general form [28; 29]:

$$Fuel \rightarrow volatiles + solid\ residue \quad \textbf{(2-1)}$$

The rate of this reaction can be described by a first order Arrhenius equation:

$$k_c = k_0 \exp(-Q/RT) \quad \textbf{(2-2)}$$

where k_c is rate constant of chemical reaction (s^{-1}), k_0 is pre-exponential factor (s^{-1}), Q is activation energy(J/mole), R is gas constant (J/(moleK), and T is temperature (K).

During heating of coal in an inert atmosphere, volatile substances such as water, steam, methane, carbon dioxide, carbon monoxide, nitrogen, volatile tar and gases are liberated [28]. Appreciable evolution of these gases typically starts at about 277°C. Volatile product release rates are very sensitive to temperature but are very insensitive to pressure [27; 30]

The rate of release of the individual *j*-th volatile product in a single reaction of the *N*-th order from 1kg coal (water and ash free state) can be calculated from the following equation [28]:

$$\frac{dm_j}{dt} = k_{0j} \exp(-Q_j/RT) \left(m_{\infty j} - m_j\right)^{N_j} \quad \textbf{(2-3)}$$

where m_j is mass of the *j-th* volatile products released from coal (kg), $m_{\infty j}$ is mass of volatiles released from coal after very long residence time ($t \rightarrow \infty$) (kg), N_j is order of reaction of the *j*-th product formation, and *t* is time (s).

Although a one-step mechanism for such a chemical reaction is the most convenient for mathematical modeling of coal decomposition one must be aware that the accuracy of such models are not very high [28]. For instance for the chemical reaction in Eq. (2-1) the total amounts of volatile can be described by kinetic equation [28]:

$$\frac{dm_v}{dt} = k_{0v} \exp(-Q_v/RT) \left(m_{\infty v} - m_v\right) \quad \textbf{(2-4)}$$

where m_v is mass of volatile products released from coal (kg), and $m_{\infty v}$ is the volatile content of coal (kg).

Eq. (2-4) can only be applied for the limited experimental conditions upon which they were based. Quantitative understanding of coal and/ or biomass thermal decomposition is significant for the efficient development of better coal-biomass combustion processes. For a given set of conditions, the values of k_{0v} and Q from different authors may vary. In addition, $m_{\infty v}$ is dependent on both the experimental temperature and the technique. For example, the value of $m_{\infty v}$ obtained from a rapid devolatilsation of a pulverised coal dispersed in carrier gas is considerably larger than that those obtained by the relatively slow heating of a small bed of pulverised coal in a crucible [31].

The typical values of pre-exponential factor and the activation energy are given in Table 2-1[28]:

Table 2-1 Kinetic data of coal devolatilisation [28]

Kinetic data	Highly swelling coals	Weakly swelling coals
k_{0v}, s^{-1}	6.0E+05	1.5E+05
Q_v, kJ/mol	74	74

In addition a multi-step model for coal devolatlization has been suggested by Tomeczek [28]:

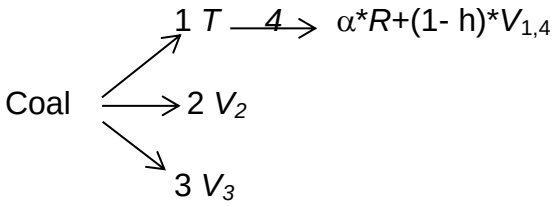

(2-5)

where V is volatile matter in coal, T is temperature (K) and h is heat transfer coefficient ($W/(m^2K)$).

For which the following kinetic equations have been suggested by Tomeczek [28]:

$$\frac{dm_T}{dt} = k_{01}\exp(-Q_1/RT)\,(m_{\infty 1} - m_T)^2 \qquad \textbf{(2-6)}$$

$$\frac{dm_{V1,4}}{dt} = k_{01}\exp(-Q_1/RT)\,(m_{\infty 1} - m_T) - k_{04}\exp(-Q_4/RT)\,m_T(1-h) \quad \textbf{(2-7)}$$

$$\frac{dm_{V2}}{dt} = k_{02}\exp(-Q_2/RT)\,(m_{\infty 2} - m_{v2})^2 \quad \textbf{(2-8)}$$

$$\frac{dm_{V3}}{dt} = k_{03}\exp(-Q_3/RT)\,(m_{\infty 3} - m_V)^2 \quad \textbf{(2-9)}$$

For coal with ash content of 6.2% in a dry state, volatile matter of 35.7% (dry and ash free state), and carbon content of 64.3% (dry and ash free state) *h* (heat transfer coefficient, W/m^{2}K) is 0.8 and kinetic constants are given in Table 2-2 [28]:

Table 2-2 Kinetic constants of above models [28]

Kinetic data	Model 1	Model 2	Model 3	Model 4
k_{0v}, s^{-1}	1.7E+12	8.4E+03	3.7E+06	2.70E+04
Q_v, kJ/mol	188	72.2	142.5	60
m_∞%, kg/kg (waf)	16.9%	9.0%	6.5%	

Kinetic data of coal devolatilisation are summarised in Table 2-3 assuming that the volatiles contain only CO, CO_2, H_2O, CH_4, C_2H_6, and C_6H_6. C_6H_6 represents the mass of liquid hydrocarbons.

Table 2-3 Kinetic data of coal devolatilisation [28]

Volatiles	k_{0v}, s^{-1}	Q_v, kJ/mole	m_∞%, kg/kg(waf)
H_2O	1.0E+12	312	4.2
CH_4	1.5E+04	85	2.01
CO	5.0E+03	75	5.67
CO_2	1.8E+02	40	4.85
C_2H_6	1.5E+03	65	1.11
C_6H_6	1.5E+07	120	12
C_6H_6	1.0E+12	312	3.6

2.2.2 Volatile combustion models

The volatiles produced during coal/biomass devolatilization can be combusted close to the surface of the particle, immediately after they are released from the porous coal

structures, or at some distance from the surface. Volatiles combustion is normally modelled in a two-step process: oxidation to carbon monoxide with subsequent oxidation to carbon dioxide. For the main products (CO, CO_2, H_2O, CH_4, C_2H_6, and C_6H_6) of coal devolatilzation the following homogeneous gas-phase reactions and rate expressions are presented in Table 2-4 [28]:

Table 2-4 Rates of homogeneous gas-phase reactions [28]

Reaction	Reaction rate, mole/(m^3s)
$CH_4 + 1.5O_2 \rightarrow CO + 2H_2O$	$\dot{R} = 2.8 * 10^9 \exp(-\frac{202.64}{RT})[CH_4]^{-0.3}[O_2]^{1.3}$
$C_2H_4 + 2.5O_2 \rightarrow 2CO + 3H_2O$	$\dot{R} = 7.31 * 10^9 \exp(-\frac{125.604}{RT})[C_2H_6]^{0.1}[O_2]^{1.65}$
$C_2H_6 + 4.5O_2 \rightarrow 6CO + 3H_2O$	$\dot{R} = 1.35 * 10^9 \exp(-\frac{125.604}{RT})[C_6H_6]^{-0.1}[O_2]^{1.85}$
$CO + 0.5O_2 \rightarrow CO_2$	$\dot{R} = 2.238 * 10^{12} \exp\left(-\frac{167.472}{RT}\right)[CO][O_2]^{0.25}[H_2O]^{0.5}$
$CO_2 \rightarrow CO + 0.5O_2$	$\dot{R} = 5 * 10^8 \exp(-\frac{167.472}{RT})[CO_2]$

where $\dot{R}$ is rate of the homogeneous reaction (mole/m^3s), R is the universal gas constant (J/moleK), T is temperature (K), and $[i]$ is volatiles concentration (mole/m^3).

Compared with coal, biomass is characterized by a higher volatile content. As for coal, biomass volatiles contain mainly CO, CO_2, H_2, CH_4, and C_xH_y. H_2, CH_4, and C_xH_y are subsequently oxidised to form H_2O and CO respectively. CO is further oxidized to form CO_2. Rates equation for such homogeneous gas-phase reactions are given in Table 2-5 [32].

Table 2-5 Rates expression of homogeneous gas-phase reactions [32]

Reaction	Reaction rate, mole/(m^3s)
$H_2 + O_2 \rightarrow 2H_2O$	$\dot{R} = 51.8 * T^{1.5} \exp(-\frac{3420}{T})[H_2]^{1.5}[O_2]$
$CH_4 + 1.5O_2 \rightarrow CO + 2H_2O$	$\dot{R} = 1.6 * 10^{10} \exp(-\frac{24157}{T})[CH_4]^{0.7}[O_2]^{0.8}$
$C_xH_y + (x/2+y/2.5)O_2 \rightarrow xCO + y/2H_2O$	$\dot{R} = 2.7 * 10^{8} * T^{0.5} \exp(-\frac{20131}{T})[C_xH_y][O_2]$
$CO + 0.5O_2 \rightarrow CO_2$	$\dot{R} = 3.25 * 10^{7} \exp\left(-\frac{15098}{T}\right)[CO][O_2]^{0.5}[H_2O]^{0.5}$

2.2.3 Mineral matter decomposition models

"The mineral matter refers to the inorganic constituents of coal and is all elements that are not part of the organic coal substance (carbon, hydrogen, nitrogen, oxygen, and sulfur)" [33]. Elements such as carbon, hydrogen, oxygen, and sulfur can be present in both organic and inorganic parts of coals. The mineral matter is the major source of the elements that form ash when the coal is combusted in air or oxygen [33]. Therefore, knowledge of the mineral species involved is of great importance in interpreting problems, taking place in thermal power industry, such as boiler deposit formation, high-temperature corrosion etc. [34].

The mineral matter of coal may be classified in the form of two major groups [35; 36]:

- Extraneous minerals: This includes material that is added to coal/biomass from extraneous sources. In the case of coal, geologic processes and mining techniques contribute much of these minerals whereas for biomass fuel processing is likely to contribute the majority of it. Extraneous minerals containing more than 90% wt of fuel mineral matter, are dominant contributor to fly ash particles larger than around 10μm. Pyrite (FeS_2) and kaolinite ($Al_2Si_2O_5(OH)_4$), Silica, Calcite, and Illite are examples of extraneous minerals.
- Inherent minerals: these become incorporated in the fuel matrix through the oxygen-containing functional groups and do not separate from organic particles prior to combustion. The potential quantity of inherent minerals is larger in biomass than in most coals as a result of the higher oxygen content of biomass.

Examples of inherent minerals include derivatives of the alkali and alkaline earth metals such as some sodium or potassium compounds.

During coal/biomass heating some of these minerals will be decomposed or react with organic matter [28]. Decomposition of mineral matter and conversion can lead to the formation of gases and vapours which undergo homogeneous chemical reactions with subsequent heterogeneous or homogeneous condensation. Moreover, the fine inherent minerals with particle sizes of smaller than 0.1μm transform within the char particles and are gradually liberated during char fragmentation. The homogeneous condensation and the fragmentation of inherent minerals produce fly ash of size 0.02-0.2μm. Furthermore, coalescence of the fine fragments of inherent mineral matter forms ash particles of medium size 0.2-10μm. Finally, the largest ash particles (10-90μm) derive from the transformed extraneous mineral particles [36]. This process is shown in Figure 2.1:

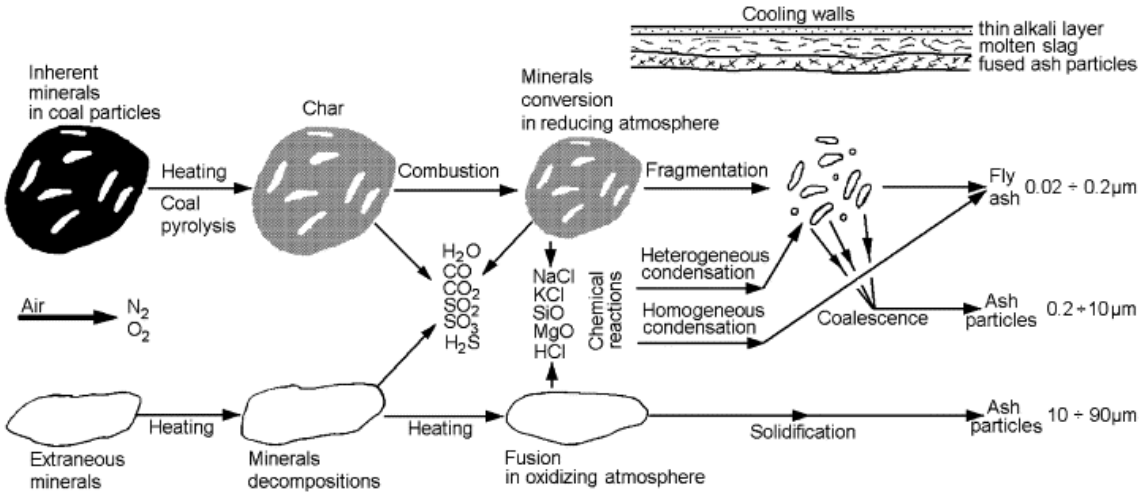

Figure 2.1 Mineral matter transformation mechanism [36]

Coal mineral matter decomposition can be modelled well as a mixture of individual minerals that suggests no substantial mass loss as a result of solid-phase reactions below 1700K. Kaolinite ($Al_4Si_4O_{10}(OH)_8$), Illite ($KAl_2(OH)_2(AlSi_3O_{10})$), Pyrite ($FeS_2$), Calcite ($CaCO_3$), Anhydrite ($CaSO_4$), Gypsum($CaSO_4.2H_2O$), Sylivite (KCl), Halite (NaCl), and Magnetite (Fe_3O_4), as typical minerals in coals, were selected as inputs in the mineral transformation models [36].

The kinetic parameters of the main coal mineral transformations at temperatures up to 1700K can be used to calculate the mass loss of the minerals as well as the amount of

ash produced in slow and rapid heating conditions. The decomposition reactions of the individual minerals and their corresponding kinetic data are given in [36; 37]. Mineral matter transformations can be considered as taking place in inert or reactive atmospheres [36].

Inert atmosphere: In an inert atmosphere, the decomposition rate of mineral matters $A_{(s)}$, the formation rate of fly ashes $D_{(s)}$ and gases $C_{(g)}$, $A_{(s)} \rightarrow xD_{(s)}+yC_{(g)}$, are given by the following kinetic equation [36]:

$$-\frac{d[A]}{dt} = k_c[A] \qquad \textbf{(2-10)}$$

where $[A]$ is the mass concentration of mineral matters $A_{(s)}$ (mole/m^3), and k_c is rate constant of mineral matter transformation reaction (s^{-1}).

Reactive atmosphere: In a reactive atmosphere, the decomposition rate of mineral matters $A_{(s)}$, the formation rate of fly ashes $D_{(s)}$ and gases, $C_{(g)}$, $A_{(s)}+B_{(g)} \rightarrow xD_{(s)}+yC_{(g)}$, can be obtained by te following equation [36]:

$$\frac{d[A]}{dt} = k_c[A]{p_B}^N \qquad \textbf{(2-11)}$$

where p_B is the partial pressure of gaseous reactant (e.g. O_2) (Pa), N is the reaction order and k_c is rate constant of mineral matter transformation reaction (Pa^{-1}s^{-1})..

2.2.4 Char particle combustion models

The solid body that remains after coal and biomass devoaltilisation is called char, or coke, and contains carbon, organic substances and ash [28]. The heterogeneous reaction of char oxidation is the last step of coal/biomass combustion. It lasts longer than all other preceding steps. Therefore it determines the duration of the entire combustion process [38]. The combustion process of a char particle (a devolatlised coal particle) can be described as the diffusion of oxygen through the boundary layer surrounding the particle to the surface of the particle and then through the gases within the pore of the particle to the internal surface. Finally the oxygen reacts with the particles on their outer and inner surfaces. Subsequently reaction products diffuse through the pores to the outer

surface and also to the bulk of the gases surrounding the particle through the boundary layer. Let us consider a simplified single stage mechanism of char combustion [28]:

$$C + O_2 \rightarrow CO_2 \quad \textbf{(2-12)}$$

The rate of the char combustion reaction presented by Eq. (2-12) can be calculated by Eq.(2-13) [28]:

$$\dot{R_c} = k_0 \exp(-\frac{Q}{RT_P}) A_P P^N{}_{O2} \quad \textbf{(2-13)}$$

where $\dot{R_c}$ is the rate of chemical reaction (mole/m^{3}s), k_0 is pre-exponential factor (s^{-1}), Q is activation energy (J/mole), R is gas constant (J/moleK), and T_P is particle temperature (K), A_P is particle surface area (m^2), P_{O2} is oxygen partial pressure, and N is the reaction order (Pa).

The kinetic data of char combustion reaction (Eq. (2-13)) is described by Tomeczek [28].

The single step mechanism of combustion, during which only CO_2 is produced, is too simplified. The key question in combustion research is"what are main products of reaction; CO or CO_2?" Both CO and CO_2 are the main products and the ratio of CO/CO_2 produced at the solid surface increases with temperature increase and decreases with pressure [28]:

$$\frac{CO}{CO_2} = A \exp\left(\frac{-Q}{RT_P}\right) \quad \textbf{(2-14)}$$

For the temperature range of 400-900°C A=2500 and Q=52kJ/mole. For temperatures higher than 900°C the ratio CO/CO_2 =12. At higher surface temperatures (> 1000°C) the concentration of CO_2 at the particle surface can be assumed to be negligible [28]. In Ref [39] slightly different values for the kinetic constants of CO/CO_2 ratio are given where A=2400 and Q=51.8kJ/mole.

In Eq. (2-15) the char combustion of pulverized coal is simulated by a first-order diffusion/dynamics combined rate model in which the combustion product is only CO at the particle surface. It determines the rate of char particle combustion with an

assumption that the particle shape is spherical and the particle size is constant during combustion [40]:

$$\frac{dm_{char}}{dt} = -\pi {d_p}^2 \frac{1}{\frac{1}{k_{diff}} + \frac{1}{k_s}} p_{O_{2,g}} \quad \textbf{(2-15)}$$

where m_{char} is the single char mass (kg), $P_{O2,g}$ is partial pressure of oxygen, and k_{diff} $(m/s)^{-1}$ and k_s $(m/s)^{-1}$ are specific oxygen diffusion rate and char oxidation coefficients respectively.

Specific oxygen diffusion rate coefficient (k_{diff}) can be calculated as follows:

$$k_{diff} = 0.75 \frac{Sh}{d_p} \frac{D_{O2} W_{O2}}{R T_g} \quad \textbf{(2-16)}$$

And char oxidation coefficients (k_s):

$$k_s = \frac{1}{6} \rho_p d_p k_{c0} \left(\frac{-Q_c}{R T_P}\right) \quad \textbf{(2-17)}$$

where Sh is Sherwood number, D_{O2} is mass diffusivity of oxygen (m^2/s), W_{O2} is molecular mass of oxygen (g/mole), ρ_p is particle density (kg/m^3), T_P is particle temperature (K), and T_g is gas temperature (K). k_{0c} is the pre-exponential factor (1/(sPa) and Q_c is activation energy of char heterogeneous oxidation (J/mole).

Finally, kinetic data of char combustion to be used in Eq. (2-17) for both coal and biomass is given in Table 2-6 [40]:

Table 2-6 Kinetic constants of char combustion

Fuel	k_{0c}, 1/(s.Pa)	Q (J/mole)
Coal	1.37	1.15E+05
Biomass	1.19E+03	1.45E+05

2.3 Deposit formation on the heat transfer surfaces

2.3.1 Introduction

Heat exchanger tubes are exposed to deposit formation due to homogenous or heterogeneous condensation of inorganic vapours, diffusion of fume particles, and/or inertial impact of large sticky particles onto clean surfaces or onto glue deposits [36]. There are two types of deposit forming in utility boilers [41]:

- Slagging deposits
- Fouling deposits

Slagging deposits form in the combustion or furnace zone and are in a molten and highly viscous state. Fouling deposits appear in the post combustion or convection pass of the boiler and are formed by condensed species vaporized earlier during combustion [28; 41].

At the beginning of the deposition process, when the tube is clean, only vapours (KCl, K_2SO_4, NaCl, Na_2SO_4) and fine particles (e.g. Al_2O_3, SiO_2) will accumulate on the surface in a sticky condition. Inertial impaction contributes to the ash deposition process only after the initial deposit is formed. The deposit surface temperature goes up when the thickness of the deposit increases. Consequently a molten film on the outer part of the deposit can flow down the side and form drops at the bottom of the deposit. Finally these drops detach the tube when the surface tension is no longer capable of supporting the weight of the drops [42]. Generally the following five main mechanisms contribute to deposit growth on the cooling surfaces [35; 42]:

- Condensation (*C*)
- Thermophoresis(*TH*)
- Brownian and eddy diffusion (*BE*)
- Impaction (*I*)
- Chemical reaction

2.3.2 Condensation(C)

“Condensation is the mechanism by which vapours are collected on a surface cooler than the local gas”[35]. It happens either heterogeneously on the tube surface, or homogeneously leading to a fume which deposits by thermophoresis on the surface

[43]. The flue gases are cooled in vicinity of the heat exchanger tube boundary layer, thus the vapours (KCl, K_2SO_4, NaCl, and Na_2SO_4) diffuse towards the cooling surfaces and condense on it, creating a sticky layer on the surface. The presence of this sticky layer is then essential for solid particles to be captured on the tube surface. The deposit outer surface temperature increases as it thickens so at certain temperature, higher than the saturation temperature of the condensable species the condensation process stops [43]. The schematic presentation of condensation process is shown in Figure 2.2:

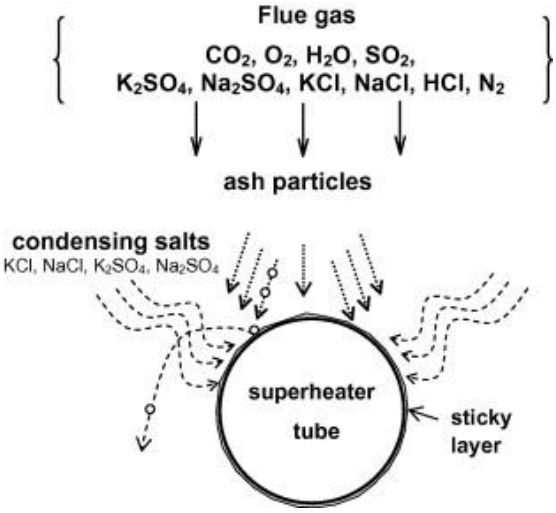

Figure 2.2 Schematic presentation of vapours condensation [43]

Deposits formed by condensation are more uniformly collected on the tube than either thermophoresis or inertial impaction derived deposits. The overall condensation rate of vapours on the material surface, controlled by mass transfer is given by Baxter [35]:

$$C_i = \xi_i \theta_{bf} \beta_i \left(X_{i,b} - X_s\right) + X_{i,b} \sum_i C_i \qquad \textbf{(2-18)}$$

Where ξ_i is condensation efficiency, θ_{bf} is blowing factor (near unity for this application), β_i is mass transfer coefficient of i-th component (m/s), X_b and X_s are mole fraction of species i in bulk gas and at tube surface respectively, and $X_{i,b}\Sigma c_i$ is convective transport to the surface.

The following model can also be used to calculate the rate of condensation of vapours forming sticky layer on heat exchanger surfaces [43]:

$$C_i = \beta_i \frac{p_i - p_{si}}{p_g} \rho_g \quad \textbf{(2-19)}$$

Where p_g is total gas pressure (Pa), ρ_g is gas density (kg/m^3), p_i is partial pressure of *i-th* gaseous component, and p_{si} is its saturation pressure at surface temperature, and βi is mass transfer coefficient of *i*-th component (m/s), calculated on basis of the Sherwood number, diffusion coefficient *Di* (m^2/s) and tube diameter D_c (m) as shown in Eq.(2-20):

$$\beta_i = \frac{ShD_i}{D_c} \quad \textbf{(2-20)}$$

The pressure p_i must be considered for the flue gas before the boundary layer of the tube. The saturation pressure of condensable vapours can be obtained by the following formula [43]:

$$\frac{p_{si}}{p_n} = exp(A_i - B_i/(T + c_i)) \quad \textbf{(2-21)}$$

where $P_n = 10^5$ Pa, and A_i, B_i, c_i are constants given in Table **2-7**.

Table 2-7 Constants related to saturation pressure of condensable vapours [43]

Component	A_i	B_i, K	c_i, K	Temperature range, K
K_2SO_4	18.08	39.449	0	1150-1800
Na_2SO_4	15.03	37.452	0	1150-1800
KCl	11.01	17.132	-122.7	1094-1680
NaCl	11.68	19.315	-82.6	1138-1738

2.3.3 Thermophoresis (TH)

Thermophoresis is a process of particle deposition from a gas due to local temperature gradients. The deposition of particles by thermophoresis takes place due to either a temperature gradient in the stream gas which carries the particle or as a result of temperature gradients in the particle itself. When the temperature difference between heat transfer surface and the flue gas is large enough the submicron particles of KCl and K_2SO_4 may be deposited on the surface due to thermophoretic forces. When the deposit build-up on the tube surfaces increases this temperature gradient decreases, thus the

deposition by thermphoretic forces decreases and ultimately disappears [35; 42]. Deposits formed by thermophoresis are finer grained and more equally distributed around a tube surface than deposits produced by direct inertial impaction. A thermophoretic force can be calculated based on a functional form that should apply over a broad range of Knudsen numbers (ratio of the gas mean-free-path to the particle diameter). It is based on particle-gas momentum exchange integration over the surface of the particle [35]:

$$F_T = -6\pi\mu_g d_p f(Kn)\nabla T_g \quad \textbf{(2-22)}$$

With μ_g is dynamic viscosity (Pa.s) of the gas, d_p is particle diameter (m), $f(Kn)$ is function of Knudsen number, and ∇T_g is local temperature gradient in the gas (K).

The local flux of particles due to thermophoresis is equal [44]:

$$J = H.\lambda.C_W\left[\frac{n_w.\nabla T}{T}\right]_W \quad \textbf{(2-23)}$$

where C_w is particle concentration at the wall of the cold surfaces (Kg/m^3), H is thermophoretic coefficient (m/s), λ is thermal diffusivity (m^2/s), and n_w is the unit normal to the wall.

2.3.4 Brownian and eddy diffusion (BE)

Brownian diffusion can be an important mechanism for the condensation and solidification of vapour species onto heat exchanger surfaces. Smaller particles, not large enough to be affected by inertial deposition, can be deposited on the surface through molecular diffusion. The random impacts of molecules on the particles induce movement through the laminar boundary layer and cause particles to spread along a concentration gradient. As particle size decreases Brownian diffusion increases. In addition, because of the mixing effect of turbulent eddies the boundary layers becomes turbulent thus particles diffusion increases dramatically. The deposition rate via Brownian and eddy diffusion mechanism can be increased by thermophoresis if temperature gradient is present. In this condition the collection efficiency of particle deposition onto a cooling surface is [45; 46]:

$$\eta_{0,D} = (1 + R_c) - \frac{1}{(1 + R_c)} \quad \textbf{(2-24)}$$

where the collection parameter is equal R_c:

$$R_c = \frac{2x_0}{D_c} \quad \textbf{(2-25)}$$

where x_0 is the limiting distance from the cylinder surface (m) at $\theta = \frac{\pi}{2}$, and D_c is the cylinder diameter (m).

The flux of small particles through a turbulent boundary layer can be calculated by integrating a modified Fick's law of diffusion [47]:

$$J = -(D_B + D_t)\frac{d_{\rho_p}}{d_Y} \quad \textbf{(2-26)}$$

where D_B is Brownian diffusivity (m^2/s), D_t is turbulent diffusivity (m^2/s), $\frac{d_{\rho p}}{d_Y}$ is the gradient of particle partial density, and Y is perpendicular distance from the surface (m).

Brownian diffusivity is calculated by the following formula [47]:

$$D_B = \left(\frac{k_B T}{6\pi\mu r}\right) C_C \quad \textbf{(2-27)}$$

where k_B is the Boltzmann constant (JK^{-1}), r is the radius of a particle (m), μ is dynamic viscosity of gas (Pa.s), and C_C is Cunningham's factor.

2.3.5 Impaction mechanism (I)

2.3.5.1 Direct inertial impaction

In practical cases inertial impaction is the most important deposition process for large particles (> 10μm) in which the particle capture probability plays a dominant role [43]. Particles larger than 10μm may impact on the upstream side of the tube due to their inertia which prevents them following the gas stream [42]. The rate of inertial impaction depends onto target geometry, flue gas velocity, particle size, density, and concentration

and gas flow properties [35]. Figure 2.3 shows the bell-shaped deposit accumulated on the up-stream side of the superheater tubes after, for example, 9 months operation:

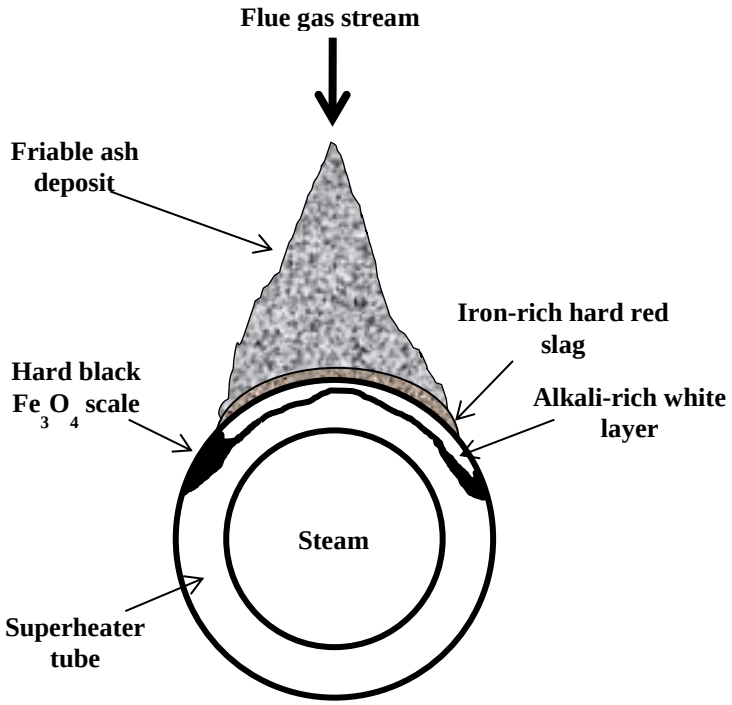

Figure 2.3 Bell-shaped deposit on the up-stream side of the superheater tubes [48]

The deposition flux by large particle impaction on the upstream side of the tube is a function of the local mass concentration of fly ash, the gas velocity, and the sticking coefficient of the particles on the surface [42]:

$$I_f(t,\theta) = u_f.\ C_{ash,1}\,.\eta_1.f_{stick} \qquad \textbf{(2-28)}$$

where u_f is the bulk gas velocity (m/s), $C_{ash,1}$ is the mass concentration of large fly ash particles (kg/m^3), η_1 is the local impaction efficiency, and f_{stick} is total sticking coefficient.

The combined stickiness of the deposit surface and the incoming ash particles is given by the equation below [42]:

$$f_{stick=}f(T_f) + f(T_S).\{1-f(T_f)\} - K_e\,.\{1-f(T_f)\}.\{1-f(T_s)\} \qquad \textbf{(2-29)}$$

where T_f and T_S are the temperatures of the flue gas and deposit surface respectively (K), k_e is the erosion coefficient, and $f(T)$ represents sticking coefficient.

In the model, we assume no erosion (K_e = 0). Assuming the stickness efficiency increases linearly with the melt fraction, then the sticking coefficient has been expressed as [42]:

$$f(T) = \begin{cases} 0 & f_{am} = 0 - 1 \\ 1.67 \, . f_{am} - 0.167 & f_{am} = 0.1 - 0.7 \\ 1 & f_{am} = 0.7 - 1 \end{cases} \quad \textbf{(2-30)}$$

where f_{am} is ash melt fraction.

Ash melt fraction can be calculated through equations and data developed by Zhou et al and Hansen [42; 49]. However, different models for sticking coefficient *f*(*T*) were suggested by Huang et al and Walsh et al [50; 51]:

$$f(T) = \begin{cases} \frac{\mu_{ref}}{\mu} & \mu > \mu_{ref} \\ 1 & \mu \leq \mu_{ref} \end{cases} \quad \textbf{(2-31)}$$

where μ_{ref} and μ are reference and practical viscosity respectively (Pa.s).

Particle viscosity μ is a function of both temperature and ash composition which enables it to account for changes in sticking behavior owing to variations in both the composition and the temperature of the incoming particles [52]. The value of μ_{ref} has been a subject of much research and various authors have proposed different values for critical viscosity. Values such as 8, 10^4, and 10^8Pas have been adopted for reference viscosity [50].

Local impaction efficiency can also be obtained from Eq. (2-33) [53]:

$$\eta_I = \frac{\pi}{2} \frac{\eta_t}{\theta_m} \cos\left(\frac{\pi}{2} \frac{\theta}{\theta_m}\right) \quad \textbf{(2-32)}$$

where η_t is target efficiency, θ is angle of impaction (°), and θ_m is maximum angle of impaction (°).

Target efficiency η_t and maximum angle of impaction θ_m can be calculated through a range of correlations [53]:

$$\Gamma = a\ ln(8Stk_e) + b(Stk_e - 0.125) + c(Stk_e - 0.125)^2 \quad \textbf{(2-33)}$$

$$\Gamma = 1 + a(Stk_e - 0.125)^{-1} + b(Stk_e - 0.125)^{-2} + c(Stk_e - 0.125)^{-3} \quad \textbf{(2-34)}$$

Where *a*, *b*, *c* are constants, and Stk_e is effective Stokes number which is a function of particle Reynolds number in the flue gas stream.

Eq. (2-33) and Eq. (2-34) are applied when is Stk_e number is in the range of $0.125 < Stk_e < 0.5$ and $Stk_e > 0.5$ respectively [53]. In addition, [50; 54] introduced different values for *a*, *b*, and *c* to be used in Eq. (2-33) and Eq. (2-34).

Reference [45] gives an alternative formula for calculating the target efficiency:

$$\eta_I = \frac{Stk^2}{(Stk + 0.25)^2} \quad \textbf{(2-35)}$$

where *Stk* is the dimensionless Stokes' expression.

2.3.5.2 Eddy impaction

Furthermore, the middle-sized particles (<10μm) follow the large vortices and penetrate into the near wake of the tube from which some of them can finally be centrifuged out by eddies and potentially impact and stick on the downstream side of the tube. Deposition flux of middle-sized particles may be expressed as [42]:

$$I_w(t, \theta) = u_r . C_{ash.2} . f_p \quad \textbf{(2-36)}$$

where u_r is maximum reverse velocity of the gas (m/s), $C_{ash.2}$ is mass concentration of the middle-sized particle (kg/m^3), and f_p is probability of the particles to be centrifuged out of the eddy and subsequently impact and stick on the tube surface.

The probability of particles being centrifuged out of eddies and subsequently impacting and sticking onto the tube surface, f_p is equal to:

$$f_p = 1.1 f_v \quad \textbf{(2-37)}$$

where f_v (s^{-1}); (1.1s) is the frequency of vortex shedding which is characterised by Strouhal number, *Sr*:

$$f_v = S_r \frac{u_f}{D} \quad \textbf{(2-38)}$$

where D is tube diameter (m), and u_f is the bulk gas velocity (m/s)

2.3.5.3 Alternative models for deposition by impaction

The following deposition models are based on the ash state in the flue gas stream: melted particles, solid particles, and vapours. Particles, heated in the flame region above the melting temperature, hit the cooling surfaces. The rate of melted particles deposition on the surface area can be calculated by equation [55]:

$$\dot{m}_1 = B P_1 P_2 C_{p,m} u \quad \textbf{(2-39)}$$

where B is a constant, P_1 is probability of particles hitting the surface, P_2 is probability of melted particle sticking to the surface, $C_{p,m}$ is concentration of melted particles in the flue gases before the tube (kg/m^3), and u is gas velocity component perpendicular to the local surface (m/s).

In this model, as for large and middle-sized particles in section 2.3.5.1 and 2.3.5.2, it has been assumed that the large particles (>10μm) hit the front parts of the tube whereas the particles smaller than 10μm follow the flue gas flow lines which form a recirculation zone behind the tubes where particles may stick to the surface. Therefore for the front part of the tube $C_{p,m}$ is related to d_p> 10μm while for the rear part it is related to d_p< 10μm. The possibility of particles to hit the heat exchanger surface is equal [55]:

$$P_1 = \frac{A_{duct} - A_{free}}{A_{duct}} \quad \textbf{(2-40)}$$

where A_{duct} is surface area of target (m^2), and A_{free} is and cross section of free path for flue gases (m^2).

In addition to Eq. (2-30) and Eq. (2-31) the following equation has been suggested to calculate the sticking probability of the melted particles P_2 based on the temperature [55]:

$$\begin{cases} P_2 = 0, & T \le 1450K \\ P_2 = 0.1, & 1450K < T < 1800K \\ P_2 \approx 0.1 + \dfrac{10\left(T_p - T_m\right)}{T_m}, & 1980K > T > 1800K \\ P_2 = 1 & T > 1980K \end{cases} \quad \textbf{(2-41)}$$

where T_m and T_p are melting and particle temperatures respectively.

The deposition rate of solid particles on the tube surfaces approaching the tubes with the concentration $C_{p,s}$ can be described by the model [55]:

$$\dot{m}_2 = P_1 P_3 C_{p,s} u \quad \textbf{(2-42)}$$

where P_3 is probability of solid particle sticking to the surface, and $C_{p,s}$ is concentration of solid particles in the gas stream (kg/m^3).

In cooler parts of the boiler, where all particles are in solid phase the only possibility for the particles to remain on the surface when they hit the surface is the presence of a sticky layer, coming from condensed vapours on the tube surface or on the surface of particles that deposited earlier. Therefore, the sticking probability of solid particles P_3 is proportional to the rate of condensation of vapours forming sticky layers [55]:

$$P_3 = 62 C_i \quad \textbf{(2-43)}$$

where the unit is 62 (kg/m^{2}s)$^{-1}$ and *Ci* is the condensation rate of vapours (kg/m^{2}s).

Finally, deposition build-up rate at an angular position (θ) is the difference between the deposit growth rates due to Condensation (C), Thermophoresis (T_H), Brownian and eddy diffusion (B_E), as well as Impaction (I) mechanisms and shedding rates [42]:

$$\frac{dm(t,\theta)}{dt} = C(t,\theta) + T_H(t,\theta) + B_E(t,\theta) + I(t,\theta) - S_H(t,\theta) + S_f(t,\theta) \quad \textbf{(2-44)}$$

where m is the deposit weight (kg), S_H is shedding rate by drop detachment (kg/s), S_f is mass accumulation rate in a control domain caused by melt film movement (kg/s).

Figure 2.4 shows typical appearance of superheater and reheater tubes after ash deposit formation in utility boilers.

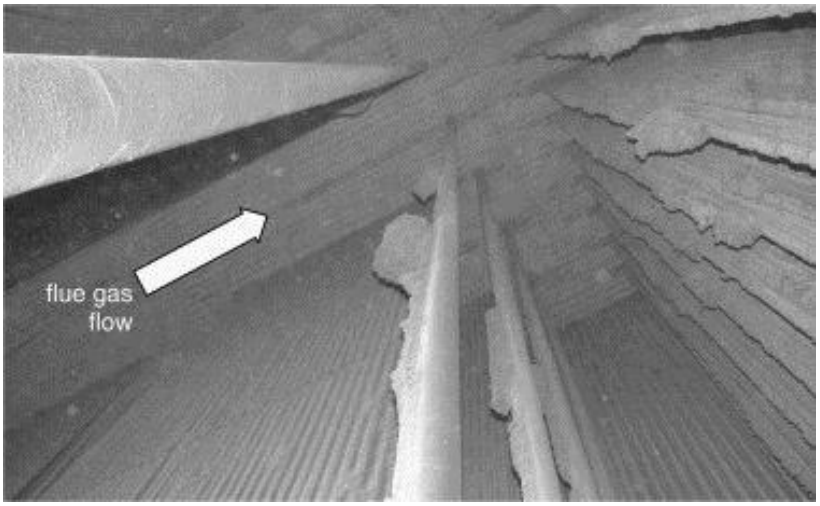

Figure 2.4 Appearance of superheater tubes after deposit accumulation [43]

2.3.6 Chemical reaction

2.3.6.1 Introduction

The review of mechanisms by which ash can be accumulated in a deposit is completed by chemical reactions. These reactions include the heterogeneous reactions of gases with species in the deposit. The most significant chemical reactions with respect to deposit formation are [35]:

- Sulphidation
- Alkali absorption
- Oxidation

2.3.6.2 Sulphidation

Compounds containing the alkali metals (*Na* and *K*) are primary species of concern. Condensed hydroxides and chlorides of potassium and sodium are susceptible to sulphidation [35].

2.3.6.3 Alkali absorption

Silica absorbs alkali material to produce Silicates. They have a higher melting point than silica at lower temperatures. The conversion of silica to silicates in deposits can cause sintering and considerable changes in deposit properties. Alkali absorption is relatively slow compared to sulphidation [35].

2.3.6.4 Oxidation

Any remaining char often deposits with the mineral matters on heat transfer surfaces. However, locally available oxygen oxidises the residual char to produce deposits with very little residual carbon [35].

2.3.7 Contributions to the deposit growth by different deposit formation mechanisms

The inertial impaction deposition on the upstream side is a major contributor to ash build-up on superheater/ reheater tubes. The magnitude of the deposition rate caused by condensation and eddy impaction are in the same level but much smaller than the inertial impaction. The amount of ash deposited via themophoresis is even smaller than that deposited via condensation. Finally, the contributions by the Brownian and eddy diffusions are negligible. These concepts have been observed in an ash deposit experiment in a straw fired boiler [42].

2.4 Fireside corrosion of heating surfaces

2.4.1 Introduction

Fireside corrosion, also referred to as fuel-ash corrosion, is the reaction of superheater/reheater materials with the gaseous, molten and/or solid products of combustion fuels, e.g. coal and biomass. It is a major threat to the remaining service life of superheater/reheater materials in coal/biomass fired power stations, with perforated tubing leading to costly plant unavailability and repair [56]. Coal and biomass have salts of sodium and potassium impurities that are retained in the ash and/or transferred by vapour condensation route. As discussed in deposition model, these impurities deposit on the outer surfaces of heat exchanger tubes. At the temperature of operation, these salts can be in the liquid state or they get transformed into complex salt mixtures in the presence of sulphur bearing flue gases. Furthermore, such complex mixtures melt at much lower temperatures, producing a corrosive liquid melt on the surface of the tube. Corrosion in the presence of such liquid melts of salts is known as hot corrosion [57]. In addition, corrosion products from initial reactions with the surfaces of the tube materials

can also get involved in further corrosion processes [48]. Therefore, in assessing this form of degradation it is necessary to consider both immediate results of deposition processes and the many potential further reactions that can occur [48].

Compounds that have been recognised as having the potential to form in deposits and cause fireside corrosion of tube surfaces include:

- Sulphate deposits [48]
    - Pyro-sulphates, e.g. $(Na,K)_2S_2O_7$
    - Alkali-iron tri-sulphates, e.g. $(Na,K)_3FeS_2(SO_4)_3$
    - Mixed sulphates, e.g. $(Na,K, Fe)_xSO_4$
- Chloride deposits, with mixed compositions including Na, K, Fe, Ca, Mg, and other metal elements depending on the fuel used [48] ;
- Carbonates, with mixed compositions including Na, K, Fe, Ca, Mg, and other metal elements depending on the fuel used [48];
- Sulphate-chloride-carbonate soup containing all the compounds above [48].

In considering the possibility for such compounds to both form in deposits and cause corrosion damage, it is essential to assess the melting point of the compounds and the conditions necessary for their formation. For instance, both pyro-sulphates and alkali-iron tri-sulphates need sufficient quantity of SO_3 around them for their stability to be maintained. Moreover, the lowest melting points of pyro-sulphates and alkali-iron tri-sulphates are ~545 and ~560°C respectively [48]. This is shown in phase diagram of such sulphate species in Figure 2.5 and Figure 2.6:

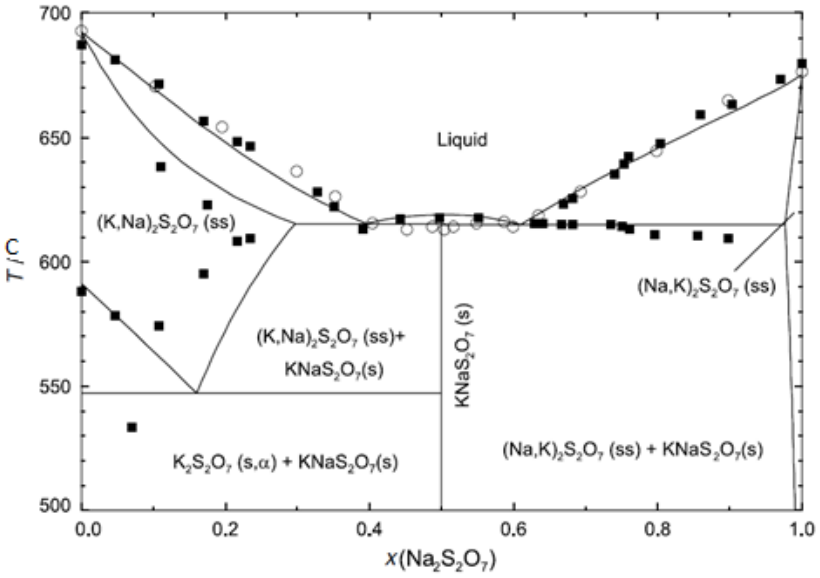

Figure 2.5 Phase diagram for alkali pyro-sulphates [48; 58]

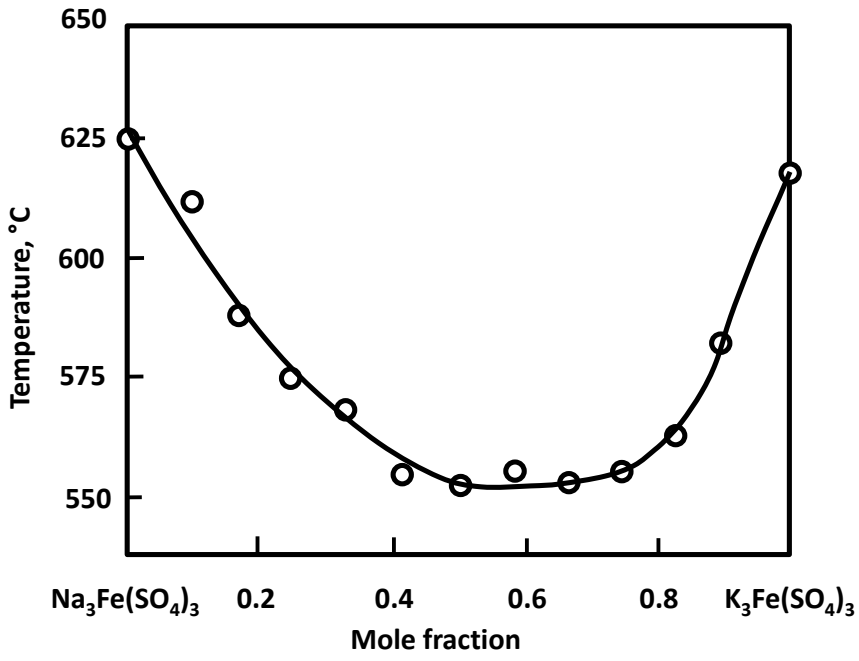

Figure 2.6 Phase diagram for alkali-iron tri-sulphates [48]

For biomass derived deposits containing higher levels of potassium chlorides and sulphates, the alkali chloride-sulphate phase diagram is more useful [48]. For example, Figure 2.7 gives an example with the lowest point of a mixed alkali chloride-sulphate being ~517°C [48].

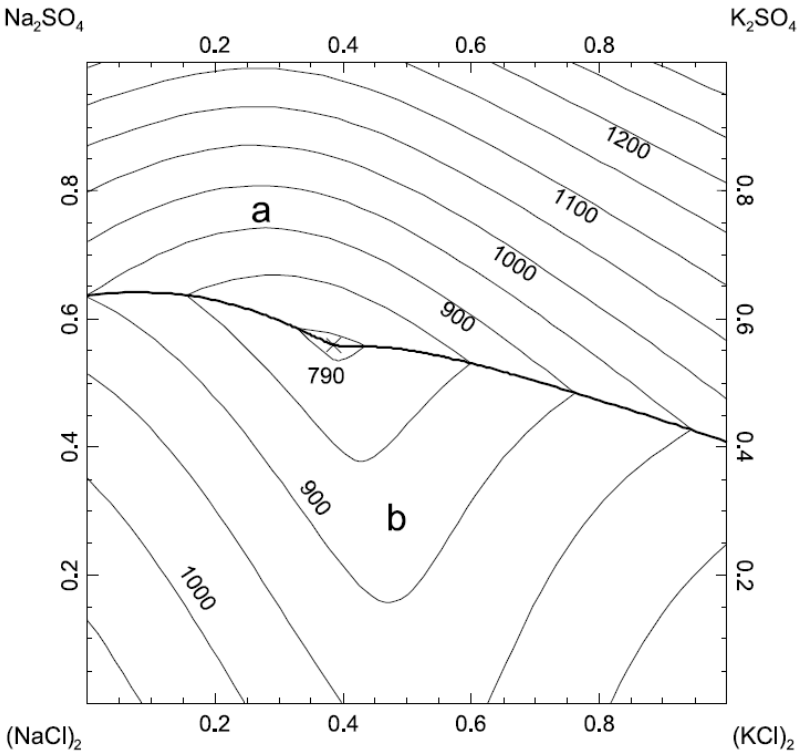

Figure 2.7 Phase diagram for alkali sulphates-chlorides (Temperatures in Kelvin) [58]

For waste-fired power plants, heavy metal chlorides compound need to be considered in detail, as these can cause deposit to have much lower melting points; potential mixtures contain combination of alkali metals, Fe, Pb, Zn, Cd and Sn as oxides, chlorides, sulphates and carbonates [48].

Fireside corrosion rates of superheater tubes generally increase very rapidly with tube surface temperature up to 735°C after which the wastage rates tend to drop off, thereby producing a bell-shaped curve [14] as shown in Figure 2.8:

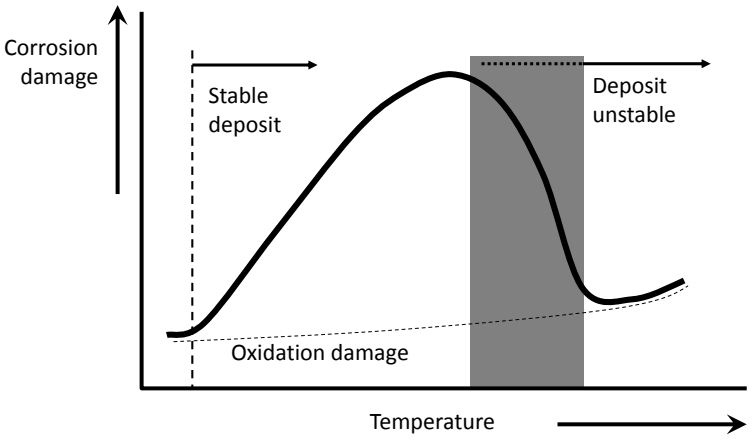

Figure 2.8 Characteristic bell-shaped curve for a fireside wastage mechanism [48]

Furthermore, Figure 2.9 shows multiple bell-shaped corrosion peaks attributed to different compounds forming in deposits on variety of different heat exchangers [48]:

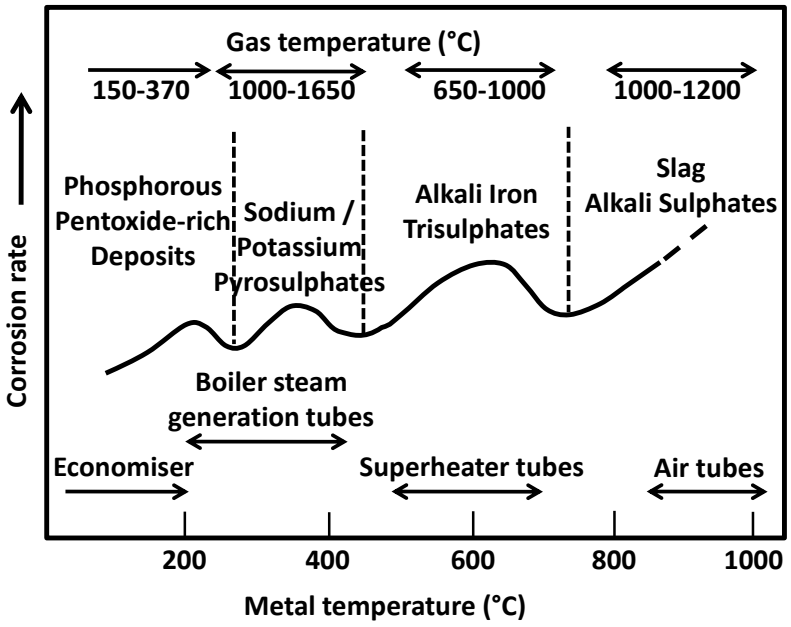

Figure 2.9 Effects of metal temperatures on corrosion rates of different heat exchanger tubes in conventional pulverised-fuel-fired power stations [48; 59]

This main reason for this bell-shaped is that with increasing metal temperatures such compounds, causing fireside corrosion, can be become unstable for variety of different reasons including:

- Vapour condensation dew points being exceeded [48]

- Insufficient SO_3 being available to stabilise some sulphate phases, as the SO_3/SO_2 balance favours SO_3 at lower temperatures [48].

Figure 2-10: Illustrates the enhanced fireside corrosion of a superheater tube associated with formation molten alkali salts on the tube walls.

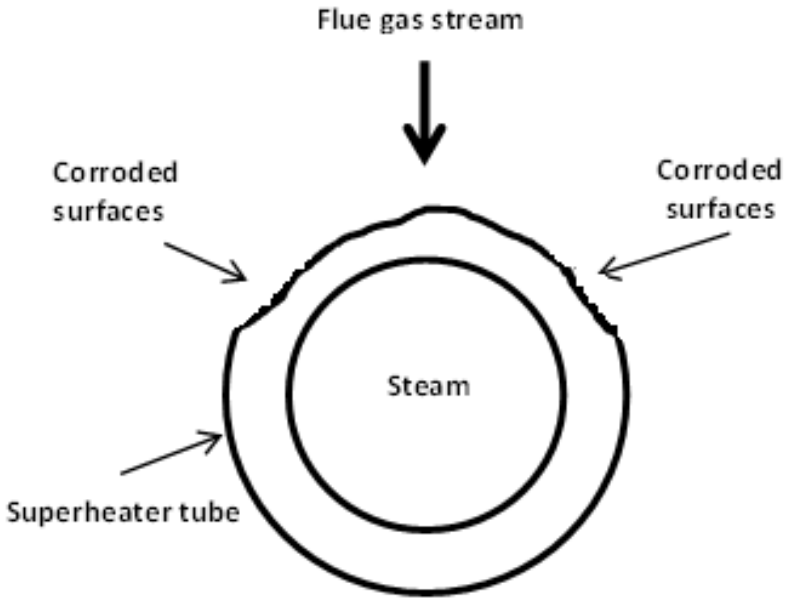

Figure 2.10 Typical cross-sectional appearance of a superheater tube which has fireside corrosion [48]

Although superheater/reheater corrosion are influenced by fuel impurities, a relatively stable and protective oxide scale is usually formed by the reaction of the tube surfaces with oxygen and water vapour present in the flue gas stream [56].

Heat exchanger tube materials will respond in different ways to the aggressive deposits on their surfaces. For low alloy ferritic steels, the fluxing reactions in the molten deposits lead to rapid corrosion, whereas for high alloy ferritic steels, the chromia scale formed is more protective and can provide some protection against such deposit [48].

2.4.2 Metal oxidation

In gaseous atmospheres (e.g. air) metal alloys are oxidised where an oxide layer or scale forms on the surface of the metal [60]. This phenomenon is called scaling or dry corrosion in the literature. The oxide layer formation is an electrochemical process which can be expressed by the following equation for metal *M* [60].

$$M_{(s)} + \frac{1}{2} O_{2,(g)} \rightarrow MO_{(s)} \quad \textbf{(2-45)}$$

In pure steam, the oxygen required for the oxide growth process is generated by the dissociation of steam:

$$H_2O_{(g)} \leftrightarrow H_{2(g)} + 1/2\, O_{2(g)} \quad \textbf{(2-46)}$$

Eq. (2-45) is composed of oxidation and reduction half-reactions. The oxidation reaction produces metal ions, taking place at the metal-scale interface [60]:

$$M_{(s)} \rightarrow M^{2+} + 2e^- \quad \textbf{(2-47)}$$

Simultaneously, oxygen ions are formed by the reduction half-reaction, occurring at the scale-gas interface:

$$\frac{1}{2} O_{2\,(g)} + 2e^- \rightarrow O^{2-} \quad \textbf{(2-48)}$$

Figure 2.11 shows the schematic presentation of the metal-scale-gas reactions in oxidation process:

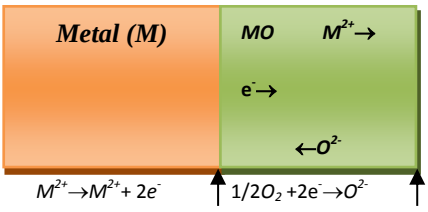

Figure 2.11 Schematic presentation of metal oxidation [60]

For the oxide scale to grow electrons must be conducted to the scale-gas interface. Moreover, M^{2+} ions must diffuse away from the metal-scale interface and/or O^{2-} ions must diffuse in opposite direction of M^{2+}. The oxide layer may protect the metal from rapid oxidation by acting as a barrier to ionic diffusion and/or electrical conduction [60]. The protectiveness of the oxide scales depends on the rate of ionic transport through the scale, its mechanical properties, and its adhesion to the metal surface [56].

2.4.3 Vapour-ash corrosion chemistry

Combustion of coal and biomass generates very complex and corrosive media. These environments contain gases and fly ashes at high temperatures [61]. The severe fireside

corrosion of tube materials is caused by condensation/accumulation of low melting-point salts from the flue gas onto the tube surface since salts containing chlorides and sulphates of sodium and potassium, easily liquefy at the operating metal temperatures [62]. Sulphidation of alkali metals in the gaseous phase can be described by the following reactions [55]:

$$S_{2(g)} + 2O_{2(g)} \rightarrow 2SO_{2(g)} \quad \textbf{(2-49)}$$

$$2MCl_{(s)} + SO_{2(g)} + \frac{1}{2}O_2 + H_2O_{(g)} \rightarrow M_2SO_{4(s)} + 2HCl_{(g)} \quad \textbf{(2-50)}$$

where *M = Na* or *K*

Reaction of alkali sulphates (Na_2SO_4, K_2SO_4) with Fe-oxides (deriving from oxide scales or ashes) in the presence of SO_3 ($SO_2 + 1/2O_2 \rightarrow SO_3$) will result in the formation of alkali-iron trisulphates $(Na,K)_3Fe(SO_4)_3$ held responsible for the degradation of coal-fired plant superheater tubes [61]:

$$3M_2SO_{4(S)} + Fe_2O_{3(S)} + 3SO_{3(g)} \rightarrow 2M_3Fe(SO_4)_{3(S,l)} \quad \textbf{(2-51)}$$

$$9M_2SO_{4(S)} + 2Fe_3O_{4(S)} + 9SO_{3(g)} + \frac{1}{2}O_2 \rightarrow 6M_3Fe(SO_4)_{3(S,l)} \quad \textbf{(2-52)}$$

where *M = Na* or *K*

Alkali-iron-trisulphates have low melting temperatures thus being molten at operating conditions [61].These molten species can either take part in dissolution of the protective oxide scales, already formed on the tube surface, or react with the metal to form internal sulphides [61]:

$$2M_3Fe(SO_4)_3 + 6Fe \rightarrow 3/2FeS + 3/2\,Fe_3O_4 + Fe_2O_3 + 3M_2SO_4 + 3/2\,SO_2 \quad \textbf{(2-53)}$$

Na_2SO_4 and/or K_2SO_4 may also react with SO_3 to produce pyrosulphates [57]:

$$M_2SO_{4(s)} + SO_{3(g)} \rightarrow M_2S_2O_{7(L)} \quad \textbf{(2-54)}$$

where $M = Na$ or K

Pyrosulphates can also react aggressively with any protective iron oxide scales resulting in accelerated corrosion through fluxing of the oxides [57].

Additionally, HCl and Cl_2, as being the most common chlorine-containing species, may cause gas-phase corrosion attack. Chlorine can influence the corrosion of superheater tubes by three mechanisms [63]:

- Gases containing Cl_2, HCl, NaCl, and KCl results in a direct corrosion by accelerating the oxidation of the metal alloys (active oxidation).
- Such gases may also influence the corrosion caused by molten alkali sulphate.
- Corrosion induced by combination of these two mechanisms.

The liberated HCl, coming from alkali metals sulphidation reaction, can diffuse towards the metal surface to form volatile metal chlorides [63]:

$$M_{(s)} + 2HCl_{(g)} \rightarrow MCl_{2(g)} + H_{2(g)} \quad \textbf{(2-55)}$$

where $M = Fe$ or Cr or Ni.

Alternatively, HCl could be actively oxidised to H_2O and Cl_2 [63]:

$$2HCl_{(g)} + \frac{1}{2}O_{2(g)} \rightarrow H_2O_{(g)} + Cl_{2(g)} \quad \textbf{(2-56)}$$

Chlorine can penetrate the protective oxide layer, possibly through pores and cracks, and react with metal alloys to form metal chlorides [63]:

$$M_{(s)} + Cl_{2(g)} \rightarrow MCl_{2(s)} \quad \textbf{(2-57)}$$

where $M = Fe$ or Cr or Ni.

Continuous evaporation may occur since metal chlorides have high vapour pressures at the metal scale interface [63]:

$$MCl_{2(s)} \rightarrow MCl_{2(g)} \quad \textbf{(2-58)}$$

where *M* = *Fe* or *Cr* or *Ni*.

The oxygen concentration goes up at higher distances from the metal. This leads to oxidation of the metal chlorides to solid metal oxides [63]:

$$3MCl_{2(g)} + 2O_{2(g)} \rightarrow M_3O_{4(s)} + 3Cl_{2(g)} \quad \textbf{(2-59)}$$

where*M* = *Fe* or *Cr* or *Ni*.

This loose oxide layer provides no protection against further attack. Chlorine, released from this gaseous phase reaction, can diffuse to the flue gas or back to the metal surface thus a cycle is formed providing a continuous transport of metals away from the metal surface toward higher oxygen partial pressures with little net consumption of chlorides [63]. Reaction of alkali chlorides with the metal scale can also result in a breakdown of protective oxide layers (e.g. Cr_2O_3) [63]:

$$Cr_2O_{3(s)} + 4NaCl_{(g)} + \frac{5}{2}O_{2(g)} \rightarrow 2Na_2CrO_{4(s,l)} + 2Cl_{2(g)} \quad \textbf{(2-60)}$$

2.4.4 Fireside corrosion models

The development of validated superheater/reheater tube corrosion rate model in coal/biomass fired power plants would facilitate optimisation of the plant design and operation, and enable the correct materials selection for specific boiler, fuel and combustion parameters. This would then help to ensure that adequate material corrosion allowance is specified, permitting optimisation of tube residual lives, plant availability and minimisation of expensive plant maintenance activities [56].

In the below model the corrosion rate (mm/h) can be assessed by comparing measurements of the wall thickness of the tubing. These measurements are usually made at intervals of 5000 hours, especially during the early life of the boiler [21]:

$$Corrosion\ rate = \frac{n\sum w_t t - \sum w_t \sum t}{n\sum t^2 - (\sum t)^2} \quad \textbf{(2-61)}$$

where w_t is minimum wall thickness, t is operating time and n is number occasions at which the minimum wall thickness was measured.

Chlorine strongly promotes the release of both sodium and potassium during coal/biomass combustion and the released alkali salts are transformed to fusible sulphates, which on the superheater tube surfaces can cause high temperature corrosion [56].The following equation gives the correlation between the chlorine content of UK coals and the rate of fireside corrosion (nm/h) of austenitic superheater and reheater tubes [64]:

$$Corrosion\ rate = A.B.\left(\frac{T_g}{1000}\right)^{2.4}\left(\frac{T_{sur}-550}{100}\right)^{2}(Cl-0.06) \quad \textbf{(2-62)}$$

where T_g is flue gas temperature, T_{sur} is tube's surface temperature, Cl is coal chlorine content ,and A and B are constants.

The above model is valid for theses ranges as follows: 870°C < T_g < 1200°C, 605°C < T_{sur} < 680°C, and 0.12% < Cl < 0.58% (UK coal only).

The constant A include the relative performance of the different austenitic steels, equal to 1 for 18%Cr steels (T316, T321, T347, Esshete 1250) and 0.4 for Type 310. Moreover, the constant B is equal to 300 for leading tubes (tubes that directly face the hot flue gases) and 160 for non-leading tubes (tubes that indirectly face the hot flue gases), reflecting the fact that leading tubes corrode at a faster rate than non-leading tubes [64].

In addition, the next model relates corrosion of austenitic materials as well as Inconel 671 with coal/biomass chlorine content [64]:

$$Corrosion\ rate = A.L.B.(Cl-a)(T_{sur}-b)^{C}(T_g-d)^{e} \quad \textbf{(2-63)}$$

where A, a, b, c, d, and e are constants, L is a constant being equal to 2.2 for leading tubes and 1 for non-leading tubes, The constant B is equal to 1 for 18%Cr steels (T316, T321, T347), 0.3 for Type 310 and 0.1 for Inconel 671 (52Ni-48Cr).

Finally, the below model relates the concentration of SO_x in the flue gas and deposition fluxes of alkali sulphates to the rate of fireside corrosion (nm/h) of heat exchanger's tube [1]:

$$Corrosion\ rate = exp[-\frac{a[SO_x] + b(C_{K_2SO_4} + C_{Na_2SO_4}) + c}{RT_{sur}} + d[SO_x] + e(C_{K_2SO_4} + C_{Na_2SO_4}) + f] \quad \textbf{(2-64)}$$

T_{sur} is tube's surface temperature (K), $[SO_x]$ is concentration of SO_x in flue gas (ppm), C_i is mass flux of species *i* in deposits (μg/(cm^{2}h)) , and *a, b, c, d, e,* and *f* are constants.

Eq. (2-64) can calculate the corrosion rate of austenitic steels and high alloy ferritic based on the different values of *a, b, c, d, e,* and *f.*

2.5 Steamside oxidation of heating surfaces

2.5.1 Background

A steam boiler has a series of heat exchangers that transfer the heat produced in the furnace to the working fluid (water/steam) circulating to a turbine generator. The electrical energy is generated by using the steam to drive a steam turbine, which simultaneously drives an electrical generator. Steam-side oxidation occurs on the steam-touched inner surfaces of superheater and reheater tubes where the materials are exposed to highest steam temperatures and pressures. As a result of global warming issues, there are demands to increase boiler efficiencies in order to produce the same amount of energy by burning less fuel and so produce lower emissions. This can be accomplished by increasing the steam temperature and pressure [65]. For example an increase in steam temperature from 580 to 760°C results in a thermal efficiency increase from 35 to 47%, while reducing CO_2 emissions by approximately 30%. This leads to more severe conditions in which the superheater/reheater tubes must operate [12-14].

Apart from metal temperature and oxygen as the most significant factors for steam-side oxidation of the tube metal there are other parameters that have implications in oxidation reaction rates such as geometries of the tube, mass flow rate of steam, and fire side convection coefficient and flue gas temperature [19]:

- Geometries of the tube: the thinner tube has less incremental scale formation.
- Mass flow rate is used to determine steam-side convection coefficient. The lower mass flow rate of steam will increase the oxide scale formation rate on the inner surface.

- The higher fire side convection coefficient and higher flue gas temperature also result in larger growth rate of steam-side scales.

Oxidation resistance can be optimised by changing the inherent nature of the protective oxide scale. The influence of chromium additions to iron-base alloys is one of the most dramatic approaches towards this issue. For example, during service, carbon steels form a scale consisting of one or more layers of wustite, hematite and magnetite depending upon the specific operating conditions. The addition of chromium to the alloys changes the scale such that the inner layer is an iron-chromium spinel in low alloy ferritic or martensitic steels. Further increase in chromium will eventually cause the formation of chromia, e.g. in austenitic stainless steels [66].

The formation of porous, thick oxide scales has several consequences for the remaining service life of heat exchanger tubes:

- The available load-bearing cross section of the tube is reduced due to the metal loss caused by the formation of the oxide scales on the tube surface, thus the stresses acting on the heat exchanger rise as oxidation proceeds. For example, for a thin-walled tube (P92) of 6mm wall thickness a 1.5mm material loss would have great effects for the service life at 600°C. The thin-walled tube (P9) would experience a rupture life reduction from 250 000 to 60 000 hours. [13].
- The matrix becomes depleted in those constituent elements that are selectively oxidised to form thick oxide scale. For example, in the ferritic Fe25Cr5Al exposed at 1100°C Al is depleted in the matrix as the oxide scale grows. This lead to a catastrophic oxidation of the metal since there is insufficient Al left in the matrix to sustain the Al_2O_3 protective oxide [13].
- The thick oxide scales which act as a thermal barrier coating cause heat transfer reduction across the tube wall and its overheating. Each degree temperature rise in tube operating temperature will reduce the remaining service life by 3% [13].
- The oxides may spall during the service and block the tube, leading again to its overheating [13].

2.5.2 Kinetics of steam oxidation

2.5.2.1 Introduction

For engineering design, the kinetics of steam oxidation is very important as it allows the prediction of the service life of a tube to be used at a specific temperature. There are four types of rate laws commonly encountered [57]:

- Linear
- Parabolic
- Logarithmic
- Combinations of them such as paralinear (combination of linear and parabolic) etc.

2.5.2.2 Logarithmic law

The oxidation kinetics of most metals heated at low temperatures obeys a logarithmic law. Initially the rate of oxidation is very fast and then slows down, either following a direct or inverse logarithmic law [57]:

$$X = k_c \log t \tag{2-65}$$

$$\frac{1}{X} = k_c{}' \log t \tag{2-66}$$

where X can be change in the weight as a result of oxidation, thickness of the oxide formed (g or μm), the amount of oxidation consumed per unit surface area of the metal, or the amount of the metal transformed to oxide, k_c is the reaction constants (s^{-1}) and t is time.

2.5.2.3 Parabolic law

For a parabolic law the rate of oxide layer growth is controlled by ionic diffusion where the oxide is nonporous and bonds strongly to the surface [60]. Most engineering alloys obey parabolic kinetics at high temperatures. With the parabolic law, the oxide growth takes place with a decreasing oxidation rate. Consequently, the rate of the oxidation is inversely proportional to the oxide thickness or weight of the oxide formed [57]:

$$\frac{dX}{dt} = \frac{K_p}{X} \tag{2-67}$$

where K_p is the parabolic rate constant ((μm)^2/h or (gcm^{-2})^2/s).

2.5.2.4 Linear law

The linear rate law is usually followed when a protective oxide cracks or spalls, resulting in direct access of gas to metal. This leads to very high oxidation rates invariably following linear kinetics and is independent of amount of gas or metal previously consumed in the reaction [57]:

$$\frac{dX}{dt} = K_L \qquad \textbf{(2-68)}$$

where K_L is the linear rate constant (μm/h).

2.5.2.5 Combination of oxidation laws

Sometimes oxidation kinetics does not follow the three laws mentioned above. For example many metals at low temperature follow a cubic law. This can imply a combination of the logarithmic and parabolic law. It is assumed that the reaction obeys the logarithmic law at the beginning of oxidation and then changes to the parabolic law [57].

Combinations of parabolic and linear laws, however, happen at high temperatures. For example, the oxidation kinetics following a parabolic rate law suddenly changes to linear kinetics; this occurs when the oxides gets partially cracked. Therefore, a direct access of gas leads to a very fast oxidation rate, following linear kinetics [57] .

2.6 Heat transfer process

Due to highly emitting and absorbing nature of a pulverized-coal flame, radiation becomes the most significant or dominant mode of thermal transfer in the furnace of pulverized-coal fired boilers. Convection and conduction do contribute heat transfer process, but still 95% of the heat transfer in the furnace is due to radiation [67].

Figure 2.12 shows a schematic representation of a cross section through an idealised superheater tube which suggests the form of temperature gradient as well as the corresponding heat transfer path which is from the combustion gas to the steam. Therefore, the temperature of the alloy will be higher than that steam-side oxide which, in turn, will be higher than that of the steam [68]. For example the metal temperature on

the fireside (steamside) of the tube wall (T22) increased from 586 (560)°C to almost 595 (570)°C at a steam-side oxide thickness of 360µm. In this condition the gas temperature and the heat flux were 1100°C and 50W/m^2 respectively. The boiler tube of interest had an outside diameter of 50mm and a wall thickness of 11mm [69].

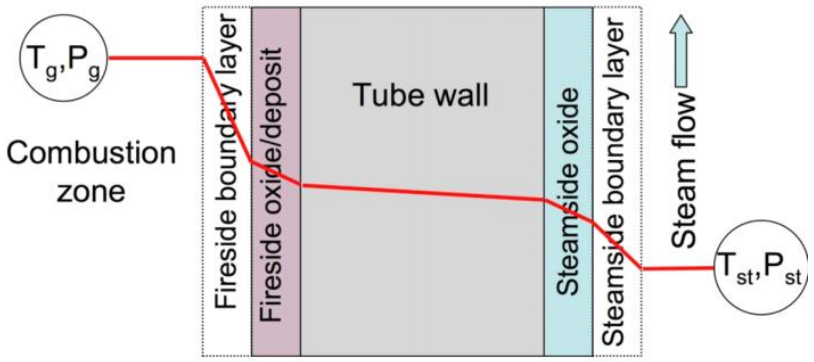

Figure 2.12 Schematic representation of heat transfer path through the wall of a steam tube [68]

The heat is transferred from flue gases to the deposit surface by the net radiation and convection in the vicinity of superheater/reheater tubes. Subsequently, heat is conducted through deposit layers and outer oxide scales to the tube metal as well as inner oxide scales. Finally, the inner oxide scales may transfer the heat by convection to the steam. Therefore, the total thermal resistance between the flue gas and the flowing steam inside the tube includes a resistance associated with convection and radiation, which act in parallel, conduction resistances of deposit layers, outer oxide scales, tube metal and inner oxide scales and a convection resistance between the inner oxide scales and steam. Accordingly, the thermal circuit for such a composite system is of the following form (Figure 2.13) [42; 70]:

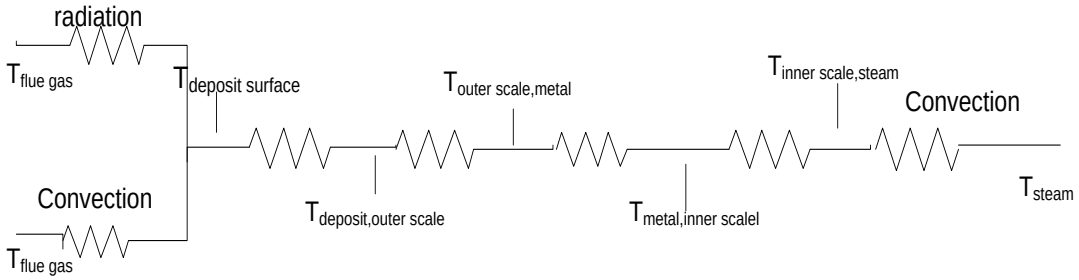

Figure 2.13 Series-parallel thermal circuit for heat exchanger' tubes in coal-biomass fired power plants

Furthermore, the total resistances R_t (mK/W)) is [70]:

$$\sum R_t = (2\pi h_r r_4 l + 2\pi h_f r_4 l)^{-1} + \frac{ln\frac{r_4}{r_3}}{2\pi k_{deposit} l} + \frac{ln\frac{r_3}{r_2}}{2\pi k_{outer\ oxide} l} + \frac{ln\frac{r_2}{r_1}}{2\pi k_{metal} l} + \frac{1}{2\pi h_{steam} r_0 l} \quad \textbf{(2-69)}$$

where h_r, h_f, and h_{steam}, are the fireside radiation heat transfer coefficient, fireside convection heat transfer coefficient, and steam side convection coefficient, respectively W/(m^{2}K), k is thermal conductivity (W/(mK)), r_i is the corresponding radius (m) when inner and outer oxides as well as deposits are formed on the tube surfaces and l is tube's length (m).

Finally, the heat transfer rate (W/m), q, between flue gas and the flowing steam, inside the tube given by [70]:

$$q = \frac{T_f - T_{steam}}{\sum R_t} \quad \textbf{(2-70)}$$

The overall heat transfer in terms of Nusselt number (*Nu*) around a tube is typically related to a power law relationship [71]:

$$Nu = cRe^m Pr^n \quad \textbf{(2-71)}$$

Regardless of the effects of free stream turbulence, tunnel blockage, thermal boundary condition, and surface roughness this correlation assumes that the Nusselt number is proportional to Reynolds number (Re) to the power of *m* and *Pr* (Prandtl number) to the power of *n* [71].

Fireside *Nu* number is as cosine function for the upstream side of the tube and it is a constant from 85 to 180° [42]:

$$Nu = \begin{cases} 0.67Re^{0.5}Pr^{0.35}\left(1+\cos\left(\frac{\pi}{180}\theta\right)\right) & \theta \leq 85^{\circ} \\ 0.73Re^{0.5}Pr^{0.35} & 85^{0} < \theta \leq 180^{\circ} \end{cases} \quad \textbf{(2-72)}$$

Due to the turbulent flow of steam, the heat transfer inside the boiler tube is considered as forced convection thus the *Nu* number in steam-side of the tube is equal to [70]:

$$Nu = 0.023Re^{0.8}Pr^{0.4} \quad \textbf{(2-73)}$$

Eq. (2-73) is valid for $0.7 \leq Pr \leq 160$, $Re \geq 10000$, $l/D \geq 10$ (l is tube length and D is inner tube diameter).

Deposits, corrosion products, refractories, and other materials on external surfaces reduce heat transfer rates to superheater/reheater tubes in coal/biomass fired power stations. The magnitude of this reduction mainly depends on the thickness, thermal conductivity, and absorptivity of the deposits. As the deposit grows, the deposit surface temperature increases, while the tube surface temperature drops due to the insulating effect of the deposit. The thermal resistance of the tube may also cause a very small decrease in temperature across the wall [72; 73].

However, when considering heat transfer through the steam-side surfaces, the effect of oxides are reversed. As mentioned before, the thermal insulation effect of thick inner oxide scales reduces the heat transfer across the tube wall and lead to temperature increase of the tube metal. This is because as the steam-side oxides thicken, the thermal resistance through the tube wall will be increased or thermal conductivity of the tube will be decreased, leading to a higher metal temperature [13; 68]. This phenomenon has been reported in references [13; 19; 74]. The thermal conductivity of steam-side scale is approximately 5% that of steel [20].

To obtain the tube mid-wall temperature the "half-wall drop" is subtracted from the surface temperature. The "half-wall drop" is obtained as follows [21]:

$$\Delta T = \frac{H_F W_{th}}{2k_t} \quad \textbf{(2-74)}$$

$$T_{mid} = T_{sur} - \Delta T \quad \textbf{(2-75)}$$

where ΔT is half-wall drop (°C or K), H_F is heat flux (W/m^2), W_{th} is tube wall thickness (m) and k_t is thermal conductivity of the tube material (W/(mK)).

However there are many rules of thumb used by the operating engineers to calculate the mid-wall metal temperature. In the superheater zone it is internal steam temperature at the location plus 50°C for radiant heat transfer surface and 40°C for convective heat transfer zone [75].

2.7 Creep of heat exchangers

2.7.1 Background

Elastic deformation: Deformation in which stress and strain are in a linear relationship is referred to as elastic deformation [60]. This type of deformation is not permanent and is reversible which means once the forces (load) are no longer applied, the object returns to its original shape. In elastic deformation stress and strain are proportional to each other according to Hooke's law [60]:

$$\sigma = E\varepsilon \quad \textbf{(2-76)}$$

where σ is stress (Pa), ε is strain, and E the constant of proportionality (modulus of elasticity) (Pa).

Plastic deformation: is type of permanent, non-recoverable (non-reversible) changes of shape of a material when exposed to applied forces [60].

Ductility: is a measure of the degree to which a structure will deform plastically prior to fracture. Ductility can, for example, be explained quantitatively by percent reduction in area, R_A [60]:

$$R_A = \left(\frac{A_0 - A_f}{A_0}\right) \times 100 \quad \textbf{(2-77)}$$

where A_0 is original cross-sectional area (m^2), and A_f is cross-sectional area at the point of fracture (m^2).

Yield strength: yield strength or yield point of a material is the stress level at which a material begins to deform plastically. Below the yield stress the material will deform elastically and will return to its original shape when the applied stress is released. Therefore, the magnitude of the yield stress (MPa) for a metal represents its resistance to plastic deformation [60].

Tensile strength: it is the maximum stress that a structure can sustain in tension beyond which fracture will result. At tensile stress a small neck begins to form at some point of the metal, indicating all subsequent deformation and ultimate fracture takes place at this neck [60].

2.7.2 Applied stress

When the pressure inside a cylinder of a diameter *D*, wall thickness *t* and length *L* is larger than the pressure outside, it causes stress around the cylinder (σ_C) and along the cylinder (σ_L) as shown in Figure 2.14 [76]:

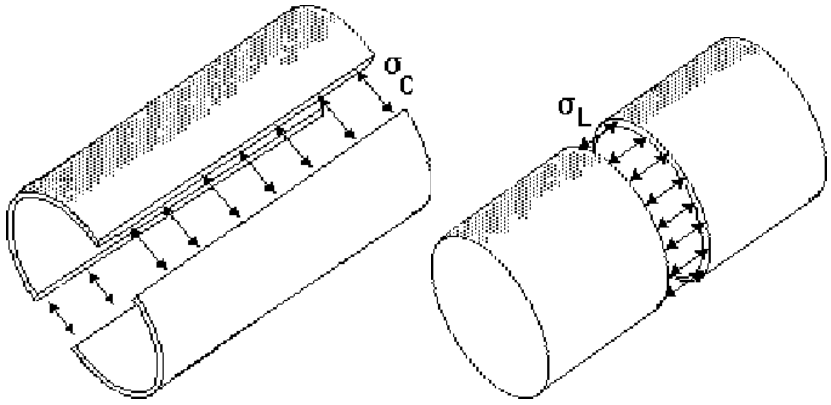

Figure 2.14 Applied stress acting on circumferential (left) and longitudinal direction (right) of the tubes

The stress produced in longitudinal direction is called longitudinal stress (σ_L) and the one acting on circumferential direction (σ_C) is called circumferential stress. The latter is also called hoop or tangential stress [76]. Hoop stress is twice that of the longitudinal (axial) stress [77].

Different stress equations may be applied for thin-walled and thick-walled tubes. A cylinder is regarded as thin-walled when the wall thickness is less than 1/10 of the radius. When the wall thickness is bigger than this, it is regarded as a thickwall [76].

The hoop stress σ (Pa) acting on a thick-walled tube can be calculated as follows [20]:

$$\sigma = P\left(\frac{{r_o}^2 + {r_i}^2}{{r_o}^2 - {r_i}^2}\right) \quad \textbf{(2-78)}$$

where P is internal steam pressure (Pa), r_o is outside radius (m), and r_i is inside radius (m).

The hoop stress σ (Pa) acting on a thin-walled tube can be calculated by the following equation [20; 21]:

$$\sigma = \frac{P\left(r_O - \frac{W_{th}}{2}\right)}{W_{th}} \quad \textbf{(2-79)}$$

where r_O is outside radius of the heat exchanger's tube (m), and W_{th} is its wall thickness (m).

Eq. (2-80) is another hoop stress equation to be used for a thin-walled tube [78; 79]:

$$\sigma = \frac{PD}{2W_{th}} \quad \textbf{(2-80)}$$

where D is mean diameter (r_O-W_{th}/2) of the tube (m).

And the last hoop stress for a thin-walled tube is equal [80]:

$$\sigma = P\frac{\left(r_i + \frac{W_{th}}{2}\right)}{W_{th}} \quad \textbf{(2-81)}$$

For thick-walled superheater tubes, choice of the right stress formula is quite significant. On the other hand, for thin-walled reheater tubes and for thick-walled superheater tubes under severe corrosion conditions, choice of the correct stress model is not crucial [18].

During operation, fireside corrosion and steam-side oxidation continuously reduce the wall thickness of superheater/reheater tubing and thereby increase the hoop stress within the tube wall [21].

2.7.3 Creep (deformation)

Failures resulting from long-term over-heating take place in water and steam cooled tubes such as water-walls, superheater and reheaters. Almost 90% of this failure happens in superheater and reheater tubes. Over-heating can happen due to many reasons such as internal deposits, low coolant flow through the tube, excessive fireside heat input, or being near or opposite burners. In long-term overheating conditions metal temperatures exceed design limits for a long period of time. Creep rupture (stress rupture) is a form of long-term over heating damage that usually creates thick-lipped rupture at the apex of a bulge, sometimes called fish mouth failure [73].

Materials that are placed in service at elevated temperatures and exposed to static mechanical stresses will deform. Deformation under such circumstances is called creep. Creep as a time-dependent and permanent deformation of materials is often the limiting factor in the life time of the component. At a temperature below $0.4T_m$ the strain (deformation) is almost independent of time. For metals creep becomes an important phenomenon at temperatures higher than $0.4T_m$ (absolute melting temperature) according to Figure 2.15 [60]:

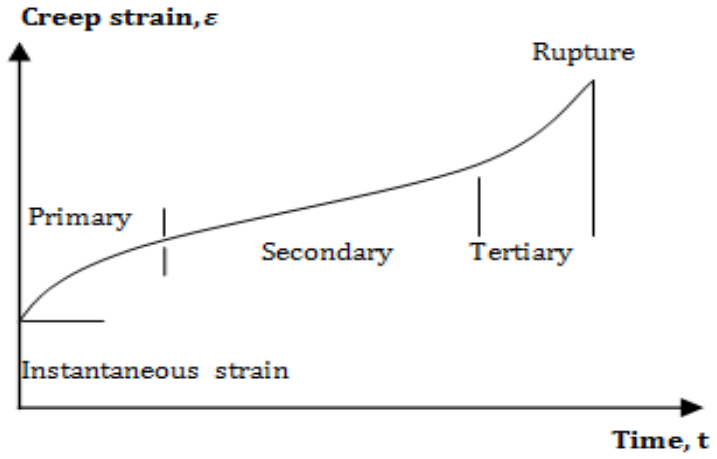

Figure 2.15 Change of creep strain with time

In this curve both the applied stress and the elevated temperature are constant. The creep curve is composed of three regions [60]:

- Primary creep takes place first where creep rate decreases continuously and the slope of the curve reduces with time.

- For secondary creep (steady-state creep) the plot becomes linear thus the creep rate is constant. This stage is longest stage of the creep behaviour.
- In tertiary creep, the rate of creep is accelerated which results in ultimate failure of the metal, frequently termed rupture.

2.7.4 Tube failures

The rupture in materials is caused by micro-structural and metallurgical changes such as grain boundary separation, and the formation of internal cracks, cavities, and voids. The slope of the secondary portion of the creep curve $\left(\frac{\Delta\varepsilon}{\Delta t}\right)$ in Figure 2.13 is termed minimum or steady-state creep rate $\dot{\varepsilon_s}$ [60]. Creep rupture failure of superheater/ reheater tubes is a main cause of forced outages of steam generating boilers. It accounts for 23.4% of the failures in the boilers. The following is a tabulation of the top 10 cause of failures [18; 20]:

Table 2-8 Top 10 failure causes [20]

Failure causes	Statistics
Creep (long-term overheating)	23.4%
Fatigue	13.9%
Ash corrosion	12.0%
Hydrogen damage	10.6%
Weld failures	9.0%
Short-term over heating	8.8%
Erosion	6.5%
Oxygen pitting	5.6%
Caustic attack	3.5%
Stress corrosion attack	2.6%
Total	95.9%

At known stresses and temperatures, the following model was suggested by Norton and Bailey [78]:

$$\dot{\varepsilon_s} = k_{cr}\sigma^n \quad \textbf{(2-82)}$$

where $\dot{\varepsilon_s}$ is creep rate (h^{-1}), k_{cr} is creep pre-exponential factor ($(MPa)^{-n}/h$), n is stress exponent and σ is hoop stress (MPa).

Since creep is a thermally activated process, its temperature sensitivity would be expected to follow an Arrehenius-type expression, with a characteristic activation energy for rate-controlling mechanism. Eq. (2-82) can therefore be rewritten as [78]:

$$\dot{\varepsilon_s} = k_{cr}\sigma^n e^{-\frac{Q_{cr}}{RT}} \quad \textbf{(2-83)}$$

where Q_{cr} is creep activation energy (J/mole).

During creep the circumference of the tube expands thus the wall thickness decreases so as to conserve volume [77]. To calculate wall thickness decrease (ΔW_{th}) due to creep we require knowing the strain in *z* direction which defined as [76] :

$$\varepsilon_z = \frac{1}{E}[\sigma_z - \upsilon(\sigma_x + \sigma_y)] \quad \textbf{(2-84)}$$

where σ_x and σ_y are the axial (longitudinal) and circumferential (hoop) stresses respectively, *E* is modulus of elasticity and ν is Poisson's ratio.

σ_z is sufficiently small everywhere on the tube's wall that $\sigma_z \approx 0$. In addition, the longitudinal stress is half of the hoop stress. Finally, changes in wall thickness (m) can be calculated as follows [76]:

$$\Delta W_{th} = W_{th}.\varepsilon_z \quad \textbf{(2-85)}$$

2.7.5 Material selection

Although the materials of superheater tubes are superior compared to other tubes, failures of superheater tubes take place most frequently. The steels have been classified into four groups for use in the increasing order of operating temperature which include [10]:

1. Carbon steels (0Cr)
2. Low alloy ferritic (1-2.25Cr)
3. High alloy ferritic (9-12Cr)
4. Austenitic steels (17-25Cr)

Some of the important factors to be considered for selection of such steels are resistance to creep deformation and rupture, resistance to fireside corrosion and steamside oxidation etc [10].

Low alloy ferritic steels (e.g. T22) are widely used in pressurised application in coal/biomass-fired boilers in a temperature range where mild steel become too susceptible to creep. They have good tensile strength at temperatures up to 450°C, creep strength at temperatures up to 550°C and resistance to steam oxidation. The high ferritic steels (e.g. T91) are used for tubing in superheater tubes where the alloys are exposed to high pressure steam (33MPa) at temperature of 620°C [66].

Austenitic steels, often referred as 300-series stainless steels, are higly alloyed steels with austenitic structure. Austenitic steels usually have good high temperature strength and creep resistance due to their austenitic structure, and corrosion resistance due to high chromium content. They are more expensive than ferritic steels and have relatively poor thermal conductivity [66].

2.7.6 Remaining creep life of superheater/reheater tubes

The increase in hoop stress due to the tube wall thickness reduction and also increase in metal temperature due to thermal insulation effects of internal oxide scales lead to a decrease in creep life of the superheater tubes or time to the failure [20]. The creep life of a boiler tube is very sensitive to the metal temperature. According to a rule of thumb, for every 10K decrease in the metal temperature, the creep life of the tube will rise by a factor of two [81].

There are 4 methods to predict the rupture lifetime of a boiler tube [82]:

1. Monkman-Grant method
2. The Orr-Sheryy-Dorn life prediction method
3. The larson-Miller parameter
4. Manson-Succop method

The Monkman-Grant relationship relates the rupture life time of the tube to its minimum creep rate as [83]:

$$t_r = \frac{C}{\dot{\varepsilon}^m} \quad \textbf{(2-86)}$$

where t_r is rupture lifetime of the component (h), *C* and *m* are material constants.

For the metals and alloys initially evaluated by Monkman-Grant, the exponent *m* had values between 0.8 and 0.95, while the constant *C* varied between 3 and 20 [83].

The Orr-Sheryy-Dorn life prediction method defined as [82]:

$$P_{OSD} = Logt_r - \frac{Q}{RT} \quad \textbf{(2-87)}$$

where *Q* is a characteristic activation energy (J/mole) for the process and *R* is universal gas constant (J(/moleK)) and T is temperature (K)

The Larson-Miller parameter is similar to the Orr-Sheryy-Dorn parameter but different assumptons were made in its derivation [82]:

$$P_{LM} = T(Logt_r + C) \quad \textbf{(2-88)}$$

where *C* = 20 for many materials.

Finally, the method of Manson-Succop is as follows [82]

$$P_{MS} = Logt_r - BT \quad \textbf{(2-89)}$$

where *B* is a constant.

For many alloy systems, the relation between the minimum creep rate and time to rupture can be described by Monkman-Grant relationship in which different alloys possess different material constants [82].

The technological importance of the Monkman–Grant relationship is that once the constants *C* and *m* have been determined from a limited number of creep tests on a given material, Eq. (2-86) can be used to calculate the time to rupture of a long-time test as soon as the secondary creep rate is reached and to check the reliability of individual creep-rupture tests [83].

The scientific significance of the Monkman–Grant relationship is that it is a significant guide to the identification of creep rupture mechanisms. While the Monkman–Grant relationship was originally proposed as a phenomenological correlation, it can be theoretically derived by involving individual high-temperature fracture mechanisms [83].

Furthermore, the Larson–Miller or Orr–Sherby–Dorn parameters can predict the failure time based on the testing temperature and stress. However, because plots of stress vs Larson–Miller or Orr–Sherby–Dorn parameter often exhibit a pronounced curvature, these methods can be used reliably for extrapolation of failure time only over a limited range of stress and temperature [83]. It has to be pointed out that the Larson–Miller method is a reliable technique for rupture lifetime prediction of boiler tubing as long as the alloy microstructure is stable during prolonged exposure at high temperature [82].

3 UNDERSTANDING OF THE MATERIALS AND SYSTEMS

3.1 Understanding of the materials

3.1.1 Coal

Coal is a black, inhomogeneous, organic fuel, formed mainly from partially decomposed and metamorphosed materials. Coal formation has taken place over long time periods, often under high overburden pressures and at elevated temperatures. The components present in coals are influenced by differences in plant materials and in their extend of decay. The process of transformation of plant materials such as peat to coal is called as coalification, producing a variety of coal products. Some of these coal types are as follows [67]:

- Lignite
- Subbituminous
- Bituminous
- Anthracite

Lignite as the lowest rank of coal was formed from peat which was compacted and altered. It comprises recognizable woody materials imbedded in pulverized and partially decomposed vegetable matter. Lignite displays high moisture content and a low heating value when compared with the higher rank of coals [67; 84].

Subbituminous coal is dull, black coloured and shows little woody material. It has lost some moisture content, but is still of relatively low heating value. On the other hand bituminous coal is dense, compacted, and brittle and is dark black coloured. It has low moisture content, a variable volatile matter content from high to medium and a high heating value [67; 84].

Anthracite, as the highly metamorphosed coal, is jet-black in colour, hard and brittle and displays a high lustre. Its moisture content is low while its carbon content is high [67; 84].

Properties of coal samples can vary with time and temperature. Therefore, it is necessary to declare the state of coals in order to characterise these physical properties. In practice the following four states are typically used [28; 85]:

- "*a*" refers to analytical state in which coal is in thermodynamic equilibrium with ambient air.
- "*d*" or *"wf*" describes dry or water free state which can be obtained after 2 hours residence of coal sample in a furnace of temperature 105-110°C :

$$\mathrm{C} + \mathrm{H} + \mathrm{O} + \mathrm{N} + \mathrm{S} + \mathrm{Cl} + \mathrm{ash} = 100 \quad \textbf{(3-1)}$$

- "*waf*" stands for water and ash free state:

$$\mathrm{C} + \mathrm{H} + \mathrm{O} + \mathrm{N} + \mathrm{S} + \mathrm{Cl} = 100 \quad \textbf{(3-2)}$$

- "*af*" means ash free state of the coal sample.
- "*ar*" stands for as received which refers to weight percentage of the material in its original form (including ash and moisture):

$$\mathrm{C} + \mathrm{H} + \mathrm{O} + \mathrm{N} + \mathrm{S} + \mathrm{Cl} + \mathrm{ash} + \text{water content} = 100 \quad \textbf{(3-3)}$$

The ash content of a coal can be expressed in weight% on dry basis and on as received basis. The weight percentage of ash on dry basis can be calculated through the following equation [85]:

$$\text{Ash content (wt\% dry)} = \frac{\text{ash content (wt\% ar)} * 100}{(100 - \text{water content (wt \%)}} \quad \textbf{(3-4)}$$

The amount of volatiles is expressed in weight% (dry basis), as received basis or dry and ash free basis. The amount of fixed carbon, in dry, water ash free and as received state is calculated through the following formulas respectively [85]:

$$\text{fixed C} = 100 - \text{ash (dry)} - \text{volatiles (dry)} \quad \textbf{(3-5)}$$

$$\text{fixed C} = 100 - \text{volatiles (waf)} \quad \textbf{(3-6)}$$

$$\text{fixed C} = 100 - \text{ash (ar)} - \text{water content} - \text{volatiles (ar)} \quad \textbf{(3-7)}$$

Coals vary significantly in their composition. According to a research carried out by Bituminous Coal Research Institute, of 1200 coals categorised no two had the same composition [67]. Typical coal compositions are as follows: 65-95% carbon, 2-7%

hydrogen, up to 25% oxygen up to 10% sulphur, and 1-2% nitrogen. Inorganic mineral matter levels commonly vary from 5 to 15%, but values as high as 50% have been observed. Moisture as high as 70% has also been observed but values of2 to 20% are more typical [67].

For example in USA standards, the composition of coal is traditionally determined by ASTM proximate analysis or ASTM ultimate analysis. The former deals with the moisture content, volatiles, ash, and fixed carbon of coal. While, ASTM ultimate analysis gives elemental composition for carbon, hydrogen, nitrogen, sulphur, and oxygen. The residual mineral matter is shown as ash [67]. Table 3-1 shows typical proximate and ultimate analyses for two types of coal i.e. Daw Mill coal and El-Cerrejon coal [86]:

Table 3-1 Typical proximate and ultimate analyses for two types of coal

Coal	El-Cerrejon	Daw Mill
Proximate analysis (%wt, *ar*)		
Moisture	5.80	4.60
Ash	8.60	4.20
Volatile matter	34.80	31.30
Calorific value (kJ/kg)		
Gross calorific value	27850	25260
Net calorific value	27122	24107
Ultimate analysis (%wt, *ar*)		
Carbon	69.20	74.15
Hydrogen	4.80	4.38
Nitrogen	1.42	1.17
Oxygen	9.98	10.49
Sulphur	0.58	1.28
Chlorine	0.02	0.20

The calorific value of coal is direct measurement of the chemical energy stored in the fuel and thus is a crucial parameter for determining the value of coal as fuel. The calorific value of coal can be estimated from ultimate composition of the fuel as follows [87]:

$$\mathrm{CV} = 144.5X_C + 610X_H - 62.5X_O + 40.5X_S \quad \textbf{(3-8)}$$

where *CV* is the calorific value on dry, ash-free basis X_i denotes the weight percentages of carbon, hydrogen, oxygen and sulphur respectively.

Or from proximate analysis of coal [87]:

$$\mathrm{CV} = 14760 + \mathrm{a(VM)} \quad \textbf{(3-9)}$$

where *VM* is the percentage of volatile matter, and *a* is a constant that is a function of *VM*.

Moreover, the residual mineral matter is presented as ash. Ash in coals contains significant amount of several elements, together with small amounts of several elements, as shown in Table 3-2 for Daw Mill and El-Cerrejon coals. Ash includes 5 to 20% of the mass of coal and is a major source of pollution. Mineral matter can generate fly ash particulates during combustion [67].

Table 3-2 Example of Fuel Ashes analyses [86]

Ash composition (%wt, *ar*)	El-Cerrejon	Daw Mill
SiO_2	60.69	36.80
Al_2O_3	22.01	23.90
Fe_2O_3	7.43	11.20
TiO_2	0.92	1.10
CaO	2.27	12.00
MgO	2.90	2.50
Na_2O	1.06	1.50
K_2O	2.32	0.50
Mn_3O_4	0.06	0.40
P_2O_5	0.21	
BaO	0.11	

Of greater concern is the mineralogical composition of coal ash. The abundance and distribution of inorganic components, as well as the size and type of mineral grains in the coal can be quantified using a combination of computer controlled scanning electron microscopy (CCSEM) and chemical fractionation techniques. Chemical fractionation is applied to quantify the abundance of organically associated elements

[88]. Table 3-3 shows the composition of mineral matter for three types of coal based on the weight percentages of total mineral matter:

Table 3-3 The composition of mineral matter for three types of coal based on their weight percentages [36; 89; 90]

Mineral matter	Chemical formula	Silesia, wt%	Daw Mill, wt%	El-Cerrejon, wt%
Kaolinite	$Al_4Si_4O_{10}(OH)_8$	40.5	54	16.9
Illite	$KAl_2(OH)_2(AlSi_3O_{10})$	18.1		9.4
Calcite	$CaCO_3$	6.3	14	
Dolomite	$CaMg(CO_3)_2$	3.0	12	
Magnesite	$MgCO_3$	4.6		
Pyrite	FeS_2	8.1	20	12.9
Halite	NaCl	0.2		
Sylvite	KCl	0.3		
Quartz	SiO_2	9.8		54.2
Hematite	Fe_2O_3	5.9		
Magnetite	Fe_3O_4	4.0		
Coquimbite	$Fe^{+3}{}_2(SO_4)_3.9H_2O$			3.5
Bassanite	$CaSO_4.0.5H_2O$			3.2
Gypsum	$CaSO_4.2H_2O$	2		

The use of coal as a fuel is an overwhelming choice in a new steam boiler in most parts of the world (but not the UK or some other part of the EU). The type of coal will dictate the design of a steam boiler. The composition of the coal and the way in which it is burnt dictates the corrosiveness of the deposits that form on heat exchangers which in turn dictates the materials used for superheater and reheater tubes [20]. For example, there is a difference between the inorganic constituents of Eastern and Western US coals. By definition, Western US coals are usually lignites or subbituminous coals for which CaO+MgO content exceeds the Fe_2O_3 content of the ash, while the opposite is true for Eastern coals [91].

Eastern US coal which are mainly bituminous in rank, are predominantly in the form of discrete mineral particles. Kaolinite and Illite are normally dominant

followed by quartz and pyrite. In addition, in bituminous coals, the calcium content is typically low (CaO<5%) while the calcium content of Western coals is high (CaO≈10 to 30). On the other hand, minerals such as Illite, which incorporate most of the potassium in bituminous or Eastern coals, are normally low in lignite and subbituminous (Western) coals. In Western coals, sodium and potassium exist as salts of humic or carboxylic acids [91].

3.1.2 Biomass

Biomass consists of biological material derived from the five kingdoms in biology including plants, animals, fungi, protists and monerans. It is a renewable resource which indicates that it is part of a flow of resources that arises naturally and repeatedly in the environment. The sun's energy, in the form of photosynthesis from the photoactive properties of radiation induces the renewability of biomass [92].

Biomass can be classified into [92]:

- Woody biomass: this includes all standing biomass in natural forests, woodlands and commercial tree plantations. Moreover, bush trees, urban trees and on-farm trees are other types of woody biomass.

- Non woody biomass: this includes agricultural crops that are grown specifically for food, fodder, fiber or energy production. Crop and plant residues produced in the field such as cereal straw, leaves and plant stems are assumed to be non woody biomass as well. In addition, sawdust, saw mill offcuts, bagasse, nutshells and husks resulting from the agro-industrial conversion or processing of crops known as processing residues are other types of non-woody biomass.

- Animal waste: waste from intensive and extensive animal husbandry forms the last type of biomass.

In comparison with the conventional fossil fuels, fresh biomass has the following disadvantages [92] :

- They have a modest thermal content compared with fossil fuels.

- The moisture content of biomass is often high, resulting in the inhibition of its ready combustion, causing significant energy loss on combustion, mainly as latent heat of steam.

- Biomass usually has low bulk density, which results in the use of relatively large equipment for handling, storage and burning.

Biomass has lower heating values than coal on a similar weight basis. Specifically, the heating value of biomass is in the range of 15–19GJ/t, where heating values for agriculture residues and woody materials are 15–17 and 18–19GJ/t, respectively, compared to 20–30GJ/t for coals. However, in comparison to coal, biomass has much higher volatile matter content, 80% in biomass vs. 20% in coal, hence, biomass has a high ignition stability and can be more easily processed thermo-chemically into other higher-value fuels, such as methanol and hydrogen [93].

The high moisture content is one of the most significant disadvantages biomass as a fuel source. To maintain a stable combustion process, the moisture content (on wet basis) of biomass cannot be higher than 65% [93]. There is a negative linear relationship between the moisture content and the heating value. Another key feature of biomass fuel is its high oxygen content. Typically, the oxygen content of biomass is as high as 35%wt, roughly ten times higher than that of a high-rank coal, which is below 4%wt [93].

The identification and characterization of chemical and phase compositions of biomass is the initial and most vital step during the investigation and application of such fuel. These compositions characterize and determine the properties, quality, potential applications and environmental problems related to any biomass. As for coal, structural analysis, proximate analysis, ultimate analysis, ash analysis, and mineralogical analysis can be applied to characterise biomass [94] .

The structural composition is related to the organic and inorganic constituent of biomass. Biomass contains a wide range of organic materials, which generally include cellulose, hemicellulose, lignin, lipids, proteins, simple sugars and starches. Among these compounds, cellulose, hemicellulose, and lignin are the three main constituents. Biomass also contains inorganic constituents and a fraction of water [93]. For example, the composition of mineral matter in wood is dependent on the soil conditions under

which the tree grew, and the location of the sample within the tree. Mineral matters necessary for plant growth and other minerals are transported from the soil through the roots. The minerals are mainly composed of salts of calcium, potassium and magnesium, with other salts in lesser amounts. The acid radicals are carbonates, phosphates, silicates, sulphates and oxalates. In some species, sub-micron crystals of calcium oxalate (CaC_2O_4) have been observed. For bark, in addition to the minerals transported from the soil, there are other source of minerals such as wind-blown minerals and minerals picked up during harvesting. Relatively little mineral matter is extractable from wood with water [95]. The mineral matter in biomass is normally much less than in coal, excluding animal biomass and some varieties from herbaceous, agricultural and contaminated biomass [96].

Ultimate analysis is one of the significant factors when studying biomass fuels properties. It analyses the percentage of nitrogen, sulphur and chlorine to study the environmental impact of biomass. In addition, it helps to calculate the percentage of carbon, hydrogen and oxygen to estimate the heating value of these fuels [94].

Proximate analysis measures the percentage of volatile matter, fixed carbon and ash content. This analysis is very important to study the combustion phenomenon of biomass. For instance, the ash content in biomass fuels can lead to ignition and combustion problems [94]. Table 3-4 shows typical heating value, proximate and ultimate analyses for two types of biomass i.e. C.C.P (Cereal Co-Products) and Miscanthus:

Table 3-4 Typical proximate and ultimate analyses for two types of biomass [86]

Biomass	Miscanthus	C.C.P
Proximate analysis (%wt, *ar*)		
Moisture	10.80	8.10
Ash	4.60	4.20
Volatile matter	70.70	70.80
Calorific value (kJ/kg)		
Gross calorific value	17824	17610
Net calorific value	16478	16340
Ultimate analysis (%wt, *ar*)		
Carbon	43.59	43.30
Hydrogen	4.80	5.80
Nitrogen	0.58	2.70
Oxygen	35.52	35.57
Sulphur	0.11	0.16
Chlorine	0.09	0.17

The composition of ashed biomass fuel strongly depends on the species and part of the biomass plant. The available nutrients, soil quality, fertilizers and weather conditions have a significant influence on the contents of potassium, sodium, chlorine and phosphorus especially in agro-biomass fuel ashes [94]. Table 3.5 gives typical fuel ash compositions of the biomass fuels i.e. C.C.P and Miscanthus:

Table 3-5 Ashes analyses of two biomass fuels [86]

Ash composition (%wt, *ar*)	Miscanthus	C.C.P
SiO_2	55.58	44.36
Al_2O_3	3.14	2.79
Fe_2O_3	2.12	2.47
TiO_2	0.19	0.12
CaO	8.77	7.78
MgO	3.76	3.96
Na_2O	0.50	0.36
K_2O	12.69	24.72
Mn_3O_4	0.15	0.10
P_2O_5	12.30	12.04
BaO	0.03	0.05

Generally ashed woody biomass is normally rich in calcium and potassium. Herbaceous or agricultural biofuels are rich in silicon. However, some of the fuels, like straws of cereals have also relatively high potassium and chlorine contents [94]. Biomass currently contributes to 14% of the world's primary energy demand and is considered as the fourth largest energy source. In Canada almost 4.7% of the national primary energy for 2006 was derived from the conversion of renewable biomass and waste [93].

Bioenergy can be obtained from biomass via two major processing routes [93]:

- Thermo-chemical
- Bio-chemical/biological processes.

Generally, thermo-chemical processes have higher efficiencies than bio-chemical/biological processes since they require a lower reaction time (e.g. a few seconds or minutes for thermo-chemical processes vs. several days, weeks or even longer for bio-chemical/biological processes) and have a greater ability to destroy most of the organic compounds. For example, lignin materials are typically considered to be non-fermentable and thus cannot be completely decomposed via biological processes, whereas they are decomposable via thermo-chemical approaches [93].

Direct combustion, pyrolysis, gasification, and liquefaction are the main thermo-chemical conversion processes. The energy stored within the biomass can be released directly as heat via combustion/co-firing, or could be transformed into solid (e.g. charcoal), liquid (e.g. bio-oils), or gaseous (e.g. synthetic gas) fuels via pyrolysis, liquefaction, or gasification for various purposes [93].

Combustion is the most commonly used process for biomass conversion. It contributes to over 97% of bioenergy production in the world. In some less-developed countries, combustion of biomass (e.g. wood) is the main source of energy available for cooking and heating. However, direct combustion of unconverted biomass to produce heat is relatively inefficient due to heat wastage in volatilization of moisture, heat losses from the equipment and the requirement of excessively large and expensive equipment in relation to heat yield. Some preliminary pretreatment of biomass is necessary in order to

upgrade the efficiency of its combustion; this includes, chopping, grinding, briquetting or drying. Biomass combustion takes place in three main stages [92; 93]:

1. Drying,
2. Pyrolysis and reduction
3. Combustion of volatile gases and solid char.

The combustion of volatile gases contributes to more than 70% of the overall heat generation. It happens above a fuel bed and is generally evident by the presence of yellow flames. In addition, the presence of small blue flames in the fuel bed is the sign of char combustion. The combustion of biomass on a large scale is still considered to be a complex process with technical challenges associated with the fuel characteristics, types of combustors, and the challenges of co-firing processes [93].

In principle, there are two possibilities for biomass utilisation in power plants: biomass can either be burnt as single fuel in combined heat and power plants or they can be co-fired in existing coal-fired power stations [97].

Co-firing biomass and coal has been proven to be a cost-effective technology to achieve the goal of increasing the use of biomass for power generation in UK and EU. This is because of the few modifications that are required to upgrade originally coal-based power plants. According to IEA (International Energy Agency), more than 150 coal-fired power plants (50–700MWe) in the world, to date, have been co-firing coals and woody biomass or waste materials [98]. Various types of biomass can be easily co-fired with different types of coal in percentage fractions as high as 15%. Biomass co-firing with coal can reduce fouling and corrosion of the boiler tubes, when compared to using biomass alone, due to the dilution and the consumption of alkali metals via interactions with sulphur or silica in the coal [93; 98]. There are three general techniques for co-firing [93] :

1. Direct co-firing which involves mixing the biomass and coal in the fuel handling system and feeding that blend to the boiler. Due to the poor physical properties of biomass (e.g., higher moisture contents, low bulk densities, etc.), co-firing processes for this category normally are limited to low co-firing ratios.

2. Parallel co-firing by which biomass is prepared separately from coal and introduced into the boiler without impacting the conventional coal delivery system.

3. Indirect co-firing in which biomass is gasified and then can be burnt in either a boiler or a combined cycle combustion turbine generating plant. This technique is particularly suitable for co-combustion with natural gas and for the utilization of low-grade biomass and wastes.

Direct co-firing is the least expensive, most straightforward, most commonly applied approach of co-firing in power generation industry. In contrast, indirect co-firing can offer a high degree of fuel flexibility, and the fuel gas can be cleaned prior to combustion to minimize the impact of combustion products on the performance and integrity of the boiler [94].

There are some barriers to co-firing biomass with coal including biomass procurement practices to obtain low-cost fuels in a long term reliable manner; the impact co-firing on ash composition (e.g. alkali salts); the balance between the impact of biomass on emissions and fuel cost relative to the impact of biomass on boiler efficiency [94].

3.2 Coal and biomass burning systems

The function of any boiler is to burn coal in order to heat some material or process stream (e.g. water, steam).The burner introduces the fuel and air, or other oxidants (e.g. oxygen) and mixes them to maintain a stable flame. According to design constraints, the combustion chamber must be large enough to contain the flame to permit maximum transfer of heat (thermal efficiency) to waterwall, superheater and reheater tubes as well to provide sufficient space for complete combustion and to permit proper removal of the products of combustion and ash [87]. Coal may be fired in three primary ways [87]:

- In a fixed bed on a grate
- In a fluidised bed
- In a pulverised or entrained bed

Fixed-bed systems have been extensively used for biomass and combustion for a number of years. Simply, a fixed-bed system comprises one combustion chamber with a

grate [99]. In grate firing, coal/biomass is piled on a perforated support (grate) and air is blown through the bed from underneath which is called under-fire air or primary air. The reactions in the bed are primarily pyrolysis and gasification [87]. Generally, as soon as the new fuel (biomass or coal) is introduced into the furnace, it is pyrolysed into volatile gases and chars. Primary and secondary air supplies are provided under and above the grate for the combustion of chars and volatile gases, respectively. The heat produced through the combustion of chars is responsible for providing enough heat for the pyrolysis of newly added fuel. Biomass fixed-bed combustion systems look similar to fixed-bed combustion systems for coal, but the actual furnace designs are different. In particular, the high volatile matter content of biomass requires a large combustion chamber above the grate in biomass-fired furnaces. For the same reason, biomass furnaces require a higher proportion of secondary to primary air than coal-fired furnaces. A fixed-bed biomass combustion system usually operates at 850–1400°C [93; 99].

In a fixed bed, fresh fuel can be supplied in only three ways: from the top, from the side and from underneath [87].

Typical examples of fixed-bed feed systems are: manual-fed systems, spreader-stoker systems, under-screw systems, through-screw systems, static grates, and inclined grates. For relatively small operations, special feeding systems such as screw feeders and spreader stokers have been developed. Screw-feeder systems are developed for small- to medium-sized fuel particles. The under-screw system is applied for fuel sizes in the range of 40 x 30 x 15mm (length x width x height). The fuel is pushed up in the centre of the combustion zone and ash is removed from the sides, manually or automatically [99].

The through-screw system is used for larger fuel pieces (approximate length of 100 and diameter of 50mm). The fuel is burned while being screw-fed through the combustion zone. The remaining bottom ash is dropped into the bottom ash collector. This type of system is especially suitable for fuels that have high ash content. The inclined grate was initially developed during the 1920s and 1930s for coal combustion systems. The fuel is supplied at the top and moves down-ward during the combustion process. The ash is removed at the bottom [99].

Various stoker designs and applications have been introduced to solve the problems of fuel supply and combustion and of ash removal in grate firing (fixed bed) including: spreader stoker, travelling grate stoker and underfeed stoker. For example, in a spreader stoker fuel can be distributed uniformly or can be heaped toward one side when ash removal is required. In travelling grate stoker, however, fuel is fed out of the hopper onto the chain grate which then carries the coal across the chamber, delivering the ash to ash pit [87].

The cyclonic combustion system, viewed as a modified fixed-bed system, and suitable for the combustion of agricultural residues and particulate wood wastes at a high efficiency is the recent developments have been made to enhance the combustion efficiency [93; 99]. The schematic diagram of a fixed bed gasifier is given in the Figure 3.1:

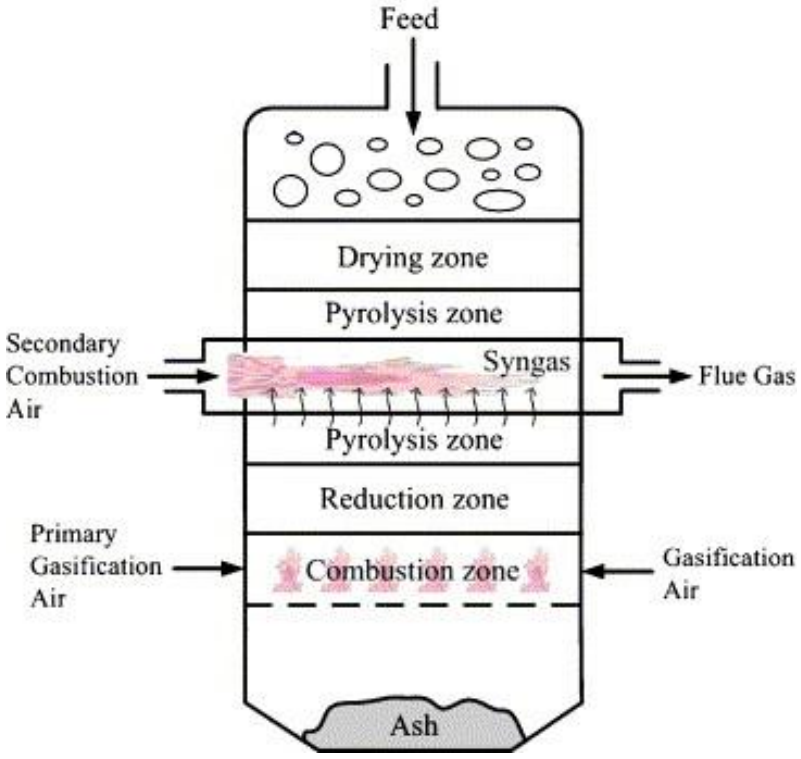

Figure 3.1 Schematic diagram of a modified fixed bed gasifier [100]

In circulating fluidized bed combustion system the combustion chamber is surrounded by water walls and superhetears are located in the gas pass after the cyclone. The flue gas temperature approaching the superheaters is ~860-880°C. The steam system operates with final superheater output at 480°C/8MPa [48].

Compared with fixed-bed systems, fluidised systems have higher combustion efficiencies and they are more suitable for large scale operations normally exceeding 30MWth [101]. Fluidised-bed systems employ silica sand, limestone, dolomite, or other non-combustible materials for the bed material. The typical operating temperature of bed material is 700–1000°C, which is lower than that of fixed-bed systems. The bed materials act as a heat transfer media which are fluidised by the air flow coming from the bottom. Depending on the air velocity, fluidised-bed systems can be further divided into bubbling fluidised-bed (BFB) and circulating fluidised-bed (CFB) systems [93; 99].

In a bubbling fluidised bed the reactor is divided into two zones: a zone containing freely moving sand particles supported by upward-streaming air (giving the impression of a bubbling fluid) and a "freeboard" zone above the fluidised bed. Conversely, in a circulating fluidised bed, the air velocity is so high that bed and fuel particles except for the large, heavy fuel particles flow upward with the gas stream [93; 99].

Circulating fluidised-bed systems have several advantages, such as the flexibility to various fuels with different properties, sizes, shapes, and moisture (up to 60%) and ash contents (up to 50%). Furthermore, the CFB units can accomplish high heat transfer and reaction rates with a compact construction [93; 99].

In the fluidised bed the particle size (roughly 1-5mm) is small enough for the combustion air rising through the bed to entrain the small particles. The particles move up and down in groups. However, when the particles are too small (below 1mm) they tend to be rapidly entrained and lost as unburned combustibles. Fly ash reinjection and a special burn-up cell are the solutions to control combustible loss [87]. Figure 3.2 shows schematic diagram of a fluidised-bed combustion boiler:

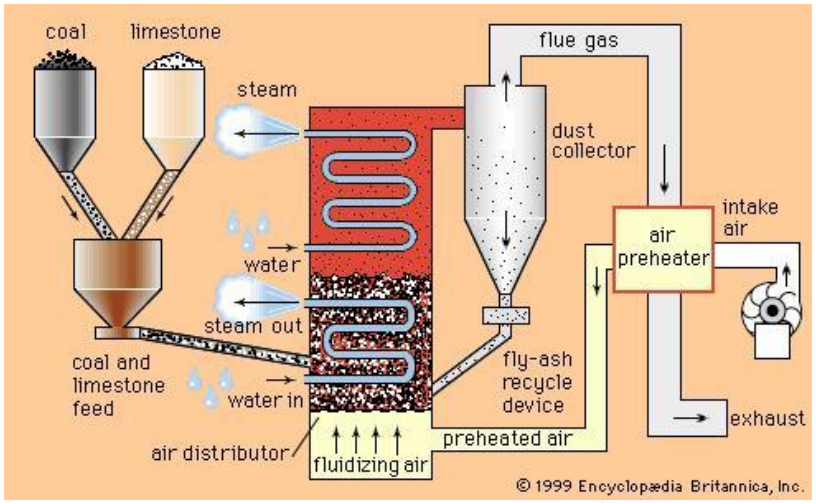

Figure 3.2 Schematic diagram of a fluidised-bed combustion boiler [102]

The hot gas paths of combustion systems contain a series of heat exchangers to produce high temperature/high pressure steam from water [48]. Figure 3.3 illustrates a flow diagram for a typical water/steam system, with series of heat exchangers being an economiser, evaporator and superheater before the steam enters the high pressure steam turbine. In this system, the steam is reheated before entering the intermediate pressure steam turbine. The highest steam temperatures in such system are reached in the final stages of the superheater and reheater [48].

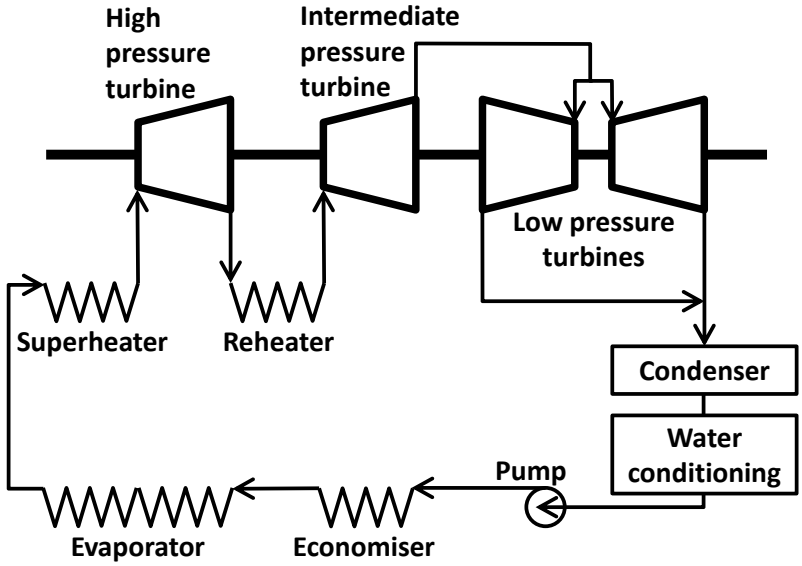

Figure 3.3 Schematic flow diagram of a power plant steam/water system showing the main component parts [48]

Pulverised coal power plants account for about 97% of the world's coal-fired capacity. They can have a size of up to 1000MW and are commercially available worldwide [103]. Pulverised coal firing was particularly successful from the 1920s onward in the boiler capacity of 350000lb steam per hour, which was the limit of mechanical stoker. In pulverised coal firing the particles must be fine enough to be carried by the combustion air or some fraction of it. This implies that the majority of particles must be less than 100μm and conveying velocity must be about 18m/s [87]. Therefore, in such boilers coal is first pulverised into a fine powder and then burned at temperatures of between 1300 and 1700°C [103].

This process heats water in tubes, located in the boiler, so that it becomes steam. This steam is then superheated before being passed into a turbine to produce electricity (Figure 3.4). The average net efficiency (energy produced minus energy used within the plant) can be up to 45% in pulverised coal power plants, which means that 45% of the energy in one unit of coal is converted into electricity [103]. Plants that were built in the 1960s-1970s often have steam systems that operate with maximum steam parameters of about 14-16MPa /540-560°C and currently operate with efficiencies of ~35-37% [4]. However, new coal systems use individual boilers of similar sizes, but operate with maximum steam parameters of approximately 29MPa/620°C giving efficiencies of 46-47% [4].

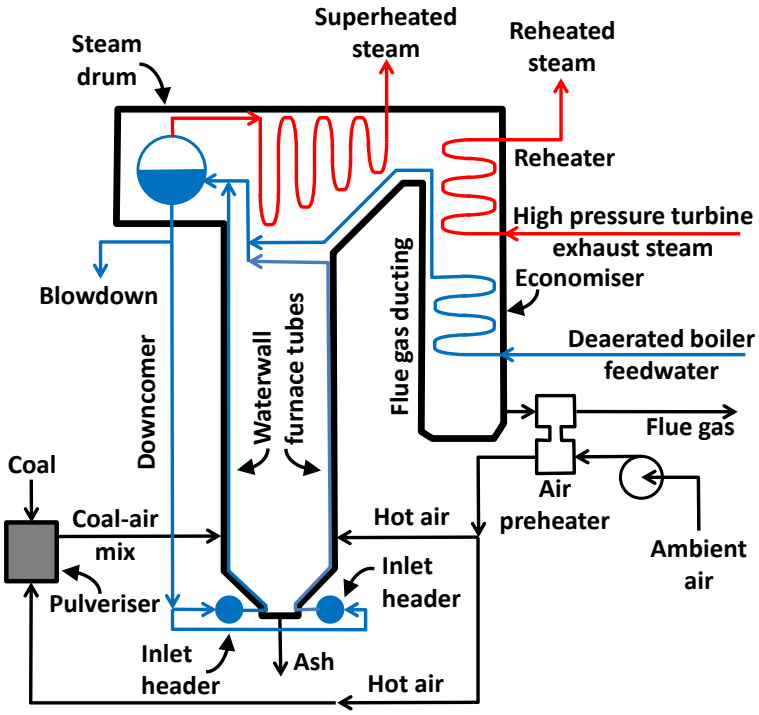

Figure 3.4 Schematic diagram of a pulverised coal power plant showing the position of the main heat exchangers [48]

Figure 3.4 describes the layout of the heat exchangers around conventional pulverised-fuel fired power plant; this shows that the combustion zone is surrounded by waterwalls and that the hot gases from the combustion process then flow past the various superheater and reheater tubes before going through the economiser. In such a system, the waterwalls are relatively cool (up to 400°C) despite facing the fuel burners and combustion gases of up to 1600°C, but have high heat fluxes (up to ~0.4MW/m^2). The combustion gases have decreased to 1000-1200°C by the time they pass through the superheaters and produce heat fluxes of ~0.2MW/m^2; the steam temperatures exiting the superheaters can be ~540-620°C depending on the age of the power station. The combustion gases continue cooling through the superheaters, reheaters and economisers. The exit of the reheaters is at similar steam and metal temperatures (but lower pressures) compared to superheaters [48].

4 INTEGRATION OF COMPONENT LIFE PREDICTION MODELS

4.1 Introduction

There are several approaches in literature to assess the remaining service life of superheater/reheater tubes. One method, introduced by C.E.R.L (Central Electricity Research Laboratories), is based on an assessment of the total life fractions consumed from the stress and temperature history, together with stress rupture data for the alloy [21]. In this approach, knowledge of fireside corrosion rate, hoop stress, the actual operating time, the expected creep life at hoop stress σ in the absence of fireside corrosion and mid-wall metal temperature are required [21].

The expected creep life (E) at hoop stress and in the absence of fireside corrosion is given by [21]:

$$E_{life} = \frac{A_{op}}{L} \quad \textbf{(4-1)}$$

where A_{op} is actual operating time and L is total fraction of life consumed.

Total fraction of life consumed can be calculated through hoop stress, metal temperature and stress rupture properties of the steel. However, the expected creep life (X_{life}) of the tube under combined effects of hoop stress and fireside corrosion (E_{life} is the expected creep life in the absence of fireside corrosion) is the function of the original wall thickness of the tube (W) and the corrosion rate (C_{rate}):

$$\frac{X_{life}C_{rate}}{W} = f\left(\frac{E_{life}C_{rate}}{W}\right) \quad \textbf{(4-2)}$$

Finally, the residual service life of the superheater/reheater tubes is as follows:

$$R_{life} = X_{life} - A_{op} \quad \textbf{(4-3)}$$

As for the C.E.R.L method, Zarrabi's method [17] is applicable when the dominant mode of failure is creep followed by fracture in the presence of tube thickness loss caused by fireside corrosion as well as stress.

A third method relates the steam-side oxide scale thickness and metal temperature to the time to rupture [20]. Several correlations have been published in [104; 105]. For

example, scale thickness was correlated with Larson-Miller parameter for 1 to 3% chromium steels (T11 and T22) by French and Rehn et al [20; 105]:

$$logX = 0.00022(T + 460)(20 + logt) - 7.25 \quad \textbf{(4-4)}$$

where X is oxide scale thickness (m), T is metal temperature (K) and t is time to rupture (h).

Finally, life assessment of superheater/reheater tubes proposed by Viswanathan et al [18] is based on the knowledge of fireside oxidation, steam-side oxidation and the hoop stress.

Less research has been found about the impact of coal and/or biomass fuels on rupture lifetime of superheater/reheater tubes. To fully understand the impact of new fuel mixes on the rupture lifetime of heat exchangers, an integration of models for combustion, deposition, fireside corrosion, steam-side oxidation, and creep, (alongside heat transfer) is necessary. In the following section, models for these 5 processes will be integrated alongside heat transfer model.

4.2 A conceptual framework that integrates the five processes

Combustion of coal and biomass in air will produce a gas stream containing a complex mixture of gas, vapour phase species and ash particles. As this combustion gas stream passes the heat exchanger tubes, vapour phase species as well as fly ash particles may deposit on them (via a number of distinct mechanisms including condensation, inertial impaction, eddy impaction, etc.).

The reaction of tube metals to the gaseous, molten and/ or solid products of fuel combustion can be referred to as fuel-ash corrosion or more commonly fireside corrosion.

During operation, fireside corrosion and steam-side oxidation (reaction of high temperature and high pressure steam with inner surface of the tube) continuously reduce the wall thickness of boiler tubing and consequently raises the hoop stress acting on the tube.

The formation of deposits and oxide scales reduces heat transfer and results in increases of tube metal temperatures.

The increase in tube metal temperature and in hoop stress promotes creep in the tube metal. Creep deformation leads to a loss of strength at high temperatures and thus a loss in remaining life of the tubes.

Figure 4.1 describes schematic relationship of these five processes (alongside heat transfer) that can limit the life of heat exchangers in coal and biomass power plants.

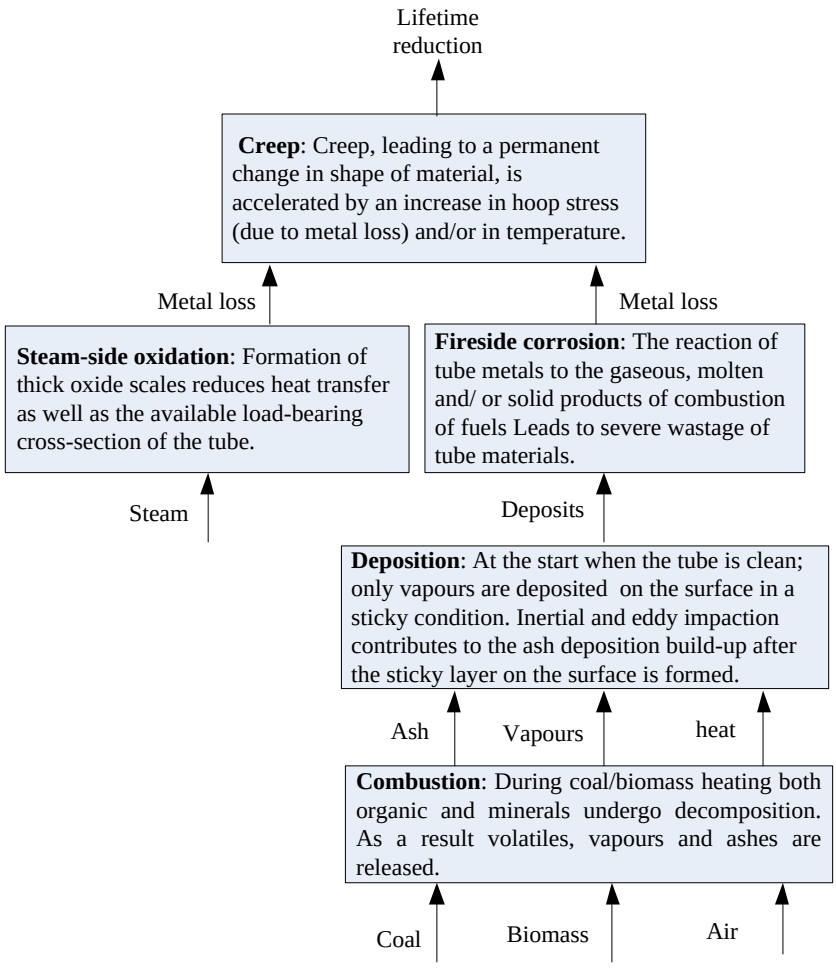

Figure 4.1 Schematic relationship of the five processes (alongside heat transfer) that can combine to limit the life of heat exchanger tubing

Based on Figure 4.1, five models for coal / biomass combustion, deposition, fireside corrosion, steam-side oxidation, and creep alongside heat transfer have been integrated as follows:

- The combustion processes were modelled by using two approaches:
    - Simplified model: a simplified fuel combustion model, based on the ultimate analysis and ash composition of the fuels were produced to predict the quantity of the flue gas emissions as well as the quantity of fly ashes released. The results were then compared with the experimental data.
    - Reaction kinetics: reaction kinetics and differential equations were used to predict the quantity of the flue gas emissions as well as the quantity of fly ashes released. The results were then compared with the experimental data.
- The depostion fluxes of vapours and fly ashes on the tube surfaces were obtained using Tomeczek et al and Zhou et al models respetively [42; 43]. The results were then compared with the experimental data.
- Fireside corrosion rate of tube metal were claculated using Simms et al model [1]. The results were then compared with the experimental data.
- Steamside oxide thickness were calcuted using a parabolic rate law equation.
- Hoop stress acting on the tubing wall were obtained by an equation for thin-walled tubes.
- Secondary creep rate of tube metal was calculated using an Arrhenius-type expression.
- Temperatures of deposit surface, tube outer and inner surface, mid-wall metal of heat exchanger tubes were calculated by heat transfer model.
- The remaining service life of boiler tubing was evaluated using the combined model and the Monkman-Grant relationship. The results were then compared with the stress rupture data.

- In addition, deposition fluxes of vapours and fly ashes, fireside wastage of tube metal, and hoop stress for thick and thin-walled tubes were predicted by alternative models and compared with the results obtained from different models as well as experiments.
- Finally, a sensitivity analysis was performed to examine the effects of different model inputs on the remaining service life of boiler tubing.

4.2.1 Process frameworks that integrate the five sub-processes

4.2.1.1 Process frameworks based on the simplified combustion model

The ultimate analysis of coal and/or biomass was used in the combustion model. Composition of the fuel(s) in terms of their major elements (*C, H, O, N, S, Cl*, on as-received basis) as well as their ash compositions (Al_2O_3, SiO_2, CaO, Fe_2O_3, MgO, K_2O, Na_2O, TiO_2, BaO, Mn_3O_4, P_2O_5, wt %) were considered for the integration of models. Using these ash compositions, the amount (in moles) of the minor elements (*Si, Al, Fe, Ca, Mg, K, Na*) in flue gas can be calculated during combustion. The volatiles, considered in the model, include: H_2O, CO_2, O_2, *Ar*, N_2, NO, SO_2, HCl.

The mass flux of vapours, condensing later on the cooling surfaces can be obtained through their partial pressure, their mass transfer coefficient, their saturation pressure, as well as pressure and density of the flue gas.

Moreover, mass concentration of fly ash particles can be used to calculate the inertial and eddy impaction rate on the front and rear side of the tube respectively.

Concentration of SO_x from flue gas, deposition fluxes of alkali salts on the tube surface and tube surface temperature will be used to obtain metal loss due to fireside corrosion.

Tube's metal loss due to steam-side oxidation can also be obtained by oxidation kinetic parameters and metal temperature.

In addition, creep parameters, hoop stress and metal temperature are the input of creep model from which the creep rate and rupture lifetime of the tube can be obtained. The mathematical relationship of the five models is shown in Figure 4.2:

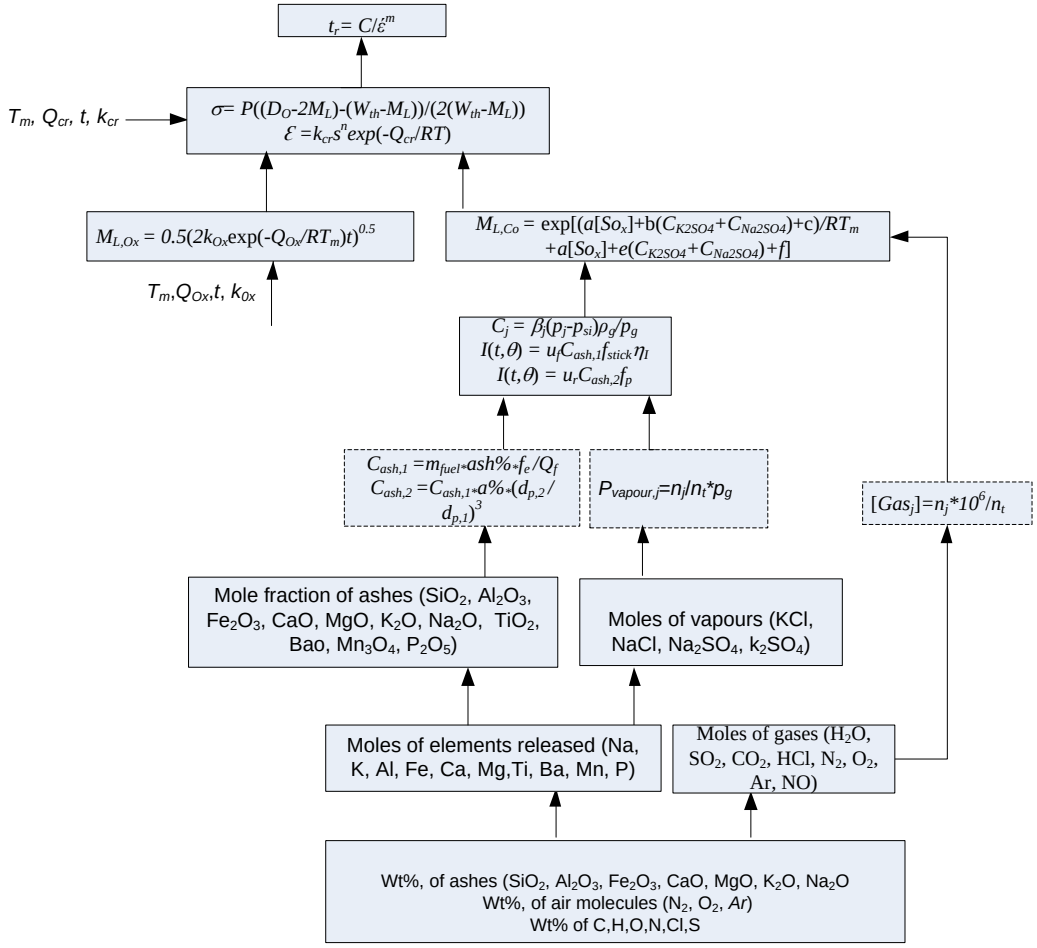

Figure 4.2 Mathematical relationships of the five processes alongside heat transfer that can combine to limit the life of heat exchanger tubing (static)

4.2.1.2 Process frameworks based on the reaction kinetics combustion model

Later development was the fuel mineral matter composition as a better representation of combustion model. Kinetic constants of coal devolatilisation, kinetics of mineral matter transformation as well as mass content of minerals, and partial pressure of oxygen (inside the fuel and air) can also be applied to calculate the mass of volatiles, partial pressure of vapours and mass concentration of fly ashes in the vicinity of the tubes (see Figure 4.3):

The approach for calculating the mass fluxes of vapours, deposition fluxes of fly ash particles, fireside corrosion rate steam-side oxidation rate, steady state creep rate and rupture lifetime of the tube are identical to that model expressed in Figure 4.2.

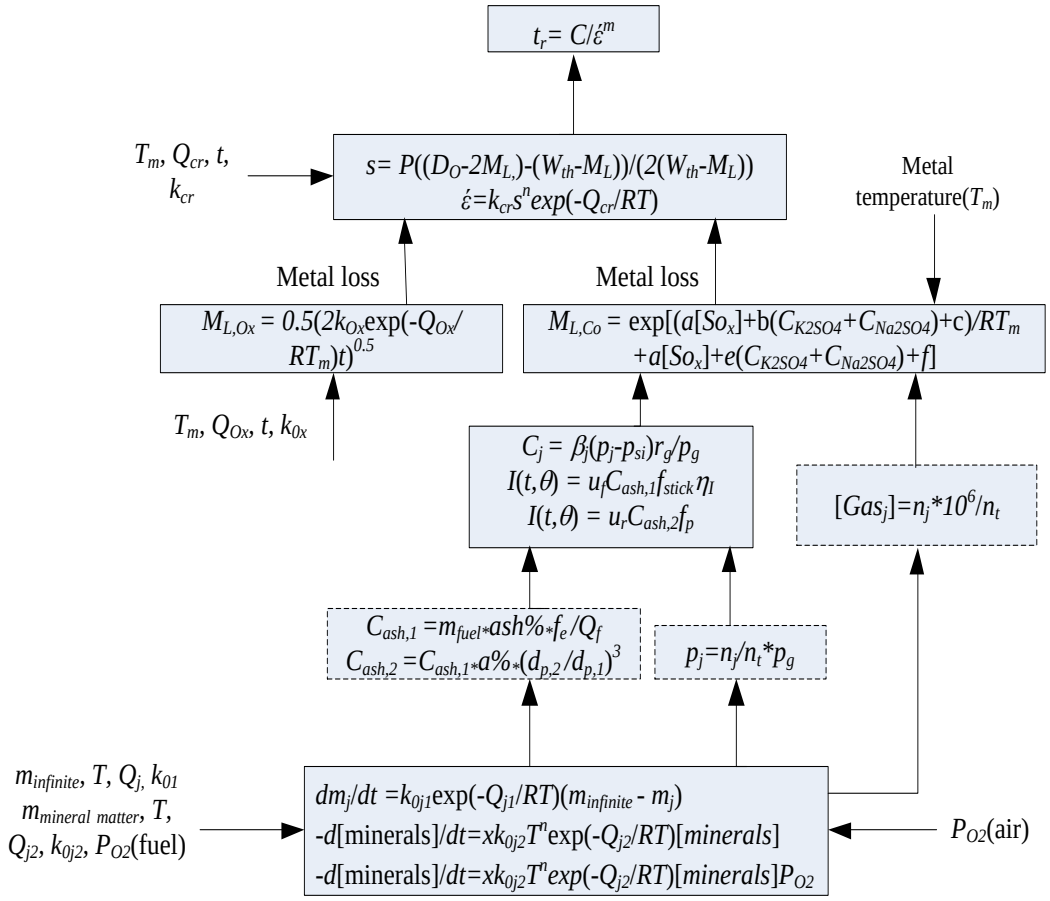

Figure 4.3 Mathematical relationships of the five processes alongside heat transfer that can combine to limit the life of heat exchanger tubing (dynamic)

4.3 Results and Discussion

4.3.1 Experimental data

Experimental data for combustion and deposition models validation were supplied by Khodier et al [26]. The experiment facility is shown in Figure 4.6:

A pilot scale combustion rig with ~ 50kW$_{th}$ capacity in a fluidised bed combustor (FBC) and ~ 100kW$_{th}$ capacity in a pulverised fuel combustor (PF) with ~ 12-15kg/h feed rate (based at Cranfield University) was used for this study. Before each run, the natural gas-fired pilot burners were first put into operation for about 18 hours. This helped raise the combustor chamber temperature to above 800°C. Figure 4.4 shows the layout of combustion rig.

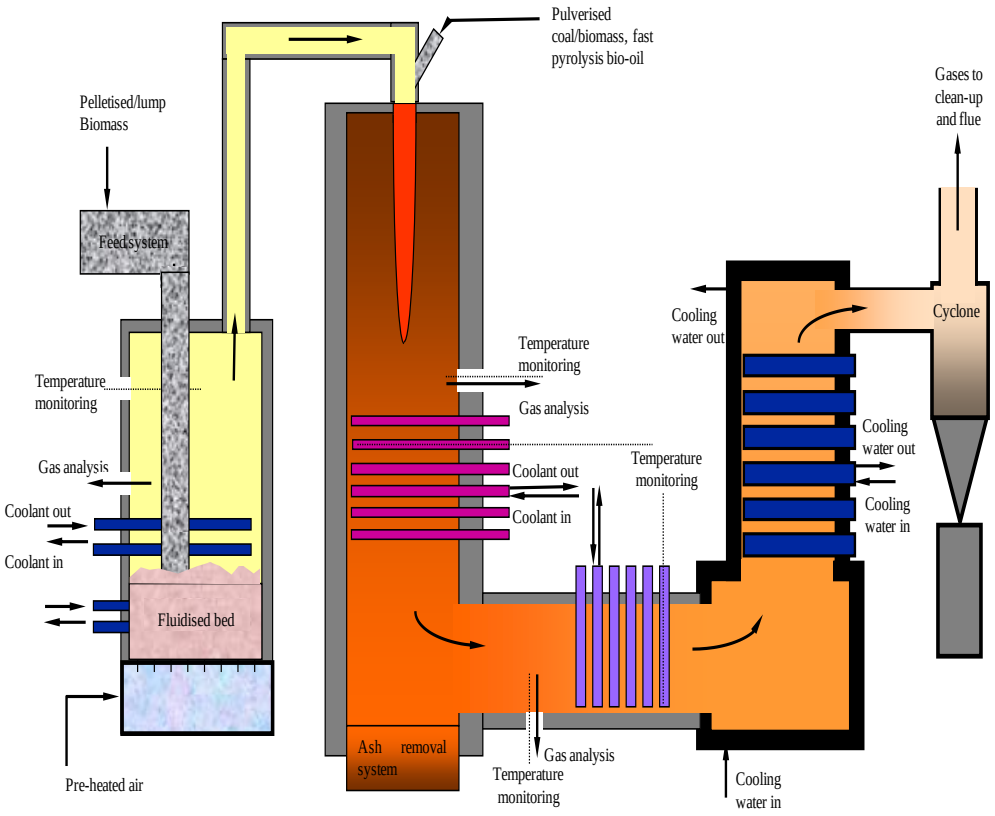

Figure 4.4 Schematic diagram of the fluidised bed (left) pulverised fuel rig facility [86]

Combustor air feed rate and natural gas feeding rate were 1730 and 40L/min respectively. The fuels burnt were as follows:

- Pure pulverised fuels (100% wt):
  - El-Cerrejon coal
  - Daw Mill coal
  - CCP
  - Miscanthus
- Mixtures of pulverised fuels:
  - CCP: El-Cerrejon coal (at 20, 40, 60 and 80% wt)
  - Miscanthus: Daw Mill coal (at 20, 40, 60 and 80% wt)

Constant feed rates of pure pulverised fuels and mixtures of pulverised fuels, applied for combustion test runs, are summarised in Table 4-1:

Table 4-1 Constant feed rates of pure pulverised fuels and mixtures of pulverised fuels [86]

Fuel	Fuel feed rates, kg/h	Fuel	Fuel feed rates, kg/h
El-Cerrejon coal (100% wt)	7.5	Daw Mill coal (100% wt)	7.4
CCP biomass (100% wt)	9.2	Miscanthus biomass (100% wt)	13.68
(CCP:El-Cerrejon, 20:80% wt)	7.9	(Miscanthus:Daw Mill, 20:80% wt)	8.1
(CCP:El-Cerrejon, 40:60% wt)	8.5	(Miscanthus:Daw Mill, 40:60% wt)	9.1
(CCP:El-Cerrejon, 60:40% wt)	9	(Miscanthus:Daw Mill, 60:40% wt)	10.2
(CCP:El-Cerrejon, 80:20% wt)	9.6	(Miscanthus:Daw Mill, 80:20% wt)	11.7

Combustion gas emission samples for CO_2, O_2, H_2O, SO_2, CO, NO, NO_2, N_2O, HCl, were obtained from a sampling port located at the side-access of the rig. Deposits were collected after pulverised combustion runs using three cooled deposition probes with surface temperatures of 700(probe 1), 600(probe 2) and 500°C (probe 3). These probes had two stainless steel rings and a removable ceramic ring (OD = 39.05mm, ID = 32.16mm, length = 60mm) on which the deposits were collected. The ceramic section of the probe was divided into three areas which represented upstream, side-stream and downstream of the deposit build up. At this stage, the deposition fluxes formed on each of the three probes for El-Cerrejon coal (100% wt), CCP biomass (100% wt) and mixed fuels (CCP:El-Cerrejon coal). The elemental compositions of the deposits were analysed using Scanning Electron Microscope (SEM) and X-ray Diffraction (XRD) analyses. Figure 4.5 shows a deposition probe.

Figure 4.5 A deposition probe [86]

In addition, Figure 4.6 demonstrates how deposits were extracted from the combustion rig by a deposition probe.

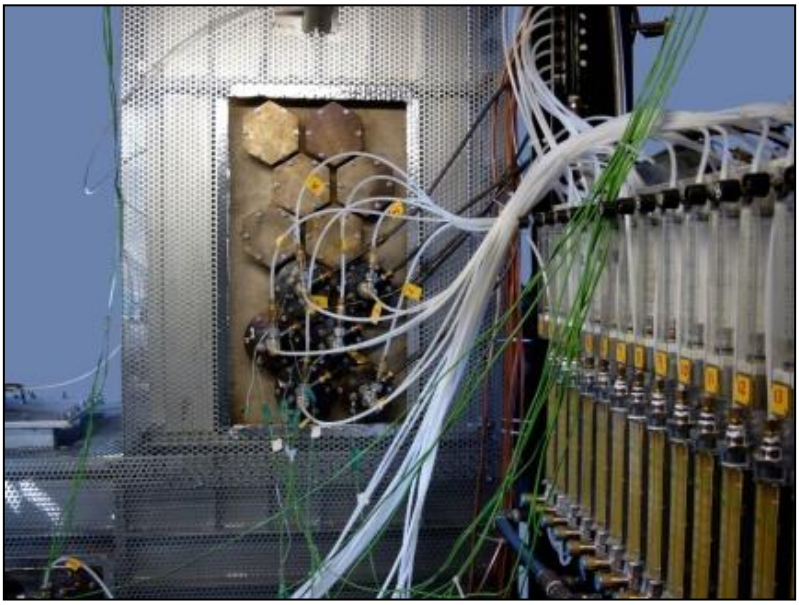

Figure 4.6 Ports used for gas and deposition samples [86]

Finally, Figure 4.7 shows a typical appearance of a deposition probe after ash deposition.

Figure 4.7 Deposits collected on the probe surfaces [86]

4.3.2 Combustion model

This section describes predictions of the fuel combustion model and comparing them with experimental data based on the combustion of pulverised fuels (El-Cerrejon coal, Daw Mill coal, CCP, Miscanthus); and a mid range of mixtures using the PF combustor.

The combustion processes were modelled by using two approaches:

1. Simplified mass balance
2. Reaction kinetics

In simplified / mass balance model the following assumptions were made:

$$\begin{cases} C \rightarrow CO_2 \\ H \rightarrow H_2O, HCl \\ N \rightarrow N_2, NO_x \\ O \rightarrow O_2, CO_2, H_2O, NO_x, SO_2 \\ Cl \rightarrow HCl \\ S \rightarrow SO_2 \end{cases} \quad \textbf{(4-5)}$$

The ultimate analysis of coal and/or biomass was applied for the simplified combustion model. The composition(s) of the fuel(s) in terms of their major elements (*C, H, O, N, S, Cl*) on as-received basis (wt%) and air composition (wt%) were used to obtain mole percentage of the flue gases (H_2O, CO_2, O_2, *Ar*, N_2, NO, SO_2, HCl).

Moreover, the mass concentration of fly ashes and mole fraction of vapours were calculated using the fuel ash compositions (Al_2O_3, SiO_2, CaO, Fe_2O_3, MgO, K_2O, Na_2O, TiO_2, BaO, Mn_3O_4, P_2O_5, wt%) (Table 3-2and Table 3-5).

Reaction kinetic model for combustion reactions was the second method of modelling fuel combustion. As mentioned previously, the volatiles produced during coal/biomass devolatilization are combusted close to the surface of the particle or at some distance from the surface. Therefore, the mole percentage of flue gases was calculated using kinetic data of coal devolatilisation and Eq. (2-4), kinetic constant of volatiles combustion as well as equations in Table 2-5 [28; 32]. In addition, kinetic constants of char oxidation [40] are required to obtain the amount of CO and CO_2 released using Eq. (2-15).Furthermore, weight percentage of fixed carbon as the main inputs of char oxidation model can be calculated by Eq. (3-7).

Using the mineral matter composition of the coal (Daw Mill, El-Cerrejon) listed in Table 3-3 (as one of the most significant inputs in the fules combistion model) and the kinetic constants for mineral matter decomposition [36; 37] as well as Eq. (2-10) and Eq. (2-11), the amount of ash species produced during coal burning was calculted in inert and oxidising atmospheres. It has to be pointed out that the sub-model of mineral matter decomposition is not included in fuel combustion model in most researches in literature. For example, biomass combustion process was divided into four successive or overlapping sub-processes by Zhou et al [32]: evaporation of moisture from straw, volatile release/char formation, burning of the volatiles, and the oxidation of char particles. Furthermore, the mineral matter transformation process is not included in coal combustion model as reported by Tomeczek [28]. The fuel combustion conditions used in the model are given in Table 4-2:

Table 4-2 Combustion conditions and assumpitions used in reaction kinetics model

Combustor air flow rate, kg/h	90
Flue gas temperature, K	1400
Combustor chamber gas temperature, K	1600
Mineral matter residence time in the flame, s	0.1

The combustor chamber gas temperature and the combustor air flow rate shown in Table 4-2 are the same as their values applied in the experiments [86]. In addition, it was assumed that the flue gas temperature decreases by 200K nearby superheater tubes and the particles residence time in the hot combustion gases was 0.1s (this is the typical residence time of the mineral matter particles in the flame region in pulverised coal power stations [31]). Finally, the fuel feed rates applied in the combustion model are the same as values used in the experiments as shown in Table 4-2. It has to be pointed out volatiles formation model (Eq. (2-11)) assumes m_{∞} is a constant which is a source of error when applying this model in broad tempreture ranges. Moreover, volatles oxidation models (shown in Table 4-2) can not be applied at temertaures higher than 1900K. Figure 4-8 shows predicted and measured amount of flue gas emissions from combustion of Daw Mill coal (100% wt), Miscanthus biomass (100% wt) and mixed fuel (Miscanthus:Daw Mill, 20:80% wt), (Miscanthus:Daw Mill, 40:60% wt), Miscanthus:Daw Mill, 60:40% wt), (Miscanthus:Daw Mill, 80:20% wt) and El-Cerrejon coal (100% wt):

a) Daw Mill coal (100% wt)

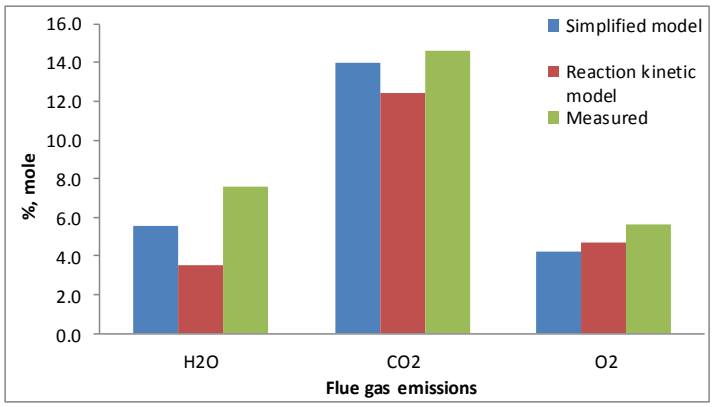

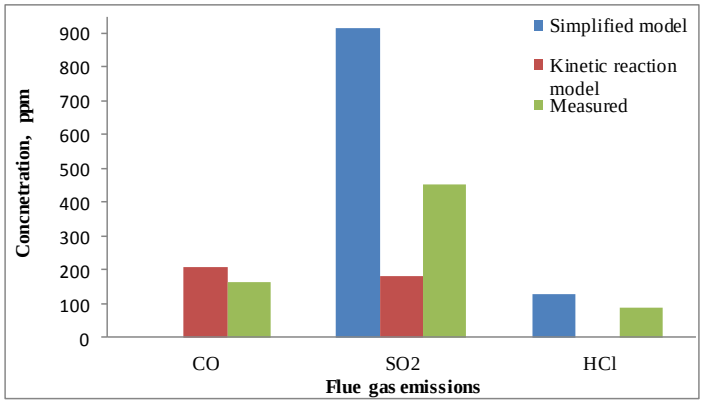

b) Miscanthus:Daw Mill (20:80% wt)

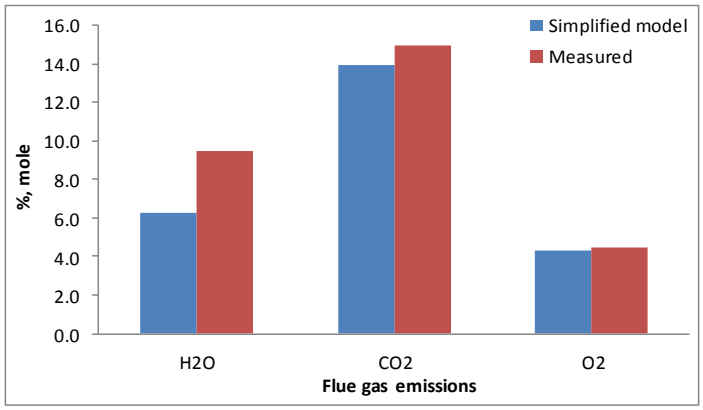

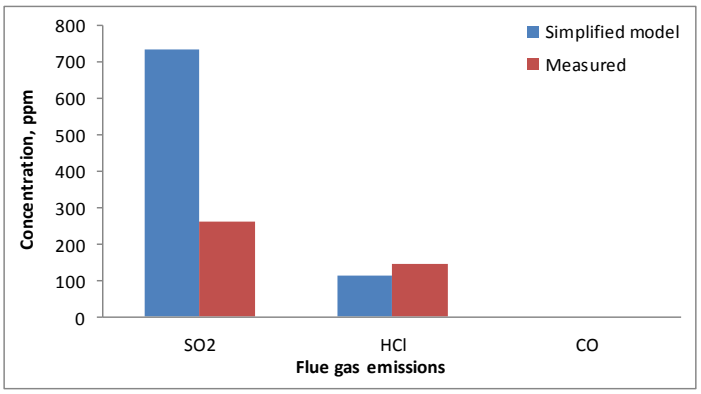

c) Miscanthus:Daw Mill (40:60% wt)

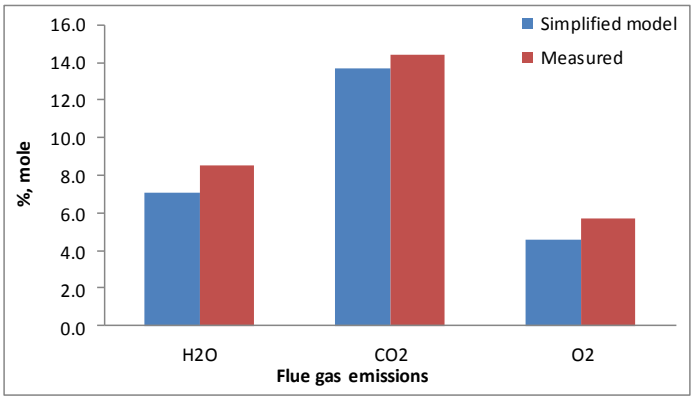

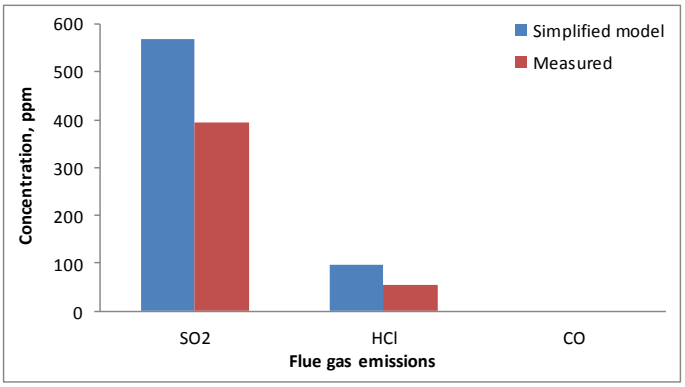

d) Miscanthus biomass (100% wt)

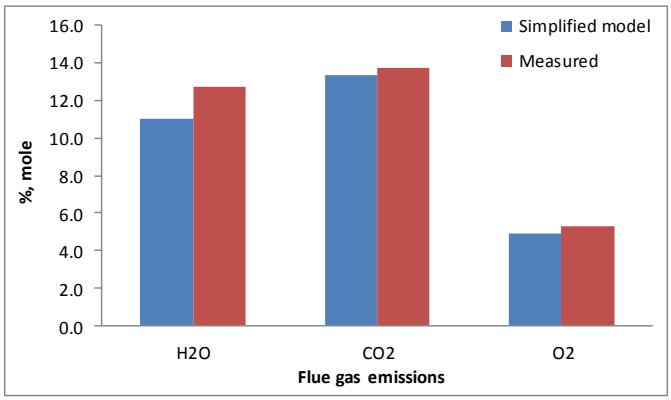

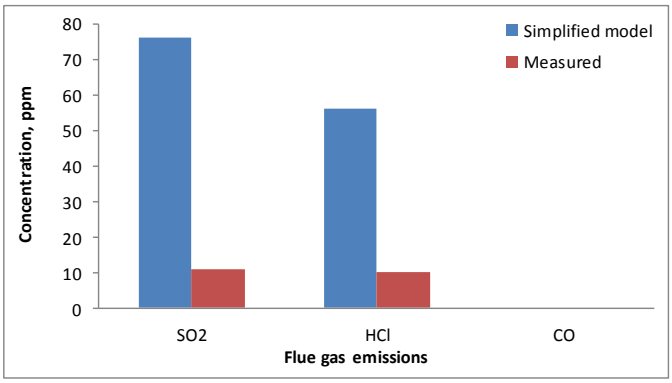

e) El-Cerrejon coal (100% wt)

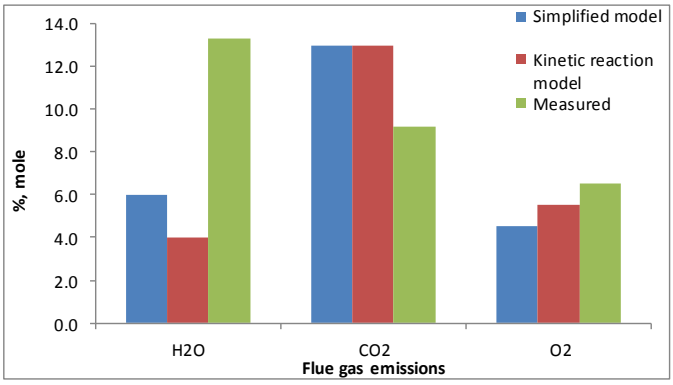

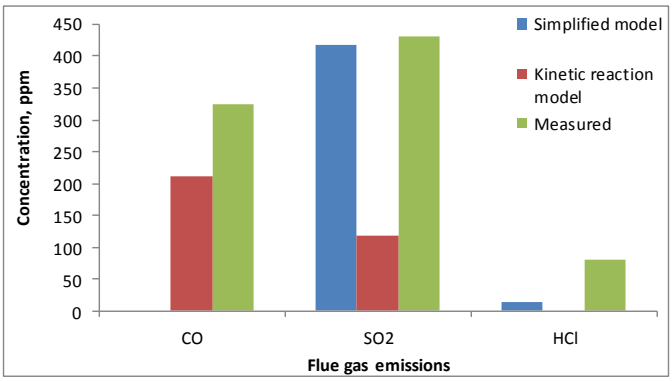

Figure 4.8 Flue gas emissions of pure and mixed pulversied fuels

The simplified combustion model predicted that the percentage of steam in the flue gas increased from 6 to 11% going from El-Cerrejon coal (100% wt), and Daw Mill coal (100% wt) to Miscanthus biomass (100% wt) as seen in Figure 4.8. This is due to the higher amount of moisture in this biomass fuel than in this coal. Conversely, the concentration of CO_2 in the flue gas showed a decrease as the amount of biomass in the fuel blends increased that is 13.9% for Daw Mill coal (100% wt) to 13.3% for Miscanthus biomass (100% wt). This results from the lower amount of carbon in

biomass than in coal (see Table 3-1, Table 3-4). However, the qauntity of CO_2 for El-Cerrejon coal (100% wt) was equal to Miscanthus biomass (100% wt). In addition, the mole percentage of O_2 in the flue gas were between 4 and 5% for all pure fuels as well as fuel blends.

The reaction kinetics model predicted smaller values for mole percentage of steam compared with values predicted by the simplified model. For instance, in the case of Daw Mill coal (100% wt) fuel, the mole percntage of H_2O predicted by the kinetic model was almost 4% whereas the one predicted by the simplified model was almost 6% (see Figure 4.8 a). The same situation occured for mole percentage of H_2O when El-Cerrejon coal (100% wt) was the fuel. The amount of steam released from combustion of El-Cerrejon coal (100% wt) was slightly larger than the one released from combustion of Daw Mill coal (100% wt) due to the higher amount of moisture in El-Cerrejon coal than Daw Mill coal as seen in Figure 4.8 (a, e).

Furthermore, the simpilfied and kinetic models predicted almost the same values for the mole percentage of CO_2 which were 13 and 14% for pure and blended fuels. Identical to the simpilfied model, the level of O_2 were in the range of 4 to 5% for both fuels (Pure Daw Mill and pure El-Cerrejon in the kinetic reaction model).

The concentrations of other species of the gas stream were also obtained by the advanced (kinetic reaction) model which includes CO, SO_2 and HCl.

The concentrations of CO predicted by the advanced model were 210 and 212ppm for pure Daw Mill and pure El-Cerrejon respectively while they were 0 predicted by simplified model. This is because in the simplified model it is assumed that all the carbon in the fuel converts to CO_2. The concentrations of CO for mixed fuels and pure Miscanthus were zero.

The concentrations of SO_2 predicted by the simplified model were much higher than those predicted by the kinetic model for all fuels since in the simplified model it is assumed that the entire sulphur in the fuel converts to SO_2 whereas in the kinetic model it may convert to S_2 and SO_3 as well.

The concentrations of HCl predicted by the simplified model decreased from 128 to 13 ppm going from pure Daw Mill coal to pure El-Cerrejon coal (see Figure 4.8 *a*, and *e*).

Obviously, this was as result of higher amounts of chlorine in Daw Mill coal than in Miscanthus and El-Cerrejon (see Table 3-1, Table 3-4). The kinetic mode did not predict any value for the concentration of HCl since the weight percentage of Halite (NaCl) and Sylvite (KCl) as the source of HCl release (in the kinetic model) were zero for both pure Daw Mill and pure El-Cerrejon (see Table 3-3 and Appendix A.2).

Generally, the simplified model's predcitions for CO_2, H_2O and O_2 were in a good agreement with the experimental data. For instance, the predicted and experimental mole percentages of CO_2 were very close to each other for all pure fuels and fuel mixtures (see Figure 4.8). There were 37, 4 and 32% differences between predicted and expermental values for the mode perntage of H_2O, CO_2 and O_2 in the case of Daw Mill coal (100% wt) fuel. The concentration of CO predicted by the simplified model agreed with the experiments for pure Miscanthus and fuel blends. The kinetic model's predictions for CO were close to the experimental data by 28 and 52% differences for pure Daw Mill and pure El-Cerrejon respectively. The model's predictions for SO_2 concentration were in poor agreements with experimental data except for all fuels used in the integrated model. In addition, the model's predictions for HCl concentration were close to the experimental data by 42, 27 and 75% differences when burning Daw Mill coal (100% wt), Miscanthus:Daw Mill (20:80% wt) and Miscanthus:Daw Mill (40:60% wt) respectively.

The models prediction can be improved by using different kinetic data for fuel devolatilisation, and volatiles combustion.

4.3.2.1 Criteria used for combustion model selection

- Zhoue et al model [32] was used to calclaute the oxidation rate of volatiles releaesd during fuel devolatilisation. The main reason for this choice was that the results were closer to the experimental data when Zhoue et al model were chosen. Similarly, Wang et al model [40] were applied to calculate char oxidation rate during fuel combustion.
- Reaction kinetic model cannot be applied for coal-biomass blends and biomass fuels combustion due to lack of kinetic data for biomass mineral matter transformation. Thus, the reaction kinetic model only predicted the quantity of

flue gas emissions and fly ashes released from pure pulverised coal fuels combustion.

- Simplified fuel combustion model was easier to use in the integrated model (due to availability of ultimate analysis and the ash composition of the fuel as inputs of the simplified model) especially when burning pure biomass or coal-biomass blends.

4.3.3 Deposition model

Condensation and impaction (inertial and eddy) are the major contributors to deposition on the superheater/reheater tube surfaces. The amount of ashes deposited via themophoresis and via the Brownian and eddy diffusions are negligible.

4.3.3.1 Vapours condensation

The flux of condensable vapours with partial pressure p_i, diffusing through the tube boundary layer towards the unit surface area and condensing onto the upstream and downstreams side of the tube (angular positions of 0^0 to 180^0) were calculated by Eq. (2-19) and constants from Table 2-7. Deposition fluxes of alkali salts, predicted by the condensation model, decreased from 0^0 to 85^0 at the upstream side of the tube, whereas they were constant at the tube downstream side (85^0 to 180^0) as seen in Table 4-3. This is because Sherwood number has been assumed to have a cosine function (by an analogy with Nusselt number in Eq. (2-36) of angle in front of the tube (0^0 to 85^0) while it is a constant at rear side (85^0 to 180^0) [42].

Table 4-3 Deposition fluxes of $K_2SO_{4\,(g)}$ around a superheater tube when burning Miscanthus biomass (100% wt)

Tube angle	$D_{i,}$ m^2/s	*Sc*	*Sh*	P_s, Pa	$(P_i - P_s)/P$	Mass transfer coefficient, m/s	Mass flux, $mg/cm^2/h$
0	9.55E-05	2.26E+00	7.28E+01	9.51E-07	2.93E-07	1.54E-01	4.17E-03
5	9.55E-05	2.26E+00	7.26E+01	6.59E-07	2.93E-07	1.54E-01	4.16E-03
10	9.55E-05	2.26E+00	7.22E+01	7.04E-07	2.93E-07	1.53E-01	4.14E-03
15	9.55E-05	2.26E+00	7.15E+01	6.90E-07	2.93E-07	1.52E-01	4.10E-03
20	9.55E-05	2.26E+00	7.06E+01	6.66E-07	2.93E-07	1.50E-01	4.04E-03
25	9.55E-05	2.26E+00	6.94E+01	6.38E-07	2.93E-07	1.47E-01	3.97E-03
30	9.55E-05	2.26E+00	6.79E+01	6.06E-07	2.93E-07	1.44E-01	3.89E-03
35	9.55E-05	2.26E+00	6.62E+01	5.71E-07	2.93E-07	1.41E-01	3.79E-03
40	9.55E-05	2.26E+00	6.42E+01	5.36E-07	2.93E-07	1.36E-01	3.68E-03
45	9.55E-05	2.26E+00	6.21E+01	5.00E-07	2.93E-07	1.32E-01	3.56E-03
50	9.55E-05	2.26E+00	5.98E+01	4.64E-07	2.93E-07	1.27E-01	3.42E-03
55	9.55E-05	2.26E+00	5.72E+01	4.30E-07	2.93E-07	1.22E-01	3.28E-03
60	9.55E-05	2.26E+00	5.46E+01	3.98E-07	2.93E-07	1.16E-01	3.13E-03
65	9.55E-05	2.26E+00	5.18E+01	3.69E-07	2.93E-07	1.10E-01	2.96E-03
70	9.55E-05	2.26E+00	4.88E+01	3.41E-07	2.93E-07	1.04E-01	2.80E-03
75	9.55E-05	2.26E+00	4.58E+01	3.17E-07	2.93E-07	9.72E-02	2.62E-03
80	9.55E-05	2.26E+00	4.27E+01	2.95E-07	2.93E-07	9.07E-02	2.45E-03
85	9.55E-05	2.26E+00	3.96E+01	2.75E-07	2.93E-07	8.40E-02	2.27E-03
90	9.55E-05	2.26E+00	3.96E+01	2.75E-07	2.93E-07	8.42E-02	2.27E-03
95	9.55E-05	2.26E+00	3.96E+01	2.75E-07	2.93E-07	8.42E-02	2.27E-03

Diffusion coefficients of vapours are equal to [42]:

$$D_{alkali\ chlorides} = 2.67 * 10^{-9}\left(T_f\right)^{1.5} \quad \textbf{(4-6)}$$

$$D_{alkali\ sulphates} = 1.78 * 10^{-9}\left(T_f\right)^{1.5} \quad \textbf{(4-7)}$$

$$Sc = \frac{\nu}{D_i} \quad \textbf{(4-8)}$$

ν is kinematic viscosity and D_i is diffusion coefficient of species *i*

Sh and P_S can be calculated from Eq. (2-20) and Eq. (2-21).

4.3.3.2 Particles impaction

The deposition rates of large fly ash particles on the upstream side of the tube as well as the deposition rates of the middle-sized fly ash particles on the downstream side of the tube can be obtained by Eq. (2-8) and Eq. (2-36) respectively. The concentrations of the large (> 10μm) and the intermediate-sized fly ash particles are the main inputs of the impaction deposition models. The flue gas velocity, local impaction efficiency and sticking coefficient of particles are other significant inputs determining deposition rate of the fly ash particles on the front side of the tube. The sticking coefficient of particles can be calculated by Eq. (2-29). The local impaction efficiency can also be predicted through Eq. (2-32). It has to be mentioned that the overall condensation rate controlled by mass transfer described by Baxter [35] (Eq. (2-8)) was used with Zhou et al models (Eq. (2-8) and Eq. (2-36)) [42] in order to calculate the overall deposition fluxes on superheater tube surfaces whereas in this research Zhou et al models [42] were applied with Tomeczek et al model [43] which is perfectly capable of calculating the mass fluxes of vapours on the upstream and downstream side of the tube. Furthermore, the ash content in the flue gas, as one of the inputs in Zhou et al models [42], was quantified by chemical analysis of the residual ash and a mass balance on the system while in this research it was obtained through the combustion model containing sub-models of volatiles formation, volatiles combustion, mineral matter transformation and char combustion. Although, Tomeczek et al [55] used the mineral matter transformation model [36] and char combustion model [28] to quantify fly ashes released, they did not incorporate the volatiles formation and volatiles oxidation models in the combustion model. The input conditions used in the deposition model calculations are listed in Table 4-4**.**

Table 4-4 Standard conditions and assumptions used in the deposit model calculations

Initial deposit/tube surface temperature, ^{0}C	600
Flue gas velocity, m/s	8
Flue gas volume flow rate, m^3/s	0.72
Large particle mean diameter, µm	58
Middle-sized particle mean diameter, µm	8
Local cross section of the boiler, m^2	0.09
Fraction of the entrained ash, %	10
Particle density, Kg/m^3	2400

The tube surface temperature and the local cross section of the boiler shown in Table 4-2 are the same as their values applied in the experiments [86]. In addition, it was assumed that the mean size of the large and middle-sized particles deposited on tube surfaces were 58 and 8µm respectively. The values for flue gas velocity, fraction of the entrained ash, and particle density in Table 4-2 were the other assumptions identical to thsoe mentioned by Zhou et al models [42]. Table 4-5 and Table 4-6 show the deposition fluxes of ash particles around a superheater tube respectively when burning Miscanthus biomass (100% wt) at intial tube surface of 600°C. Local impaction efficiency of large fly ash particles is also cosine function (Eq. (2-32)) which is why the same trend as deposition fluxes of alkali salts was repeated for large fly ash particles deposition.

Table 4-5 Deposition fluxes of Al_2O_3 on upstream surface of a superheater tube when burning Miscanthus biomass (100% wt)

Tube angle,°	The maximum reverse velocity, m/s	Al_2O_3, Kg/m^3	Tube ash deposit melt fraction, f	Fly ash particles melt fraction, f	Sticking coefficient, f_{stick}	Target efficiency, η_t	Mass flux, mg/cm^{2}h
0	8.00E+00	1.67E-09	0.00E+00	4.50E-01	5.85E-01	6.37E-01	1.79E-03
5	7.97E+00	1.67E-09	0.00E+00	4.50E-01	5.85E-01	6.37E-01	1.78E-03
10	7.88E+00	1.67E-09	0.00E+00	4.50E-01	5.85E-01	6.37E-01	1.74E-03
15	7.73E+00	1.67E-09	0.00E+00	4.50E-01	5.85E-01	6.37E-01	1.67E-03
20	7.52E+00	1.67E-09	0.00E+00	4.50E-01	5.85E-01	6.37E-01	1.58E-03
25	7.25E+00	1.67E-09	0.00E+00	4.50E-01	5.85E-01	6.37E-01	1.47E-03
30	6.93E+00	1.67E-09	0.00E+00	4.50E-01	5.85E-01	6.37E-01	1.34E-03
35	6.55E+00	1.67E-09	0.00E+00	4.50E-01	5.85E-01	6.37E-01	1.20E-03
40	6.13E+00	1.67E-09	0.00E+00	4.50E-01	5.85E-01	6.37E-01	1.05E-03
45	5.66E+00	1.67E-09	0.00E+00	4.50E-01	5.85E-01	6.37E-01	8.95E-04
50	5.14E+00	1.67E-09	0.00E+00	4.50E-01	5.85E-01	6.37E-01	7.40E-04
55	4.59E+00	1.67E-09	0.00E+00	4.50E-01	5.85E-01	6.37E-01	5.89E-04
60	4.00E+00	1.67E-09	0.00E+00	4.50E-01	5.85E-01	6.37E-01	4.48E-04
65	3.38E+00	1.67E-09	0.00E+00	4.50E-01	5.85E-01	6.37E-01	3.20E-04
70	2.74E+00	1.67E-09	0.00E+00	4.50E-01	5.85E-01	6.37E-01	2.09E-04
75	2.07E+00	1.67E-09	0.00E+00	4.50E-01	5.85E-01	6.37E-01	1.20E-04
80	1.39E+00	1.67E-09	0.00E+00	4.50E-01	5.85E-01	6.37E-01	5.40E-05
85	6.97E-01	1.67E-09	0.00E+00	4.50E-01	5.85E-01	6.37E-01	1.36E-05

The maximum reverse velocity is equal to:

$$u_r = \begin{cases} u_r * \left(1 + cos\left(\frac{\pi}{180}\theta\right)\right) & \theta \leq 85^{\circ} \\ u_r * reverse\ flow\ factor & 85^0 < \theta \leq 180^{\circ} \end{cases} \quad \textbf{(4-9)}$$

Large fly ash particles concentration is equal to [42]:

$$C_{ash,1} = \frac{\dot{m}_{fuel} * ash\% * f_e}{\dot{Q}_f} \quad \textbf{(4-10)}$$

$\dot{m}_{fuel}$ is mass flow rate of the fuel, f_e is fraction of the entrained ash and Q_f is flue gas volume flow rate.

Middle-sized particles concentration is equal to [42]:

$$C_{ash,2} = C_{ash,1} * a_f\% * \left(\frac{d_{p,2}}{d_{p,1}}\right)^{3} \quad \textbf{(4-11)}$$

a_f and $d_{p,2}$ are the accumulate frequency and the mean size of the intermediate-sized particle, and $d_{p,1}$ is the mean size of the large particle.

Table 4-6 Deposition fluxes of Al_2O_3 on downstream surface of a superheater tube when burning Miscanthus biomass (100% wt)

Tube angle, °	Velocity, m/s	Al_2O_3 concentration, Kg/m^3	Strouhal Number	Frequency of vortex shedding	Probability of the particles to be centrifuged out the eddy	Mass flux, mg/cm^2h
90	1.60E+00	5.41E-13	1.96E-01	3.48E+01	3.83E+01	1.19E-05
95	1.60E+00	5.41E-13	1.96E-01	3.48E+01	3.83E+01	1.19E-05
100	1.60E+00	5.41E-13	1.96E-01	3.48E+01	3.83E+01	1.19E-05
105	1.60E+00	5.41E-13	1.96E-01	3.48E+01	3.83E+01	1.19E-05
110	1.60E+00	5.41E-13	1.96E-01	3.48E+01	3.83E+01	1.19E-05
115	1.60E+00	5.41E-13	1.96E-01	3.48E+01	3.83E+01	1.19E-05
120	1.60E+00	5.41E-13	1.96E-01	3.48E+01	3.83E+01	1.19E-05
125	1.60E+00	5.41E-13	1.96E-01	3.48E+01	3.83E+01	1.19E-05
130	1.60E+00	5.41E-13	1.96E-01	3.48E+01	3.83E+01	1.19E-05
135	1.60E+00	5.41E-13	1.96E-01	3.48E+01	3.83E+01	1.19E-05
140	1.60E+00	5.41E-13	1.96E-01	3.48E+01	3.83E+01	1.19E-05

As the deposit thickens, its surface temperature increases which leads to an increased sticking coefficient and so more fly ash particles are captured. Comparing modelling outputs with pilot plant data the deposition fluxes, formed on the probes (tubes) with the initial surface temperature of 600°C was obtained for Daw Mill coal (100% wt), Miscanthus:Daw Mill (20:80% wt), Miscanthus:Daw Mill (40:60% wt), and Miscanthus biomass (100% wt) combustion as shown in Figure 4.9:

a) Daw Mill coal (100% wt)

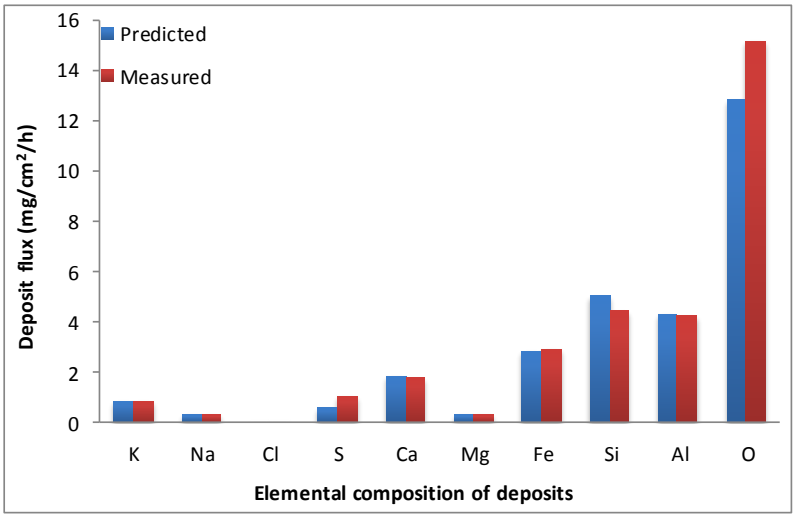

b) Miscanthus:Daw Mill (20:80% wt)

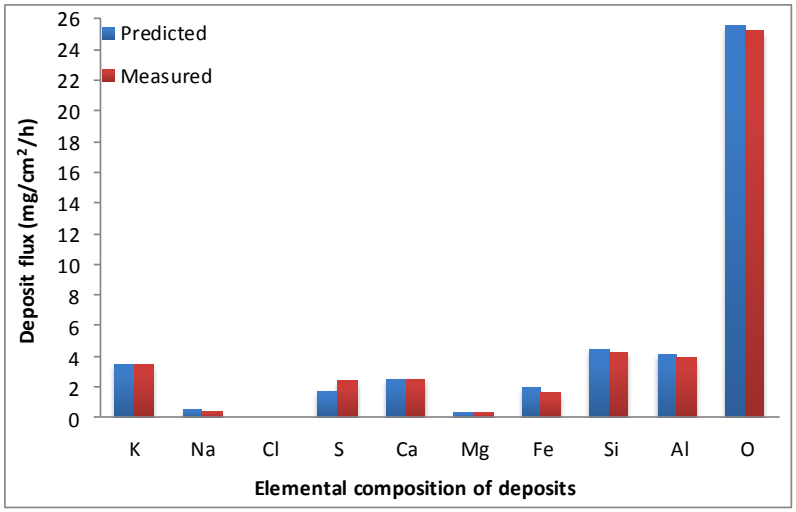

c) Miscanthus:Daw Mill (40:60% wt)

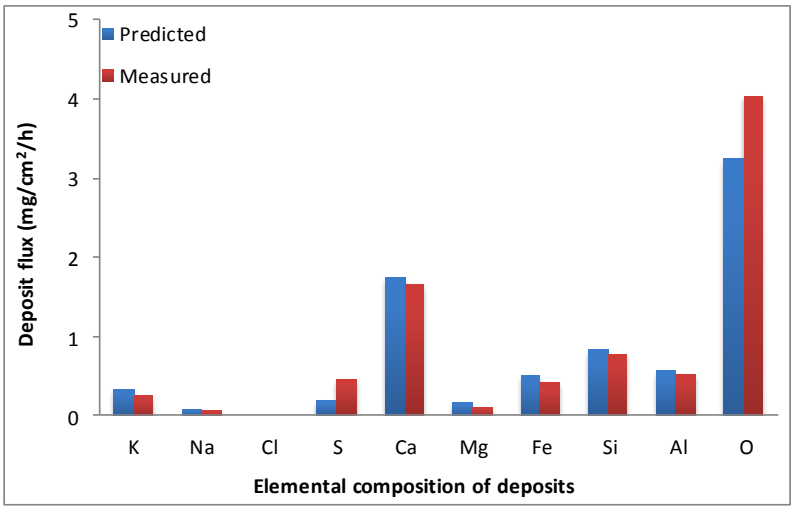

d) Miscanthus biomass (100% wt)

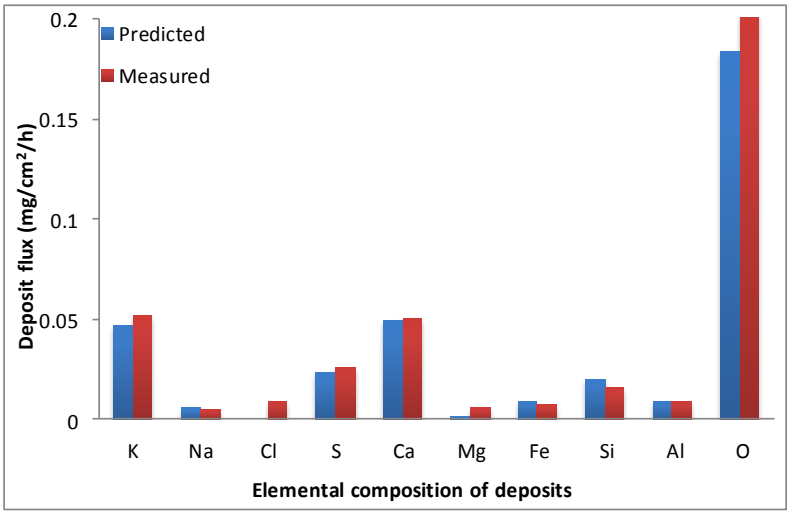

Figure 4.9 Deposition fluxes, formed on the probes with the initial surface temperature of 600°C

The deposition fluxes of oxygen for, predicted by ash deposition models, were the highest amongst other elements of the deposit for all fuels (see Figure 4.9). This agreed with the experimental data. For example, mass flux of oxygen for Daw Mill coal (100% wt) was 13mg/cm^2/h while mass fluxes of *Si*, *Al*, *Fe*, *Ca*, *Mg*, *Na*, and *K* were 5, 4, 3, 2, 0.3, 03, and 0.8mg/cm^2/h respectively as seen in Figure 4.9 a. There was an 18% difference between model prediction and the experimental data for deposition fluxes of

O. Furthermore, there were 13 and 48% differences between model predictions and the experimental data for deposition fluxes of *Si* and *S* respectively. The differences between model prediction and the experimental data for deposition fluxes of other elements were less than 2% as shown in Figure 4.9 a.

The deposition fluxes of *Al*, and *Fe* increased as the percentage of Miscanthus biomass decreased in the fuel blends due to higher percentages of these elements in Daw Mill coal than Miscanthus biomass. For instance, these values for *Fe* were 2.8, 2, 0.5 and 0.009mg/cm^2/h for Daw Mill coal (100% wt), Miscanthus:Daw Mill (20:80% wt), Miscanthus:Daw Mill (40:60% wt), and Miscanthus biomass (100% wt) respectively as seen in Figure 4.9 and Figure 4.10. These values agreed with the experimental data by 0.8, 25, 16 and 19% differences for Daw Mill coal (100% wt), Miscanthus:Daw Mill (20:80% wt), Miscanthus:Daw Mill (40:60% wt), and Miscanthus biomass (100% wt) fules respectively. The diferences between the experimental and the predicted values mainly derive from the sticking probability of ashes existing in the ash deposition model.

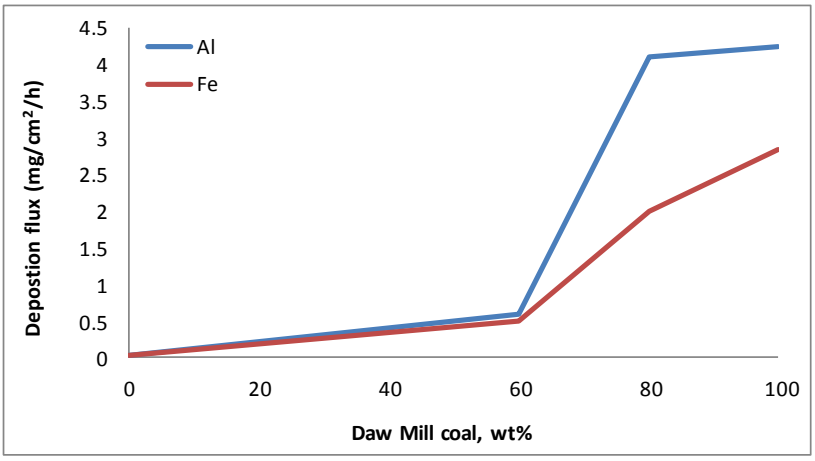

Figure 4.10 Deposition fluxes of *Al* and *Fe*, formed on the probes with the initial surface temperature of 600°C when burning pure Daw Mill coal, pure Miscanthus biomass and fuel blends

The sticking probability is one the dominating factors in inertial impaction of fly ash particles. It is a function of ash melt fraction and ash chemical composition. To obtain more accurate ash melt fraction and so more accurate sticking coefficient we need to calculate the melting point temperatures very carefully. The ash melting point

temperatures are the function of the ash chemical composition. It is therefore crucial to carefully calculate the weight percentage of fly ashes.

More realistic assumption of the entrained ash fraction in the gas stream is very important to calculate more accurately the concentration of the large fly ash particles. In addition, the more realistic assumption of accumulate frequency is a significant factor to precisely calculate concentration of the middle-sized fly ash particles.

The assumption of the flue gas temperature in the vicinity of superheater and reheater tubes is crucial since it will affect the flue gas density and viscosity as well as saturation pressure of alkali vapours. It has to be mentioned that local impaction efficiency of large fly ash particles as a significant factor in large fly ash particles deposition, is the function of fly ash physical properties too.

Furthermore, the deposition fluxes of fly ashes on superheater tubes were measured elsewhere [55] after 3, 6 and 9 months of boiler operation based on the three positions of the superheater tubes: 12, 13.5 and 15.5m distances from the burners. An industrial scale boiler producing 210t/h of steam (11MPa, 540°C) fired by subbituminous coal was chosen for experiments in which the flue gas temperature was 1600°C [55]. It was seen that within the first three months the deposit grows quickly reaching the thickness of about 25mm, while during the next six months only few millimetres deposit growth was observed. In all places of the superheater the maximum thickness of the deposit was similar and was equal to about 30mm after nine months [55]. The deposition fluxes on superheater tubes stayed between 1.44 and 1.8mg/cm^{2}h as the tube's distance from the burners and the boiler operation time varied [55].

In chapter 5 the deposition fluxes of vapours and fly ashes will be calculated by other existing deposition models. In addition, the sensitivity of fly ash deposition models to change in their inputs parameters will be discussed.

4.3.3.2 Criteria used for deposition model selection

Tomeczek et al model [43] (for vapours condensation process) was chosen in the integrated models due to the following reasons:

- The total deposition fluxes were in a good agreement with the experimental data when using Tomeczek et al model [43] in the integrated model for condensation process.
- Clear definitions of all parameters existing in the model.
- The availability of the constants in order to calculate the saturation pressure of condensable vapours.

Zhou et al model [42] (for ash impaction process) was chosen in the integrated models due to the following reasons:

- The total deposition fluxes were in a good agreement with the experimental data when using Zhou et al model [42] in the integrated model for fly ash impaction process.
- Clear definitions of all parameters existing in the model.
- The model specifies the amount of ashes deposited on the front (inertial impaction) and rear side (eddy impaction) of the tubes based on fly ash particle sizes.

4.3.4 Heat transfer model

There will be five thermal resistances when considering heat transfer around superheater/reheater tubes:

- Thermal resistances of flue gas to the tube/deposits surfaces
- Thermal resistances of fire side deposits and oxide scales
- Thermal resistances of tube metal
- Thermal resistances of steam side oxide scales
- Thermal resistance of the inner surfaces towards steam

Thermal resistances of flue gas to the tube/deposits surfaces and thermal resistance of the inner surfaces towards steam can be calculated through Eq. (2-69). To calculate the thermal resistances of fire side deposits and oxide scales, and thermal resistances of steam side oxide scales the deposit oxide thickness, and scale thickness are required.

The thickness of fireside deposits at any time was obtained by following formula:

$$l_i = \frac{m_i}{\rho_p(1-\emptyset_i)} \quad \textbf{(4-12)}$$

where l_i is the deposits thickness (m), m_i is the mass of deposit per area (kg/m^2), ρ_p is the solid particle density (kg/m^3), ϕ_i is the deposit porosity, and i refers to the current time step [52].

Furthermore, the oxide thickness was calculated by steamside oxide growth models through Eq. (2-67). Finally, the heat transfer rate from the hot flue gases to the heat transfer surfaces was calculated by Eq. (2-70). The tube outer, inner and mid-wall temperatures were then calculated using Eq. (2-70), Eq. (2-74), and Eq. (2-75).

The following assumptions were made in heat transfer model calculations:

- Flue gas temperature, in the vicinity of superheater tubes, and superheated steam temperature were constant during operation.
- Heat transfer rate were constant from the deposit surface to the internal steam

The input conditions and assumptions made in heat transfer model calculations are listed in Table 4-7.

Table 4-7 Standard conditions and assumptions used in the heat transfer model calculations

Deposit emissivity	0.5
Deposit thermal conductivity, W/(mK)	9
Outer scale thermal conductivity, W/(Mk)	0.592
Metal wall thermal conductivity, W/(mK)	49
Inner scale thermal conductivity, W/(mK)	1.5
Steam thermal conductivity, W/(mK)	0.0637
Steam velocity, m/s	60
Steam temperature, °C	540
Flue gas temperature, °C	1150

It was assumed that the superheated steam temperature is lower than the tube surface temperature by 50°C. Figure 4.11 shows an example of temperature distribution around the tube from 0^0 to 180^0 angles. The outer surface temperature of the tube and inner surface temperature were calculated using the heat transfer model.

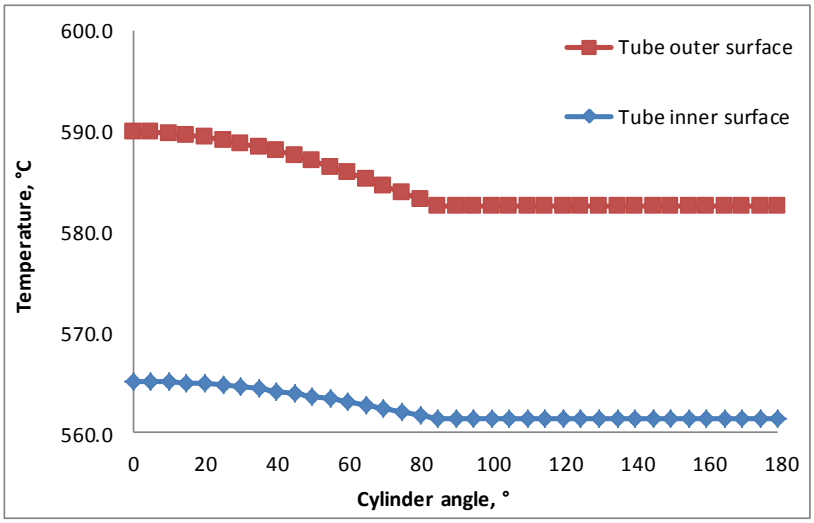

Figure 4.11 Temperature distribution around the tube

As seen in Figure 4.11the outer tube surface temperature of the tube decreased from 590°C at 0^0 to 582°C at 85^0 and then stayed constant until 180^0. Similarly, the inner tube surface was 565°C at 0^0 and decreased to 561°C at 85^0.

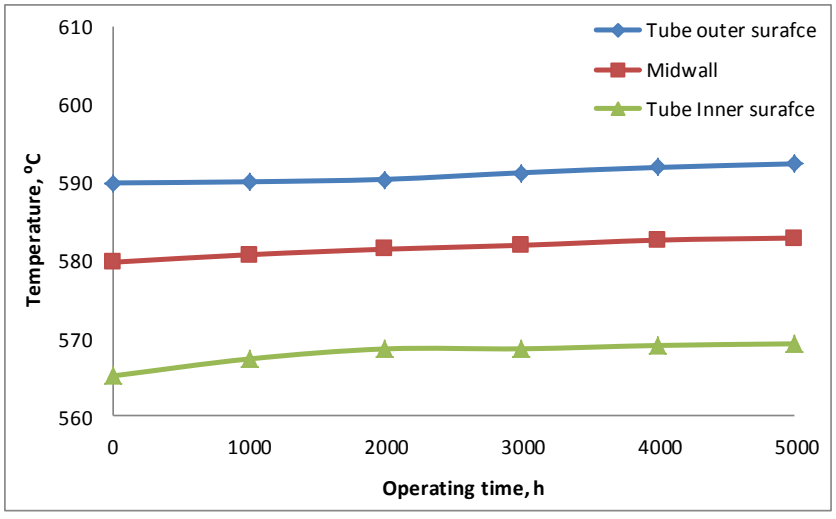

Figure 4.12 temperature of the outer surface, inner surface and mid-wall metal of superheater/reheater tubes

The heat transfer model predicted that the temperature of inner and outer surfaces of the tube as well as its mid-wall temperature increased during the operation due to thermal insulation effects of steamside and fireside deposits. This has also been reported by Ennis et al, Purbolaksono et al and Port et al [13; 19; 73]. The total thermal resistance (Eq. (2-69)) from the fireside deposits to the superheated steam increased with the thickness of the inner and outer oxide scales as well as the thickness of deposits on the tube surfaces which results in a decrease in heat transfer rate (Eq. (2-70)) from the flue gas to the steam. Therefore, the tube metal temperatures increased during operation.

For instance, mid-wall metal temperature of the tube increased from 580°C at the beginning of the boiler service to almost 583°C at the end of 5000 hours (see Figure 4.12) when the flue gas and steam temperatures were 1150 and 540°C respectively. Similar trends were repeated for the temperature of the inner and outer tube surfaces. This is an example of a gradual overheating of tube wall which will lead to reduced component life by 32% at the end of 5000 hours service.

The implication of temperature increase of boiler tubing surfaces on fireside corrosion damage rate, steamside oxidation rate, and secondary creep rate and eventually on component residual life will be discussed in next sections.

4.3.5 Fireside corrosion model

4.3.5.1 Validation data

Data for fireside corrosion model validation have been supplied by C.E.R.L (Central Electricity Research Laboratories) [21]. They are based on experience of the corrosion rates which have been recorded on UK pulverised coal operational plants for the main classes of tube material (low alloy ferritic, high alloy ferritic, and austenitic alloys) under various operating conditions. These data indicate the relationship between fuel impurities for UK coals (e.g. %Cl), metal temperature, gas temperature and the fireside corrosion rate which may be expected for superheater and reheater tube materials. Therefore, on the basis of fuel composition and knowledge of metal and gas temperature, an operator can judge the potential corrosion hazard to his plant [21]. However, it should be noted that these data were derived from UK coals, and so should be used with extreme care when other fuels are considered.

In the report the corrosion rates of ferritic low alloy, ferritic high alloy and austenitic steel, materials normally used in superheater and reheater tube materials, are given for different average mid-wall metal temperatures (540, 580, 620, 660 and 700°C) and different average local flue gas temperatures (975, 1050 and 1150°C) [21].

The corrosion rates of the tube materials are very sensitive to their metal temperatures. As shown in the report, the fireside corrosion rate increased with the tube's mid-wall metal temperature. The flue gas temperature local to the corroding metal surface also matters; the higher the gas temperatures the greater the rate of corrosion which may be expected. This is because the heat transfer rate and heat flux around superheater tubes increase with flue gas temperature resulting in an increase in tube metal temperature. For example, in a power station fired with 0.3%Cl coal an increase of 20°C in metal temperature or 200°C in local flue gas temperature could lead to an increase in the corrosion rate by a factor of 2. The corrosion rate of heating surfaces became significant at metal temperatures above 540^0C and gas temperatures above 950^0C [21].

In addition, the effects of UK coal composition (main fuel impurities) on the fireside corrosion of superheater and reheater tube materials were highlighted. Three types of coal were used in this study including coals with high chlorine content (> 0.35% Cl), medium chlorine content (0.15-35% Cl), and low chlorine content (< 0.15% Cl). For UK coal corrosion rates increase with the fuel Cl content.

Chlorine strongly promotes the release of both sodium and potassium during fuel combustion and the released alkali salts are transformed to fusible sulphates, which in tube surfaces cause high temperature corrosion [21; 56].

The corrosion rate was classified in the following manner [21]:

- < 25nm/h (Normal tolerance rate of corrosion)
- 25-50nm/h (Significant rate of corrosion)
- 50-100nm/h (Serious rate of corrosion)
- 100-200nm/h (Very serious rate of corrosion)
- > 200nm/h (Catastrophic rate of corrosion)

In general, a corrosion rate of up to 10nm/h may be tolerated without a significant reduction of creep life. Corrosion rate of up to 25nm/h are often acceptable. Corrosion rates of approximately 100nm/h imply that there will be a significant reduction in life and an estimation of the remaining creep life should be undertaken. If the corrosion rate is greater than 200nm/h remedial action is required urgently [21].

Furthermore, metals of higher chromium content (e.g. 18%Cr) exhibit a higher corrosion resistance compared to the ones with lower chromium content (2.25%Cr, 9-12%Cr). Therefore, the corrosion rate of the austenitic alloys (with 18%Cr (e.g. 347H)) was much lower than the low and high Cr ferritic alloys (such as T22 and T92) [21].

4.3.5.2 Model's prediction

Fireside corrosion model was assumed that this type of damage is a function of tube outer surface temperature, deposition fluxes of alkali salts and SO_X concentration, and tube materials (see section 2.4.4, Eq. (2-70)). Below describes how these parameters were calculated:

- The tube outer surface temperature was calculated by heat transfer model. The tube surface temperature and the corresponding mid-wall metal temperature were 590 and 580^{0}C respectively at front side of the tube (0^0) (see section 4.3.4).

- Mass fluxes of Na_2SO_4 and K_2SO_4 were obtained from the deposition (condensation) model (see section 4.3.3).

- SO_X concentration also derives from combustion model (see section 4.3.2).

- The material used for the superheater tube was T22 (Fe-2.25Cr-1Mo Wt%) which is classified as a low Cr ferritic alloy.

- Finally, the local (0 to180^0) fireside corrosion rate (μm/1000h) of the super-heater tube at flue gas temperature of 1150^{0}C and at tube surface temperature of 590^{0}C where Daw Mill coal (100% Wt 0.2% Cl) was burnt was calculated using Eq. (2-64). The results are tabulated in Table 4-8:

Table 4-8 Local (0 to 180^0) fireside corrosion rates of the tube for 1000 hours service at initial tube surface temperature of 590^{0}C and flue gas temperature of 1150^{0}C

Angle, °	T_{sur}, °C	T_{sur}, K	SO_x,ppm	Na_2SO_4, μg/cm^2/h	K_2SO_4, μg/cm^2/h	Fireside corrosion rate of T22, μm/1000h
0	589.89	862.89	904.08	36.29	70.87	76.69
5	589.86	862.86	904.08	36.22	70.74	76.64
10	589.77	862.77	904.08	36.01	70.33	76.52
15	589.62	862.62	904.08	35.67	69.66	76.31
20	589.41	862.41	904.08	35.19	68.73	76.02
25	589.14	862.14	904.08	34.59	67.55	75.66
30	588.82	861.82	904.08	33.86	66.12	75.22
35	588.44	861.44	904.08	33.01	64.46	74.71
40	588.01	861.01	904.08	32.04	62.58	74.13
45	587.53	860.53	904.08	30.97	60.49	73.49
50	587.01	860.01	904.08	29.81	58.21	72.80
55	586.44	859.44	904.08	28.55	55.76	72.07
60	585.84	858.84	904.08	27.22	53.15	71.29
65	585.21	858.21	904.08	25.81	50.41	70.48
70	584.55	857.55	904.08	24.35	47.55	69.64
75	583.86	856.86	904.08	22.84	44.61	68.79
80	583.16	856.16	904.08	21.29	41.59	67.92
85	582.44	855.44	904.08	19.73	38.52	67.05
90	582.44	855.44	904.08	19.77	38.61	67.05
95	582.44	855.44	904.08	19.77	38.61	67.05
100	582.44	855.44	904.08	19.77	38.61	67.05
105	582.44	855.44	904.08	19.77	38.61	67.05
110	582.44	855.44	904.08	19.77	38.61	67.05
115	582.44	855.44	904.08	19.77	38.61	67.05
120	582.44	855.44	904.08	19.77	38.61	67.05
125	582.44	855.44	904.08	19.77	38.61	67.05
130	582.44	855.44	904.08	19.77	38.61	67.05
135	582.44	855.44	904.08	19.77	38.61	67.05
140	582.44	855.44	904.08	19.77	38.61	67.05
145	582.44	855.44	904.08	19.77	38.61	67.05
150	582.44	855.44	904.08	19.77	38.61	67.05
155	582.44	855.44	904.08	19.77	38.61	67.05
160	582.44	855.44	904.08	19.77	38.61	67.05
165	582.44	855.44	904.08	19.77	38.61	67.05
170	582.44	855.44	904.08	19.77	38.61	67.05
175	582.44	855.44	904.08	19.77	38.61	67.05
180	582.44	855.44	904.08	19.77	38.61	67.05

Tube surface temperature was the highest at 0^0 of the tube where the front half of the tube faces the flue gas stream. Similarly, mass fluxes of Na_2SO_4 and K_2SO_4 were the largest in this position (0^0) compared with mass fluxes of alkali salts in other positions around the tube. This owes to the Sherwood number which is the largest at 0^0 of the tube. SO_X concentration was constant around the tube.

The tube surface temperature decreased from 0^0 to 85^0 at the upstream side of the tube, whereas it stayed constant at the tube downstream side (85^0 to 180^0) as seen in Table 4-8. This can be explained by an analogy between heat and mass coefficient. As for the Sherwood number, the Nusselt number is a cosine function in front of the tube thus decreasing from 0^0 to 85^0 [42]. Furthermore, Nusselt number is a constant from 85^0 to 180^0. As a result the wastage rates of the tube decreased from 0^0 to 85^0(front side) and were a constant from 85^0 to 180^0 (rear side of the tube). This is presented in Figure 4.13:

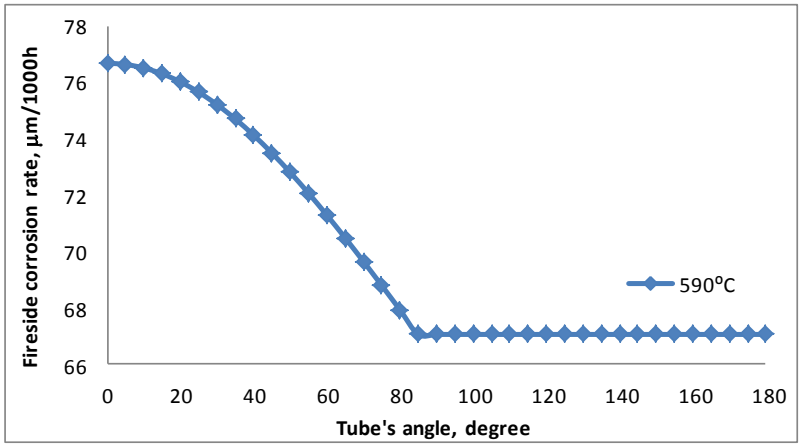

Figure 4.13 Fireside corrosion metal loss (µm/1000h) of the superheater tube (T22) resulted from combustion of Daw Mill coal (100% wt) and an initial tube surface temperature of 590°C.

The model predicted that the fireside corrosion rates of the tube's surfaces were 77µm/1000h (at 0°) where the tube outer surface and mid-wall metal temperatures were 590 and 580°Crespectively. This agreed with the historical data in C.E.R.L report [21]. The corrosion rate given in C.E.R.L data for T22 at mid-wall temperatures of 580°C and at flue gas temperature of 1150°C when burning Daw Mill coal (100% wt with 0.2% chlorine) was 50-100µm/1000h.

The corrosion rate declined from 77μm/1000h at 0^0 to 67μm/1000h at $85^0$and then maintained at 67μm/1000h until 180^0. Therefore, the tube wall thickness reduction at upstream side of the tube was larger than on rear side of the tube. As seen in Table 4-8, the corrosion rate of tube metal at upstream side was larger than on rear side of the tube due to the larger tube surface temperature. Furthermore, larger tube surface temperature at 0^0 led to a higher partial saturation pressure of alkali vapours which should result in lower deposition fluxes but the effects of Sherwood number on deposition fluxes of alkali vapours are more than the effect of partial saturation pressure of alkali vapours. The higher Sherwood numbers at upstream side of tube lead to higher deposition fluxes of alkali salts (see Table 4-3) and in turn higher fireside metal loss.

The model's predictions during 5000 hours boiler service also agreed with data in reference [21] where the corrosion rate for a ferritic low alloy when burning coal (100% wt) with 0.2% chlorine was in the range of 50 and 100μm/1000h at flue gas temperature of 1150°C and mid-wall temperature of 580°C. Metal loss rates of the superheater tube (T22) due to fireside corrosion were calculated up to 5000 hours service starting with an initial tube surface temperatures of 590°C. Daw Mill coal (100% wt, 0.2% Cl) was used for this calculation as well. The results are presented in Table 4-9:

Table 4-9 Metal loss rate (μm/1000 h) of the super-heater tube (T22) up to 5000 hours service starting from an initial tube surface temperature of 590°C when burning Daw Mill coal (100 %, wt)

Operating time, h	T_m, ^{0}C	T_m, K	SO_x,ppm	Na_2SO_4, μg/cm^2/h	K_2SO_4, μg/cm^2/h	Corrosion rate, μm/1000h
1000	589.89	862.89	904.08	36.29	70.87	76.69
2000	590.04	863.04	904.08	36.21	70.59	76.85
3000	590.32	863.35	904.08	36.14	70.35	77.20
4000	591.20	864.20	904.08	35.90	69.41	78.15
5000	591.89	864.89	904.08	35.08	66.05	78.82

Deposit/corrosion is a source for overheating problems, by the formation of oxide layers and deposits on the surface of the tubes which are a barrier to heat transfer. As the deposit thickness increases, the metal temperature will also increase [11]. This result in an increase in fireside corrosion rate of superheater/reheater tubes and, in turn, more tube wall thickness reduction during the boiler operation as seen in Figure 4.14.

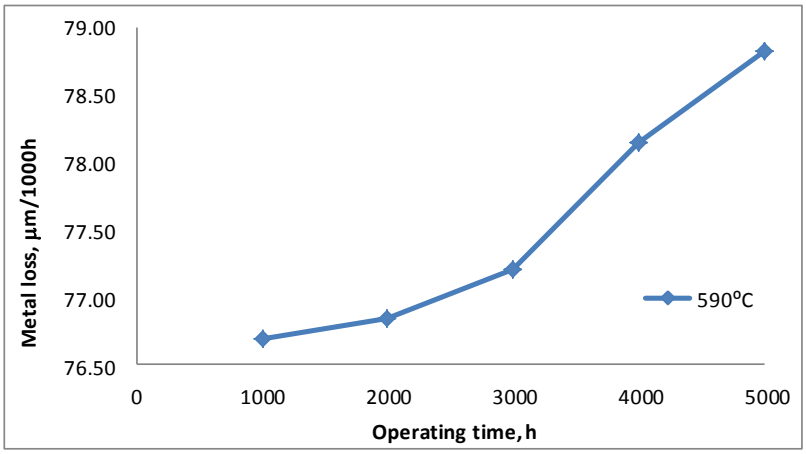

Figure 4.14 Metal loss rate (µm/1000 h) of the super-heater tube (T22) up to 5000 hours service starting from an initial tube surface temperatures of 590°C when burning Daw Mill coal (100% wt, 0.2% Cl)

It has to be mentioned that Simms et al model [1] cannot be applied for pure biomass fuels since the chloride attack has different attack from that sulphate attack. In chapter 5 the fireside corrosion damage of the tube surfaces for given fuels and operational conditions will be evaluated with a different fireside corrosion model. In addition, the sensitivity of fireside corrosion model to change in mid-wall metal temperature alongside model validation will be discussed.

4.3.5.3 Criteria used for fireside model selection

Simms et al model [1] (for fireside corrosion process) was chosen in the integrated models due to the following reasons:

- The model can calculate the fireside corrosion rate of low and high ferritic alloys as well as austenitic alloys based on different constants existing in the model.
- The model is a function of deposition fluxes of alkali salts and SO_X concentration from combustion model.
- The fireside corrosion rates predicted by Simms et al model [1] were in corrosion rates ranges given in C.E.R.L report [21].

4.4 Steamside oxidation model

Steamside oxidation models are a function of tube inner surface temperature, oxidation parameters related to the tube material and the operating time (see section 2.5.2). The

tube inner surface temperature can be calculated using the heat transfer model as described in section 4.3.4. Alternative models and oxidation parameters for alloys are given in EPRI report [106].

Most engineering alloys obey parabolic kinetics at high temperatures [57] thus Eq. (2-67) describing parabolic oxidation rate law, was used to calculate the oxide thickness grown on the inner surfaces of the superheater tube (T22) at initial tube inner surface temperature of 565°C and at steam temperature of 540°C. The oxidation parameters for T22 (2.25Cr-1Mo) alloy are: A=2.05E+20(μm)2/h and Q=327 kJ/mole [106]. Time intervals of 1000 hours were used in applying this model. The steamside oxide thickness grown in T22 after 5000 hours service was calculated. The results are summarised in the Table 4-10.

Table 4-10 Oxide thickness grown on the inner of T22 after 5000 hours service

Operation time, h	Inner scale/metal, ^{0}C	Initial inner oxide thickness, μm	Cumulative inner oxide thickness, μm	Metal loss, μm
1000	565.03	0.00	41.21	20.61
2000	567.22	41.21	60.15	30.07
3000	568.51	60.15	75.37	37.68
4000	568.53	75.37	88.00	44.00
5000	568.96	88.00	99.29	49.64

Thick oxide scales forming on tube internal surfaces act as thermal barriers and cause tube metal temperatures to increase during service (by approximately 2°C per 25μm of scale thickness) and thus, reduced creep life as reported by Ennis et al, Purbolaksono et al, Sabau et al and EPRI [13; 19; 69; 106]. Heat transfer model revealed that the temperature of the inner tube surface increased from 565 to about 569^{0}C after 5000 hours service. The superheated steam temperature was at 540^{0}C. As the tube metal temperature increased the rate of steam side oxidation increased leading to thicker oxide scales. For example, the oxide thickness increased from 41μm at 1000 hours to 99μm at the end of 5000 hours service as seen in Table 4-10. The model predictions were in a reasonably good agreement with the results from Purbolaksono et al and Viswanathan et al [19; 104] where the oxide thickness at the end of 1000 hours service (at initial tube inner surface temperature of 565°C and at steam temperature of 540°C.) was 0.045mm (45μm) for T22 materials. In addition, the amount of oxide formed on the inner surface

of the tube was 0.1mm (100µm) at the end of 5000 hours service [19; 104]. In addition, steamside scale thickness up to 100000 hours for initial tube metal temperatures of 566, 580, and 607°C for a typical superheater and reheater (T22) was reported by French [20]. The oxide thicknesses reported by French [20] were 50 and 101µm at initial tube metal temperature of 566°C after 1000 and 5000 hours operation respectively.The available cross-sectional area of the tube is reduced due to the metal loss posed by formation of the oxide scales. It has been reported that the steam side wall loss is equivalent to half the steam side scale thickness [18]:

$$steam\ side\ wall\ loss = \frac{steamside\ scale\ thickness}{2} \quad \textbf{(4-13)}$$

Figure 4.15 presents the metal loss of steamside surfaces a superheater/reheater T22 due to steamside oxidation up to 5000 hours exposure to steam.

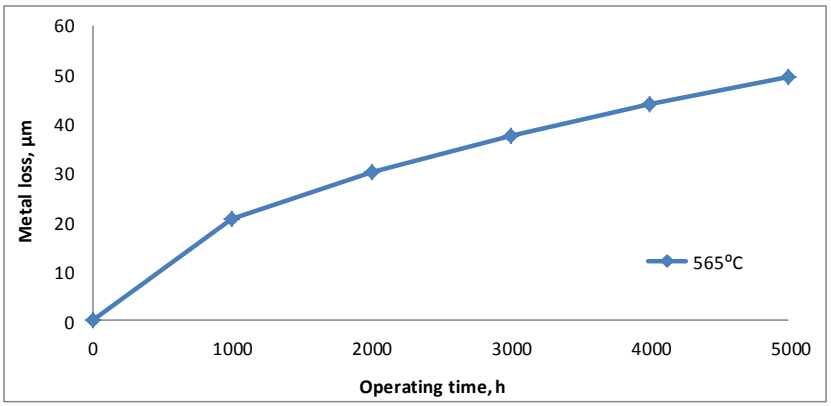

Figure 4.15 Steamside metal loss of the superheater tube (T22) up to 5000 hours service starting from an initial tube inner surface temperature of 565^{0}C versus operating time

The internal metal loss increased from 20µm at 1000 hours to almost 50µm at the end of 5000 hours exposure causing an increase in the stress on the tubing wall. Furthermore, Figure 4.16 illustrates the steamside metal loss after 50000 hours service.

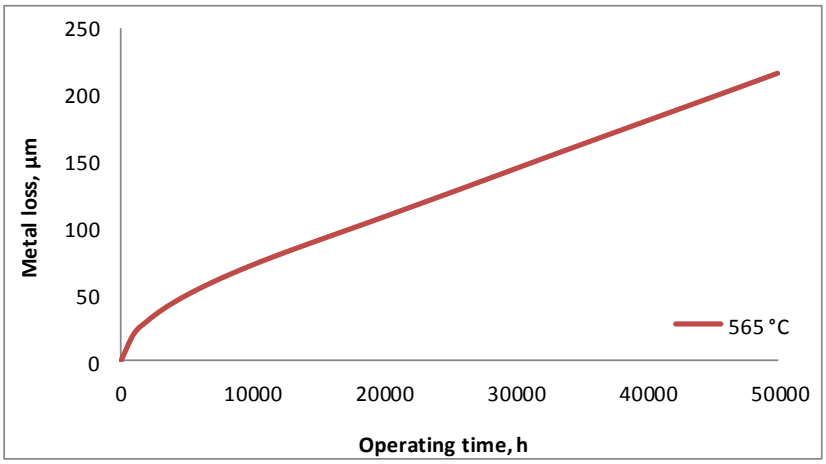

Figure 4.16 Steamside metal loss of the superheater tube (T22) up to 50000 hours service starting from an initial tube inner surface temperature of 565^{0}C versus operating time

Heat transfer model predicted that the temperature of the superheater tube inner surfaces increased from 565^{0}C at the beginning of the service to approximately 589^{0}C after 50000 hours service which resulted in the oxide thickness of 432µm or the internal metal loss of 216µm. The oxide thickness given in [19] at tube inner surface temperature of 589^{0}C was 325µm.

In chapter 5 the sensitivity of steamside oxidation model to change in its input parameters such as inner surface temperature and oxidation parameters will be studied.

4.5 Creep model

The creep of a tube metal is a function of hoop stress, mid-wall metal temperature and creep parameters for the material. These parameters have been calculated as follows:

- Hoop stress acting on tubing wall was calculated by Eq. (2-81). In addition, the hoop stress itself is a function of internal steam pressure as well as tube's dimensions (wall thickness and diameter) (see section 2.7.2).
- The tube mid-wall temperature was calculated from Eq. (2-75).
- Finally, Eq. (2-83) was used to calculate secondary creep rate of the tube metal.

Furthermore, dimension of superheater tube, operating conditions (assumptions) and creep parameters used in the creep model calculation are summarised in Table 4-11 for T22 [69; 107].

Table 4-11 Material specifications, dimension of superheater tube, operating conditions assumed and creep parameters used in the creep model calculations

Material	T22 (Fe-2.25Cr-1Mo, wt%)
Superheated steam temperature	540^0C
Superheated steam pressure	18MPa
Outer tube diameter	45mm
Tube wall thickness	7.5mm
k_{cr}	7191.18 $(MPa)^{-n}/h$
n	3.3
Q_{cr}/R	30190K

Superheated steam pressure and temperatures were assumed to be 18MPa and 540^0C respectively based on the operating conditions assumed by Chaudhuri et al and Rahman et al [10; 16].

4.6 Combined model

4.6.1 Stress rupture data

Stress rupture data for the common boiler tube materials (Low alloy ferritic, high alloy ferritic and austenitic) are given in C.E.R.L report [21]. The graphs are based on the tube creep life, metal temperature and the hoop stress. Creep life between 103 hours and 107 hours are estimated for the tube steels with stress ruptures between 10 and 300MPa. Finally, the metal temperature between 450 and 650°C are considered for most alloys. Obviously, in every graph, the superheater/reheater tubes have a larger creep life at a lower temperature and a lower rupture stress. Figure 4.16 shows the stress rupture data of 2.25Cr-1%Mo steel for metal temperatures between 450 and 650°C and hoop stress between 25 and 300MPa [21].

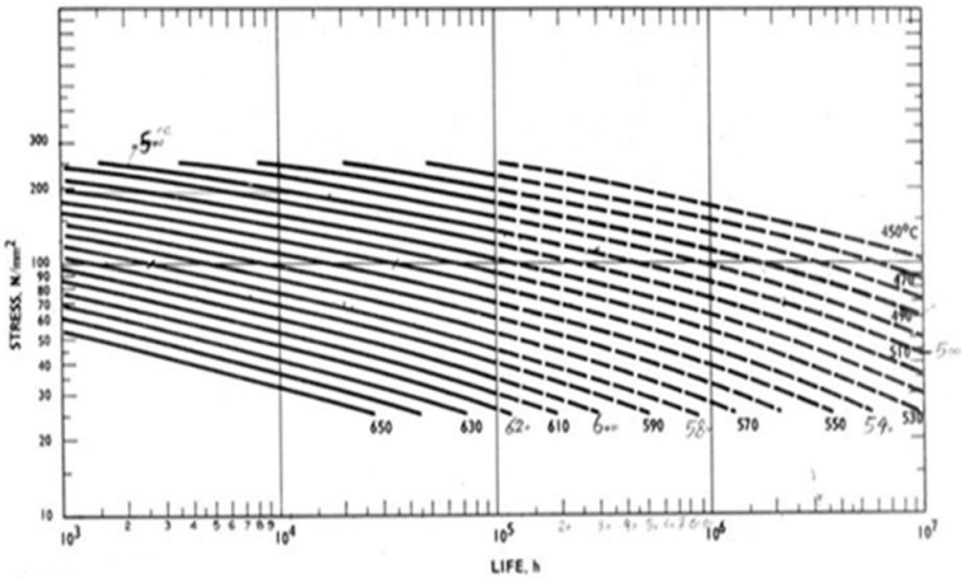

Figure 4.17 Stress rupture properties of 2.25Cr-1%Mo steel [21]

4.6.2 The remaining creep life of superheater/reheater tubes

To obtain the remaining service life of a superheater/reheater tube the following factors need to be considered:

- Initial dimensions of the tubing which includes wall thickness and its diameter
- Internal superheated steam pressure
- The actual operating time: simply means the operating hours up to the time of the evaluation
- Metal loss due to fireside corrosion
- Metal loss due to steamside oxidation
- Metal loss due to secondary creep rate
- Hoop stress initially acting on the tubing
- Mid-wall metal temperature of the tubing
- Secondary creep rate of the tubing

Initial dimensions of an example tubing, as well as internal superheated steam pressure, are listed in Table 4-11. The actual operating time simply means the operating hours up to the time of the evaluation. Time intervals of 1000 hour were applied in the model.

The outer diameter of the tubing will be reduced by corrosion on the fireside of the tube. For a constant fireside corrosion rate the outer diameter of the tube ($D_{O,t}$) at any time (t) can be expressed as:

$$D_{o,t} = D_O - 2 * corrosion\ rate * t \quad \textbf{(4-14)}$$

where D_O is the initial outer diameter, corrosion rate = metal loss (nm/h) and t is time (h)

The tube wall thickness is also reduced by fireside corrosion, steamside oxidation and creep deformation. The wall thickness of the tube ($W_{th,t}$) at any time (t) can be calculated by the following formula:

$$W_{th,t} = W_{th,0} - (ML_{co} + ML_{ox} + ML_{cr}) \quad \textbf{(4-15)}$$

where $W_{th,t}$ is the wall thickness at a given time, $W_{th,0}$ is the initial wall thickness, and ML_{co}, ML_{ox}, ML_{cr} are the metal loss at a given time due to fireside corrosion, steamside oxidation and creep deformation respectively.

It has to be pointed out that the metal loss due to creep strain can be obtained by Eq. (2-85).

To calculate the hoop stress the internal steam pressure, the tube wall thickness and the diameter at any time are required. Eq. (4-14) and Eq. (4-15) were used to calculate the remaining outer diameter and the remaining wall thickness of the tube at the end of each period. The calculation was based on 1000 hour time interval. This was repeated for 5000 hours to observe the implication of metal temperature, fireside damage, steamside damage and creep damage on the hoop stress and more importantly on the creep life of the superheater tubes as the exposure time increases. The predictions are summarised in Table 4-12 when burning Daw Mill coal (100% wt, 0.2% Cl):

Table 4-12 Hoop stress acting on the tubing wall at internal steam pressures of 18MPa when burning Daw Mill coal (100% wt, 0.2% Cl)

Operation time, *h*	Outer diameter at the start of exposure period, *m*	Wall thickness at the start of exposure period, *m*	Fireside damage after X hours, m/1000h	Steamside damage after X hours, m/1000h	Creep damage after X hours, m/1000h	Outer diameter at the end of exposure period, *m*	Wall thickness at the end of the exposure period, m/1000h	Hoop stress, MPa
0	4.50E-02	7.50E-03	0	0	0	4.50E-02	7.50E-03	45.00
1000	4.50E-02	7.50E-03	7.67E-05	2.06E-05	6.33E-07	4.48E-02	7.40E-03	45.53
2000	4.48E-02	7.40E-03	7.68E-05	3.01E-05	6.32E-07	4.47E-02	7.29E-03	46.14
3000	4.47E-02	7.29E-03	7.72E-05	3.77E-05	6.31E-07	4.45E-02	7.18E-03	46.83
4000	4.45E-02	7.18E-03	7.82E-05	4.40E-05	6.30E-07	4.44E-02	7.06E-03	47.60
5000	4.44E-02	7.06E-03	7.88E-05	4.96E-05	6.30E-07	4.42E-02	6.93E-03	48.45

The magnitude of hoop stresses depend on the steam internal pressure and tube dimension as well as inner and outer tube surface temperatures. For example, in the presence of the metal losses (fireside, steamside and creep damages) and when the tube surface temperatures were constant (580°C) the hoop stress increased from 45MPa at the start of boiler operation to 284MPa after 40000 hours service.

At the beginning of the service in the absence of fireside damage, steamside damage and creep damage the hoop stress was 45MPa whereas the hoop stress increased to 45.53MPa at the end of the 1000 hours as a result of wall thickness decrease. Fireside damage, steam-side damage and creep damage were 7.67E-05, 2.06E-05 and 6.33E-07m respectively after 1000 hours. Fireside damage was the larger than the steamside and creep damages. This is because of the higher temperature of the outer surface than the inner surfaces and existence of corrosive alkali salts on the outer surface of the tube which are the driving forces of the metal deterioration on the fireside. The wall thickness decrease due to creep is very small as result of small metal strain in *z* direction (Eq.(2-85)).“Creep deformation results in little or no reduction in wall thickness but produces measurable creep elongation or increases in diameter in superheater/reheater tubes” [78].

During plant operation both fireside damage and steamside damage are expected to go up due to the temperature increases of the outer and inner tube surfaces. Both cause a wall thickness decrease and so a hoop stress increase. The wall thickness decreased from 7.40E-03m after 1000 hours to 6.93E-03m at the end of 5000 hours (see Table 4-12). Furthermore, tube outer diameter decreased from 4.48E-02 to 4.42E-02m in the same condition. In parallel hoop stress increased to 48.45MPa after 5000 hours service. In this situation fireside damage, steam-side damage and creep damage were 7.88E-05, 4.96E-05 and 6.30E-07m/1000h respectively (see Figure **4.18**).

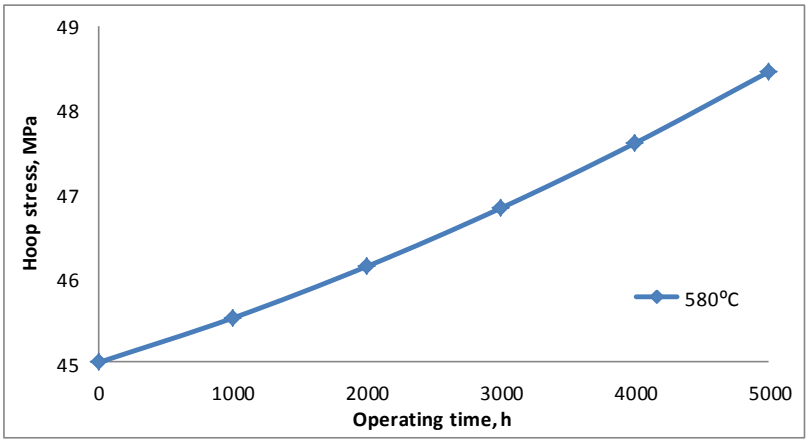

Figure 4.18 **Hoop stress acting on the thin-walled superheater tube starting from an initial metal temperature of 580^{0}C when burning Daw Mill coal versus operating time**

Finally, by knowing the secondary creep rate of tube metal the remaining service life the superheater/reheater tubes can be calculated through the Monkman-Grant relationship (Eq. (2.86)). The Monkman-Grant relationship constants for T22 are [107]: C = 2.3 and m = 0.772. The results are shown in Table 4-13.

Table 4-13 Creep rates and rupture lifetime for a superheater/reheater tube at internal steam pressures of 18MPa and starting from an initial temperature of 580^{0}C when burning Daw Mill coal (100% wt, 0.2% Cl)

Operating time, h	Tube mid-wall temperature, ^{0}C	Tube mid-wall temperature, K	Creep rate, 1/h	Residual life, h
0	579.67	852.67	8.62E-07	1.11E+05
1000	580.65	853.65	9.33E-07	1.04E+05
2000	581.36	854.36	1.00E-06	9.82E+04
3000	581.86	854.86	1.08E-06	9.31E+04
4000	582.43	855.43	1.16E-06	8.77E+04
5000	582.79	855.79	1.26E-06	8.29E+04

It must be emphasized that the creep life of a superheater/reheater is very sensitive to metal temperature and therefore an accurate estimate of mid-wall metal temperature (the temperature at middle of the tube thickness) is required for a reliable remaining service life prediction. An error of 10^{0}C will give rise to life errors of up to a factor of 2 [21]. Eq. (2-74) and Eq. (2-75) were applied in the model to calculate the mid-wall temperature of the superheater tube. The initial mid-wall temperature was 580^{0}C and increased to about 583^{0}C at the end of the 5000 hours as result of an increase in thermal resistance from flue gas to steam deriving from oxide and deposit thickness increase which eventually causes a decrease in the heat flux. The secondary creep rate of the tube material can be expected to rise as consequence of hoop stress and metal temperature increases. The secondary creep rate is expected to increase from 8.62E-071/h at 0 hour to 1.26E-061/h at 5000 hours (Table 4-13). The remaining service life of the tube decreased with creep rate increase as seen in Figure 4.19:

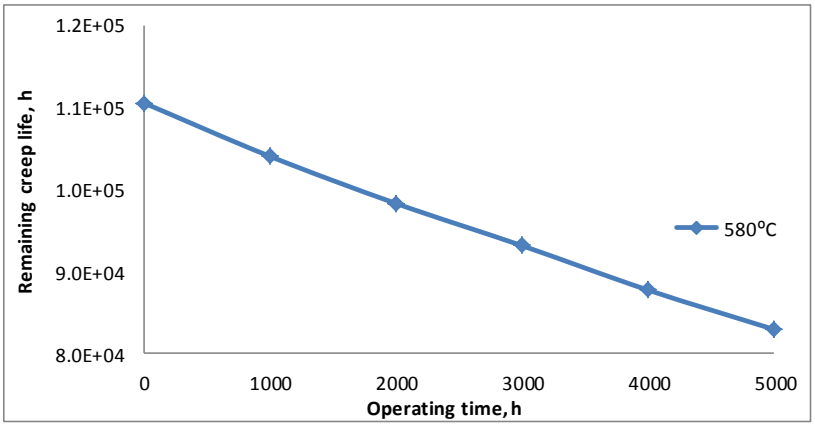

Figure 4.19 Remaining creep life the super-heater tube at initial mid-wall metal temperature of 580^{0}C when burning Daw Mill coal (100% wt, 0.2% Cl) versus operating time

The remaining creep life of the tube was 1.11E+05 hours at beginning of the exposure time and was reduced to 8.29E+04 hours after 5000 hour service. This indicates the interaction between metal temperature, hoop stress and secondary creep rate on the life of the tube during the operation.

The remaining life model predictions for T22 (2.25Cr-1Mo) were close to the stress rupture data provided by C.E.R.L [21] (Figure 4.19). The creep life of T22 at 45MPa and at 580^{0}C (mid-wall temperature) is 1.12E+05 hours as seen in Figure 4.19. This is in a good agreement with model's prediction which was 1.11E+05 hours at the same condition. In addition, Figure 4.20 was produced from the following equation:

$$t_r = \frac{C}{(k_{cr}\sigma^n exp(-\frac{Q_{cr}}{RT}))^m} \quad \textbf{(4-16)}$$

Eq. (4-16) is a detailed verion of the Monkman-Grant relationship. The creep parameters as well as the Monkman-Grant relationship constant parametrs for T22 used in the claculation to produce Figure 4.20 were identical to those applied in the model: C = 2.3 and m = 0.772, k_{cr} = 7191.18 (MPa)$^{-n}$/h, n=3.3, Q_{cr}/R = 30190K.

The creep lives of superheater/reheater tube were calculated for hoop stress between 30 to 100MPa at constant temperatures of 570, 580 and 590°C.

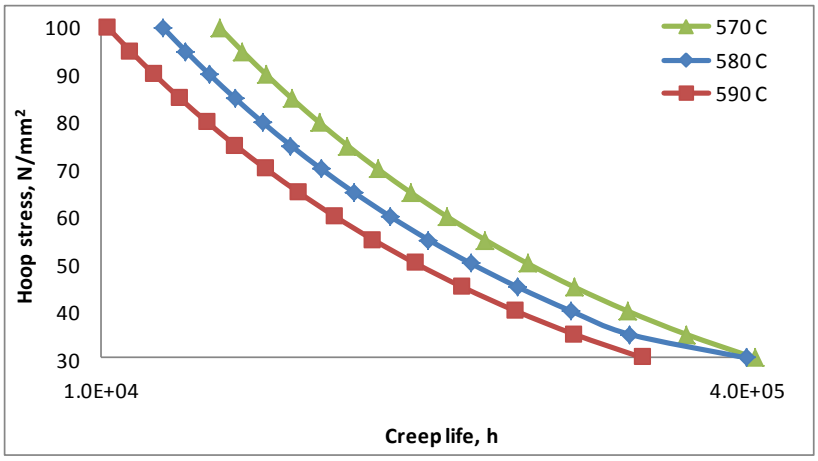

Figure 4.20 Stress rupture properties of T22 (2.25-1Mo) steel

The results, obtained by Eq. (4-16) at lower stresses (30 to 50MPa), were very close to the ones produced by C.E.R.L [21] as seen in. The differences between the results in and Figure 4.20 mostly derive from the creep constants and the Monkman-Grant constants used in Eq. (4-16). Particularly, small changes in the Monkman-Grant constants could improve the results significantly.

Furthermore, Figure 4.21 illustrates the remaining service live of T22 when burning Daw Mill coal (100% wt, 0.2% Cl) up to 50000 hours service.

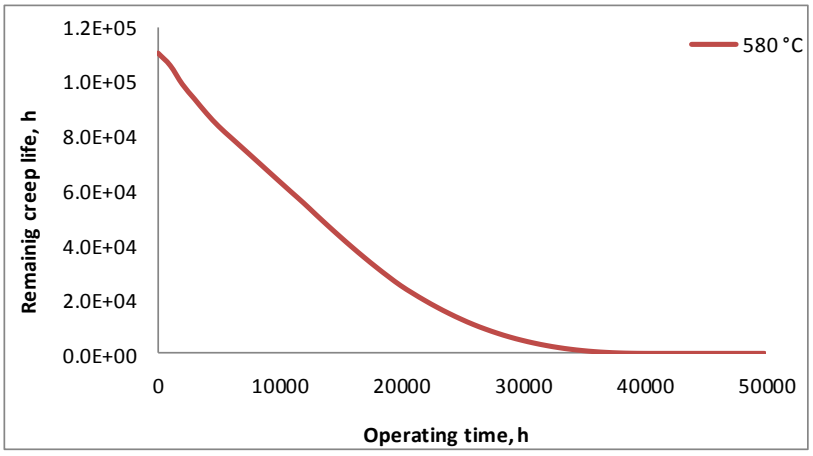

Figure 4.21 Remaining creep life 0f the superheater tube at initial mid-wall metal temperature of 580^{0}C when burning Daw Mill coal (100% wt, 0.2% Cl) versus operating time

The wall thickness decreased from 7.50E-03m at the beginning of the service to 2.27E-04m at the end of 40000 hours (see Appendix E) leading to a an increase in hoop stress that was 1542MPa. In addition, the tube mid-wall metal temperature increased to 594°C after 40000 hours service. Consequently, the remaining creep life of T22 was reduced to 8.66E+00 hours after 40000 hours service as shown in Figure 4.21.

Furthermore, French [20] reported that the remaining service life of T22 (2.25-1Mo) at hoop stress of 34.5MPa (5000psi) and at metal temperature of 580°C (1075°F) was 2.55E+05 hours using Larson miller parameter of 39000. Operating at lower hoop stress (34.5MPa) than the one predicted (45MPa) was the primary reason why the lifetime of T22 material reported by French is much bigger than the one predicted in this research which was 1.11E+05 hours.

In addition, Zarrabi [17] developed a method which relates the tube life to its wall thickness so that by measuring the tube thickness at any time the remaining service life of the tube can be estimated. For example, the creep life of T22 steel (2.25-1Mo) predicted by this method with wall thickness of 7.5mm and at tube metal temperature of 575°C was 9.5 years (83220 hours) [17]. It has to be pointed out that Zarrabi's method is applicable when the tube wall is thinned by corrosion and / or erosion processes only [17].

Finally, the failure of a reheater tube (1.25Cr–0.5Mo steel) in a 500MW boiler was reported by Chaudhuri [10]. The operating pressure was 2.5MPa and steam outlet temperature was 535°C. The design temperature of flue gas in the zone was 700–720°C. The tube had suffered extensive damage on the outer surface in the form of pits. The dimension of the pits at some places was as big as 40mm × 10mm with a maximum depth of 2mm. The failure had occurred after about 24,000 hours of service life [10]. The creep life of this reheater tube is much smaller than the one predicted in this research (1.11E+05 hours at steam pressure of 18MPa and at steam temperature of 540°C) despite being exposed to a lower steam pressure (2.5MPa) and temperature (535°C) as well as lower flue gas temperature (720°C). This is because of lower corrosion and lower creep resistant of 1.25Cr–0.5Mo steel than 2.25Cr-1Mo materials.

In chapter 5 the sensitivity of the combined model (remaining creep life model) to change in its input parameters such as hoop stress, creep constants, mid-wall metal temperature, and tube materials will be discussed.

4.6.3 Criteria for combined model selection

The thin-walled hoop stress formulas Eq. (2-79) or Eq. (2-81) were selected in the integrated models due to the following reasons:

- The residual life of superheater tubes predicted was closer to C.E.R.L data [21] when using Eq. (2-79) and Eq. (2-81) for hoop stress calculation in the integrated model.
- Eq. (2-79) and Eq. (2-81) are the most convenient equations for most boiler tube applications involving failure analysis and are sufficiently accurate for all stress calculations. They both derive from Eq. (2-80) (which is why they produced identical values for hoop stress) in which the mean diameter can include either outer radius or inner radius of the tube [20].

The application of creep models in the integrated model:

- Eq. (2-79) was used in the integrated model in order to calculate creep rate of P92 due to lack of the creep activation energy data for P92 in literature whereas an Arrehenius-type expression (Eq. (2-79)), with a characteristic activation energy for rate-controlling mechanism was used in the integrated model in order to calculate creep rate of T22 due to availability of the creep activation energy data for T22 in literature.

The Monkman-Grant relationship was selected to calculate the remaining service life of superheater/reheater tubes due to the following reasons below:

- The remaining service life predicted by The Monkman-Grant relationship was much closer to the C.E.R.L historical data than the values predicted by the Larson-Miller parameter.
- The availability of the constants for the specific materials in the literature (e.g. T22) to be used in The Monkman-Grant relationship.

5 SENSITIVITY ANALYSIS AND GENERAL DISCUSSION

5.1 Introduction

Sensitivity analyses have been performed to show how different model input values affect the rupture lifetime of superheater/reheater tubes. Model inputs that have been considered for sensitivity analysis of the residual life of the tubes include:

- Ash and vapour deposition models
- Tube metal temperature (mid-wall metal and inner surface)
- Flue gas temperature
- Fuel
- Fireside corrosion models
- Steamside oxidation parameters
- Hoop stress formulas
- Tubing diameter and wall thickness
- Tube materials
- Secondary creep rate parameters

5.2 Deposition models

5.2.1 Different fly ash deposition models

The deposits that can form on superheater/reheater tube surfaces lead to both reduced heat transfer rates and increased corrosion rates of boiler tubing, and so result in tube failure and in reduced generating capacity [52]. It is, therefore, important to accurately calculate the deposition fluxes of fly ashes on heat transfer surfaces to assess the heat transfer rate from the flue gas to steam and fireside corrosion rate of superheater tube metals. The mass fluxes estimates of fly ashes vary from model to model. In the sensitivity analysis below the deposition fluxes of ashes predicted by Zhou et al model [42] were compared with the ones obtained by Tomeczek et al model at initial surface temperature of 600°C when burning Daw Mill coal (100% wt) [55]. The results are shown in:

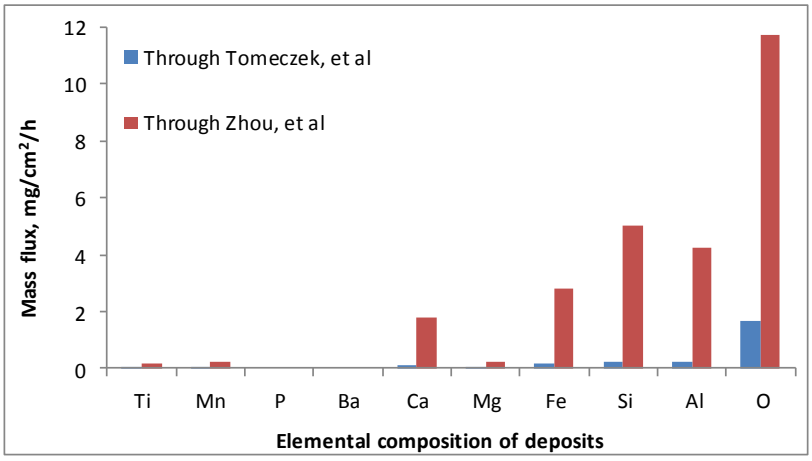

Figure 5.1 Deposition fluxes of fly ashes predicted when using Tomeczek et al and Zhou et al model in the integrated model at initial surface temperature of 600°C when burning Daw Mill coal (100% wt)

The deposition fluxes of ashes predicted when using Tomeczek et al model [55] in the integrated model were much lower than those predicted when using Zhou et al model [42] in the integrated model. This is mostly because of sticking probability of ashes on the tube surfaces in Tomeczek et al model which is much lower than the one in Zhou's model. The sticking probability in Tomeczek model is directly proportional to the condensation fluxes of alkali vapours forming sticky layers on the tube surfaces (Eq. (2-43)) while the sticking probability in Zhou et al model (Eq. (2-29)) derives from ash melt fraction which in turn is a function of melting temperatures and ash chemical compositions. Models predictions were closer to each other in the case of *Ti*, *Mn* and *Mg* compared with other elements such as *Fe*, *Si*, *Al*, *Ca* and *O*. For instance, the deposition fluxes of *Ti* were 0.013 and 0.036mg/cm^2/h predicted by Tomeczek et al model and Zhou et al model as shown in Figure 5.1. In addition, the mass fluxes of *O*, for example, were 1.7 and ≈ 12mg/cm^2/h obtained through Tomeczek et al model and through Zhou et al model respectively.

The sticking coefficient of Tomeczek et al model was much smaller than Zhou et al model's which led to much smaller deposition fluxes of deposit elements.

The ash deposition fluxes, predicted when using Zhou et al model [42] for impaction mechanism, were in a reasonably good agreement with the experimental data (see Figure 4.9) thus this model was finally used in the integrated model. For example, there

were a 13 and 18% difference between model prediction and the experimental data for the deposition fluxes of *O.* and *Si* respectively. Furthermore, the differences between model prediction and the experimental data for deposition fluxes of other elements (*Mg*, *Al*, *Fe*, and *Ca*) were less than 2% as shown in Figure 4.9 a.

In the next section (5.2.2) the sensitivity of Zhou et al model to change in its input parameters will be studied.

5.2.2 Implication of stickness efficiency on fly ash particles deposition

Zhou et al model Eq. (2-28) assumed that deposition of the large fly ash particles (d_p > 10μm) on upstream side of the tube is a function of fly ash particles concentration and its velocity, local impaction efficiency and particles stickness efficiency.

Local impaction efficiency (η) and particles stickness efficiency (f_{stick}) are found to be important parameters (see Table 4-5). In this sensitivity analysis the deposition fluxes of fly ashes were calculated for stickness efficiencies of 40, 50, 60 and 70 % to examine the implication of particles capture efficiency on fly ashes deposition. The sensitivity analyses were performed at deposit/tube surface temperature of 600°C and at flue gas temperature of 1150°C when burning Daw Mill coal (100% wt, 0.2% Cl). The results are shown in Figure 5.2.

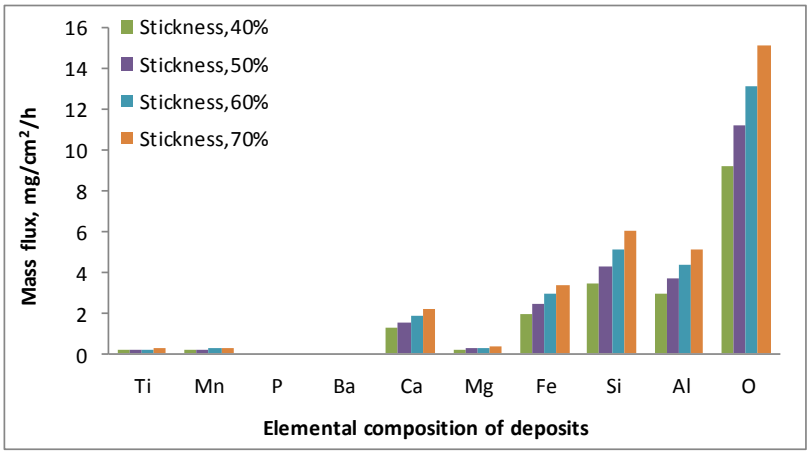

Figure 5.2 Implication of stickness efficiency on fly ash particles deposition at tube surface temperature of 600°C and at flue gas temperature of 1150°C when burning Daw Mill coal (100%wt)

The model predicted that the mass fluxes of elements in deposits increased with stickness efficiency by 40% as shown in Figure 5.2. For example, the mass fluxes of *Al* increased from 2.5mg/cm^2/h for 40% stickness efficiency to 5mg/cm^2/h for 70% stickness efficiency. Similar trends were noticed for deposition fluxes for other elements. From the above results it can be concluded that particles stickness efficiency is one of the determining factor for the large fly ash particles deposition on boiler tubing surfaces.

5.2.3 Different vapour condensation models

The deposition fluxes of alkali vapours (K_2SO_4 and Na_2SO_4) are one of the most important determining factors of fireside corrosion rates of superheater and reheater tubes in coal/biomass fired power plants. Thus, it is important to calculate the condensation fluxes of vapours on the tube surfaces to be able to predict its corrosion rate and, in turn, to predict its residual life more accurately. The deposition fluxes of vapours were calculated through Tomeczek model Eq. (2-18) [43] and were compared with the results obtained when using Christensen et al model [7].

$$C_i = 2\pi D_i D_O W_i \frac{p_i - p_{si}}{RT_g} C_{FS} \quad \textbf{(5-1)}$$

where D_i is diffusion coefficient of condensing gas in flue gas (m^2/s), D_O is outer diameter of tube (m), W_i is molecular weight of condensing gas (g/mole), C_{FS} is Fuchs-Sutugin correction factor, p_i is partial pressure of *i-th* gaseous component (Pa), p_{si} is its saturation pressure at surface temperature (Pa), R is universal gas constant (J/(moleK)), and T_g is flue gas temperature (K).The results are seen in Figure 5.3.

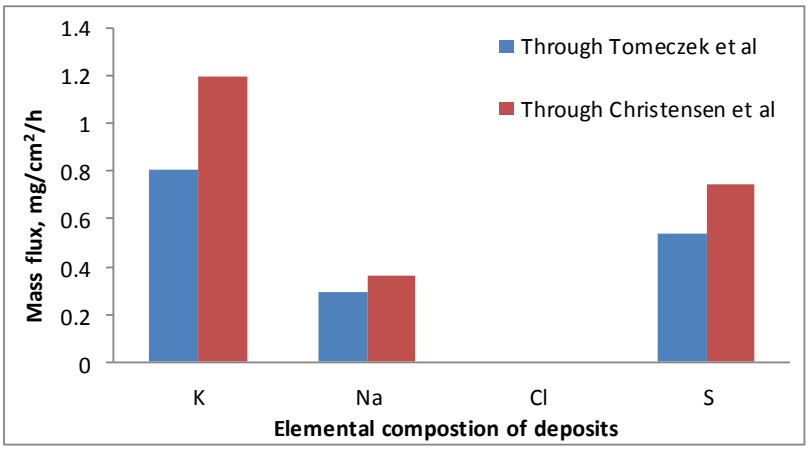

Figure 5.3 Deposition fluxes of vapours predicted when using Tomeczek et al and Christensen et al model in the integrated model at initial surface temperature of 600°C when burning Daw Mill coal (100% wt)

There was a 50% difference between models' predictions (Figure 5.3). For example, Christensen model predicted mass flux of 1.22mg/cm^2/h for potassium while this mass flux predicted by Tomeczek model were 0.8mg/cm^2/h. The mass fluxes of chlorine obtained from both of models using Daw Mill coal (100% wt) and at initial surface temperature of 600°C were zero.

The deposition fluxes of *K* and *Na* predicted by Tomeczek et al model were in a good agreement with the experimental data. The differences between model prediction and the experimental data for deposition fluxes of *K* and *Na* were less than 2% (see Figure 4.9) thus this model was finally used in the integrated model. In the section 5.2.4 the sensitivity of Tomeczek et al model to change in its input parameters will be studied.

5.2.4 Implication of deposit/tube surface temperature on deposition fluxes of vapours

Tomeczek et al model Eq. (2-19) was assumed that deposition fluxes of condensing alkali salts on the tube surfaces is a function of flue gas pressure, flue gas density, partial pressure of alkali vapours and its saturation pressure at surface temperature, and mass transfer coefficient of gaseous components. The deposit outer surface temperature increases as its thickness increases so at certain temperatures, higher than the saturation temperature of the condensable species, the condensation process stops (see section

2.3.2). Therefore, sensitivity analyses were performed at a variety of different deposit/tube surface temperatures to examine the effect of deposit/tube surface temperature on deposition fluxes of alkali salts. The sensitivity analyses were run at surface temperatures of 500, 600, 700, 800, 900, 1000 and 1100°C and at flue gas temperature of 1150°C when burning Daw Mill coal (100% wt, 0.2% Cl).

The saturation pressure model, Eq. (2-21), relates the deposit/tube surface temperatures to the deposition fluxes of alkali salts in Eq. (2-19). Figure 5.4 displays the increase of saturation pressure of alkali salts with surface temperatures.

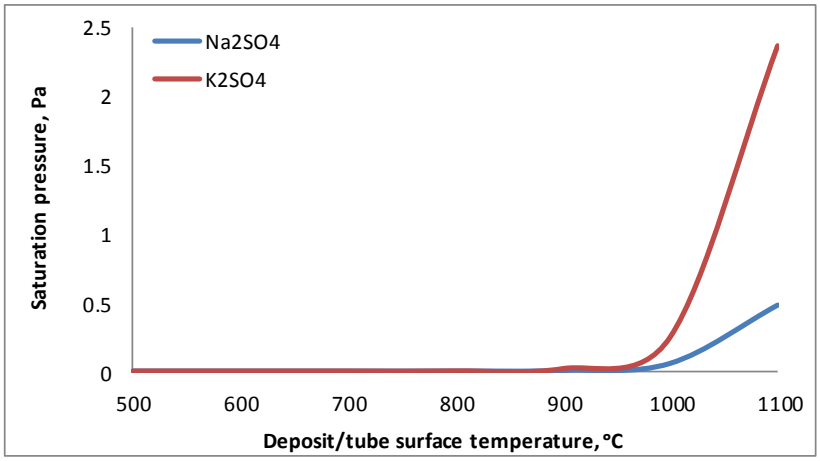

Figure 5.4 Saturation pressures of alkali salts versus deposit/tube surface temperatures at flue gas temperature of 1150°C when burning Daw Mill coal (100%, wt)

The saturation pressures of vapours were reasonably stable up to 900°C and increased dramatically from 1000 to 1100°C as shown in Figure 5.4. This leads to a decrease in deposition fluxes of alkali salts (see Figure 5.5).

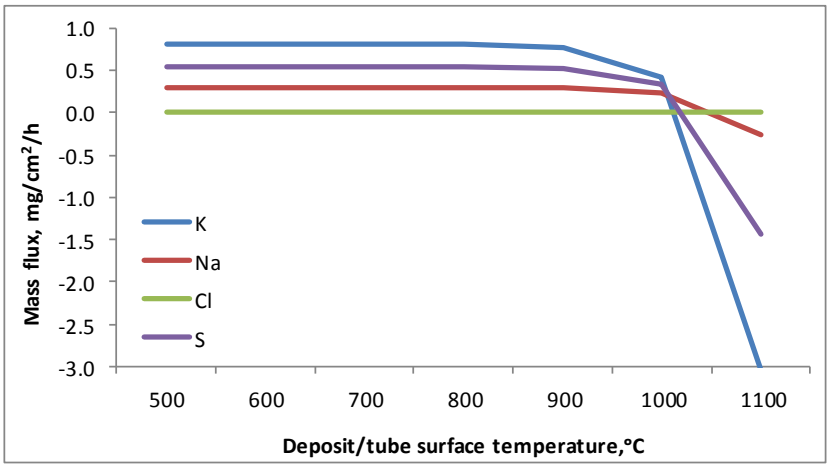

Figure 5.5 Implication of deposit/tube surface temperature on deposition of condensing alkali salts at flue gas temperature of 1150°C when burning Daw Mill coal (100%, wt)

The decrease in deposition fluxes of elements was very negligible up to 900°C. Subsequently, the deposition fluxes went down dramatically, particularly in the case of potassium. The deposition fluxes of potassium decreased by 3.4% at 900°C and then declined by 87% at 1000°C. The same trends were repeated for the deposition fluxes of sodium and sulphur.

5.3 Fireside corrosion model

5.3.1 Fireside corrosion rate obtained by different models

The corrosion rate of the stainless steel T347 was predicted by Eq. (2-64) as model 1 and Eq. (2-62) as model 2 at mid-wall temperatures of 540, 580, 620 and 700°C and at flue gas temperature of 1150°C. The fuel used in these trials was Daw Mill coal (100% wt with 0.2% chlorine). The results predicted by fireside corrosion model were compared with C.E.R.L data [21] as seen in Figure 5.6. The following corrosion rates were given from C.E.R.L data for T347 based on the above conditions:

- < 25nm/h at 540°C
- 25-50nm/h at 580°C
- 50-100nm/h at 620°C

- > 200nm/h at 660°C
- > 200nm/h at 660°C

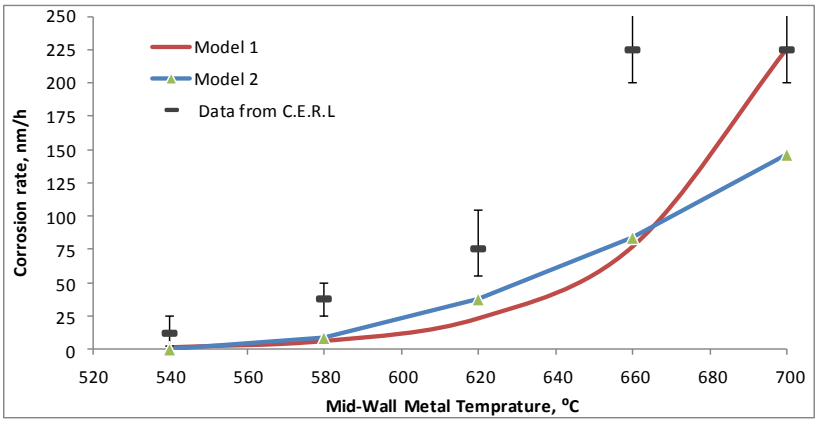

Figure 5.6 Corrosion rate of T347 predicted by two different models at flue gas temperature of 1150°C versus tube's metal temperature when burning Daw Mill coal (100% wt)

The models prediction were reasonably close to each other at all mid-wall temperatures, apart from the corrosion rates at 700°C which were 227 and 147nm/h predicted by model 1 and model 2 respectively. The wastage rates predicted at 540 and at 580°C were the closest to each other (Figure 5.6). For example the wastage rates had the values of 6.3nm/h and 9.3nm/h at 580°C. T347 is a high chromium content (18%Cr) alloy which is why its deterioration rate is considerably smaller than those T92 (9%Cr) and T22 (2.25%Cr). Both models predictions were lower than the C.E.R.L data due to the below possible reasons:

- Eq. (2-62) giving the correlation between the chlorine content of UK coals and the rate of fireside corrosion (nm/h) of austenitic stainless steels does not include the deposition fluxes of alkali salts in the model.
- In addition, constants applied for austenitic stainless steels in Eq. (2-64) were different from the ones used for T92.

Gagliano et al [21] also evaluated corrosion resistance of high-strength austenitic stainless steel alloys (Super304H, 347HFG, HR3C) at metal temperatures ranging from 650°C to 870°C and steam pressures in excess of 35MPa under coal-ash and flue gas

conditions that were typical of three North American coals: Eastern (mid-sulfur bituminous), Midwestern (high-sulfur bituminous), and Western (low sulfur sub-bituminous) coal types. For example the fireside corrosion rate of 347HFG was 266nm/h, at 700°C when burning North American coals (Midwestern) whereas the corrosion rates predicted by Eq. (2-64) as model 1 and Eq. (2-62) as model 2 at 700°C were 227 and 147nm/h when burning Daw Mill coal (a UK coal).

In addition, the corrosion rates of Types 347 stainless steel in a boiler fired with a UK coal containing 0.45%wt chlorine at a metal temperature of 649°C and a flue gas temperature of about 1149°C was 205nm/h as reported by Wright et al [64]. The corrosion rates predicted by Eq. (2-64) as model 1 and Eq. (2-62) as model 2 at a metal temperature of 650°C and a flue gas temperature of about 1150°C were 74 and 80nm/h when burning Daw Mill coal containing 0.2% wt chlorine (a UK coal). The lower corrosion rates predicted by Eq. (2-64) as model 1 and Eq. (2-62) as model 2 might be due to the lower chlorine content of Daw Mill coal (0.2% wt) than the coal (0.45% wt) reported by Wright et al [64].

5.3.2 Mid-wall metal temperature, gas temperature, tube material variation and fuel variation impact on fireside corrosion

In chapter 4 it has been shown that fireside corrosion decreases the remaining service life of superheater/reheater tubing due to wall thickness reduction and the resultant hoop stress increase in the tubing wall. Particular attention should be paid to flue gas and metal temperatures as well as to fuel compositions, as these are the most important factors determining corrosion rates. The significance of the levels of these parameters can be judged by running a sensitivity analysis and comparing the results with the experimental data.

Fireside corrosion is a thermally activated process thus is sensitive to the media's temperature. Corrosion will normally be more severe on any part operating above its design temperature; those parts at greatest risks are the superheater and reheater tubes. The effect of fireside corrosion can become significant with metal temperatures above 550°C and flue gas temperatures above 950°C. Corrosion rates of up to 25nm/h are acceptable. Wastage rates of about 100nm/h indicate that there will be a significant reduction in tube life and an estimation of the remaining life should be undertaken [21].

The corrosion rate of the superheater tubes (Fe-2.25Cr-1Mo) were calculated by Eq. (2-64) at mid-wall temperatures of 540, 580, 620 and 700°C and at flue gas temperature of 1150°C. The fuel used in this trial was Daw Mill coal (100% wt) with 0.2% chlorine. The results predicted by fireside corrosion model were compared with C.E.R.L data [21] as seen in Figure 5.7. The following corrosion rates were given from C.E.R.L data for T22 at mid-wall temperatures of 540, 580, 620 and 700°C and at flue gas temperature of 1150°C when burning Daw Mill coal (100% wt with 0.2% chlorine):

- 25-50nm/h at 540°C
- 50-100nm/h at 580°C
- 100-200nm/h at 620°C
- > 200nm/h at 660°C
- > 200nm/h at 700°C

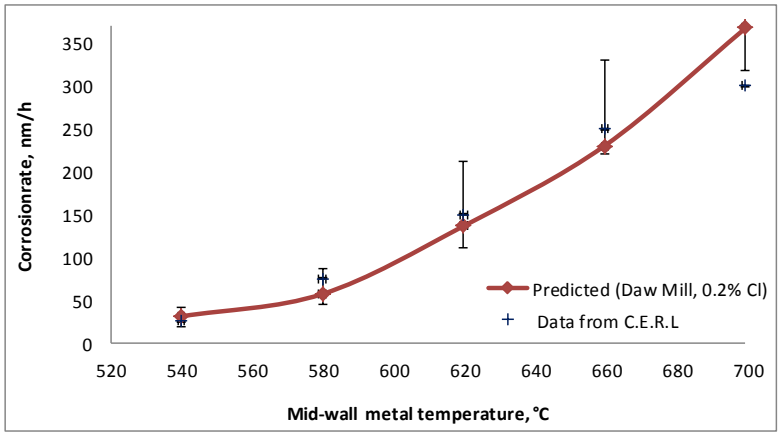

Figure 5.7 Corrosion rate of T22 at flue gas temperature of 1150°C versus tube's metal temperature when burning Daw Mill coal (100%, wt)

The model predicted wastage rate of 31, 57, 136, 230 and 360nm/h at 540, 580, 620, 660 and 700°C respectively. The corrosion rates were increased with mid-wall metal temperatures increase. These were in agreement with C.E.R.L data as shown in Figure 5.7. Moreover, the corrosion rate of a leading (leading tubes directly face the hot flue gases) T22 steel in a boiler fired with a UK coal containing 0.33%wt chlorine at a mid-wall temperature of 540°C and a flue gas temperature of about 1160°C was 24nm/h

as reported by Wright et al [64] whereas the corrosion rate of the same material predicted by Eq. (2-64) at mid-wall metal temperature of 540°C and a flue gas temperature of about 1150°C was 31nm/h when burning Daw Mill coal (a UK coal).

For the same operating conditions, the fireside corrosion rate of T92 (9Cr) was also predicted by Eq. (2-64) for Daw Mill coal (100% wt with 0.2% chlorine). The following corrosion rates were given from C.E.R.L data for T92 at mid-wall temperatures of 540, 580, 620 and 700°C and at flue gas temperature of 1150°C when burning Daw Mill coal (100% wt with 0.2% chlorine):

- < 25nm/h at 540°C
- 25-50nm/h at 580°C
- 100-200nm/h at 620°C
- > 200nm/h at 660°C
- > 200nm/h at 700°C

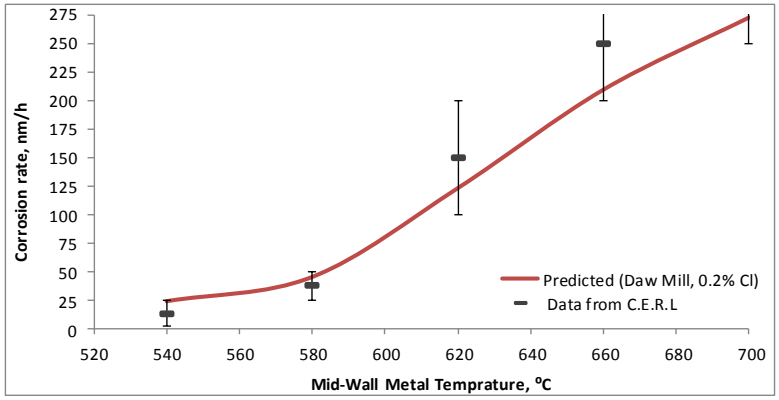

Figure 5.8 Corrosion rate of T92 at flue gas temperature of 1150°C versus tube's metal temperature when burning Daw Mill coal (100% wt)

Corrosion rates of 24, 45, 123, 209 and 272nm/h were predicted for T92 at 540, 580, 620, 660 and 700°C respectively. These were in a good agreement with C.E.R.L data (Figure 5.8). The wastage rate of T92 was smaller than T22 due to better resistance of T92 to corrosion. In coal-fired boilers, metals of higher chromium content have higher

corrosion resistance and the limit of acceptable wastage rate is reached at a higher metal temperature.

Figure 5.9 also shows the corrosion rate of the tube (T92) at flue gas temperature of 1050°C and at mid-wall metal temperatures of 540, 580, 620, 660 and 700°C predicted by fireside corrosion model. The fuel was Daw Mill coal (100% wt with 0.2% chlorine). In these conditions the following corrosion rates were given in C.E.R.L data:

- < 25nm/h at 540°C
- < 25nm/h at 580°C
- 25-50nm/h at 620°C
- 100-200nm/h at 660°C
- > 200nm/h at 700°C

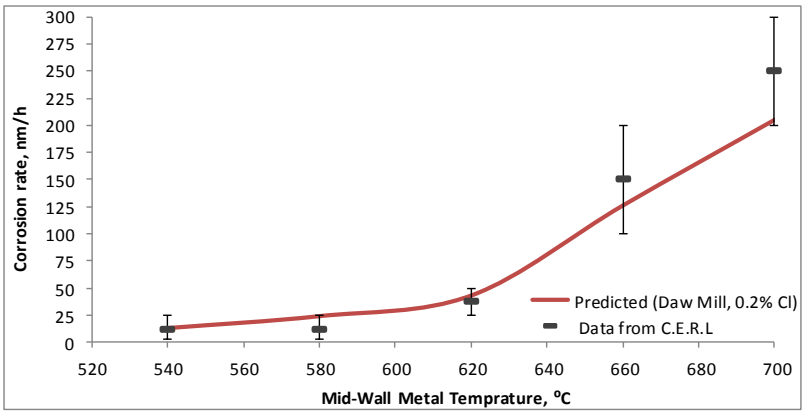

Figure 5.9 Corrosion rate of T92 at flue gas temperature of 1050°C versus tube's metal temperature when burning Daw Mill coal (100%, wt)

Figure 5.9 shows that the corrosion rate of the tube decreased with the local flue gas temperature decrease. The model predicted wastage rate of 13, 24, 43, 126, and 205nm/h at 540, 580, 620, 660 and 700°C respectively. Figure 5.9 shows that the corrosion rate T92 decreased significantly at 1050°C compared with its corrosion rate at 1150°C and the same mid-wall metal temperatures.

The changes that may take place in the type of fuel used can have a dramatic effect on the steam boiler performance [20]. A change in the nature of the fuel can directly affect

the risk of corrosion. For example, a coal with a more fusible ash can lead to slagging or an increase in the amount of alkali metal deposits on superheater/reheater tubes. Corrosive coals are those with mineral matters producing a low fusion temperature ash and/or a high proportion of volatile alkali salts [21].

The following example is this type of failure. New SA213-T12 (1Cr-0.5%Mo) primary superheater tubes were fitted in a boiler unit in August 2004 [80]. The tubes had outer diameter of 50.8mm and wall thickness of 5mm. It was reported that the boiler had operated normally until a new type of coal was used. The failure took place in less than 10 days (226 hours) in June 2007 after a new firing pattern was introduced. The failed tube had only operated at around 28,194 hours at average steam pressure of 14.1MPa. The new type of coal had low ash fusion temperature of 1210°C whereas the average furnace flame temperature was 1400°C leading to firing problems (e.g. slagging). Therefore, operation of a new type of coal having low ash fusion temperature was the main root cause of the superheater tube failure [80].

Finally, Figure 5.10 shows the corrosion rate of T22 at flue gas temperature of 1150°C and at the same mid-wall metal temperatures as above cases when a different type of coal is introduced to the boiler (El-Cerrejon coal (100% wt) with 0.02% chlorine). In these conditions the following corrosion rates were given in C.E.R.L report:

- < 25nm/h at 540°C
- 25-50nm/h at 580°C
- 100-200nm/h at 620°C
- > 200nm/h at 660°C
- > 200nm/h at 700°C

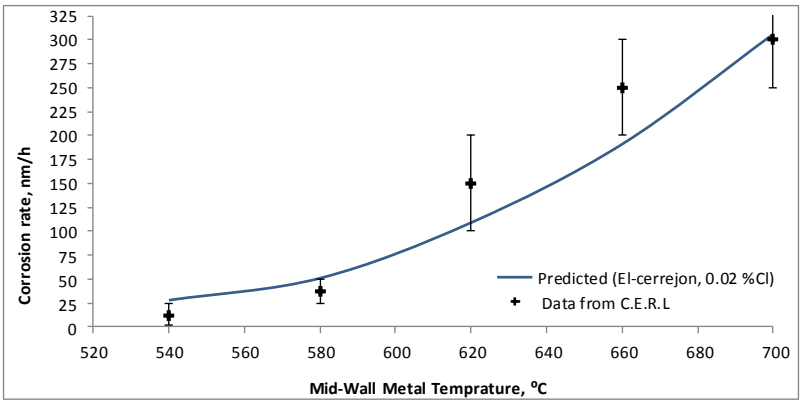

Figure 5.10 Corrosion rate of T22 at flue gas temperature of 1150°C versus tube's metal temperature when burning El-Cerrejon coal (100%, wt)

The wastage rates predicted were 28, 51, 109, 191 and 306nm/h at 540, 580, 620, 660 and 700°C respectively. The corrosion rates in the case of El-Cerrejon coal (100%, wt) with flue gases at 1150°C were smaller than the ones in the case of Daw Mill coal (100% wt) due to the lower chlorine and sulphur content of El-Cerrejon coal than Daw Mill coal and different mineral matter content leading to a lower alkali salts release during the fuel combustion. However, different scenarios were shown by Li et al [108] for three types of coal with different chlorine and sulphur contents where they induce different corrosion rates on superheater tube surfaces during 500 hours test. The tested material was a low chromium steel SA-213T-22. The gas temperature at the location where the probes were placed was 786°C. Furthermore, air flow introduced into the probe from the air compressor was used to cool the probes to give the disks a temperature around 537°C. The metal loss of T22 obtained from combusting coal with lower chlorine content was higher than that obtained from combusting coal with higher chlorine content as a result of higher sulphur content of the first coal [108].

5.3.3 Implication of fireside corrosion on boiler tubing life

During boiler operation, fireside corrosion continuously reduces the wall thickness of tubing from the outside of the tube and raise the hoop stress and the corresponding creep rate. This leads to a creep life reduction of boiler tubing. In this sensitivity analysis fireside corrosion damage was calculated by a factor of 10% decrease to examine different outputs of fire side damage on the residual life of superheater tubes (T22). The results were then compared with the residual of the tube when the fireside

corrosion model is in its normal mathematical state as shown in Figure 5.11. The initial hoop stress and the initial mid-wall metal temperature were 45MPa and 580^{0}C respectively. Furthermore, the fuel applied for this sensitivity analysis was Daw Mill coal (100% wt, 0.2% Cl).

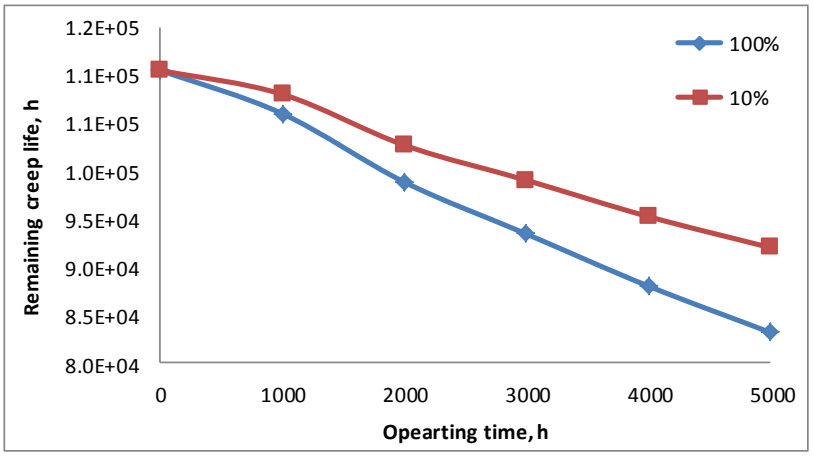

Figure 5.11 The impact of different fireside corrosion rates on the remaining service life of T22 at initial stress of 45MPa and at initial metal temperature of 580°C

At the beginning and when the corrosion rates were zero the tubing lives were identical (1.11E+05 hours). However, during operation and when the outside diameter and the wall thickness are affected by fireside damage of different rates (corrosion rate; 100% and corrosion rate, 10%) the remaining creep life of T22 were different. These differences became more obvious at larger operating times (see Figure 5.11). The normal fireside corrosion model and the one with factor of 10% revealed that, after 1000 hours operation, the residual life of the tubing were 1.06E+05 hours and 1.08E+05 hours respectively. The residual life of the superheater / reheater tube was decreased to 8.32E+04 hours at the end of 5000 hours exposure while when the factor of 10% was included in fireside wastage rate formula the life became 9.42E+04 hours at the same operating time as a result of a lower fireside corrosion rate in the case of 10% fireside corrosion rates. Furthermore, the Impact of 10, 50, 75, 100, 125 and 150% fireside corrosion rates on the remaining service life of T22 at initial hoop stress of 45MPa and at initial metal temperature of 580°C were obtained for 50000 hours service (see Figure 5.12). The creep life of the component decreases steadily during the operation.

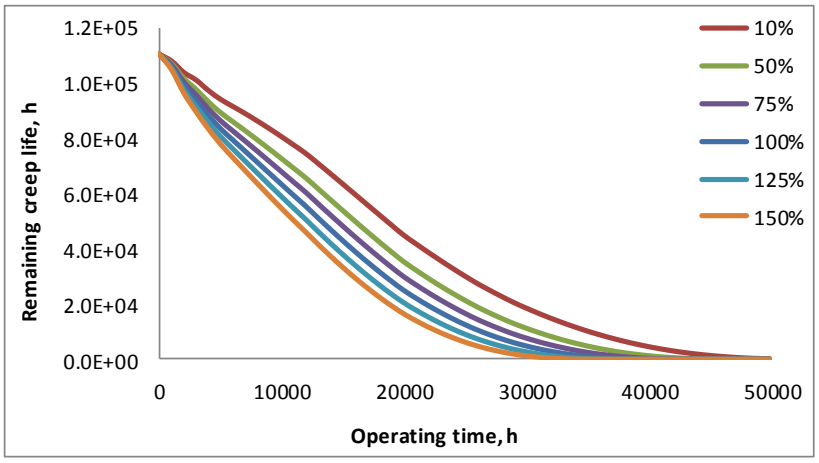

Figure 5.12 Impact of 10, 50, 75, 100, 125 and 150% fireside corrosion rates on the remaining service life of T22 at initial stress of 45MPa and at initial metal temperature of 580°C versus operating time

Figure 5.12 shows that the remaining service life of T22 decreased from 10 to 150% of fireside corrosion damage. For instance, the creep life of the superheater tube decreased from 9.42E+04 hours for 10% of fireside corrosion damage to 7.80E+04 hours for 150% of fireside corrosion damage at the end of the 5000 hours service. Moreover, the life of the tube was 1.32E+02 hours for 10% of fireside corrosion damage after 50000 hours operation whereas the tube had failed after 36000 hours exposure for 150% of fireside corrosion damage.

5.4 Steamside oxidation

5.4.1 Different steamside oxidation models

Besides temperature, steamside oxidation reaction rate is a function of other exposure parameters as well; according to Arrhenius' equation (Eq. (2-67)). Therefore, different values of these oxidation parameters must produce different oxide thickness. The following sensitivity analysis was performed to assess the effects of oxidation parameters on steamside wall loss (as well as tube remaining life when burning Daw Mill coal (100% wt 0.2% Cl)). Various oxidation parameters are given in [106] for T22 and other alloys used in superheater and reheater tubes. Oxidation parameters of T22 are tabulated in Table 5-1:

Table 5-1 Steamside oxidation parameters of T22 (Fe-2.25Cr-1Mo, wt%) [106]

Oxidation parameters	A,(μm)^2/h	Q, kJ/mole
a	1.51E+14	223
b	6.22E+20	326
c	2.05E+20	327
d	5.98E+23	381
e	1.26E+18	288

The inside surface wall loss of T22 due to steam side oxide growth were calculated using Eq. (2-67) based on different oxidation parameters. The results are shown in Figure 5.13:

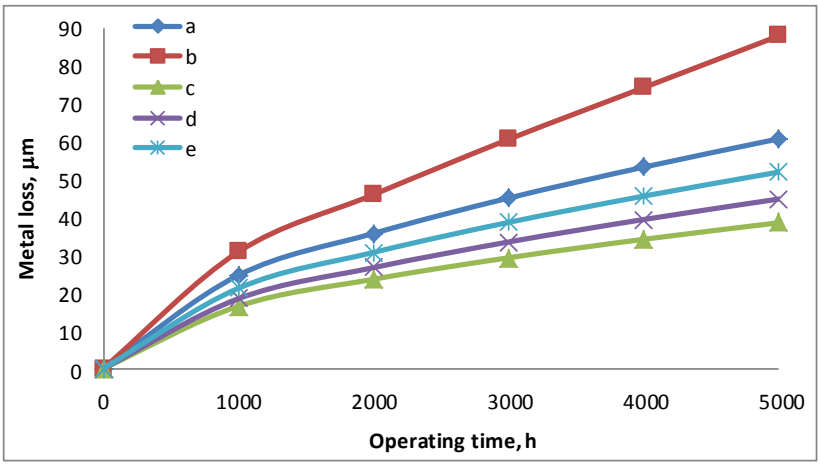

Figure 5.13 Metal losses of T22 based on different oxidation parameters versus operating time

Evidently, different oxidation parameters resulted in different amounts of steamside oxide thickness and different amount of steamside wall losses in T22 at a constant temperature (Figure 5.13). For example, the amount of wall loss predicted by constants in the rows of *a*, *b*, *c*, *d*, and *e* were approximately 25, 31, 19 and 21μm respectively after 1000 hours exposure to superheated steam temperature of 540°C. The metal losses became much bigger at the end of 5000 hours exposure: 61, 88, 39, 45 and 52μm for constants in rows *a*, *b*, *c*, *d*, and *e* respectively. In this sensitivity analysis, the tube initial inner surface temperature was 565°C.

The formation of an oxide scale results in an effective loss in wall thickness and so a corresponding increase in hoop stress level. Consequently, the creep rate increases

leading to residual life reduction of superheater/reheater tubes and possibly their premature failures. The remaining creep life of T22 resulted from above steamside wall losses are presented in Figure 5.14:

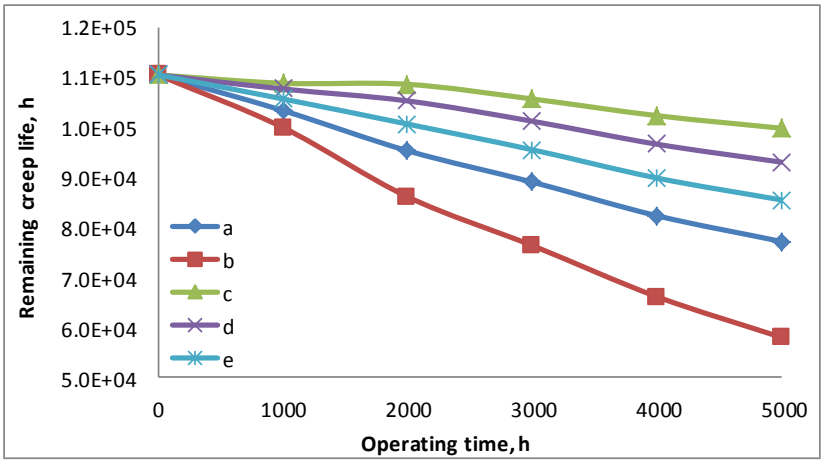

Figure 5.14 Remaining creep life of T22 based on different oxidation parameters versus operating time

The lower wall losses led to a larger remaining service lives for tubes, as shown in Figure 5.14. For instance, due to the small wall thickness losses predicted, the creep life of the tube predicted by the row *b* of oxidation parameters were the largest for the potential oxidation parameters of T22. Conversely, the creep life of the tube predicted by the row *b* were the lowest amongst this group of oxidation parameters due to the bigger wall loss resulted from the oxidation constants in row *b*.

The model predicted the residual service life of 7.72E+04, 5.79E+04, 9.98E+04, 9.30E+04, and 8.55E+04 hours for the row *a*, *b*, *c*, *d*, and *e* of oxidation parameters respectively after 5000 hours boiler operation whereas at the start of boiler operation and in the absence of steamside oxidation the creep life for all cases were identical to each other having value of 1.11E+05 hours.

Finally, it was decided to use oxidation parameters of row *c* in Table 5-1 in the model since they produced smaller metal losses or larger creep life for superheater and reheater tubes.

5.4.2 Implication of tube surface temperature variation on steamside oxidation

Steamside oxidation occurs when the superheater and reheater tubes are exposed to high temperature steam. As for fireside corrosion, steamside oxidation is a thermally activated process. The oxide scales thickness as well as metal loss of T22 were calculated at three inner tube surface temperatures such as 545, 555 and 565°C using Eq. (2-67). The results are presented in Figure 5.15:

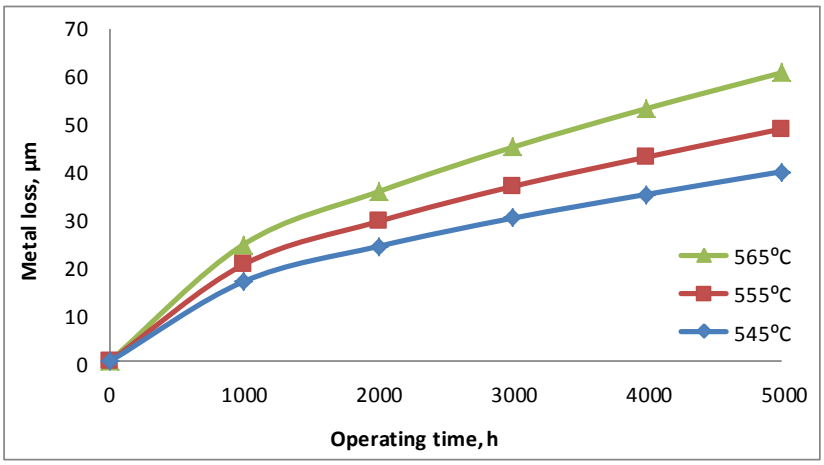

Figure 5.15 Metal losses of T22 at different inner tube surface temperatures versus operating time

The oxide thickness growth obviously followed a parabolic pattern (Figure 5.15). The magnitude of metal loss predicted increased with the temperature increase. For instance, the tube metal loss was 17µm at 545°C after 1000 hours operation whereas the metal losses, for the same amount of operating time, were increased to 21 and 25µm at 555°C and 565°C respectively. Finally, the steamside metal losses were increased to 40, 49 and 61µm at inner surface temperatures of 545, 555 and 565°C respectively at the end of 5000 hours as seen in Figure 5.15. In this sensitivity analysis, the hottest tubes (the tubes with the thickest steamside oxide scales) commonly experienced the greatest wastage rates. These metal losses will reduce the wall thickness and raise the hoop stress on the tubing wall leading to the remaining life reduction of the tube.

Furthermore, the steamside metal losses of the superheater tube were calculated for 50000 hours exposures to the superheated steam at inner surface temperatures of 545, 555 and 565°C. The results are shown in Figure 5.16.

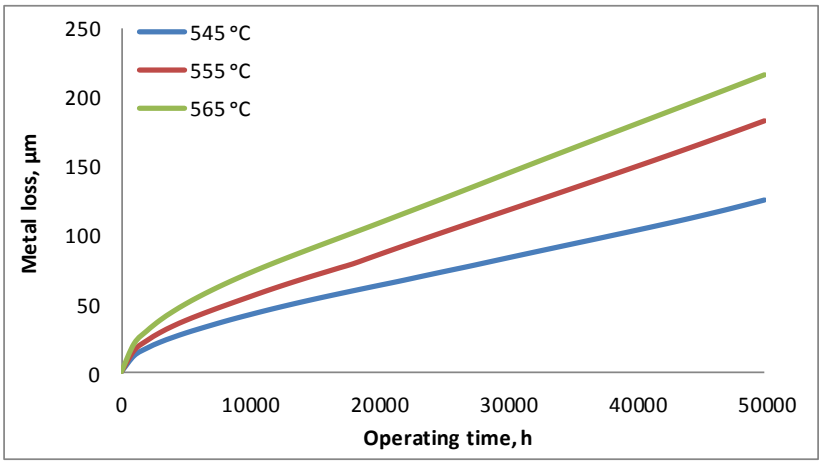

Figure 5.16 Metal losses of T22 at different inner tube surface temperatures versus operating time

The metal losses increased to 125, 182 and 216µm for 545, 555 and 565°C respectively at the end of 50000 hours service due to inner oxide thickness increase and, in turn, an increase in tube inner surface temperatures.

Furthermore, French [20] calculated steamside scale thickness up to 100000 hours for initial tube metal temperatures of 566, 580, and 607°C for a typical superheater and reheater tubes (T22) using Eq. (2-83). It is obvious that the model predicted different oxide scale thicknesses at different temperatures. However the oxide thickness curves overlapped each other up to 5000 hours service at temperatures of 566 and 580°C (the oxide thickness was 101µm after 5000 hours operation). The oxide thickness increased during the boiler operation as a result of the tube metal temperature increase. For example, the oxide thicknesses calculated by Eq. (2-83) were 228, 279 and 965µm at temperatures of 566, 580, and 607°C respectively after 50000 hours service [20]. The oxide thicknesses were increased to 304, 457 and 1828µm at temperatures of 566, 580, and 607°C respectively after 100000 hours service [20].

5.5 Creep model

5.5.1 Creep parameters implication

Besides temperature, secondary creep rate is a function of creep parameters as well (Eq. (2-83)). Therefore, different creep constants must produce different secondary creep rate for tube metal and different corresponding remaining service life for superheater tubes.

The following sensitivity analysis was performed to assess the effects of creep parameters on creep rate of tube metal and, more importantly, on remaining life T22 at initial metal temperature of 580°C and at initial hoop stress of 45MPa. In addition, the fuel used for this analysis was Daw Mill coal (100% wt 0.2% Cl). Various creep parameters of T22 [69; 107] are tabulated in Table 5-2:

Table 5-2 Various creep parameters of T22 (Fe-2.25Cr-1Mo wt%) [69; 107]

Creep parameters	A_{cr}, $(MPa)^{-n}/h$	*n*	Q_{cr}/R ,K
a	5.08E+07	4.86	4.28E+04
b	6.02E+04	4.57	3.61E+04
c	8.27E+09	5.06	4.81E+04
d	7.19E+03	3.3	3.02E+04
e	4.30E+07	4.57	4.10E+04

The creep life calculated through the above creep parameters are given in Figure 5.17.

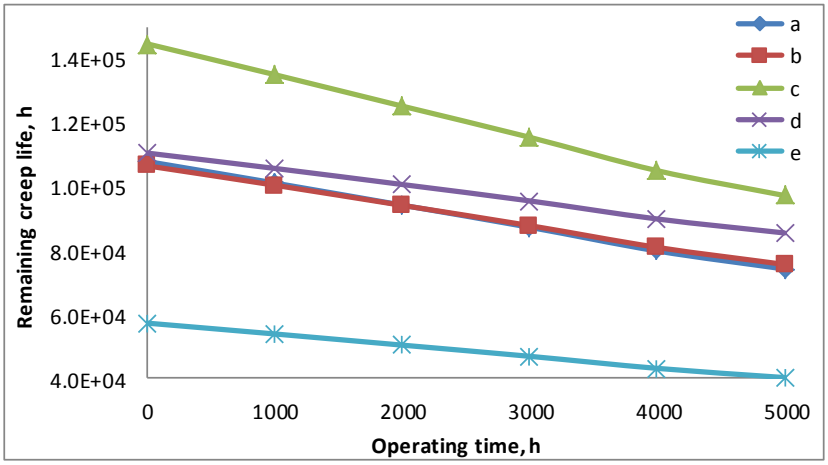

Figure 5.17 Creep life of T22 resulted from various creep parameters at 580°C and at 45MPa when burning Daw Mill coal (100% wt) versus operating time

The creep life of the superheater/reheater predicted by creep constant in rows *a*, *b* and *d* in Table 5-2 were very close to each other compared with the ones predicted by creep constant in rows *c* and *e*. The predicted lives were 1.08E+05, 1.07E+05 and 1.11E+05 hours at the start of boiler operation for creep constants in rows *a*, *b* and *d*, respectively as shown in Figure 5.17. Yet the life predicted by creep constants in rows *c* and *e* were 1.45E+05 and 5.72E+04 hours respectively. The model prediction for creep constants in rows *a*, *b*, *c* and *d* are in a good agreement with stress rupture data in [21]. The

predictions deriving from creep constant in row *c* were closer to the stress rupture data (see section 4.6) thus they were used in the model.

The remaining service life of boiler tubing was reduced during operation typically due to fireside corrosion, steamside oxidation and creep strain causing an effective loss in wall thickness (see Figure 5.17). For instance, the remaining creep life the supeheater tube was 1.45E+05 hours at the start of boiler operation and then decreased to 9.72E+04 hours at the end of 5000 hours (see Figure 5.17 line *c*). Similar trends were observed for creep life of T22 predicted by other creep parameters listed in Table 5-2.

In addition, the creep life of the superheater tube were calculated using creep constants listed in Table 5-2 for 50000 hours operation as shown in Figure 5.18.

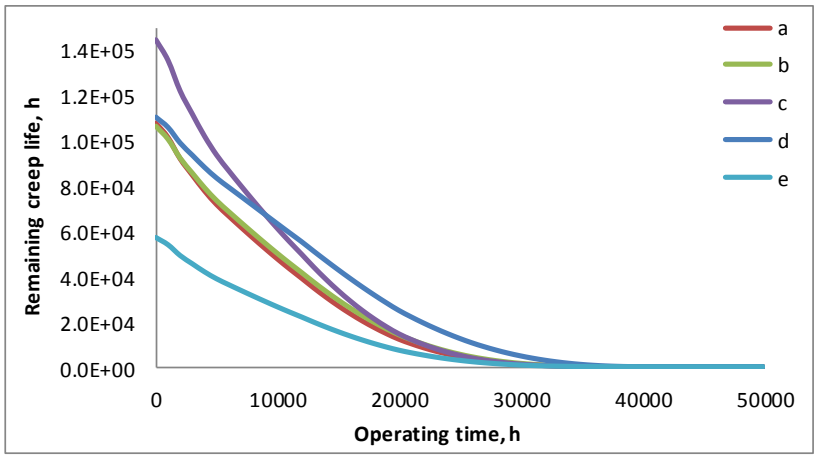

Figure 5.18 Creep life of T22 resulted from various creep parameters at 580°C and at 45MPa when burning Daw Mill coal (100% wt) versus operating time

The creep life of the tube decreased steadily for each of creep constant during operation as shown in Figure 5.18. For instance, the remaining life of the tube was 8.56E+00 hours, predicted by creep constants in row *d* in Table 5-2, at the end of 40000 hours after which the tube failed.

5.6 Combined model

5.6.1 Implication of co-firing biomass on creep life of superheater tubes

Biomass fuels differ from the coals. Biomass contains less sulphur variable quantities of chlorine, and more readily releasable aggressive deposit-forming species such as alkali

metals. This leads to a higher fireside corrosion rate of superheater/reheater tubes. Thus, a sensitivity analysis was performed to evaluate the effects of co-firing of biomass with coal on the residual life of the boiler tubing. The remaining service life of T22 were calculated at initial metal temperature of 580°C and at initial hoop stress of 45MPa when burning Miscanthus:Daw Mill (20:80%wt). The results were then compared with remaining lives of T22 at the same operational conditions when the fuel burnt was Daw Mill coal (100%wt) as seen in Figure 5.19:

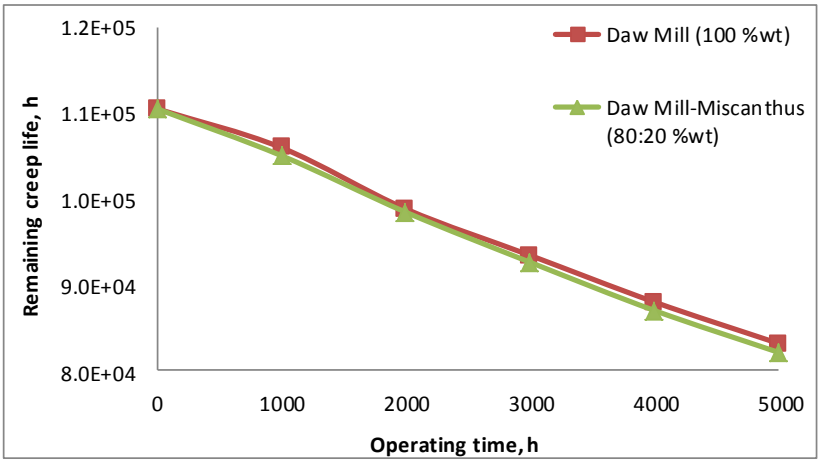

Figure 5.19 Remaining creep life of T22 when co-firing Daw Mill coal with Miscanthus versus operating time at initial metal temperature of 580°C

When firing Miscanthus at 20%, the metal wastage of T22 were increased compared with those predicted with Daw Mill coal alone due to higher amounts of alkali metal and, in turn, higher mass fluxes of alkali salts in deposit. This caused creep life reduction of T22 when co-firing Miscanthus with Daw Mill coal. After 1000 hours operation the creep life of superheater tube was 1.06E+05 hours in the case of Daw Mill coal (100 %wt) and it was 1.05E+05 hours when burning Miscanthus:Daw Mill (20:80%wt). the creep life of T22 were decreased to 8.32E+04 hours and 8.21E+04 hours at the end of 5000 hours exposure when burning Daw Mill coal alone and Miscanthus:Daw Mill (20:80%wt) respectively.

A power station combusting 100% biomass is vulnarable to severe fireside corrosion of superheater/reheater, due to highly aggressive alkali salts in deposits. In many UK coals, potassium is predominantly bound to aluminosilicate clays and are thus relatively inert while most sodium species are more readily releasible. However, the alkali metals

in biomass fuels are loosley associated with organic matters or present as simple salts. Therefore, they are more readilly released during combustion of the fuels, and can actively participate in corrosion process [56].

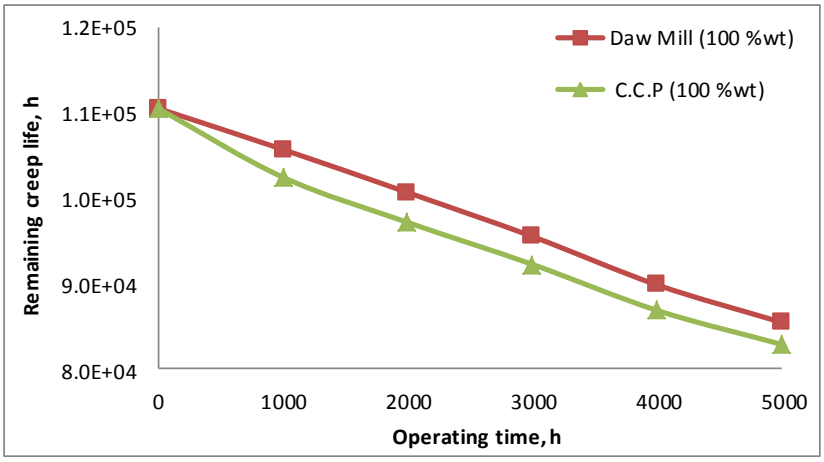

Figure 5.20 Remaining creep life of T22 when burning Daw Mill coal and C.C.P versus operating time at initial metal temperature of 580°C

According to fireside corrosion model predictions, there was biomass has a very high alkali metal content and in turn, high mass fluxes of alkali salts on superheater tube surfaces. This results in an increase in the corrosion rate when burning CCP (100% wt) which leads to wall thickness loss and, in turn, considerable reductions in creep life for T22 (see Figure 5.20). The residual life of the boiler tubing was decreased from 1.11E+05 hours at the start of boiler operation to 8.29E+04 hours at the end of 5000 hours service when CCP (100% wt) was used as the fuel while after 5000 hours exposure the residual life of the tubing was 8.55E+04 hours when Daw Mill coal (100% wt) fuel was combusted.

5.6.2 Mid-wall metal temperature variation

The remaining creep life is very sensitive to mid-wall metal temperature and therefore accurate estimates of *T* (mid-wall) are essential for reliable life predictions. An increase of 10°C has been reported to give decrease to life by a factor of 2 [21]. The following sensitivity analysis is run to assess the effects of mid-wall metal temperature change on the superheater/reheater tube remaining life at initial hoop stress of 45MPa and when burning Daw Mill coal (100% wt, 0.2% Cl). Three temperatures were chosen for this

analysis which includes 560, 570 and 580°C. The tube material for this analysis was T22 (Fe-2.25Cr-1Mowt%) which is classified as low alloy ferritic. The results are shown in Figure 5.21.

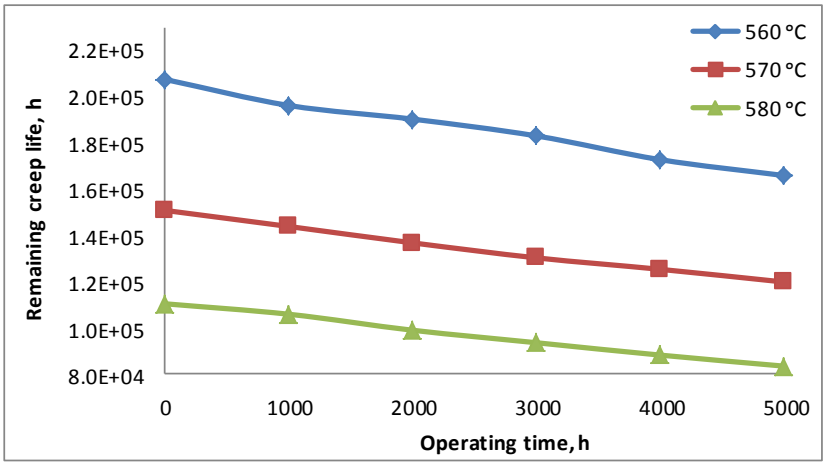

Figure 5.21 Remaining creep life of T22 at initial mid-wall metal temperatures of 560, 570, and 580^{0}C and at constant hoop stresses of 45MPa when burning Daw Mill coal (100%, wt 0.2% Cl) versus operating time

As expected there was a significant difference between creep life of T22 every 10°C increase in temperature. At the start of boiler operation when the effects of fireside corrosion, steamside oxidation and creep deformation were zero the residual life of T22 predicted were 1.11E+05, 1.51E+05 and 2.08E+05 hours at initial metal temperatures of 580, 570 and 560°C respectively. There were 0.9, 3 and 20% differences between predicted and the values given in C.E.R.L report [21] for remaining service life of superheater tubes at metal temperatures of 580, 570 and 560°C respectively as seen in Figure 4.17

After 5000 hours service the tube life decreased for each of three initial metal temperatures. For example the remaining life of the tube decreased to 1.20E+05 hours after 5000 hours service at initial metal temperature of 570°C. Similar trends were seen for the other two temperatures (560 and 580°C) due to effects of fireside corrosion, steamside oxidation and creep deformation as well as hoop stress on creep life. Yet there were differences between the remaining lives of the component for each of the three temperatures at the end of 5000 hours exposure due to influence of mid-wall

temperatures on the creep life. The remaining life of T22 were 8.35E+04 and 1.66E+05 hours after 5000 hours service at initial temperatures of 580 and 560°C respectively.

In addition, the remaining creep life of T22 was calculated after 50000 hours service for the same mid-wall temperatures as seen Figure 5.22.

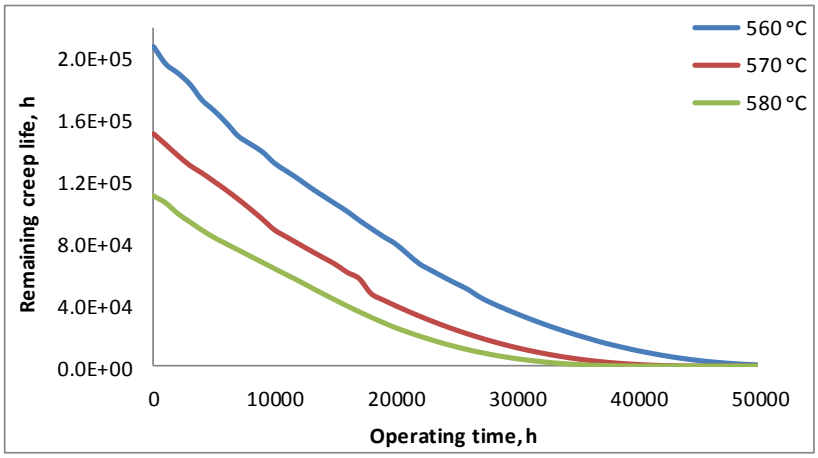

Figure 5.22 Remaining creep life of T22 at initial mid-wall metal temperatures of 560, 570, and 580^{0}C and at constant hoop stresses of 45MPa when burning Daw Mill coal (100% wt 0.2% Cl) versus operating time

The remaining service lives of T22 decreased steadily during operation with increasing mid-wall metal temperatures and decreasing wall thickness. The residual life of the tube were, for example, 7.17E+02 hours after 50000 hours service for mid-wall metal temperature of 560°C while the superhetaer tube had failed after 46000 hours operation at initial mid-wall metal temperature of 570°C and after 41000 hours service at initial mid-wall metal temperature of 580°C as shown in Figure 5.22.

5.6.3 Implication of fireside corrosion and steamside oxidation

During boiler operation, fireside corrosion and steamside oxidation continuously reduce the wall thickness of tubing and raise the hoop stress and the corresponding creep rate. This leads to a creep life reduction of boiler tubing. The following sensitivity analysis evaluates the effects of fireside corrosion and steam side oxidation as well as creep damage on the creep life of superheater and reheater tubing. The remaining service life of tubing at initial hoop stress of 45MPa and at initial mid-wall metal temperature of

580^{0}C and flue gas temperature of 1150^{0}C were calculated for 50000 hours service in the following conditions:

- No metal losses (fireside corrosion and steamside oxidation and creep damage) and the same mid-wall metal temperatures
- Metal losses (fireside corrosion and steamside oxidation and creep damage) and the same mid-wall temperatures
- No fireside corrosion and increasing temperature
- Metal losses (fireside corrosion and steamside oxidation and creep damage) and increasing mid-wall temperatures

The fuel applied for this sensitivity analysis was Daw Mill coal (100% wt, 0.2% Cl). The results are summarised in Figure 5.23.

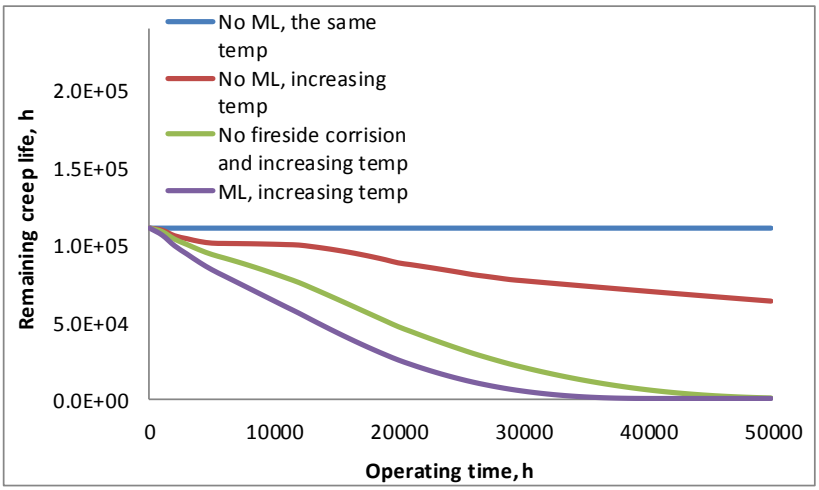

Figure 5.23 The impact of fireside corrosion, steamside oxidation and mid-wall metal temperature on remaining service life of T22 at initial stress of 45MPa and at initial mid-wall metal temperature of 580°C

In the absence of fireside corrosion, steamside oxidation and creep damage as well as constant mid-wall metal temperature the life of tubing predicted stayed constant (1.11E+05 hours) during operation as shown in Figure 5.23. However, the life of tubing decreased from 1.11E+05 hours at the start of boiler operation to 6.32E+04 hours after 50000 hour operation in the absence of the metal losses and increasing mid-wall metal

temperatures (see Figure 5.23) because of an increasing creep rate of the tube metal. In addition, the life of the tube declined to 3.38E+02 hours after 50000 hours operation in in the absence fireside corrosion (and in the presence of steamside oxidation) and increasing mid-wall metal temperatures due to an increasing creep rate of the tube metal and the steam side metal losses. Finally, the remaining creep life of the superheater tube was 8.56E+00 hours after 40000 hours service after which the tube failed in the vicinity of the metal losses and increasing mid-wall metal temperatures.

5.6.4 Different hoop stress formula

5.6.4.1 Introduction

In pressurized cylinders hoop stress is the principal stress in a tubular cross section. A boiler tube fails when the hoop stress, as result of the internal steam pressure, equals the strength of the tube material [20]. Thus, to predict the remaining service life of superheater/reheater tubes the magnitude of hoop stress acting on the wall of tubes is required. Three equations may be used for this purpose. One is the equation for thick-walled cylinders (Eq. (2-78)) which is used if W > (r /10). The second and third equations are used for thin-walled tubes W < (r /10) Eq. (2-79) and Eq. (2-81). The issue of selecting the appropriate stress formula to calculate the hoop stress in superheater/reheater tubes can affect the remaining life estimates.

5.6.4.2 Creep life of thick-walled tubes

Each of these three formulas mentioned above was used in this sensitivity analysis to calculate the hoop stress on the tubing wall (T22) at internal steam pressure of 18MPa and at initial mid-wall metal temperatures of 580^0C. Material specifications, dimension of superheater tube, operating conditions and creep parameters used in the creep model calculations are summarised in Table 4-11. The fuel used was Daw Mill coal (100%wt 0.2% Cl). The results are shown in Figure 5.24:

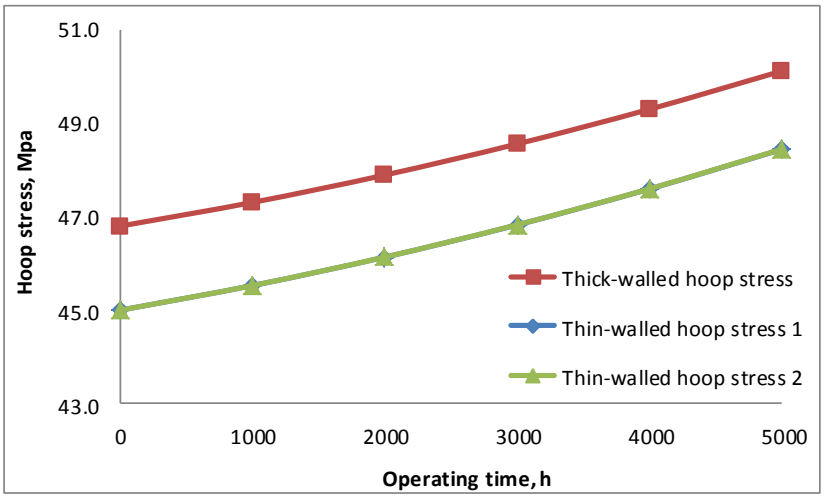

Figure 5.24 Hoop stress acting on a thick-walled tube (T22) based on different stress formulas versus operating time at initial mid-wall metal temperatures of 580^{0}C

The tube used for this analysis was a thick-walled tube (see Table 4-11). Generally, the hoop stress deriving from thick-walled hoop stress formula (Eq. (2-78)) was higher than those deriving from thin-walled hoop stress equation Eq. (2-79) and Eq. (2-81). The thick-walled hoop stress was ≈ 47MPa at the start of boiler operation and increased to 50MPa after 5000 hours operation. On the other hand, the thin-walled hoop stress model predicted that the hoop stress was 45MPa at zero operating time and became 48MPa after 5000 hours. These values of hoop stresses affected the remaining service life T22 as shown in Figure 5.25.

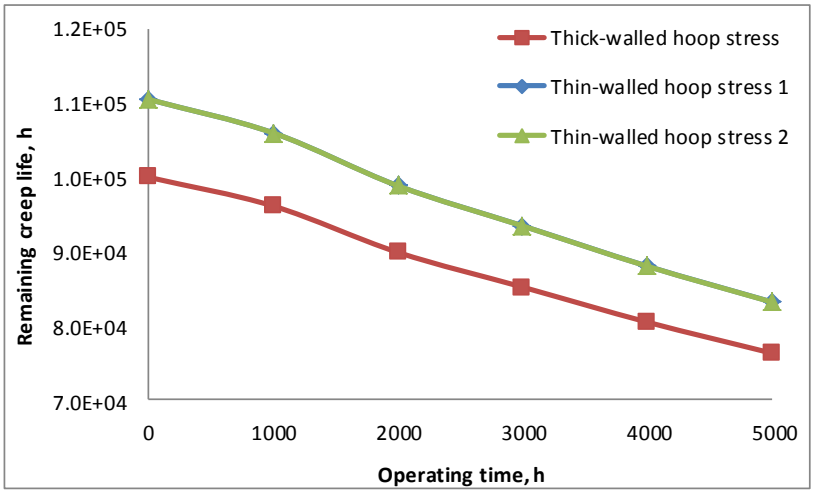

Figure 5.25 Creep life of a thick-walled tube (T22) based on different stress formulas versus operating time at initial mid-wall metal temperatures of 580^{0}C

The creep life predicted by the thin-wall hoop stress formulas Eq. (2-79) and Eq. (2-81) were obviously larger than those predicted by the thick-walled hoop stress formulas. For example creep life of T22 (W_{th} = 7.5mm and OD = 45mm) obtained from the thin-wall hoop stress formulas was 1.11E+05 hours whereas the one calculated by the thick-walled hoop stress formula Eq. (2-78) was 1.00E+05 hours as a result of higher hoop stresses deriving from the thick-walled hoop stress formula than the ones calculated by the thin-wall hoop stress formulas. There was a 4% difference between predicted and the C.E.R.L data for the remaining service life of T22 when using the thick-walled hoop stress formula (Eq. (2-78)) in the integrated model whereas there a was 1.4% difference between predicted and the C.E.R.L data for the remaining service life of the tube when applying the thin-walled hoop stress formulas (Eq. (2-79) and Eq. (2-81)) in the integrated model.

The thin-walled hoop stress formulas Eq. (2-79) and Eq. (2-81) are the most convenient equations for most boiler tube applications involving failure analysis and are sufficiently accurate for all stress calculations. Generally, there was a 10% difference between lifetime predictions when using the thin-walled and thick-walled hoop stress formulas. They both derive from Eq. (2-80) (which is why they produced identical values for hoop stress) in which the mean diameter can include either outer diameter or inner radius of the tube in hoop stress equation. Finally, Eq. (2-79) was used in the model.

Furthermore, a sensitivity analysis were performed to assess the implications of fireside, steamside metal losses, and creep damage as well as tube surface temperatures (inner and outer surfaces) on hoop stress after 50000 hours service (see Figure 5.26). The hoop stress acting on the tubing wall was evaluated in the following conditions:

- No metal losses (fireside corrosion and steamside oxidation and creep damage) and the same tube surface temperatures
- Metal losses (fireside corrosion and steamside oxidation and creep damage) and the same tube surface temperatures
- Metal losses (fireside corrosion and steamside oxidation and creep damage) and increasing tube surface temperatures

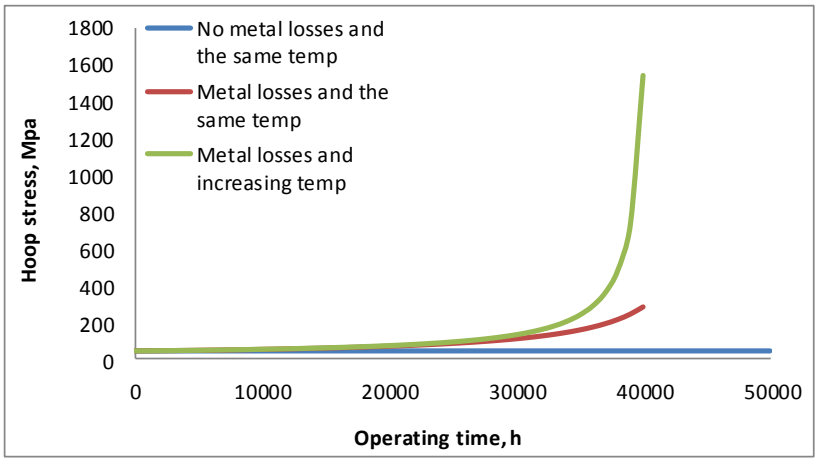

Figure 5.26 Hoop stress of a thick-walled tube (T22) in the presence and the absence of metal losses as well as constant and increasing tube surface temperatures versus operating time

Model predicted that the hoop stress stayed constant (45MPa) in the absence of fireside corrosion damage, steamside oxidation and metal losses due to creep during operation (50000 hours) as seen in Figure 5.26. However, in the presence of the metal losses (fireside corrosion damage, steamside oxidation and creep damage) and when the tube surface temperatures were constant the hoop stress increased from 45MPa at the start of boiler operation to 284MPa after 40000 hours service. This process became even more severe when surface temperatures were increasing in the presence of the metal losses, causing hoop stress to increase from 45MPa at the start of boiler operation to 1542MPa after 40000 hours service. In this situation the tube mid-wall metal temperature increased from 580°C at the beginning of boiler service up to almost 595°C at the end of 40000 hours service.

5.6.4.3 Creep life of thin-walled tubes

The tube used for this analysis was a thin-walled tube; $W_{th} < (Do/20)$. Material specifications, dimension of superheater tube, operating conditions and creep parameters used in the creep model calculations are summarised in Table 5-3.

Table 5-3 Material specifications, dimension of superheater tube, operating conditions and creep parameters used in the creep model calculations

Material	T22 (Fe-2.25Cr-1Mo, wt%)
Superheated steam temperature	540^0C
Superheated steam pressure	18MPa
Outer tube diameter	92.25mm
Tube wall thickness	4.5mm
k_{cr}	7191.18 $(MPa)^{-n}/h$
n	3.3
Q_{cr}/R	30190(1/K)
C	2.3
m	0.772

As for the thick-walled tubes, Eq. (2-78), Eq. (2-79) and Eq. (2-81) were used in this sensitivity analysis to calculate the hoop stress on the thin-walled tube (T22) at internal steam pressure of 18MPa and at initial mid-wall metal temperatures of 580^0C when burning Daw Mill coal (100% wt). The results are shown in Figure 5.27:

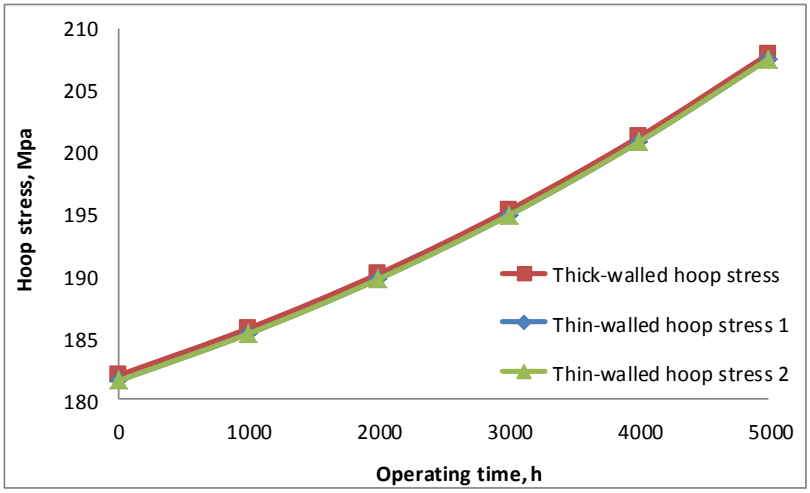

Figure 5.27 Hoop stress acting on a thin-walled tube (T22) based on different stress formulas versus operating time at initial mid-wall metal temperatures of 580^0C

Generally, the hoop stresses deriving from thick-walled hoop stress formula (Eq. (2-78)) as well as those deriving from thin-walled hoop stress Eq. (2-79) and Eq. (2-81) overlapped each other as seen in Figure 5.27. The three hoop stress models predicted the hoop stress of 181MPa at the start of boiler operation and 207MPa after 5000 hour operation for the thin-walled tube with dimensions mentioned in Table 5-3. The levels

of stress acting on boiler wall tubing were significantly higher compared with those for the thick-walled tube (W_{th} = 7.5mm and OD = 45mm) due to the much lower wall thickness and much bigger outer diameter of the thin-walled tube than thick-walled one at the same internal steam pressure (18MPa).

In addition, Viswanathan et al [20] report that how hoop stress to steam pressure ratio varies with outer-to-inner radius or wall thickness to outer radius ratios. As outer-to-inner radius or wall thickness to outer radius ratios become small, the magnitude of the stress as obtained by different formulas approach each other whereas at large values of those ratios the hoop stresses became appreciably different [20]. The same trend was observed in in this research (the model predictions) where the hoop stresses calculated by different formulas (Eq. (2-78)) and Eq. (2-79) were 47 and 45MPa respectively when the wall thickness was 7.5mm whereas the hoop stress obtained by either formulas (Eq. (2-78)) and Eq. (2-79) were 181MPa for the wall thickness of 4.5mm.

The increase in the levels of hoop stress led to an increase in creep rate and therefore to a significant reduction in the remaining service life of T22 as shown in Figure 5.28.

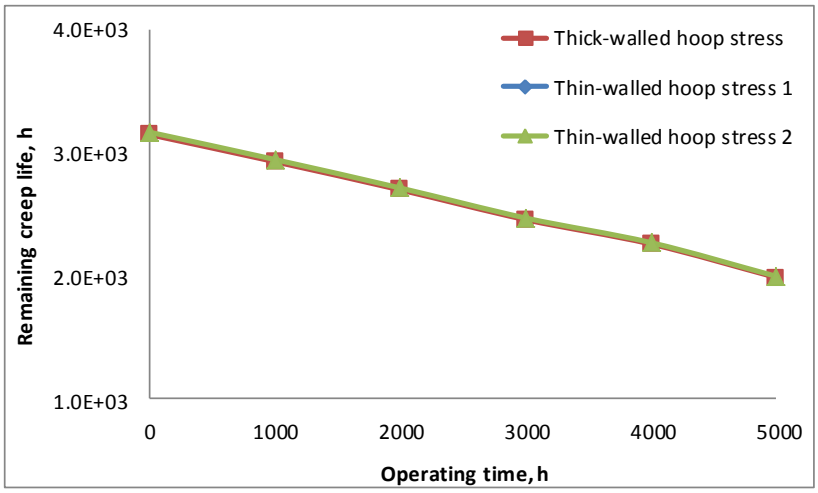

Figure 5.28 Creep life of a thin-walled tube (T22) based on different stress formulas versus operating time at initial mid-wall metal temperatures of 580^{0}C

According to the model predictions using these options, the remaining service life of T22 decreased from 3.17E+03 hours at the start of boiler operation to 2.00E+03 hours at the end of 5000 hours service. There was a poor agreement between model predictions for the superheater tube dimensions mentioned in Table 5-3 and C.E.R.L data.

5.6.5 Hoop stress variation

The hoop stress acts on the circumferential direction of superheater and reheater tubing. This stress may increase due to the following reasons:

- Effective loss in wall thickness
- Internal steam pressure increase

An increase in hoop stress is inevitable when the wall of the tube gets thinned continuously during operation by fireside corrosion and steamside oxidation. Furthermore, fluctuations in internal steam pressure may result in an increase in hoop stress. Therefore, a sensitivity analysis was performed to evaluate the influence of hoop stress increase (as a result of variations in internal steam pressure) on the remaining service life of superheater/reheater tubes at constant metal temperature of 580^0C and when burning Daw Mill coal (100% wt 0.2% Cl). The tube used for this analysis was a thick-walled tube (see Table 4-11). The initial hoop stresses chosen for the sensitivity analysis were 45, 46 and 47MPa. Figure 5.29 shows the results of the sensitivity analysis run.

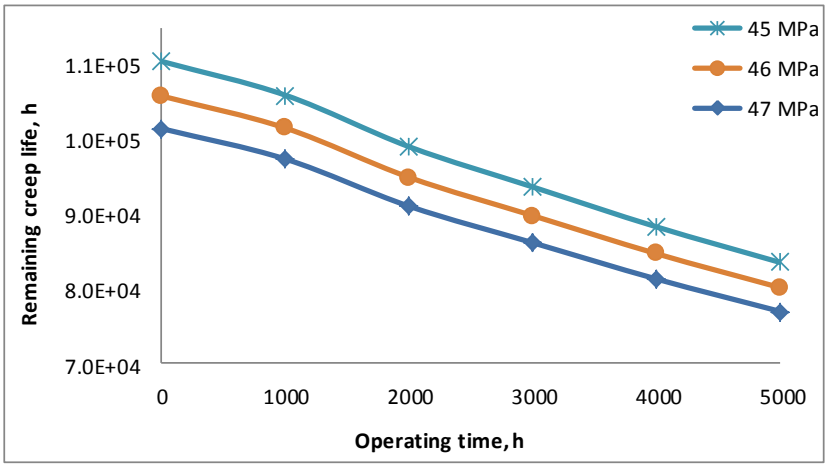

Figure 5.29 Remaining creep life of T22 versus operating time at initial hoop stresses of 45, 46 and 47MPa and at constant mid-wall metal temperatures of 580^0C

An increase in hoop stress led to creep rate rise and corresponding decrease in the remaining service life of superheater/reheater tubes as seen Figure 5.29. At the beginning of boiler service and at initial hoop stress of 45, 46 and 47MPa, the residual life of T22 predicted were 1.11E+05, 1.06E+05 and 1.01E+05 hours respectively.

There were 1.4, 3.7 and 4% differences between predicted and the C.E.R.L data for the remaining service life of T22 when the hoop stresses were 45, 46 and 47MPa respectively. The creep life were decreased from 8.36E+04 hours to 8.02E+04 hours and, 7.70E+04 hours at hoop stresses of 45, 46 and 47MPa, respectively, at the end of 5000 hours operation. In this condition the internal steam pressures were 18, 18.4 and 18.8MPa for the hoop stresses of 45, 46 and 47MPa respectively.

Moreover, the life of the tube were calculated for 50000 hours at initial hoop stresses of 45, 46 and 47MPa and at constant mid-wall metal temperatures of 580^0C (see Figure 5.30).

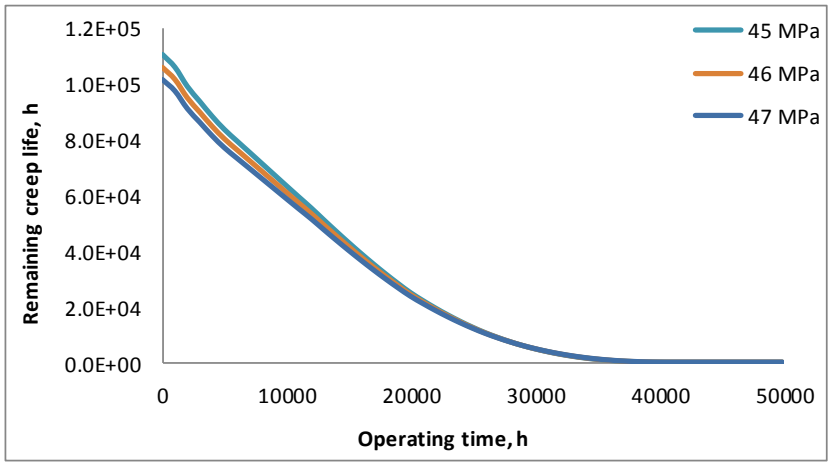

Figure 5.30 Remaining creep life of T22 versus operating time at initial hoop stresses of 45, 46 and 47MPa and at constant mid-wall metal temperatures of 580^0C

The remaining service life of T22 decreased steadily during operation due mid-wall metal temperatures and to the increasing hoop stresses resulted from the decreasing wall thickness as well as increasing tube inner surface temperatures. For instance, the life of the tube decreased to 1.64E+00 hours when the initial hoop stress was 47MPa as shown in Figure 5.30.

Moreover, the steady state creep rates, time to rupture of T22 steel were measured in air at various engineering stresses between 500 to 600°C as seen by Ray et al [107]. The creep life of the tube (T22) decreased with increasing hoop stress acting on the tubing wall at any constant tube metal temperature. For instance, the creep life of the tube, at constant temperature of 600°C, decreased from 7.34E+08 hours to 1.20E+04 hours at

hoop stress of 20MPa and 220MPa respectively. The same trend was observed for other constant temperatures of 500 and 550°C where the stress was increasing [107].

5.6.6 Remaining service life of different alloys

The creep resistance and resistance to fireside corrosion of materials normally used for superheater and reheaters in coal/ biomass fired boilers improve in this order: 1Cr-0.5Mo, 2.25Cr-1Mo, 9Cr-0.5Mo, 12Cr-1Mo and austenitic steels. Molybdenum improves the creep resistance and chromium enhances the corrosion resistance, and has some beneficial effects on creep resistance too. In coal/biomass fired power plants, low alloy ferritic steels have limited resistance against fireside corrosion and steamside oxidation when steam temperature is raised above 600°C mostly as a result of their insufficient chromium content while high alloy ferritic steels possess better corrosion resistance due to high chromium content [21; 65].

Therefore, a sensitivity analysis was performed to assess the remaining service life of T22 (Fe-2.25Cr-1Mo wt%) and P92 (9Cr-0.5Mo, wt%) under the same operational conditions and tube dimensions as Table 4.8. Material specifications, dimension of P92, operating conditions and creep parameters [109] of P92 used in the creep model calculations are listed in Table 5-4.

Table 5-4 Material specifications, dimension of P92 and operating conditions and creep parameters of P92

Material	P92 (9Cr-0.5Mo, wt%)
Superheated steam temperature	540°C
Mid-wall metal temperature	580°C
Superheated steam pressure	18MPa
Outer tube diameter	45mm
Tube wall thickness	7.5mm
C (a Monkman-Grant constant)	0.254
m (a Monkman-Grant constant)	0.825
k_{cr}	3.16E-22 $(MPa)^{-n}/h$
n (stress exponent)	8.64

Furthermore, the oxidation parameters of high alloy ferritic steels (9Cr) are [106]: A=3.97E+11(μm)^2/h and *Q*=197 kJ/mole.

The model predations are presented in Figure 5.31.

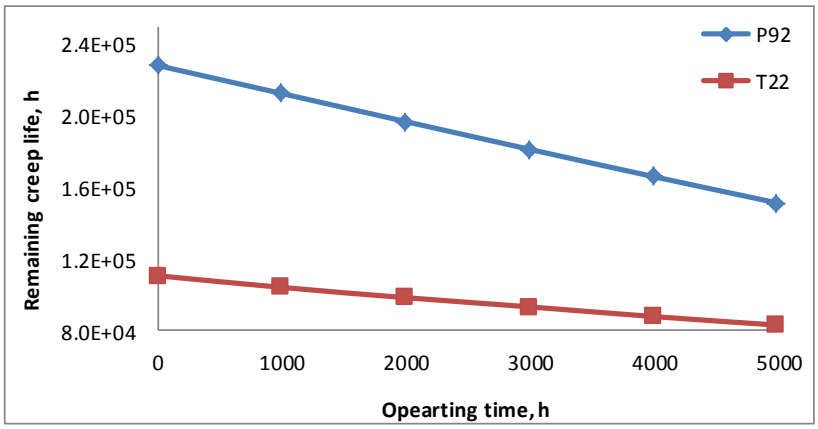

Figure 5.31 Remaining creep life of T22 and P92 at mid-wall metal temperature of 580^{0}C and at hoop stresses of 45MPa versus operating time

The remaining service lives of P92 predicted by the model were considerably larger than that T22 for two reasons:

1. The metal loss of P92 due to steamside oxidation was almost half of that T22 (see Appendix E) because of higher chromium content and thus higher resistance of P92 against oxidation.

2. The secondary creep rate of P92 was also lower than that T22 (see Appendix E) mostly because of higher creep resistance of P92 than T22.

The model revealed that, under identical operational conditions and tube dimensions, the remaining creep life of the tube was 2.28E+05 hours at beginning of the exposure. The creep life of P92 (9Cr) at 45MPa and at 580^{0}C (mid-wall temperature) was 2.30E+05 hours as reported in C.E.R.L data [21] (see Figure 5.32).The creep life of P92 then decreased from 2.28E+05 hours at start of boiler operation to 1.51E+05 hours at the end of 5000 hours operation as seen in Figure 5.32. The remaining lives of T22, however, were half that P92. At the same operating time, for example, the life of T22 declined from 1.11E+05 hours at start of boiler operation to 8.29E+04 hours.

In addition, the creep life of P92 were calculated using creep constants listed in Table 5-4 for 50000 hours operation and compared with the creep life of T22 as shown in Figure 5.32.

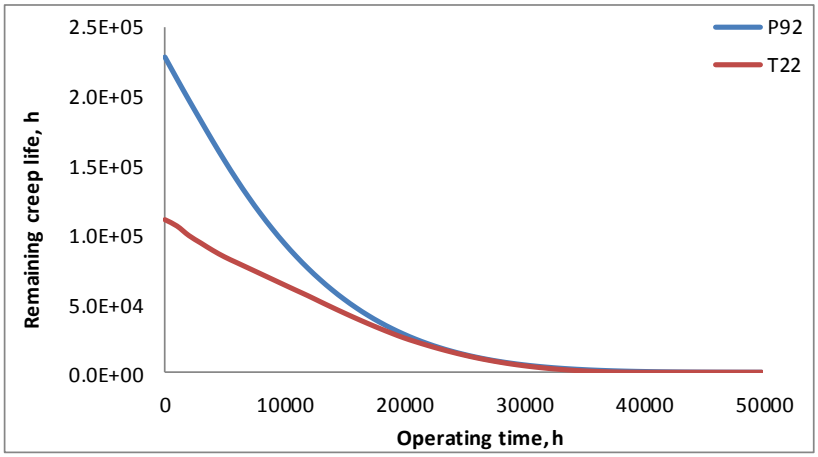

Figure 5.32 Remaining creep life of T22 and P92 at mid-wall metal temperature of 580^{0}C and at hoop stresses of 45MPa versus operating time

The creep life of the T22 and P92 decreased steadily during operation as shown in Figure 5.32. The remaining creep life of P92 was 1.55E+01 hours at the end of 50000 hours operation whereas T22 had failed after 40000 hours service mostly because of their limited resistance against fireside corrosion and steamside oxidation. **Figure 5.33** shows the stress rupture data of 9%Cr steel for metal temperatures between 500 and 650°C and hoop stress between 20 and 300MPa [21].

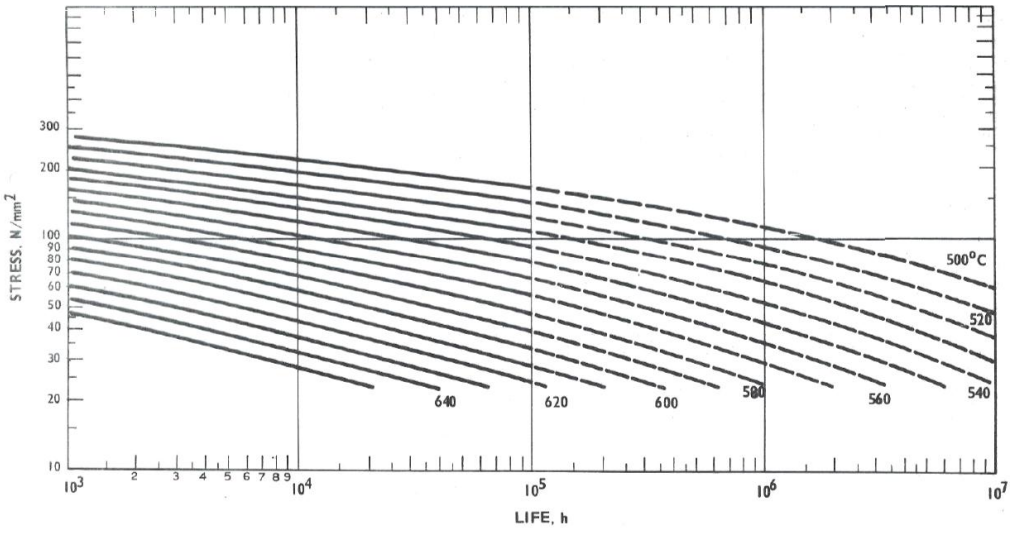

Figure 5.33 Stress rupture properties of 9%Cr steel (P92) [21]

Furthermore, the rupture lifetime of 9Cr-1Mo steel was obtained at temperatures of 550, 600 and 650°C in a creep test as reported by Anderson et al [110]. The creep life of the tube (9Cr-1Mo) decreased with increasing hoop stress acting on the tubing wall at any constant tube metal temperature. For instance, the creep life of the tube, at constant temperature of 550°C, decreased from 2.10E+03 hours to 9.60E+01 hours at hoop stress of 220MPa and 240MPa respectively. The same trend was observed for other constant temperatures of 600 and 650°C where the stress was increasing [110]. Operating at a higher stress (220MPa) resulted in a smaller remaining service life of 9Cr-1Mo compared to P92 (9Cr-0.5Mo, wt%) steel operating at initial hoop stress of 45MPa.

5.6.7 Remaining service life prediction using Larson-Miller parameters

The Larson-miller parameters (Eq. (2-88)) was also used to predict the rupture life time of superheater and reheater tubes at initial mid-wall metal temperature of 580^0C and at initial hoop stresses of 45MPa. Using C =20, the Larson-Miller parameters predicted that the remaining life of T22 was 2.57E+15 hours at the beginning of the operation which is not a reasonable values for lifetime a superheater tube operating in a severe high temperature environment. However, when C= 30.4 was used in the Larson-Miller parameters, the rupture lifetime of the tube predicted was 1.02E+05 hours at the beginning of boiler operation (see-Figure 5.32). The life of the tube predicted decreased to 5.97E+04 hours after 5000 hours service. These results were compared with results predicted by Monkman-Grant relationship (Eq. (2-86)) as seen in Figure 5.34. In addition, the rupture lifetime of the tube predicted by Monkman-Grant relationship was 1.11E+05 hours at the beginning of boiler operation and the decreased to 8.36E+04 hours after 5000 hours service.

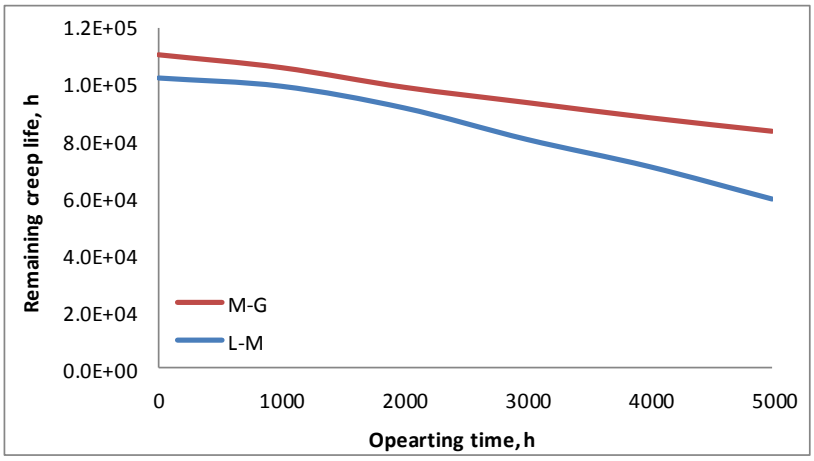

Figure 5.34 Remaining creep life of T22 at mid-wall metal temperature of 580^{0}C and at hoop stresses of 45MPa versus operating time

In addition, the creep life for superheater tubes (1.25Cr-0.5Mo) operating at 480°C and internal steam pressure of 5MPa was estimated using Monkman-Grant relationship and Larson-Miller parameters as reported by Vakili-Tahami et al [111]. The creep life of the tube obtained by Monkman-Grant relationship and Larson-Miller parameters were 4.17E+09 and 1.72E+10 hours respectively [111]. The rupture lifetime of 1.25Cr-0.5Mo materials as reported by Vakili-Tahami et al [111] was much bigger than the creep life of 2.25Cr-1Mo materials (1.11E+05 hours) despite having lower corrosion resistance and creep resistance than 2.25Cr-1Mo steel. This is because they were operating at a lower operating temperature and a lower steam pressure (5MPa, 480°C) compared to the operating conditions of 2.25Cr-1Mo materials (18MPa, 580°C).

Larsen–Miller parameter was also utilized to determine the rupture time of Inconel® 800 (21Cr) as reported by Ahmad et al [112]. The operating hoop stress for the average internal pressure of 13.8MPa was 51.04MPa. The estimated hoop stress developed in the tube was determined using Eq. (2-21) [112]. The estimated rupture lifetime calculated was more than 40 years (384,635 hours) at temperature of 650°C or below and at the Larson-Miller parameter of 19000. The rupture life time of the tube decreased from 384,635 hours to 36 hours at the tube metal temperatures of 650 and 875°C respectively [112]. Creep rupture was the cause of failure of the superheater tube. Inconel® 800 (21Cr) material possess a high corrosion resistance which is why its

remaining service life is much bigger than T22 (2.25Cr-1Mo) steel despite operating at a higher metal temperature.

5.7 General discussion

According to the above sensitivity analysis, the mid-wall temperature of superheater and reheater tubes was found to be the most important factor affecting the remaining service life of T22 boiler tubing. Every 10°C increase in tube metal temperature gave a considerable decrease in life time of the tubing (e.g. Figure 5.22). For example, the creep life of boiler tubing decreased from 1.51E+05 hours at 570°C to 1.11E+05 hours at 580°C.

Tubing wall thickness and outer diameter were another critical input in the model. Significant differences were observed between the residual life of thin-walled and thick-walled tubes, according to Figure 5.26 and Figure 5.28. In the case of thin-walled tubes, the hoop stress on the tubing wall increased dramatically and thus caused considerable reduction on the creep life superheater tube.

Superheater and reheater tubes fabricated by different materials (e.g. low alloys ferritic and high alloy ferritic steels) displayed different remaining service life in the same operational conditions as seen in Figure 5.32

Furthermore, the implication of hoop stress which is directly proportional to internal steam pressure, fireside corrosion and steamside oxidation on the creep life the tubing was found to be important. Generally, there was a 10% difference between lifetime predictions when using the thin-walled and thick-walled hoop stress formulas. The thin-walled hoop stress formula is one the most convenient equations for most boiler- tube applications involving failure analysis and is sufficiently accurate for all stress calculations.

In combustion model (reaction kinetics), finding the mineral matter composition of different fuels (coal/biomass), kinetic constants of mineral matter transformation, kinetic constants of coal devolatilisation, volatiles combustion and char combustion can be challenging whereas in the case of the simplified model, the ultimate analysis and ashed composition of fuels are available in literature almost for every biomass and coal fuels. It was, thus, more convenient to use the simplified combustion model to obtain

the quantity of flue gas emissions and fly ashes especially when burning pure biomass fuels and coal/biomass blends.

Tomeczek et al [43] was finally used in the model to calculate the condensation fluxes of alkali salts in the tube surfaces. The main reason for this decision was the availability of the constants required to obtain the saturation pressure of the condensing vapours. The saturation pressure model, Eq. (2-21), relates the deposit/tube surface temperatures to the deposition fluxes of alkali salts in Eq. (2-19). The saturation pressures of vapours were reasonably stable up to 900°C and increased dramatically from 1000 to 1100°C as shown in Figure 5.4. This leads to a decrease in deposition fluxes of alkali salts (see Figure 5.5). Therefore, the decrease in deposition fluxes of elements was negligible up to 900°C. Subsequently, the deposition fluxes went down dramatically, particularly in the case of potassium. The deposition fluxes of potassium decreased by 3.4% at 900°C and then declined by 87% at 1000°C. The same trends were repeated for the deposition fluxes of sodium and sulphur.

Moreover, Zhou et al [42] models were used to calculate the deposition fluxes of fly ashes (due to inertial and eddy impaction) mostly because this model can calculate the deposition fluxes on upstream and on downstream side of the boiler tubing based on the particle sizes and flue gas physical properties. The fraction of fly ashes impacted on the superheater tube surfaces and the fraction of the impacted ashes captured on the tube surfaces are found to be very critical (see Figure 5.2). The model predicted that the mass fluxes of elements in deposits increased with stickness efficiency by 240% as shown in Figure 5.2. For example, the mass fluxes of *Al* increased from 1.5mg/cm^2/h for 40 % capture efficiency to 5mg/cm^2/h for 70% capture efficiency.

Simms et al [1] model were used to obtain the fireside corrosion rate of superheater tubes. This model includes SO_x concentration deriving from flue gas, deposition fluxes of alkali vapours, tube material and tube surface temperature. Other fireside corrosion models lack such comprehensiveness. The superheater tube surfaces temperature was found to be one of the most significant factor for obtaining the fireside corrosion rate of a particular tube material (see section 5.3.2). The fireside corrosion damage was found to have significant effects on the remaining service life of superheater/reheater tubes as shown in Figure 5.13.

Parabolic rate law equation [106] was used to evaluate the steamside oxidation of superheater tube since most engineering alloys follow a parabolic law. Oxidation parameters of different tube materials and tube inner surface temperature are found to be the dominant factors in steamside oxidation model (see section 5.4).

Since creep is a thermally activated process as an Arrhenius-type expression was used in the model to include the activation energy in the secondary creep rate calculation. The creep constants, hoop stress and mid-wall metal temperatures are the determining parameters in secondary creep rate of superheater tube metal as shown in section 4.6.

Finally, for the remaining life prediction, the Larson–Miller or Orr–Sherby–Dorn parameters can predict the failure time based on the testing temperature and stress. However, because plots of stress vs Larson–Miller or Orr–Sherby–Dorn parameter often exhibit a pronounced curvature, these methods can be used reliably for extrapolation of failure time only over a limited range of stress and temperature [83] whereas in the Monkman–Grant relationship, once the constants C and m as well as the secondary creep rate have been known for a given material, Eq. (2-86) can be used to calculate the time to rupture of boiler tubing. Furthermore, for the constsnt C = 20, the Larson–Miller parameter did not procude reasonable lifetime values while for C = 30.4 it produced results close to results predicted by Monkman-Grant relationship as seen in Figure 5.34.

5.8 Contribution to knowledge

- Static model: a simplified model was developed from the fuel and air composition to calculate the mole percentages of flue gases and mass concentration of fly ashes. The composition(s) of the fuel(s) in terms of their major elements (ultimate analysis) on as-received basis and air composition were used to obtain mole percentage of the flue gases. Moreover, the mass concentration of fly ashes and mole fraction of vapours released during fuel combustion were calculated through the fuel ash compositions.
- Dynamic model: models of volatiles formation, volatiles oxidation, mineral matter decomposition and char combustion from different sources were combined together to calculate the mole percentages of flue gases and mass concentration of fly ashes. In addition, kinetic data of coal devolatilisation, kinetic constant of volatiles combustion and kinetic constants of char oxidation

from diffeerent sources were used to claculate the mole percentages of flue gases. Finally, using the fuel (Daw Mill, El-Cerrejon) mineral matter composition and the kinetic constants for mineral matter decomposition, the amount of ash species produced during coal burning was calculted in inert and oxidising atmospheres.

- Models of vapour condensation and ash impaction from different sources were combined together in order to obtain total deposition fluxes on the tube surfaces. The ash impaction on the upstream side is a major contributor to ash deposition on superheater/reheater tubes. The magnitude of the deposition rate caused by condensation is much smaller than the ash impaction. The amount of ash deposited via themophoresis is even smaller than that deposited via condensation. Finally, the contributions by the Brownian and eddy diffusions are negligible.

- The five groups of the models for combustion, deposition, fireside corrosion, steam-side oxidation, and creep have been integrated and validated (alongside heat transfer) in order to calculated the remaining service life of boiler tubing.

- The remaining service life of superheater/reheater tube were assessed based on:

    - Different fuels burnt: the composition of the deposits formed on the boiler tubes depends on the type and nature of the fuel and the conditions of combustion. These deposits consist of sulphur, sodium, potassium and chlorine which are known to influence fireside corrosion in conventional power plants and eventually to affect the creep life of the tubes. Different fuels contain different amount of sulphur, sodium, potassium and chlorine.

    - Different operating conditions (internal steam pressure, steam and flue gas temperatures): the rates of fireside corrosion and steamside oxidation of the tube materials are very sensitive to their metal temperatures. The fireside corrosion rate as well as steam oxidation rate increases with the tube surface temperature. The flue gas temperature local to the corroding metal surface also matters; the higher the gas temperatures the greater the

rate of fireside corrosion and steamside oxidation which may be expected. Furthermore, fluctuations in internal steam pressure may result in an increase in hoop stress. An increase in hoop stress leads to an increase in creep rate and corresponding decrease in the remaining service life of superheater/reheater tubes.

- Different steamside oxidation parameters: Besides temperature, steamside oxidation reaction rate is a function of oxidation parameters too. Obviously, different oxidation parameters results in different amounts of steamside oxide thickness and different amount of steamside wall losses of the tube at a constant temperature.

- Different creep constants: Moreover, secondary creep rate is a function of creep parameters as well as tube mid-wall temperature. Therefore, different creep constants will produce different secondary creep rate for tube metal and different corresponding remaining service life for superheater tubes.

- Different tube materials (T22, T92): the model revealed that, under identical operational conditions and tube dimensions, the remaining life of T22 (2.25Cr-1Mo wt%) were half of that P92 (9Cr-0.5Mo wt%). Molybdenum improves the creep resistance and chromium enhances the corrosion resistance, and has some beneficial effects on creep resistance too.

- Different creep and rupture lifetime models: the Larson-miller parameters was used to predict the rupture life time of superheater/reheater tubes. These results were compared with results predicted by Monkman-Grant relationship.

6 CONCLUSIONS AND FUTURE WORK

6.1 Conclusions

The five processes of combustion, deposition, fireside corrosion, steam-side oxidation, and creep have been integrated (alongside heat transfer) to investigate the remaining service life of superheater and reheater tubes in coal/ biomass fired power plants. Three frameworks have been developed by analysing those models used in depicting the five processes: one is conceptual and the other two are mathematical model based. Finally, the outputs of the integrated mathematical models were compared with the laboratory generated data from Cranfield University as well as historical data from Central Electricity Research Laboratories (C.E.R.L).

The most significant conclusions derived from this work are presented below:

- Fuel combustion: the mole percentage of flue gases and mass concentration of fly ashes and vapours produced during combustion of coal (El-Cerrejon and Daw Mill) and biomass (CCP and Miscanthus) were predicted in two ways:
    - A simplified model of fuel combustion in which the composition of the fuel(s) in terms of their major elements (*C, H, O, N, S, Cl*) on as-received basis (wt%) and air composition (O_2, Ar, N_2wt%) were used to obtain mole percentage of the flue gases (H_2O, CO_2, O_2, Ar, N_2, NO, SO_2, HCl). Moreover, the mass concentration of fly ashes and mole fraction of vapours were calculated using the ashed composition of the fuel.
    - Kinetic data for coal and/or biomass devolatilisation, volatiles combustion and the remaining char combustion were used to calculate the mole percentages of flue gas emissions. Furthermore, the kinetic data of mineral matter decomposition were used to quantify the mass loss of the minerals as well as the amount of ashes produced in slow and rapid heating conditions.
    - The results were then compared to measurements obtained from the experiments carried out at Cranfield University. Generally, the simplified models predcitions for CO_2, H_2O and O_2 were closer to the experimental

data. For example ther were 4 and 32% differences between predicted and expermental values for the mode perntage of CO_2 and O_2.The concentration of CO predicted by the simplified model agreed with the experiments for pure Miscanthus and fuel blends. The kinetic model's predictions for CO were close to the experimental data for pure Daw Mill coal. The models predictions for SO_2 concentration were in poor agreements with experimental data except for the pure El-Cerrejon. In addition, the models' predictions for HCl concentration were in poor agreements with experimental data except for Miscanthus:Daw Mill (20:80% wt). The model's predcition can be improved by using different kinetic data for fuel devolatilisation, and volatiles combustion.

  - In reaction kinetics model, finding the mineral matter composition of different fuels (coal/biomass), kinetic constants of mineral matter transformation, kinetic constants of coal devolatilisation, volatiles combustion and char combustion can be challenging whereas in the case of the simplified model, the ultimate analysis and ashed composition of fuels are available in literature almost for every biomass and coal fuels. It was, thus, more convenient to use the simplified combustion model to obtain the quantity of flue gas emissions and fly ashes.

- Ash/vapour deposition: ash and vapour deposition fluxes on the superheater/reheater surfaces were calculated by the combination effects of ash deposition mechanisms such as vapour condensation and fly ashes impaction (inertial and eddy):

  - The mass fluxes of alkali vapours were calculated by Christensen et al model [7] and were compared to the results obtained from Tomeczek et al model [55]. There was a good agreement between the results predicted by two models mentioned. The condensation model suggested by Tomeczek et al [43] was finally used in the model to obtain alkali vapours condensation fluxes on the tube surfaces. The main reason for this decision was the availability of the constants required to obtain the partial saturation of the condensing vapours. The saturation pressure

model relates the deposit/tube surface temperatures to the deposition fluxes of alkali salts in Tomeczek et al. The saturation pressures of vapours were reasonably stable up to 900°C and increased dramatically from 1000 to 1100°C. This led to a decrease in deposition fluxes of alkali salts. Therefore, the decrease in deposition fluxes of elements was very negligible up to 900°C. Subsequently, the deposition fluxes went down dramatically, particularly in the case of potassium. The deposition fluxes of potassium decreased by 3.4% at 900°C and then declined by 87% at 1000°C. The same trends were repeated for the deposition fluxes of sodium and sulphur.

- Furthermore, the deposition fluxes of fly ashes predicted by Tomeczek et al model [55] were compared to those obtained by Zhou et al model [42]. The inertial impaction and eddy impaction models suggested by Zhou et al [42] was used to calculate the ash deposition fluxes of ashes at upstream side (0 to 85°) and downstream side (85 to 180°) of a superheater tube respectively. This is because the model can calculate the deposition fluxes on upstream and on downstream side of the boiler tubing based on the particle sizes and flue gas physical properties. Finally, the model's predictions were compared with lab data generated at Cranfield University. The models predictions were in a good agreement with experimental data. For example, there was 18% difference between model prediction and the experimental data for deposition fluxes of *O* in the case of pure Daw Mill coal. The fraction of fly ashes impacted on the superheater tube surfaces and the fraction of the impacted ashes captured on the tube surfaces are found to be very critical. The model predicted that the mass fluxes of elements in deposits increased with stickness efficiency by 240%. For example, the mass fluxes of *Al* increased from 1.5mg/cm^2/h for 40% capture efficiency to 5mg/cm^2/h for 70% capture efficiency.

- Heat transfer: the heat transfer path around boiler tubing was from the hot combustion gases to the steam flowing inside the superheater/reheater tube. The

heat was transferred from flue gases to the deposit surface by the net radiation and convection which act in parallel in the vicinity of superheater/reheater tubes. Furthermore, heat was conducted through deposit layers and outer oxide scales to the tube metal as well as inner oxide scales. Finally, the inner oxide scales transferred the heat by convection to the steam. The temperature of deposit surfaces, outer tube surfaces, mid-wall metal of tube and inner tube surface were calculated by heat transfer formulas given in literature. It was found that, at the start of boiler operation and when the tube surface was clean, steam temperature was 50°C lower than outer tube surface temperature. The tube surface temperature went up during boiler operation, due to insulating effects of steamside oxide scales, leading to higher rates of fireside corrosion, steamside oxidation and creep.

- Fireside corrosion: Simms et al [1] model were used to obtain the fireside corrosion rate of superheater tubes. This model was a function of tube outer surface temperature, deposition fluxes of alkali salts and SO_X concentration and tube materials (T22, T92 and T347). In addition, local flue gas temperature and fuel composition affected the wastage rate of superheater/reheater tubes. The corrosion rate was very sensitive to tube surface temperature. The corrosion rate of T22 became serious (57nm/h) at metal temperature of 580°C or above and at flue gas temperature of 1150°C when burning Daw Mill coal (100 %, wt) with 0.2% chlorine. This agreed with C.E.R.L data. However, in the case of T92 at the same flue gas temperature and the same fuel, the corrosion rate became serious at metal temperature of 620°C. Furthermore, serious attack occurred on T92 surfaces at metal temperature of 660°C and at flue gas of 1050°C when the fuel was Daw Mill coal (100% wt). The fireside wastage rate of T347 was calculated by PE8 model [64] at flue gas temperature of 1150°C and at metal temperature of at 540, 580, 620, 660, and 700°C when burning Daw Mill coal (100% wt, 0.2% Cl) and then was compared with the results obtained from Simms et al model. The wastage rates were close to each other apart from the ones predicted at 700°C. Both models predictions were lower than the C.E.R.L data due to the possible reasons listed below:

- PE8 model giving the correlation between the chlorine content of UK coals and the rate of fireside corrosion (nm/h) of austenitic stainless steels does not include the deposition fluxes of alkali salts in the model.
- In addition, constants applied for austenitic stainless steels in Simms et al model were different from the ones used for T92.
- Fireside tube metal wastage led to the tubing wall thickness reduction and to an increase in hoop stress acting on the tubing wall. The implication of fireside corrosion damage on the tubing life was found to be significant. The remaining service life of T22 decreased from 10% to 150% of fireside corrosion damage. For instance, the creep life of the superheater tube decreased from 9.42E+04 hours for 10% of fireside corrosion damage to 7.80E+04 hours for 150% of fireside corrosion damage at the end of the 5000 hours service.

- Steamside oxidation: the steamside oxidation of superheater and reheater tubing followed a parabolic rate law. It was a function of tube inner surface temperature and the oxidation parameters. The metal losses of high alloy ferretic steels were almost half of those of low alloy ferritic steels. Similar to fireside corrosion, steamside oxidation is sensitive to tube metal temperature. Generally, for every 10°C increase in metal temperature, the metal loss increased by 20% after 1000 hours boiler operation. There was a 24% difference between steamside metal losses at inner surface temperatures of 555 and 565°C at the end of 5000 hours. The formation of an oxide scale results in an effective loss in wall thickness and so a corresponding increase in hoop stress level. Consequently, the creep rate increases leading to residual life reduction of superheater/reheater tubes and possibly their premature failures. Furthermore, steamside metal loss of T22 varied with oxidation parameters leading to different values for residual life of tubing.

- Creep strain: creep rate of tube metal was a function of hoop stress, mid-wall metal temperature and creep parameters of tube material. Mid-wall metal of supeheater tubing increased during boiler operation. Hoop stress which was a

function of internal steam pressure, outer diameter and wall thickness increased during operation causing an increase in creep rate. Outer tube diameter was reduced due to fireside metal loss. Wall thickness was reduced as a result of fireside and steamside metal loss as well as creep strain.

- Outputs from the combined model:
    - Effects of fireside corrosion, steamside oxidation and creep damage as well as mid-wall metal temperature on superheater/reheater tubing life: In the absence of fireside corrosion, steamside oxidation and creep damage as well as constant mid-wall metal temperature the life of tubing predicted stayed constant (1.11E+05 hours) during operation (after 50000 hours). However, the life of tubing decreased from 1.11E+05 hours at the start of boiler operation to 6.32E+04 hours after 50000 hour operation in the absence of the metal losses and increasing mid-wall metal temperatures because of an increasing creep rate of the tube metal. In addition, the life of the tube declined to 3.38E+02 after 50000 hour operation in the absence of fireside corrosion (and in the presence of steamside oxidation) and increasing mid-wall metal temperatures due to an increasing creep rate of the tube metal and the steam side metal losses. Finally, the remaining creep life of the superheater tube was 8.56E+00 hours after 40000 hours service after which the tube failed in the vicinity of the metal losses and increasing mid-wall metal temperatures.
    - Magnitudes of hoop stress of thick-walled and thin-walled tubes and their effect on residual life of boiler tubing: Hoop stresses predicted by the thick-walled model were higher than the thin-walled ones for a thick-walled tube and overlapped each other in the case of the thin-walled tubes. Consequently, the remaining creep life of thick-walled tubes predicted by thick-walled hoop stress model were smaller than the ones calculated by thin-walled stress formulas. However, for the thin-walled tubes the remaining creep life calculated by both thick-

walled and thin-walled hoop stress models were almost identical to each other.

- Effects of creep parameters on superheater tubing life: Creep rate of T22 varied with different creep parameters leading to different values for residual life of tubing.
- Effects of mid-wall metal temperature on the remaining service life of superheater and reheater tubing: the mid-wall metal temperature of superheater and reheater tubes was found to be the most important factor affecting the remaining service life of boiler tubing. Every 10°C increase in tube metal temperature gave a considerable decrease of 36% in life time of the tubing. The creep life of boiler tubing (T22) decreased from 1.51E+05 hours at 570°C to 1.11E+05 hours at 580°C. There were 0.9, 3 and 20% differences between predicted and the C.E.R.L historical data for remaining service life of superheater tubes at metal temperatures of 580, 570 and 560°C respectively. The remaining service life of T22 decreased steadily during operation with increasing mid-wall metal temperatures and decreasing wall thickness.
- Effects of tube materials on its residual life: The model revealed that, under identical operational conditions and tube dimensions, the creep life of P22 decreased from 2.28E+05 hours at start of boiler operation to 1.51E+05 hours at the end of 5000 hours operation. There was a 0.7% difference between model prediction and the C.E.R.L data. The remaining life of T22, however, was half that P92. The creep life of the T22 and P92 decreased steadily during operation. The remaining creep life of P92 was 1.55E+01 hours at the end of 50000 hours operation whereas T22 had failed after 40000 hours service mostly because of their limited resistance against fireside corrosion and steamside oxidation.

- Remaining creep life of boiler tubing: The Larson-Miller parameters was also used to predict the rupture life time of superheater and reheater tubes at initial mid-wall metal temperature of 580^0C and at initial hoop stresses of 45MPa.

Using C =20, the Larson-Miller parameters predicted that the remaining life of T22 was 2.57E+15 hours at the beginning of the operation which is not a reasonable value for lifetime of a superheater tube operating in a severe high temperature environment. However, when C= 30.4 was used in the Larson-Miller parameters, the rupture lifetime of the tube predicted was 1.02E+05 hours at the beginning of boiler operation. The life of the tube predicted decreased to 5.97E+04 hours after 5000 hours service. These results were compared with results predicted by Monkman-Grant relationship. Monkman-Grant relationship is a function of secondary creep rate and tube material constants. The rupture lifetime of the tube predicted by Monkman-Grant relationship was 1.11E+05 hours at the beginning of boiler operation and the decreased to 8.36E+04 hours after 5000 hours service.

6.2 Suggestions for further work

- The development of a model to predict mole percentage of gaseous emissions and deposition fluxes based on selected fuels and combustion conditions under oxy-fuel firing conditions.
- To calculate the deposit removal rate from the superheaters by
    - Ash liquid drop shedding.
    - Soot blowers
- To investigate the erosion of the tube surfaces by fly ash particles collision and its effect on tube life.
- To investigate the steamside oxide scale exfoliation rate and its effects on wall thickness loss of the tube and on rate of heat transfer around the tubing.
- To investigate the failure of superheater and reheater tubing due to thermal and corrosion fatigue.
- To develop pure biomass corrosion models (as chloride attack is a different mechanism from sulphate attack).

7 REFERENCES

[1] Simms,N. Fry, A,T. (2010), "Modelling Fireside Corrosion of Heat Exchangers in Co-fired Pulversied Fuel Power Systems", 9th Liege Conference: Materials for Advanced Power Engineering, pp. 1168-1177.

[2] Hansson, J., Berndes, G., Johnsson, F. and Kjärstad, J. (2009), "Co-firing biomass with coal for electricity generation—An assessment of the potential in EU27", *Energy Policy,* vol. 37, no. 4, pp. 1444-1455.

[3] Van Der Lans, R. P., Pedersen, L. T., Jensen, A., Glarborg, P. and Dam-Johansen, K. (2000), "Modelling and experiments of straw combustion in a grate furnace", *Biomass and Bioenergy,* vol. 19, no. 3, pp. 199-208.

[4] Simms, N. J. (2011), "Solid fuel composition and power plant fuel flexibility", in Oakey, J. E. (ed.) *Power plant life management and performance improvement,* First edition ed, pp. 3-37.

[5] Wang, X., Zhao, D., Jiang, L. and Yang, W. (2009), "The deposition and burning characteristics during slagging co-firing coal and wood: Modeling and numerical simulation", *Combustion Science and Technology,* vol. 181, no. 5, pp. 710-728.

[6] Nussbaumer, T. (2003), "Combustion and Co-combustion of Biomass: Fundamentals, Technologies, and Primary Measures for Emission Reduction", *Energy and Fuels,* vol. 17, no. 6, pp. 1510-1521.

[7] Doshi, V., Vuthaluru, H. B., Korbee, R. and Kiel, J. H. A. (2009), "Development of a modeling approach to predict ash formation during co-firing of coal and biomass", *Fuel Processing Technology,* vol. 90, no. 9, pp. 1148-1156.

[8] Senior, C. L. and Srinivasachar, S. (1995), "Viscosity of ash particles in combustion systems for prediction of particle sticking", *Energy and Fuels,* vol. 9, no. 2, pp. 277-283.

[9] Robinson, A., Baxter, L., Junker, H., Shaddix, C., Freeman, M., James, R. and Dayton, D. (1998), "*Fireside issues associated with coal-biomass cofiring*" , National Renewable Energy Laboratory, Colorado, U.S.A.

[10] Chaudhuri, S. (2006), "Some aspects of metallurgical assessment of boiler tubes—Basic principles and case studies", *Materials Science and Engineering: A,* vol. 432, no. 1–2, pp. 90-99.

[11] Neves, D. L. C., Seixas, Jansen Renato de Carvalho, Tinoco, E. B., Rocha, A. d. C. and Abud, I. d. C. (2004), "Stress and integrity analysis of steam superheater tubes of a high pressure boiler", *Materials Research,* vol. 7, no. 1, pp. 155-161.

[12] Ennis, P. J. and Quadakkers, W. J. (2007), "Mechanisms of steam oxidation in high strength martensitic steels", *International Journal of Pressure Vessels and Piping,* vol. 84, no. 1-2, pp. 75-81.

[13] Ennis, P. J. and Quadakkers, W. J. (2007), "Implications of steam oxidation for the service life of high-strength martensitic steel components in high-temperature plant", *International Journal of Pressure Vessels and Piping,* vol. 84, no. 1-2, pp. 82-87.

[14] Gagliano.M.S, Hack.H, Stanko.G. (2008), "Fireside Corrosion Resistance of Proposed USC Superheater and Reheater Materials: Laboratory and Field Test Results", *The 2008 Clearwater Coal Conference 33th International Technical Conference on Coal Utilization & Fuel Systems Clearwater, FL, USA,* June 2008, Foster Wheeler NORHT AMERICA Corp, 33th International Technicla Conference on Coal Utilization 7 Fuel Systems, FL, U.S.A, .

[15] Sathyanathan.V.T, Stonecypher. L. , *Understanding Tube Failures in High Pressure Boilers,* available at: http://www.brighthubengineering.com/power-plants/34265-understanding-tube-failures-in-high-pressure-boilers/# (accessed 04/02/2013).

[16] Rahman.M.M, K. A. K. "Failure analysis of high temperature superheater tube (HTS) of a pulverized coal-fired power station", *Proceeding of the International Conference on Advanced Science, Engineering and Information Technology 2011, Hotel Equatorial Bangi-Putrajaya,* 2011, .

[17] Zarrabi, K. (1993), "Estimation of boiler tube life in presence of corrosion and erosion processes", *International Journal of Pressure Vessels and Piping,* vol. 53, no. 2, pp. 351-358.

[18] Viswanathan.R, Paterson.S.R, Grunloh.H, Gehl.S (1994), "Life Assessment of Superheater/Reheater Tubes in Fossil Boilers", *Journal of Pressure Vessel Technology* ,vol. 116, no. 1, pp. 1-16.

[19] Purbolaksono, J., Khinani, A., Rashid, A. Z., Ali, A. A. and Nordin, N. F. (2009), "Prediction of oxide scale growth in superheater and reheater tubes", *Corrosion Science,* vol. 51, no. 5, pp. 1022-1029.

[20] French.D.N (1993), *Metallurgical Failures in Fossil Fired Boilers,* JOHN WILEY & SONS, INC.

[21] Baker, D. W. C., Hart, A. B., Hay, K. A., Holmes, D. R., Jackson, P. J., Jarman, J., King, C. W., Laxton, J. W., Mortimer, D., Toft, L. H. and Fountain, A. B. (1974), *The Control of High Temperature Fireside Corrosion,* RD/L/M 484, Central Electricity Research Laboratories, Leatherhead, Surrey.

[22] Jha.B.B,Ojha.S.N and Mirsa.B.K. (2008), "Residual life estimation of high temperature tubings based on oxide scale thickness measurement", *Remaining Life Assessment of Aged Compnenets in Thermal Power Plants and Petrochemical Industries,* vol. 2, pp. 43-56.

[23] Le May, I., da Silveira, T. L. and Vianna, C. H. (1996), "Criteria for the evaluation of damage and remaining life in reformer furnace tubes", *International Journal of Pressure Vessels and Piping,* vol. 66, no. 1-3, pp. 233-241.

[24] Lee, B. S., Chung, H. S., Kim, K., Ford, F. P. and Andersen, P. L. (1999), "Remaining life prediction methods using operating data and knowledge on mechanisms", *Nuclear Engineering and Design,* vol. 191, no. 2, pp. 157-165.

[25] Liaw, P. K., Saxena, A. and Schaefer, J. (1989), "Estimating remaining life of elevated-temperature steam pipes—Part II. Fracture mechanics analyses", *Engineering Fracture Mechanics,* vol. 32, no. 5, pp. 709-722.

[26] "Khodier.A, Simms.N, Kalligon.P, Ligrave.N" (2010), "Investigation of gaseous emissions and ash deposition in a pilot-scale PF combustor co-firing cereal co-product biomass with coal", 23rd of March, Granada (Spain), International Conference on Renewable Energies and Power Quality, .

[27] Jose M. Vargas, Daniel D. Perlmutter (1986), "Interpretation of coal pyrolysis kinetics", *Ind. Eng. Chem. Process Des. Dev*, vol. 25, no. 1, pp. 49-54.

[28] Tomeczek.J (1994), *Coal combustion*, Krieger publishing company, Malabar, Florida.

[29] Yang, Y. B., Sharifi, V. N., Swithenbank, J., Ma, L., Darvell, L. I., Jones, J. M., Pourkashanian, M. and Williams, A. (2008), "Combustion of a single particle of biomass", *Energy and Fuels*, vol. 22, no. 1, pp. 306-316.

[30] Niksa.S , Kerstein.A.R. (1991), "FLASHCHAIN theory for rapid coal devolatilization kinetics. 1. Formulation", *Energy Fuels*, vol. 5, pp. 647-665.

[31] Anthony, D. B., Howard, J. B., Hottel, H. C. and Meissner, H. P. (1975), "Rapid devolatilization of pulverized coal", *Symposium (International) on Combustion*, vol. 15, no. 1, pp. 1303-1317.

[32] Zhou, H., Jensen, A. D., Glarborg, P., Jensen, P. A. and Kavaliauskas, A. (2005), "Numerical modeling of straw combustion in a fixed bed", *Fuel*, vol. 84, no. 4, pp. 389-403.

[33] James G. Speight (2005), *Handbook of Coal Analysis*, John Wiley and Sons, Inc.

[34] O'Gorman, J. V. and Walker Jr., P. L. (1973), "Thermal behaviour of mineral fractions separated from selected American coals", *Fuel*, vol. 52, no. 1, pp. 71-79.

[35] Baxter, L. L. (1993), "Ash deposition during biomass and coal combustion: A mechanistic approach", *Biomass and Bioenergy*, vol. 4, no. 2, pp. 85-102.

[36] Tomeczek, J. and Palugniok, H. (2002), "Kinetics of mineral matter transformation during coal combustion", *Fuel*, vol. 81, no. 10, pp. 1251-1258.

[37] Akbar, S., Schnell, U. and Scheffknecht, G. (2010), "Modelling potassium release and the effect of potassium chloride on deposition mechanisms for coal and biomass-fired boilers", *Combustion Theory and Modelling*, vol. 14, no. 3, pp. 315-329.

[38] Grammelis, P. and Kakaras, E. (2005), "Biomass combustion modeling in fluidized beds", *Energy and Fuels*, vol. 19, no. 1, pp. 292-297.

[39] Desroches-Ducarne, E., Dolignier, J. C., Marty, E., Martin, G. and Delfosse, L. (1998), "Modelling of gaseous pollutants emissions in circulating fluidized bed combustion of municipal refuse", *Fuel*, vol. 77, no. 13, pp. 1399-1410.

[40] Wang, X., Zhao, D., Jiang, L. and Yang, W. (2009), "The deposition and burning characteristics during slagging co-firing coal and wood: Modeling and numerical simulation", *Combustion Science and Technology*, vol. 181, no. 5, pp. 710-728.

[41] Hatt, R. M. (1990), "Fireside deposits in coal-fired utility boilers", *Progress in Energy and Combustion Science*, vol. 16, no. 4, pp. 235-241.

[42] Zhou, H., Jensen, P. A. and Frandsen, F. J. (2007), "Dynamic mechanistic model of superheater deposit growth and shedding in a biomass fired grate boiler", *Fuel*, vol. 86, no. 10-11, pp. 1519-1533.

[43] Tomeczek, J. and Wacławiak, K. (2009), "Two-dimensional modelling of deposits formation on platen superheaters in pulverized coal boilers", *Fuel*, vol. 88, no. 8, pp. 1466-1471.

[44] Batchelor, G. K. and Shen, C. (1985), "Thermophoretic deposition of particles in gas flowing over cold surfaces", *Journal of colloid and interface science*, vol. 107, no. 1, pp. 21-37.

[45] Kaufmann, H., Nussbaumer, T., Baxter, L. and Yang, N. (2000), "Deposit formation on a single cylinder during combustion of herbaceous biomass", *Fuel*, vol. 79, no. 2, pp. 141-151.

[46] Coleman, K. (2008), *Fireside corrosion in biomass combustion plants* (unpublished PhD thesis), Cranfield University, Cranfield.

[47] Guha, A. (2008), "*Transport and deposition of particles in turbulent and laminar flow*", *Annu. Rev. Fluid Mech*. 2008, vol. 40, pp. 311–341.

[48] Simms, N. J. (2011), "Environmental degradation of boiler components", in Oakey, J. E. (ed.) *Power plant life management and performance improvement*, First ed, pp. 145-179.

[49] Hansen.L.A (1998), *Melting and Sintering of Ashes* (unpublished PhD thesis), Department of Chemical Engineering, Technical University of Denmark, Denmark.

[50] Huang, L. Y., Norman, J. S., Pourkashanian, M. and Williams, A. (1996), "Prediction of ash deposition on superheater tubes from pulverized coal combustion", *Fuel*, vol. 75, no. 3, pp. 271-279.

[51] Walsh, P. M., Sayre, A. N., Loehden, D. O., Monroe, L. S., Beér, J. M. and Sarofim, A. F. (1990), "Deposition of bituminous coal ash on an isolated heat exchanger tube: Effects of coal properties on deposit growth", *Progress in Energy and Combustion Science*, vol. 16, no. 4, pp. 327-345.

[52] Richards.G.H,Slater.P.N., Harb.J.N. (1993), "Simulation of ash deposit growth in a pulverized coal-fired pilot scale reactor", *Energy Fuels*, vol. 7, no. 6, pp. 774-781.

[53] Wessel.R.A, Righi. J. (1988), "Generalized Correlations for Inertial Impaction of Particles on a Circular Cylinder", *Aerosol Science and Technology*, vol. 9, no. 1, pp. 29-60.

[54] Israel.R, Rosner. D. E. (1983), "Use of a Generalized Stokes Number to Determine the Aerodynamic Capture Efficiency of Non-Stokesian Particles from a Compressible Gas Flow", *Aerosol Science and Technology*, vol. 2, no. 1, pp. 45-51.

[55] Tomeczek, J., Palugniok, H. and Ochman, J. (2004), "Modelling of deposits formation on heating tubes in pulverized coal boilers", *Fuel*, vol. 83, no. 2, pp. 213-221.

[56] Masters.G.L, Davis. C. J, Fry.A.T. (2008), *Modelling Firside Corrosion of Heat Exchanger Materials in Advanced Energy Systems Taks1: Review of Existing Corrosion Models*, TP/5/MAT/6/I/H0639C, E.ON UK, Racliffe on Soar, Nottinghamshire

[57] Khanna.A.S. (2002), "*Introduction to High Temperature Oxidation and Corrosion*", ASM International, U.S.

[58] Lindberg, D, Backman,R. and Chartrand, P. (2007), "Thermodynamic evaluation and optimization of the (NaCl + Na2SO4 + Na2CO3 + KCl + K2SO4 + K2CO3) system", *The Journal of Chemical Thermodynamics*, vol. 39, no. 7, pp. 1001-1021.

[59] Natesan.K, P. A., Rink.D.L (2003), "Coal-ash Corrosion of Alloys for Combustion Power Plants", *US Department of Eneregy Fossil Energy Conference*, 2003, .

[60] Callister, W. D. (2006), *Materials science and engineering : an introduction*, 7th ed, Wiley, New York.

[61] Weulersse-Mouturat, K, Moulin, G, Billard, P and Pierotti, G, (2004), "*High temperature corrosion of superheater tubes in waste incinerators and coal-fired plants*", *Materials Science Forum*, vol. 461 - 464, pp. 973-980

[62] Otsuka, N. (2002), "Effects of fuel impurities on the fireside corrosion of boiler tubes in advanced power generating systems - A thermodynamic calculation of deposit chemistry", *Corrosion Science*, vol. 44, no. 2, pp. 265-283.

[63] Nielsen, H. P., Frandsen, F. J., Dam-Johansen, K. and Baxter, L. L. (2000), "The implications of chlorine-associated corrosion on the operation of biomass-fired boilers", *Progress in Energy and Combustion Science*, vol. 26, no. 3, pp. 283-298.

[64] Wright.I.G, Krause. H. H. (1997), *Possible Effects of the Chlorine Content of Coal on Fireside Corrosion in Pulverized Coal-Fired Boilers*, TR-108107, EPRI, Palo Alto, California.

[65] Mahanen.J (2011), *Steam-side oxidation of materials for supecritical boilers* (unpublished MSc thesis), Foster Wheeler Energia Oy Research & Development, Varkaus.

[66] Fry.A, Osgerby.S, Wright.M. (2002), *Oxidation of Alloys in Steam Environments- A Review*, MATC(A)90, NPL Materials Centre, Teddington, Middlesex.

[67] Smoot.L.D, Pratt. D. T. (1979), *Pulverised-Coal Combustion and Gasification*, Plenum Press, New York.

[68] Wright, I.G., Sabau, A.S. and Dooley, R.B., (2008), "*Development of strain in oxides grown in steam tubes*", *Materials Science Forum*, vol 595-598, no. 1, pp. 387-395.

[69] Sabau, A. S. and Wright, I. G. (2010), "Influence of oxide growth and metal creep on strain development in the steam-side oxide in boiler tubes", *Oxidation of Metals*, vol. 73, no. 5-6, pp. 467-492.

[70] Incropera.F.P, D. D. P. (1996), *Introduction to Heat Transfer*, Third ed, John Wiley &Sons, New York.

[71] Sanitjai, S. and Goldstein, R. J. (2004), "Forced convection heat transfer from a circular cylinder in crossflow to air and liquids", *International Journal of Heat and Mass Transfer*, vol. 47, no. 22, pp. 4795-4805.

[72] Robinson, A. L., Buckley, S. G. and Baxter, L. L. (1998), "In situ measurements of the thermal conductivity of ash deposits", *Symposium (International) on Combustion*, vol. 27, no. 2, pp. 1727-1735.

[73] Port.R.D, Herro. H. M. (1991), "*The Nalco Guide to Boiler Failure Analysis*", McGraw-Hill, lnc, U.S.A.

[74] Bian, C., Zhou, K. and Xu, J., (2012), *On the estimation of oxide scale growth in T22 superheater and reheater tubes*.

[75] Sathyanathan.V.T, Stonecypher. L. (2011), *How Long Term Overheating Tube Failures Happen in Boilers*, available at: http://www.brighthubengineering.com/power-plants/38111-how-long-term-overheating-tube-failures-happen-in-boilers/ (accessed 18/02).

[76] Author (Year), *Tutorial 5 - Thin Walled Vessels*, D J. Dunn, Freestudy.co.uk, available at: http://www.freestudy.co.uk/statics/complex/t1.pdf (accessed 14 February 2013).

[77] Jones, D. R. H. (2004), "Creep failures of overheated boiler, superheater and reformer tubes", *Engineering Failure Analysis*, vol. 11, no. 6, pp. 873-893.

[78] Viswanathan.R (1989), *Damage Mechanisms and Life Assessment of High-Temperature Components*, 4th ed, A S M International.

[79] Swaminathan, J., Guguloth, K., Gunjan, M., Roy, P. and Ghosh, R. (2008), "Failure analysis and remaining life assessment of service exposed primary reformer heater tubes", *Engineering Failure Analysis*, vol. 15, no. 4, pp. 311-331.

[80] Purbolaksono, J., Ahmad, J., Beng, L. C., Rashid, A. Z., Khinani, A. and Ali, A. A. (2010), "Failure analysis on a primary superheater tube of a power plant", *Engineering Failure Analysis*, vol. 17, no. 1, pp. 158-167.

[81] Zarrabi.K, R. I. (2001), "Mid-Wall Temperature in an Eroded Section of an Austenitic Superheater/Reheater Tube", *Journal of Engineering Materials and Technology*, vol. 123, no. 3, pp. 334-337.

[82] Aghaie-Khafri, M. and Noori, M. (2011), "Life prediction of Ni-base superalloy", *Bulletin of Materials Science*, vol. 34, no. 2, pp. 305-309.

[83] Dunand, D. C., Han, B. Q. and Jansen, A. M. (1999), "Monkman-Grant Analysis of Creep Fracture in Dispersion-Strengthened and Particulate-Reinforced Aluminum", *Metallurgical and Materials Transactions A: Physical Metallurgy and Materials Science*, vol. 30, no. 3, pp. 829-838.

[84] Hendrickson.T.A (1975), *Synthetic Fuels Data Handbook, Inc; Denver, Colo, 1975*, Cameron Engineers, Inc, Denver, Colo.

[85] Energy research Centre of the Netherlands (ECN) (2012), *Definitions* ***used in Phyllis***, available at: http://www.ecn.nl/phyllis/defs.asp (accessed 20/07/2012).

[86] Khodier, A. H. M. (2011), *Co-firing fossil fuels and biomass : combustion, deposition and modelling* (unpublished PhD thesis), Cranfield University, U.K.

[87] C.Y.Wen, E. S. Lee. (1979), *Coal Conversion Technolog*, Addison -Wesley Publishing Company, Massachusetts.

[88] Zygarlicke, C. J., Steadman, E. N. and Benson, S. A. (1990), "Studies of transformations of inorganic constituents in a Texas lignite during combustion", *Progress in Energy and Combustion Science*, vol. 16, no. 4, pp. 195-204.

[89] López, I. C. and Ward, C. R. (2008), "Composition and mode of occurrence of mineral matter in some Colombian coals", *International Journal of Coal Geology,* vol. 73, no. 1, pp. 3-18.

[90] Bushell, A. J. and Williamson, J. (1996), "Fate of trace elements in UK coals during gasification processes", *ACS Division of Fuel Chemistry, Preprints,* vol. 41, no. 3, pp. 791-794.

[91] Huffman, G. P. and Huggins, F. E. (1986), "Reactions and transformations of coal mineral matter at elevated temperatures", *ACS Symposium Series,* vol. 301, pp. 100-113.

[92] Wereko-Brobby.C, Hagan. E. B. (1996), *Biomass Conversion and Technology*, John Wiley &Sons.

[93] Zhang, L, Xu, C. (C) and Champagne, P. (2010), "Overview of recent advances in thermo-chemical conversion of biomass", *Energy Conversion and Management,* vol. 51, no. 5, pp. 969-982.

[94] Saidur, R., Abdelaziz, E. A., Demirbas, A., Hossain, M. S. and Mekhilef, S. (2011), "A review on biomass as a fuel for boilers", *Renewable and Sustainable Energy Reviews,* vol. 15, no. 5, pp. 2262-2289.

[95] Ragland, K. W, Baker, A. J. (1987), "Mineral matter in coal and wood-implications for solid fueled gas turbines", *Combustion fundamentals and applications : spring technical meeting ofthe central states section of The Combustion Institute: Argonne*, pp. 117-122.

[96] Vassilev, S. V., Baxter, D., Andersen, L. K., Vassileva, C. G. and Morgan, T. J. (2012), "An overview of the organic and inorganic phase composition of biomass", *Fuel,* vol. 94, no. 0, pp. 1-33.

[97] Hein, K. R. G. and Bemtgen, J. M. (1998), "EU clean coal technology—co-combustion of coal and biomass", *Fuel Processing Technology,* vol. 54, no. 1–3, pp. 159-169.

[98] IEA (International Energy Agency) , *Bioenergy Project Development & Biomass Supply*, available at: www.iea.org/publications/freepublications/publication/biomass.pdf (accessed 27/02/2013).

[99] Quaak P, Knoef H, Stassen H. (1999), *Energy from biomass, a review of combustion and gasification technologies*, World bank technical paper, 422, The International Bank for Reconstruction and Development, Washington (DC).

[100] Lin, J. M. (2006), "Development of a high yield and low cycle time biomass char production system", *Fuel Processing Technology*, vol. 87, no. 6, pp. 487-495.

[101] IEA (International Energy Agency) (2002), *Biomass Combustion and Co-firing: An Overview*, available at: http://www.ieabioenergy.com/MediaItem.aspx?id=16 (accessed 28/02/2013).

[102] Encyclopædia Britannica, *fluidized-bed combustion: schematic diagram of a fluidized-bed combustion boiler*, available at:

http://www.britannica.com/EBchecked/media/113942/Schematic-diagram-of-a-fluidized-bed-combustion-boiler (Accessed 28/02/2013).

[103] climatetechwiki , *Pulverised Coal Combustion with higher efficiency*, available at: http://climatetechwiki.org/technology/sup_crit_coal (Accessed 28/02/2013).

[104] Viswanathan.R, Foulds. J. R, Roberts.D.A. (1988), "Methods for Estimating the Temperature of Reheater and Superheater Tubes in Fossil Boilers", *International Conference on Life Extension and Assessment, The Hague*.

[105] Rehn, I. M., Apblett Jr., W. R. and Stringer, J. (1983), "Controlling Steamside Oxide Exfoliation IN Utilty Boiler Superheater and Reheater", *Electric Power Research Institute, Coal Combustion Systems Division*, (*Report*) *EPRI CS*, pp. 4-15.

[106] EPRI (2007), *Program on Technology Innovation: Oxide Growth and Exfoliation on Alloys Exposed to Steam*, 1013666, Electric Power Research Institute, Palo Alto, CA.

[107] Ray, A. K., Diwakar, K., Prasad, B. N., Tiwari, Y. N., Ghosh, R. N. and Whittenberger, J. D. (2007), "Long term creep–rupture behaviour of 813 K exposed

2.25–1Mo steel between 773 and 873 K", *Materials Science and Engineering: A,* vol. 454–455, no. 0, pp. 124-131.

[108] Li, L., Duan, Y., Cao, Y., Chu, P., Carty, R. and Pan, W. (2007), "Field corrosion tests for a low chromium steel carried out at superheater area of a utility boiler with three coals containing different chlorine contents", *Fuel Processing Technology*, vol. 88, no. 4, pp. 387-392.

[109] Wang, X, Shi, Z, Pan, Q-G and Wu, H-L. (2009), "High-temperature creep properties of fine grained heat-affected zone in P92 weldment", *Transactions of Nonferrous Metals Society of China (English Edition),* vol. 19, no. SUPPL. 3, pp. s772-s775.

[110] Anderson, P., Bellgardt, T., Jones, F, L. (2010), "Creep deformation in a modefied 9Cr-1Mo steel", *Material Science and Technology,* vo1. 19, no. 2, pp. 207-213.

[111] Vakili-Tahami, F., Sajjadpour, M., Attari, P. (2011), "Experimental Study of the Creep Lifetime of the 1.25Cr 0.5 Mo Steel Pipes", *Strain*, no. 47, pp. 414-420.

[112] Ahmad, J., Purbolaksono, J., Beng, L, C. (2010), " Failure analysis on high temperature superheater Inconel® 800 tube ", *Engineering Failure Analysis* no. 17, pp. 328-333.

8 APPENDICES

8.1 Appendix A

Appendix A contains fuel combustion model calculations.

8.1.1 A.1 Simplified combustion model

Table 8-1 Fuel composition

Fuel (Daw Mill coal)	As-received (%Wt)	Mass, kg/h	MW (gr/mole)	Mole/hr	Moles (no water)
Moisture	4.6	0.34	18.00	18.91	
C	74.15	5.49	12.00	457.26	457.26
H	4.38	0.32	1.00	324.12	361.94
N	1.17	0.09	14.00	6.18	6.18
O	10.49	0.78	16.00	48.52	67.43
S	1.28	0.09	32.00	2.96	2.96
Cl	0.2	0.01	35.50	0.42	0.42
Ash	4.2	0.31			0.00
Total	100.47	7.43		858.37	896.19

Table 8-2 Air composition

Air	Mass %	MW (g/mole)	Mass, kg/h	Mole/h
N_2	75.55	28	68.75	2455.38
O_2	23.16	32	21.08	658.61
Ar	1.29	40	1.17	29.35
Total	100		91.00	3143.34

Table 8-3 Mixture of air and fuel composition

Elements	Moles (no water)	Air	Total
C	457.26		457.26
H	361.94		361.94
N	6.18	4910.75	4916.93
O	67.43	1317.23	1384.65
Ar		29.35	29.35
S	2.96		2.96
Cl	0.42		0.42
Total	896.19	6257.32	7153.51

Table 8-4 Flue gas emissions

Flue gases	Moles	Mole fraction	Mole %
H_2O	180.76	0.06	5.52
CO_2	457.26	0.14	13.97
O_2	138.63	0.04	4.23
N_2	2458.47	0.75	75.09
Ar	29.35	0.01	0.90
NO	6.18	0.00	1888.89 ppm
SO_2	2.96	0.00	904.08, ppm
HCl	0.42	0.00	127.34, ppm
Total	3274.03	1.00	3020.02

Table 8-5 Ash composition and fly ashes concentration

Ash composition (Coal)	Wt%	Moles	Elements	Moles	grams	g/kg of ash	g/? kg of fuel	Released	g/? kg of fuel	$C_{ash,1}$, Kg/m3
SiO_2	36.8	0.61	Si	0.61	17.20	172.01	53.46	0.35	0.19	1.05E-06
Al_2O_3	23.9	0.23	Al	0.47	12.65	126.49	39.31	0.4	0.16	7.77E-07
Fe_2O_3	11.2	0.07	Fe	0.14	7.83	78.34	24.35	0.43	0.10	3.92E-07
CaO	12	0.21	Ca	0.21	8.58	85.76	26.66	0.25	0.07	2.44E-07
MgO	2.5	0.06	Mg	0.06	1.51	15.07	4.68	0.2	0.01	4.07E-08
K_2O	0.5	0.01	K	0.01	0.42	4.15	1.29	250	3.23	2.52E-05
Na_2O	1.5	0.02	Na	0.05	1.11	11.13	3.46	20	0.69	9.19E-06
TiO_2	1.1	0.00	Ti	0.00	0.95	9.51	2.96	0.25	0.01	2.24E-08
BaO	0	0.00	Ba	0.00	0.00	0.00	0.00	1	0.00	0.00E+00
Mn_3O_4	0.4	0.00	Mn	0.01	0.29	2.88	0.90	1	0.01	3.25E-08
P_2O_5	0	0.00	P	0.00	0.00	0.00	0.00	1	0.00	0.00E+00

8.1.2 A.2 Reaction kinetics combustion model

Table 8-6 Combustion operating conditions

Combustion chamber gas temperature, K	Flue gas temperature, K	Fuel feed rates, Kg/h	Residence time, s	Inlet volume percentage of oxygen,%	Coal, Wt%	Biomass, Wt%	Total blend's percentage
1600	1423	7.4	0.1	10	100	0	100

Table 8-7 Volatiles products

Volatiles formation (Coal)	$m_{infinite}$ (%)	Q(kj/mole)	k_0(1/s)	k_j, 1/s	$m_{infinite}$,gr/h	$m_j = m_{infinite}(1-(exp(-k_jt)))$, gr/h	Volatiles released, moles/h
H_2O	4.2	312	1.00E+12	65.14	310.80	310.34	17.24
CH_4	2.01	85	1.50E+04	25.18	148.74	136.75	8.55
CO	1.5	75	5.00E+03	17.80	111.00	92.28	3.30
CO_2	4.85	40	1.75E+02	8.65	358.90	207.82	4.72
C_2H_6	1.11	65	1.50E+03	11.32	82.14	55.67	1.86
C_6H_6	12	120	1.50E+07	1812.81	888.00	888.00	11.38

Table 8-8 Volatiles combustion products

Volatiles combustion (Coal)	k, 1/s	Initial reactant, moles/h	reactant left, moles/h with x s reaction	reactant left, moles/h with x s reaction	Products generated, moles/h	
$CH_4 + 1.5O_2 \rightarrow CO + 2H_2O$	4.44E+03	8.55E+00	5.48E+00	5.48E+00	3.06E+00	CO
$CH_4 + 1.5O_2 \rightarrow CO + 2H_2O$	4.44E+03	8.55E+00	5.48E+00		6.13E+00	H_2O
$C_2H_6 + 2.5O_2 \rightarrow 2CO + 3H_2O$	3.71E+04	1.86E+00	0.00E+00	0.00E+00	3.71E+00	CO
$C_2H_6 + 2.5O_2 \rightarrow 2CO + 3H_2O$	3.71E+04	1.86E+00	0.00E+00		5.57E+00	H_2O
$C_6H_6 + 4.5O_2 \rightarrow 6CO + 3H_2O$	3.71E+04	1.14E+01	0.00E+00	0.00E+00	6.83E+01	CO
$C_6H_6 + 4.5O_2 \rightarrow 6CO + 3H_2O$	3.71E+04	1.14E+01	0.00E+00		3.42E+01	H_2O

$CO + 0.5O_2 \rightarrow CO_2$	2.59E+03	4.04E+02	0.00E+00	0.00E+00	4.04E+02	CO_2

Table 8-9 Fuel mineral matter transformation reactions

Mineral matter transformation reactions (Coal)	Q (kJ/mole)	k_0 (1/s) or 1/sPa	T, K	$K = K_0T^n\exp(-Q/RT)$, 1/s or 1/(Pa.s)	C_A, mole/h	reactant left, moles/hr with x *s* reaction	Products generated, moles/h	reactant left, moles/h with x *s* reaction
$Al_4Si_4O_{10}(OH)_8 \rightarrow 2(Al_2O_3.2SiO_{2)} + 4H_2O$	7.4E+01	2.0E+02	1.6E+03	7.6E-01	7.7E+00	7.2E+00	1.1E+00	7.2E+00
$Al_4Si_4O_{10}(OH)_8 \rightarrow 2(Al_2O_3.2SiO_{2)} + 4H_2O$	7.4E+01	2.0E+02	1.6E+03	7.6E-01	7.7E+00	7.2E+00	2.3E+00	
$KAl_2(OH)_2(AlSi_3O_{10}) \rightarrow$ semimetaillite + $1.53H_2O$	4.4E+01	2.5E+00	1.6E+03	9.2E-02	0.0E+00	0.0E+00	0.0E+00	0.0E+00
semimetaillite $\rightarrow$ metaillite + $0.97H_2O$	1.5E+02	9.1E+04	1.6E+03	1.2E+00				
$CaCO_3 \rightarrow CaO + CO_2$	2.1E+02	1.9E+08	1.6E+03	1.9E+01	1.0E+01	1.5E+00	8.8E+00	1.5E+00
$CaCO_3 \rightarrow CaO + CO_2$	2.1E+02	1.9E+08	1.6E+03	1.9E+01	1.0E+01	1.5E+00	8.8E+00	
$MgCO_3 \rightarrow MgO + CO_2$	2.0E+02	1.3E+12	1.6E+03	3.8E+05	0.0E+00	0.0E+00	0.0E+00	0.0E+00
$MgCO_3 \rightarrow MgO + CO_2$	2.0E+02	1.3E+12	1.6E+03	3.8E+05	0.0E+00	0.0E+00	0.0E+00	
$FeS_2 \rightarrow 0.8Fe_{1.25}S + 0.6S_2$	1.9E+02	1.9E+08	1.6E+03	1.7E+02	1.2E+01	4.2E-07	9.9E+00	4.2E-07
$FeS_2 \rightarrow 0.8Fe_{1.25}S + 0.6S_2$	1.9E+02	1.9E+08	1.6E+03	1.7E+02	1.2E+01	4.2E-07	7.4E+00	
$Fe_{1.25}S \rightarrow 1.25Fe + 0.5S_2$	9.3E+01	4.5E-01	1.6E+03	4.3E-04	1.2E+01	1.2E+01	6.6E-04	1.2E+01
$Fe_{1.25}S \rightarrow 1.25Fe + 0.5S_2$	9.3E+01	4.5E-01	1.6E+03	4.3E-04	1.2E+01	1.2E+01	2.7E-04	
$3FeS_2 + 8O_2 \rightarrow Fe_3O_4 + 6SO_2$	8.8E+01	1.7E-02	1.6E+03	2.3E-05	1.2E+01	1.2E+01	9.4E-02	1.2E+01
$3FeS_2 + 8O_2 \rightarrow Fe_3O_4 + 6SO_2$	8.8E+01	1.7E-02	1.6E+03	2.3E-05	1.2E+01	1.2E+01	5.7E-01	
$Fe_{1.25}S + 1.83O_2 \rightarrow 0.41Fe_3O_4 + SO_2$	9.3E+01	2.1E-05	1.6E+03	2.0E-08	1.2E+01	1.2E+01	2.5E-04	1.2E+01
$Fe_{1.25}S + 1.83O_2 \rightarrow 0.41Fe_3O_4 + SO_2$	9.3E+01	2.1E-05	1.6E+03	2.0E-08	1.2E+01	1.2E+01	1.0E-04	

$Fe_3O_4 + 1/4O_2 \rightarrow 3/2\ Fe_2O_3$	1.0E+02	5.3E+00	1.6E+03	2.9E-03	4.3E-04	2.3E-05	6.1E-04	2.3E-05
$Fe+ 2/3O_2 \rightarrow 1/3Fe_3O_4$	9.1E+01	1.5E+00	1.6E+03	1.7E-03	5.3E-04	9.8E-05	1.4E-04	9.8E-05

Continued from Table 8-9

Mineral matter transformation reactions (Coal)	Q (kJ/mole)	k_0 (1/s) or 1/sPa	T, K	$K = K_0T^n\exp(-Q/RT)$, 1/s or 1/(Pa.s)	C_A, mole/h	reaction time, *s*	reactant left, moles/hr with x *s* reaction	Products generated, moles/h
$KCl_{(s)} + Al_2O_3.2SiO_2 \rightarrow KCl_{(g)} + Al_2O_3.2SiO_2$	2.6E+02	2.7E+09	1.6E+03	1.2E+01	0.0E+00	1.0E-01	0.0E+00	0.0E+00
$KCl_{(s)} + Al_2O_3.2SiO_2 \rightarrow KCl_{(g)} + Al_2O_3.2SiO_2$	2.6E+02	2.7E+09	1.6E+03	1.2E+01	0.0E+00	1.0E-01	0.0E+00	0.0E+00
$2KCl_{(s)} + Al_2O_3.2SiO_2 + H_2O_{(g)} \rightarrow 2KAlSiO_4 + 2HCl_{(g)}$	1.6E+02	4.0E+05	1.6E+03	3.5E+00	0.0E+00	1.0E-01	0.0E+00	0.0E+00
$2KCl_{(s)} + Al_2O_3.2SiO_2 + H_2O_{(g)} \rightarrow 2KAlSiO_4 + 2HCl_{(g)}$	1.6E+02	4.0E+05	1.6E+03	3.5E+00	0.0E+00	1.0E-01	0.0E+00	0.0E+00
$NaCl_{(s)} \rightarrow NaCl_{(g)}$	2.9E+02	1.3E+11	1.6E+03	4.8E+01	0.0E+00	1.0E-01	0.0E+00	0.0E+00
$NaCl_{(s)} + Al_2O_3.2SiO_2 \rightarrow NaCl_{(g)} + Al_2O_3.2SiO_2$	1.8E+05	1.3E+05	1.6E+03	0.0E+00	0.0E+00	1.0E-01	0.0E+00	0.0E+00
$2NaCl_{(s)} + Al_2O_3.2SiO_2 + 1/2O_2 \rightarrow 2NaSiAlO_4 + Cl_2$	9.4E+04	2.8E+02	1.6E+03	0.0E+00	0.0E+00	1.0E-01	0.0E+00	0.0E+00
$2NaCl_{(s)} + Al_2O_3.2SiO_2 + H_2O_{(g)} \rightarrow 2NaSiAlO_4 + 2HCl$	1.0E+05	6.0E+02	1.6E+03	0.0E+00	0.0E+00	1.0E-01	0.0E+00	0.0E+00
$CaSO_4 \rightarrow CaO + SO_3$	5.3E+02	4.9E+18	1.6E+03	2.1E+01	0.0E+00	1.0E-01	0.0E+00	0.0E+00
$CaSO_4 \rightarrow CaO + SO_3$	5.3E+02	4.9E+18	1.6E+03	2.1E+01	0.0E+00	1.0E-01	0.0E+00	0.0E+00
$CaSO_4 + 4CO \rightarrow CaS + 4CO_2$	3.9E+02	2.2E+14	1.6E+03	4.1E+01	0.0E+00	1.0E-01	0.0E+00	0.0E+00
$CaSO_4 + 4CO \rightarrow CaS + 4CO_2$	3.9E+02	2.2E+14	1.6E+03	4.1E+01	0.0E+00	1.0E-01	0.0E+00	0.0E+00
$CaSO_4.2H_2O \rightarrow CaSO_4 + 2H_2O$	1.2E+02	3.2E+15	1.6E+03	3.9E+11	0.0E+00	1.0E-01	0.0E+00	0.0E+00

$CaSO_4.2H_2O \rightarrow CaSO_4 + 2H_2O$	1.2E+02	3.2E+15	1.6E+03	3.9E+11	0.0E+00	1.0E-01	0.0E+00	0.0E+00
$(2CaSO_4.(H_2O)) + H_2O_{(l)} \rightarrow (2CaSO_4.(H_2O)) + H_2O_{(g)}$	1.2E+02	4.5E+15	1.6E+03	6.3E+11	0.0E+00	1.0E-01	0.0E+00	0.0E+00

8.2 Appendix B Deposition model

8.2.1 B.1 Heat transfer model

Table 8-10 Heat transfer model

Angle, °	Nu	h, W/m^2k	Fireside convection, mK/W	Fireside radiation, mK/W	Fireside total, mK/W	Deposit, mK/W	Outer scale, mK/W	Metal, mK/W	inner scale, mK/W	Steamside convection, mK/W	Thermal resistance mK/W	Heat transferred, W/m
0	48.36	92.97	7.61E-02	3.94E-02	2.60E-02	0	0	1.15E-03	0	1.16E-03	2.83E-02	2.16E+04
5	48.27	92.79	7.62E-02	3.94E-02	2.60E-02	0	0	1.15E-03	0	1.16E-03	2.83E-02	2.16E+04
10	48.00	92.26	7.67E-02	3.94E-02	2.60E-02	0	0	1.15E-03	0	1.16E-03	2.83E-02	2.15E+04
15	47.54	91.38	7.74E-02	3.94E-02	2.61E-02	0	0	1.15E-03	0	1.16E-03	2.84E-02	2.15E+04
20	46.91	90.16	7.85E-02	3.94E-02	2.62E-02	0	0	1.15E-03	0	1.16E-03	2.85E-02	2.14E+04
25	46.10	88.61	7.98E-02	3.94E-02	2.64E-02	0	0	1.15E-03	0	1.16E-03	2.87E-02	2.13E+04
30	45.13	86.74	8.15E-02	3.94E-02	2.66E-02	0	0	1.15E-03	0	1.16E-03	2.89E-02	2.11E+04
35	43.99	84.56	8.36E-02	3.95E-02	2.68E-02	0	0	1.15E-03	0	1.16E-03	2.91E-02	2.09E+04
40	42.71	82.09	8.62E-02	3.95E-02	2.71E-02	0	0	1.15E-03	0	1.16E-03	2.94E-02	2.08E+04
45	41.28	79.35	8.91E-02	3.95E-02	2.74E-02	0	0	1.15E-03	0	1.16E-03	2.97E-02	2.06E+04
50	39.73	76.36	9.26E-02	3.95E-02	2.77E-02	0	0	1.15E-03	0	1.16E-03	3.00E-02	2.03E+04
55	38.05	73.15	9.67E-02	3.95E-02	2.81E-02	0	0	1.15E-03	0	1.16E-03	3.04E-02	2.01E+04
60	36.27	69.73	1.01E-01	3.96E-02	2.85E-02	0	0	1.15E-03	0	1.16E-03	3.08E-02	1.98E+04
65	34.40	66.13	1.07E-01	3.96E-02	2.89E-02	0	0	1.15E-03	0	1.16E-03	3.12E-02	1.96E+04
70	32.45	62.38	1.13E-01	3.96E-02	2.94E-02	0	0	1.15E-03	0	1.16E-03	3.17E-02	1.93E+04

75	30.44	58.51	1.21E-01	3.96E-02	2.98E-02	0	0	1.15E-03	0	1.16E-03	3.22E-02	1.90E+04
80	28.38	54.56	1.30E-01	3.97E-02	3.04E-02	0	0	1.15E-03	0	1.16E-03	3.27E-02	1.87E+04
85	26.29	50.54	1.40E-01	3.97E-02	3.09E-02	0	0	1.15E-03	0	1.16E-03	3.32E-02	1.84E+04
90	26.35	50.65	1.40E-01	3.97E-02	3.09E-02	0	0	1.15E-03	0	1.16E-03	3.32E-02	1.84E+04
95	26.35	50.65	1.40E-01	3.97E-02	3.09E-02	0	0	1.15E-03	0	1.16E-03	3.32E-02	1.84E+04
100	26.35	50.65	1.40E-01	3.97E-02	3.09E-02	0	0	1.15E-03	0	1.16E-03	3.32E-02	1.84E+04

Heat transfer model continued from Table 8-10

Angle, °	Deposit surface, °C	Outer scale/deposit, °C	Metal/outer scale, °C	Inner scale/metal °C,	Steam/inner scale, °C	Steam, °C
0	589.89	589.89	589.89	565.03	565.03	540.00
5	589.86	589.86	589.86	565.01	565.01	540.00
10	589.77	589.77	589.77	564.97	564.97	540.00
15	589.62	589.62	589.62	564.89	564.89	540.00
20	589.41	589.41	589.41	564.79	564.79	540.00
25	589.14	589.14	589.14	564.65	564.65	540.00
30	588.82	588.82	588.82	564.49	564.49	540.00
35	588.44	588.44	588.44	564.30	564.30	540.00
40	588.01	588.01	588.01	564.08	564.08	540.00
45	587.53	587.53	587.53	563.84	563.84	540.00
50	587.01	587.01	587.01	563.58	563.58	540.00
55	586.44	586.44	586.44	563.30	563.30	540.00
60	585.84	585.84	585.84	563.00	563.00	540.00
65	585.21	585.21	585.21	562.68	562.68	540.00
70	584.55	584.55	584.55	562.35	562.35	540.00
75	583.86	583.86	583.86	562.00	562.00	540.00
80	583.16	583.16	583.16	561.65	561.65	540.00
85	582.44	582.44	582.44	561.29	561.29	540.00
90	582.44	582.44	582.44	561.29	561.29	540.00
95	582.44	582.44	582.44	561.29	561.29	540.00
100	582.44	582.44	582.44	561.29	561.29	540.00

8.3 Appendix C Fireside corrosion model

Table 8-11 Fireside corrosion damage of a T22 superheater tube

Operation time, *h*	T_m, ^{0}C	SO_x, vpm	Na_2SO_4, mg/cm^2/h	K_2SO_4, mg/cm^2/h	Corrosion rate, μm/(1000hours)
6000	5.92E+02	9.04E+02	3.32E+01	5.80E+01	78.69
7000	5.92E+02	9.04E+02	3.12E+01	4.88E+01	78.13
8000	5.92E+02	9.04E+02	2.86E+01	3.72E+01	77.45
9000	5.92E+02	9.04E+02	2.57E+01	2.34E+01	76.71
10000	5.91E+02	9.04E+02	2.24E+01	7.93E+00	75.94
11000	5.91E+02	9.04E+02	1.89E+01	-8.80E+00	75.16
12000	5.91E+02	9.04E+02	1.53E+01	-2.64E+01	74.39
13000	5.91E+02	9.04E+02	1.16E+01	-4.45E+01	73.64
14000	5.91E+02	9.04E+02	7.88E+00	-6.29E+01	73.11
15000	5.92E+02	9.04E+02	4.17E+00	-8.14E+01	72.65
16000	5.92E+02	9.04E+02	5.05E-01	-9.97E+01	72.25
17000	5.92E+02	9.04E+02	-3.09E+00	-1.18E+02	71.93
18000	5.93E+02	9.04E+02	-6.60E+00	-1.36E+02	71.68
19000	5.93E+02	9.04E+02	-1.00E+01	-1.53E+02	71.52
20000	5.94E+02	9.04E+02	-1.33E+01	-1.70E+02	71.45
21000	5.94E+02	9.04E+02	-1.65E+01	-1.86E+02	71.46
22000	5.95E+02	9.04E+02	-1.96E+01	-2.02E+02	71.22
23000	5.95E+02	9.04E+02	-2.25E+01	-2.17E+02	71.02
24000	5.95E+02	9.04E+02	-2.54E+01	-2.32E+02	70.88
25000	5.96E+02	9.04E+02	-2.81E+01	-2.46E+02	70.77
26000	5.96E+02	9.04E+02	-3.08E+01	-2.60E+02	70.72
27000	5.97E+02	9.04E+02	-3.33E+01	-2.73E+02	70.71
28000	5.97E+02	9.04E+02	-3.57E+01	-2.86E+02	70.60
29000	5.97E+02	9.04E+02	-3.81E+01	-2.98E+02	70.52
30000	5.98E+02	9.04E+02	-4.03E+01	-3.09E+02	70.47
31000	5.98E+02	9.04E+02	-4.25E+01	-3.21E+02	70.29
32000	5.98E+02	9.04E+02	-4.45E+01	-3.31E+02	70.13
33000	5.99E+02	9.04E+02	-4.65E+01	-3.42E+02	69.99
34000	5.99E+02	9.04E+02	-4.84E+01	-3.52E+02	69.86
35000	5.99E+02	9.04E+02	-5.02E+01	-3.62E+02	69.75
36000	5.99E+02	9.04E+02	-5.20E+01	-3.71E+02	69.66
37000	6.00E+02	9.04E+02	-5.37E+01	-3.80E+02	69.57
38000	6.00E+02	9.04E+02	-5.54E+01	-3.89E+02	69.50
39000	6.00E+02	9.04E+02	-5.70E+01	-3.97E+02	69.45
40000	6.00E+02	9.04E+02	-5.85E+01	-4.05E+02	69.40
41000	6.01E+02	9.04E+02	-6.00E+01	-4.13E+02	69.37
42000	6.01E+02	9.04E+02	-6.14E+01	-4.21E+02	69.35
43000	6.01E+02	9.04E+02	-6.28E+01	-4.28E+02	69.34

Operation time, *h*	T_m, ^{0}C	SO_x, vpm	Na_2SO_4, mg/cm^2/h	K_2SO_4, mg/cm^2/h	Corrosion rate, μm/(1000hours)
44000	6.01E+02	9.04E+02	-6.42E+01	-4.35E+02	69.34
45000	6.02E+02	9.04E+02	-6.55E+01	-4.42E+02	69.35
46000	6.02E+02	9.04E+02	-6.67E+01	-4.49E+02	69.36
47000	6.02E+02	9.04E+02	-6.80E+01	-4.55E+02	69.39
48000	6.03E+02	9.04E+02	-6.91E+01	-4.62E+02	69.43
49000	6.03E+02	9.04E+02	-7.03E+01	-4.68E+02	69.48
50000	6.03E+02	9.04E+02	-7.14E+01	-4.74E+02	69.53

8.4 Appendix D Steamside oxidation model

Table 8-12 Steamside metal losses

Time, h	Inner scale/metal, ^{0}C	Inner scale/metal, K	Initial inner oxide thickness, µm	Cumulative inner oxide thickness, µm	Metal loss, µm
5000	568.79	841.79	87.55	98.79	49.40
6000	568.99	841.99	98.79	108.99	54.49
7000	569.37	842.37	108.99	118.50	59.25
8000	569.69	842.69	118.50	127.45	63.72
9000	569.98	842.98	127.45	135.94	67.97
10000	570.27	843.27	135.94	144.06	72.03
11000	570.55	843.55	144.06	151.87	75.93
12000	570.84	843.84	151.87	159.41	79.70
13000	571.13	844.13	159.41	166.71	83.36
14000	571.61	844.61	166.71	173.90	86.95
15000	572.13	845.13	173.90	181.00	90.50
16000	572.69	845.69	181.00	188.04	94.02
17000	573.30	846.30	188.04	195.06	97.53
18000	573.96	846.96	195.06	202.07	101.03
19000	574.67	847.67	202.07	209.11	104.56
20000	575.43	848.43	209.11	216.21	108.11
21000	576.26	849.26	216.21	223.40	111.70
22000	576.80	849.80	223.40	230.57	115.28
23000	577.36	850.36	230.57	237.73	118.87
24000	577.94	850.94	237.73	244.90	122.45
25000	578.54	851.54	244.90	252.10	126.05
26000	579.16	852.16	252.10	259.33	129.67
27000	579.81	852.81	259.33	266.62	133.31
28000	580.33	853.33	266.62	273.91	136.95
29000	580.85	853.85	273.91	281.21	140.60
30000	581.39	854.39	281.21	288.53	144.26
31000	581.77	854.77	288.53	295.82	147.91
32000	582.15	855.15	295.82	303.07	151.54
33000	582.52	855.52	303.07	310.30	155.15
34000	582.90	855.90	310.30	317.51	158.76
35000	583.27	856.27	317.51	324.70	162.35
36000	583.64	856.64	324.70	331.87	165.94
37000	584.02	857.02	331.87	339.03	169.52
38000	584.39	857.39	339.03	346.18	173.09
39000	584.76	857.76	346.18	353.33	176.66
40000	585.12	858.12	353.33	360.47	180.23

8.5 Appendix E Combined model

8.5.1 E.1 Hoop stress and the remaining service life of superheater/reheater tubes

Table 8-13 Hoop stress acting on T22 superheater tube wall

Operation time, h	Outer diameter of the tube at the start of exposure period, *m*	Wall thickness at the start of exposure period, *m*	Fireside damage rate after X hours, *m*/1000 *h*	Steamside damage after X hours, *m*/? *h*	Change in wall thickness due to creep strain, *m*/? *h*	Outer diameter at the end of exposure period, *m*	Wall thickness at the end of the exposure period, *m*	Thin-walled hoop stress, MPa
6000	4.42E-02	6.93E-03	7.87E-05	5.45E-05	6.29E-07	4.41E-02	6.80E-03	49.36
7000	4.41E-02	6.80E-03	7.81E-05	5.92E-05	6.29E-07	4.39E-02	6.66E-03	50.36
8000	4.39E-02	6.66E-03	7.74E-05	6.37E-05	6.29E-07	4.38E-02	6.52E-03	51.44
9000	4.38E-02	6.52E-03	7.67E-05	6.80E-05	6.28E-07	4.36E-02	6.37E-03	52.60
10000	4.36E-02	6.37E-03	7.59E-05	7.20E-05	6.28E-07	4.35E-02	6.22E-03	53.85
11000	4.35E-02	6.22E-03	7.52E-05	7.59E-05	6.28E-07	4.33E-02	6.07E-03	55.20
12000	4.33E-02	6.07E-03	7.44E-05	7.97E-05	6.28E-07	4.32E-02	5.92E-03	56.65
13000	4.32E-02	5.92E-03	7.36E-05	8.34E-05	6.28E-07	4.30E-02	5.76E-03	58.22
14000	4.30E-02	5.76E-03	7.31E-05	8.70E-05	6.29E-07	4.29E-02	5.60E-03	59.92
15000	4.29E-02	5.60E-03	7.26E-05	9.05E-05	6.29E-07	4.27E-02	5.43E-03	61.75
16000	4.27E-02	5.43E-03	7.22E-05	9.40E-05	6.29E-07	4.26E-02	5.27E-03	63.75
17000	4.26E-02	5.27E-03	7.19E-05	9.75E-05	6.30E-07	4.24E-02	5.10E-03	65.92
18000	4.24E-02	5.10E-03	7.17E-05	1.01E-04	6.30E-07	4.23E-02	4.92E-03	68.30
19000	4.23E-02	4.92E-03	7.15E-05	1.05E-04	6.30E-07	4.21E-02	4.75E-03	70.90
20000	4.21E-02	4.75E-03	7.14E-05	1.08E-04	6.31E-07	4.20E-02	4.57E-03	73.77
21000	4.20E-02	4.57E-03	7.15E-05	1.12E-04	6.32E-07	4.19E-02	4.38E-03	76.95
22000	4.19E-02	4.38E-03	7.12E-05	1.15E-04	6.32E-07	4.17E-02	4.20E-03	80.48

Operation time, h	Outer diameter of the tube at the start of exposure period, *m*	Wall thickness at the start of exposure period, *m*	Fireside damage rate after X hours, *m*/1000 *h*	Steamside damage after X hours, *m*/? *h*	Change in wall thickness due to creep strain, *m*/? *h*	Outer diameter at the end of exposure period, *m*	Wall thickness at the end of the exposure period, *m*	Thin-walled hoop stress, MPa
23000	4.17E-02	4.20E-03	7.10E-05	1.19E-04	6.33E-07	4.16E-02	4.01E-03	84.42
24000	4.16E-02	4.01E-03	7.09E-05	1.22E-04	6.34E-07	4.14E-02	3.81E-03	88.84
25000	4.14E-02	3.81E-03	7.08E-05	1.26E-04	6.35E-07	4.13E-02	3.61E-03	93.83
26000	4.13E-02	3.61E-03	7.07E-05	1.30E-04	6.36E-07	4.11E-02	3.41E-03	99.51
27000	4.11E-02	3.41E-03	7.07E-05	1.33E-04	6.37E-07	4.10E-02	3.21E-03	106.04
28000	4.10E-02	3.21E-03	7.06E-05	1.37E-04	6.38E-07	4.09E-02	3.00E-03	113.60
29000	4.09E-02	3.00E-03	7.05E-05	1.41E-04	6.39E-07	4.07E-02	2.79E-03	122.46
30000	4.07E-02	2.79E-03	7.05E-05	1.44E-04	6.40E-07	4.06E-02	2.57E-03	132.97
31000	4.06E-02	2.57E-03	7.03E-05	1.48E-04	6.41E-07	4.04E-02	2.35E-03	145.63
32000	4.04E-02	2.35E-03	7.01E-05	1.52E-04	6.43E-07	4.03E-02	2.13E-03	161.17
33000	4.03E-02	2.13E-03	7.00E-05	1.55E-04	6.44E-07	4.02E-02	1.91E-03	180.67
34000	4.02E-02	1.91E-03	6.99E-05	1.59E-04	6.46E-07	4.00E-02	1.68E-03	205.86
35000	4.00E-02	1.68E-03	6.98E-05	1.62E-04	6.47E-07	3.99E-02	1.44E-03	239.63
36000	3.99E-02	1.44E-03	6.97E-05	1.66E-04	6.49E-07	3.97E-02	1.21E-03	287.24
37000	3.97E-02	1.21E-03	6.96E-05	1.70E-04	6.50E-07	3.96E-02	9.68E-04	359.33
38000	3.96E-02	9.68E-04	6.95E-05	1.73E-04	6.52E-07	3.95E-02	7.24E-04	481.28
39000	3.95E-02	7.24E-04	6.94E-05	1.77E-04	6.54E-07	3.93E-02	4.78E-04	731.93
40000	3.93E-02	4.78E-04	6.94E-05	1.80E-04	6.56E-07	3.92E-02	2.27E-04	1542.00
41000	3.92E-02	2.27E-04	6.94E-05	1.84E-04	6.57E-07	3.90E-02	-2.64E-05	-13300.10

Table 8-14 Remaining service life of T22 superheater tube

Operation time, h	Tube midwall temperature, °C	Creep rate, 1/*h*	Rupture lifetime, h
6000	582.62	1.32E-06	7.95E+04
7000	582.64	1.41E-06	7.54E+04
8000	582.68	1.52E-06	7.14E+04
9000	582.72	1.64E-06	6.74E+04
10000	582.78	1.77E-06	6.33E+04
11000	582.86	1.93E-06	5.93E+04
12000	582.95	2.11E-06	5.54E+04
13000	583.25	2.34E-06	5.12E+04
14000	583.59	2.61E-06	4.70E+04
15000	583.99	2.93E-06	4.30E+04
16000	584.44	3.31E-06	3.91E+04
17000	584.95	3.78E-06	3.53E+04
18000	585.51	4.35E-06	3.17E+04
19000	586.15	5.05E-06	2.82E+04
20000	586.84	5.92E-06	2.50E+04
21000	587.26	6.92E-06	2.21E+04
22000	587.71	8.17E-06	1.95E+04
23000	588.18	9.75E-06	1.70E+04
24000	588.67	1.18E-05	1.47E+04
25000	589.19	1.44E-05	1.26E+04
26000	589.73	1.79E-05	1.06E+04
27000	590.15	2.24E-05	8.93E+03
28000	590.59	2.87E-05	7.39E+03
29000	591.04	3.74E-05	6.02E+03
30000	591.33	4.96E-05	4.84E+03
31000	591.63	6.78E-05	3.80E+03
32000	591.93	9.59E-05	2.91E+03
33000	592.23	1.42E-04	2.15E+03
34000	592.53	2.20E-04	1.53E+03
35000	592.83	3.68E-04	1.03E+03
36000	593.13	6.78E-04	6.43E+02
37000	593.43	1.44E-03	3.60E+02
38000	593.74	3.81E-03	1.69E+02
39000	594.04	1.54E-02	5.77E+01
40000	594.35	1.82E-01	8.56E+00
41000	594.66	#NUM!	#NUM!

Table 8-15 Hoop stress acting on P92 superheater tube wall

Operation time, *h*	Outer diameter of the tube at the start of exposure period, *m*	Wall thickness at the start of exposure period, *m*	Fireside damage rate after X hours, m/1000h	Steamside damage after X hours, m/?h	Change in wall thickness due to creep strain, m/?h	Outer diameter at the end of exposure period, *m*	Wall thickness at the end of the exposure period, m/?h	Thin-walled hoop stress, MPa
0	4.50E-02	7.50E-03	0	0	0	4.50E-02	7.50E-03	45.00
1000	4.50E-02	7.50E-03	7.67E-05	1.02E-05	6.33E-07	4.48E-02	7.41E-03	45.45
2000	4.48E-02	7.41E-03	7.40E-05	1.44E-05	6.32E-07	4.47E-02	7.32E-03	45.93
3000	4.47E-02	7.32E-03	7.31E-05	1.76E-05	6.31E-07	4.46E-02	7.23E-03	46.44
4000	4.46E-02	7.23E-03	7.46E-05	2.04E-05	6.30E-07	4.44E-02	7.14E-03	47.00
5000	4.44E-02	7.14E-03	7.48E-05	2.28E-05	6.29E-07	4.43E-02	7.04E-03	47.59
6000	4.43E-02	7.04E-03	7.46E-05	2.50E-05	6.28E-07	4.41E-02	6.94E-03	48.21
7000	4.41E-02	6.94E-03	7.37E-05	2.69E-05	6.27E-07	4.40E-02	6.84E-03	48.87
8000	4.40E-02	6.84E-03	7.27E-05	2.88E-05	6.26E-07	4.38E-02	6.73E-03	49.55
9000	4.38E-02	6.73E-03	7.17E-05	3.05E-05	6.26E-07	4.37E-02	6.63E-03	50.26
10000	4.37E-02	6.63E-03	7.07E-05	3.22E-05	6.25E-07	4.35E-02	6.53E-03	51.01
11000	4.35E-02	6.53E-03	6.97E-05	3.37E-05	6.24E-07	4.34E-02	6.42E-03	51.78
12000	4.34E-02	6.42E-03	6.87E-05	3.52E-05	6.24E-07	4.33E-02	6.32E-03	52.59
13000	4.33E-02	6.32E-03	6.77E-05	3.66E-05	6.23E-07	4.31E-02	6.21E-03	53.44
14000	4.31E-02	6.21E-03	6.69E-05	3.80E-05	6.23E-07	4.30E-02	6.11E-03	54.32
15000	4.30E-02	6.11E-03	6.61E-05	3.93E-05	6.22E-07	4.28E-02	6.00E-03	55.24
16000	4.28E-02	6.00E-03	6.53E-05	4.06E-05	6.22E-07	4.27E-02	5.90E-03	56.20
17000	4.27E-02	5.90E-03	6.46E-05	4.19E-05	6.21E-07	4.26E-02	5.79E-03	57.20
18000	4.26E-02	5.79E-03	6.40E-05	4.31E-05	6.21E-07	4.25E-02	5.68E-03	58.26
19000	4.25E-02	5.68E-03	6.34E-05	4.43E-05	6.21E-07	4.23E-02	5.57E-03	59.36
20000	4.23E-02	5.57E-03	6.29E-05	4.55E-05	6.20E-07	4.22E-02	5.46E-03	60.52

Operation time, *h*	Outer diameter of the tube at the start of exposure period, *m*	Wall thickness at the start of exposure period, *m*	Fireside damage rate after X hours, m/1000h	Steamside damage after X hours, m/?h	Change in wall thickness due to creep strain, m/?h	Outer diameter at the end of exposure period, *m*	Wall thickness at the end of the exposure period, m/?h	Thin-walled hoop stress, MPa
21000	4.22E-02	5.46E-03	6.24E-05	4.66E-05	6.20E-07	4.21E-02	5.35E-03	61.73
22000	4.21E-02	5.35E-03	6.18E-05	4.77E-05	6.20E-07	4.20E-02	5.24E-03	63.00
23000	4.20E-02	5.24E-03	6.13E-05	4.89E-05	6.20E-07	4.18E-02	5.13E-03	64.34
24000	4.18E-02	5.13E-03	6.08E-05	4.99E-05	6.19E-07	4.17E-02	5.02E-03	65.75
25000	4.17E-02	5.02E-03	6.04E-05	5.10E-05	6.19E-07	4.16E-02	4.91E-03	67.23
26000	4.16E-02	4.91E-03	5.99E-05	5.21E-05	6.19E-07	4.15E-02	4.80E-03	68.80
27000	4.15E-02	4.80E-03	5.95E-05	5.31E-05	6.19E-07	4.14E-02	4.68E-03	70.45
28000	4.14E-02	4.68E-03	5.91E-05	5.41E-05	6.19E-07	4.12E-02	4.57E-03	72.20
29000	4.12E-02	4.57E-03	5.87E-05	5.51E-05	6.19E-07	4.11E-02	4.46E-03	74.04
30000	4.11E-02	4.46E-03	5.83E-05	5.61E-05	6.19E-07	4.10E-02	4.34E-03	76.00
31000	4.10E-02	4.34E-03	5.79E-05	5.71E-05	6.19E-07	4.09E-02	4.23E-03	78.08
32000	4.09E-02	4.23E-03	5.75E-05	5.80E-05	6.19E-07	4.08E-02	4.11E-03	80.29
33000	4.08E-02	4.11E-03	5.72E-05	5.90E-05	6.19E-07	4.07E-02	3.99E-03	82.65
34000	4.07E-02	3.99E-03	5.68E-05	5.99E-05	6.19E-07	4.05E-02	3.88E-03	85.16
35000	4.05E-02	3.88E-03	5.65E-05	6.08E-05	6.19E-07	4.04E-02	3.76E-03	87.84
36000	4.04E-02	3.76E-03	5.62E-05	6.17E-05	6.19E-07	4.03E-02	3.64E-03	90.72
37000	4.03E-02	3.64E-03	5.58E-05	6.26E-05	6.19E-07	4.02E-02	3.52E-03	93.80
38000	4.02E-02	3.52E-03	5.55E-05	6.35E-05	6.19E-07	4.01E-02	3.40E-03	97.13
39000	4.01E-02	3.40E-03	5.53E-05	6.43E-05	6.19E-07	4.00E-02	3.28E-03	100.71
40000	4.00E-02	3.28E-03	5.50E-05	6.52E-05	6.19E-07	3.99E-02	3.16E-03	104.60
41000	3.99E-02	3.16E-03	5.47E-05	6.60E-05	6.20E-07	3.98E-02	3.04E-03	108.81
42000	3.98E-02	3.04E-03	5.45E-05	6.69E-05	6.20E-07	3.97E-02	2.92E-03	113.40
43000	3.97E-02	2.92E-03	5.42E-05	6.77E-05	6.20E-07	3.95E-02	2.79E-03	118.43

Operation time, *h*	Outer diameter of the tube at the start of exposure period, *m*	Wall thickness at the start of exposure period, *m*	Fireside damage rate after X hours, m/1000h	Steamside damage after X hours, m/?h	Change in wall thickness due to creep strain, m/?h	Outer diameter at the end of exposure period, *m*	Wall thickness at the end of the exposure period, m/?h	Thin-walled hoop stress, MPa
44000	3.95E-02	2.79E-03	5.40E-05	6.85E-05	6.20E-07	3.94E-02	2.67E-03	123.94
45000	3.94E-02	2.67E-03	5.38E-05	6.93E-05	6.21E-07	3.93E-02	2.55E-03	130.02
46000	3.93E-02	2.55E-03	5.36E-05	7.01E-05	6.21E-07	3.92E-02	2.42E-03	136.76
47000	3.92E-02	2.42E-03	5.34E-05	7.09E-05	6.21E-07	3.91E-02	2.30E-03	144.26
48000	3.91E-02	2.30E-03	5.32E-05	7.17E-05	6.21E-07	3.90E-02	2.17E-03	152.68
49000	3.90E-02	2.17E-03	5.30E-05	7.25E-05	6.22E-07	3.89E-02	2.05E-03	162.18
50000	3.89E-02	2.05E-03	5.28E-05	7.32E-05	6.22E-07	3.88E-02	1.92E-03	172.98

Table 8-16 Remaining service life of P92 superheater tube

Operation time, *h*	Tube mid-wall temperature, ^{0}C	Creep rate, 1/h	Rupture lifetime, *h*
0	579.67	6.07E-08	2.28E+05
1000	580.05	6.62E-08	2.13E+05
2000	581.10	7.25E-08	1.97E+05
3000	581.67	7.98E-08	1.82E+05
4000	582.22	8.84E-08	1.67E+05
5000	582.55	9.85E-08	1.53E+05
6000	582.62	1.10E-07	1.40E+05
7000	582.64	1.24E-07	1.27E+05
8000	582.68	1.40E-07	1.15E+05
9000	582.72	1.58E-07	1.04E+05
10000	582.78	1.79E-07	9.35E+04
11000	582.86	2.04E-07	8.39E+04
12000	582.95	2.34E-07	7.51E+04
13000	583.25	2.68E-07	6.71E+04
14000	583.59	3.09E-07	5.97E+04
15000	583.99	3.57E-07	5.30E+04
16000	584.44	4.14E-07	4.68E+04
17000	584.95	4.83E-07	4.13E+04
18000	585.51	5.65E-07	3.62E+04
19000	586.15	6.65E-07	3.17E+04
20000	586.84	7.85E-07	2.76E+04
21000	587.26	9.32E-07	2.40E+04
22000	587.71	1.11E-06	2.07E+04
23000	588.18	1.33E-06	1.79E+04
24000	588.67	1.61E-06	1.53E+04
25000	589.19	1.95E-06	1.30E+04
26000	589.73	2.38E-06	1.11E+04
27000	590.15	2.92E-06	9.35E+03
28000	590.59	3.61E-06	7.85E+03
29000	591.04	4.49E-06	6.56E+03
30000	591.33	5.62E-06	5.44E+03
31000	591.63	7.10E-06	4.49E+03
32000	591.93	9.04E-06	3.68E+03
33000	592.23	1.16E-05	3.00E+03
34000	592.53	1.50E-05	2.42E+03
35000	592.83	1.96E-05	1.94E+03
36000	593.13	2.59E-05	1.54E+03
37000	593.43	3.46E-05	1.22E+03
38000	593.74	4.68E-05	9.48E+02
39000	594.04	6.40E-05	7.32E+02

Operation time, *h*	Tube mid-wall temperature, ^{0}C	Creep rate, 1/h	Rupture lifetime, *h*
40000	594.35	8.88E-05	5.59E+02
41000	594.66	1.25E-04	4.22E+02
42000	594.97	1.79E-04	3.14E+02
43000	595.28	2.60E-04	2.31E+02
44000	595.59	3.85E-04	1.67E+02
45000	595.90	5.82E-04	1.19E+02
46000	596.21	9.00E-04	8.27E+01
47000	596.53	1.43E-03	5.65E+01
48000	596.85	2.33E-03	3.77E+01
49000	597.17	3.93E-03	2.45E+01
50000	597.49	6.86E-03	1.55E+01